AN EXPERIMENTAL AND NUMERICAL INVESTIGATION OF A TURBULENT AIRFOIL WAKE IN A 90^{o} CURVED DUCT

A thesis submitted for the degree of Doctor of Philosophy

By

Nadarajah Piradeepan

Department of Mechanical Engineering, Brunel University

April 2002

This thesis is dedicated to the memory of my late father

Dr. K. Nadarajah

Abstract

A wake behind solid bodies subjected to extra rates of strain due to streamwise curvature and pressure gradient occurs in numerous engineering applications. The broad aim of this experimental and numerical study was to improve the present understanding of an airfoil wake subjected to simultaneous effects of streamwise curvature and pressure gradient.

The experimental work was conducted using an open return type wind tunnel, which consisted of a square closed working test section incorporating a straight upstream tangent and a 90° bend with radius to height ratio of 1.17. A symmetrical NACA 0012 airfoil of 0.150 m chord length was used as the wake generating body, where the trailing edge of which was located at a distance of one chord length upstream of the bend entry plane. The measurement stations, 1 to 5, were located at one duct height upstream of the bend, at 0°, 45°, 90° and also at one duct height downstream of the bend. At each station, the mean and turbulence quantities were obtained in both normal (radial) and spanwise directions using hot-wire anemometry. The measured turbulence quantities were the normal intensities $\overline{u'^2}$, $\overline{v'^2}$, $\overline{w'^2}$ and turbulence shear stresses $-\overline{u'v'}$ and $-\overline{u'w'}$. In addition, the static pressure distributions along the concave and convex walls of the test section, on the airfoil and in the normal (radial) direction at each station were measured. The measurements were carried out at three mainstream velocities, namely, 10, 15 and 20 m/s.

In the numerical part of the work, the three-dimensional, incompressible, steady state and turbulent flow in the duct with the airfoil was computed using four different turbulence models, namely, the standard k-ε model, Reynolds Stress Model, Realizable k-ε model and RNG k-ε model. The mean and turbulence quantities obtained experimentally at one duct height upstream of the bend were used as the inlet boundary conditions for the simulation. The discretisation of the governing equations was based on the finite volume technique where two discretisation schemes, namely, QUICK and upwind were used in conjunction with the above turbulence models. The modelling of the turbulent flow near the walls was achieved using the two-layer zonal model.

The profiles obtained experimentally in the spanwise direction showed that the mean and turbulence quantities were symmetrical with respect to the central plane (z/H = 0.5) of

the flow domain. The normal profiles at two spanwise locations, namely, z/H = 0.5 and 0.6 at each measuring station showed an asymmetric wake structure about the wake centreline due to the simultaneous effects of streamwise curvature and pressure gradient. The results showed that the turbulence intensities and shear stresses were affected strongly by the combined curvature and pressure gradient.

The three-dimensional computation predicted the overall features of the flow satisfactorily. All turbulence models predicted the trends exhibited in the experimental static pressure distribution on the concave and convex walls closely. However, at each measuring station, the peak value and the shift of the wake region were over-predicted by all turbulence models. The predicted Reynolds stresses $\overline{u'^2}$, $\overline{v'^2}$, $\overline{w'^2}$ and $-\overline{u'v'}$ showed good agreement with the experimental profiles at stations 2 to 4. The comparison with the standard k-ε model confirmed that the additional terms and functions in the RNG and Realizable k-ε models can significantly improve the prediction of complex flows. Also, the use of the two-layer zonal model on the airfoil was found to be superior to the standard wall functions method, which led to improved results, particularly in the wake region.

Contents

Page

Acknowledgements

I would like to express my gratitude to my supervisor Dr. M. R. Mokhtarzadeh-Dehghan for his continuing support, personal encouragement, careful reading and correction of the thesis, supervision of the work and numerous other kinds of help during the past years of the study. All these contributed significantly to improve the standard of my thesis. Also, thanks to my second supervisor Dr. I. Barton for his helpful discussion and advice during the transfer to PhD examination.

I am grateful to the former head of Mechanical Engineering Department, Professor. N. Ladommatos and also Professor. L. Wrobel for providing me the position as a research student in the department and the financial support from Brunel University.

I would like to take this opportunity to thank the technicians and administrative staff of Mechanical Engineering Department, particularly Mr. Robert Bob Webb, Mr. John Langdon, Mr. Tony Whitby, Mr. Brian Dear, Mr. Clive Barrett, Mr. Keith Withers and late Mr. Allan Dunton for their support of the experimental work.

I would like to give my special thanks to Mr. Peter Jones from DANTEC Ltd for his kind visits and technical support with respect to the use of the hot-wire anemometry system employed in the experimental investigation.

I am deeply grateful to my mother, sister, brothers and wife for their invaluable support and encouragement during my PhD studies.

Last, but not least, I would like to thank my colleagues in the Mechanical Engineering Department, particularly Dr. Sukin Nadarajan for his support in relation to the presentation of the work.

Declaration

The work presented in this thesis has not been previously submitted for a degree or other qualification of any university or institution.

Nomenclature

A	King's law constant
A_t, A_d	Two-layer zonal model constants
A	Area
A_0	Constant in Realizable k-ε model
A_s	Function of velocity gradient in Realizable k-ε model
a	Matrix coefficient
B	King's law constant
b	Wake width
b'	Wake half-width
b'_{total}	Sum of inner and outer wake half-widths
C	Dimensionless constant, Convective term
C_1, C_2, C_3, C_4	Turbulence model constants
C_p	Pressure coefficient
C_μ	k-ε model constant
c	Airfoil chord length, Constant
D	Diffusion term
D_{ij}^T	Turbulent diffusion term in RSM transport equation
d	Circular cylinder diameter, Distance
E	Output voltage of hot-wire Anemometry
E	Log-law constant
e_{ij}	Rate of strain tensor
F_{max}	Highest frequency
f_s	Sampling frequency
f_0	Frequency scale
g	Gravitational acceleration
H	Shape factor = δ^*/θ, Duct height
h	Height
h	Pitch factor coefficient
k_1	Yaw coefficient
k	Turbulence kinetic energy
L	Duct length

ℓ	Length
n	King's law constant
$\mathbf{n}$	Normal vector
O_{ij}	Rotation term in RSM transport equation
$\mathbf{P}_k$	Shear production of k in k-ε model
P	Pressure
$\overline{P}$	Time-averaged Pressure
P'	Pressure correction
P_{ij}	Shear production term in RSM transport equation
P^*	Guessed pressure
P^{**}	Correct pressure field
R	Radius of curvature, Universal gas constant, Residual
R_i, R_o	Duct inner radius and outer radius, respectively
Re	Reynolds number
S	Source term, Span
T	Temperature
t	Time
U,V,W	Instantaneous velocity component in x-, y- and z- directions
$\overline{U},\overline{V},\overline{W}$	Time-averaged velocity component in x-, y- and z- directions
U_o	Mainstream velocity
U_p	Wake centreline potential velocity
$\mathbf{U}$	Velocity vector
U^*	Guessed velocity, Function of velocity gradient in Realizable k-ε model
U^{**}	Correct velocity field
U_N, U_T, U_Z	Velocity components in normal- tangential- and spanwise-directions of hot-wire sensor
U_1, U_2	Velocity components in probe coordinate system
U_e	Effective cooling velocity
U_{cal}	Calibration velocity
Urms	Streamwise intensity, $\sqrt{\overline{u'^2}}$
U'	Velocity correction
U_i	Velocity tensor

u^+	Non-dimensional velocity in wall region
u', v', w'	Fluctuating velocity component in x-, y- and z- directions
$\overline{u'^2}$, $\overline{v'^2}$, $\overline{w'^2}$	Time-averaged fluctuating velocity component in x-, y- and z- directions
$-\overline{u'v'}$	Turbulence shear stress
$-\overline{u'w'}$	Turbulence shear stress
Vrms	Normal intensity, $\sqrt{\overline{v'^2}}$
$-\overline{v'w'}$	Turbulence shear stress
W	Duct width
Wrms	Spanwise intensity, $\sqrt{\overline{w'^2}}$
w	Width
x, y, z	Cartesian coordinates
y^+	Non-dimensional distance from wall

Greek symbols

α	Angle
α_k , α_ε	RNG turbulence model constants
β	RNG turbulence model constant
Γ	Diffusion coefficient
Δh	Pressure difference
δ^*	Displacement thickness
δ	Boundary layer thickness, Control volume width
δ_{ij}	Kronecker delta
δ_x	Distance between cell nodes
ε	Rate of dissipation of kinetic energy
θ	Momentum thickness, Variable in QUICK scheme
$\bar{\theta}$	Mean angle between hot-wire sensor and x-axis
ϑ	Velocity scale
κ	Log-law constant
μ	Dynamic viscosity
μ_t	Turbulent viscosity
μ_{eff}	Effective viscosity

ν	Kinematic viscosity
ρ	Density
σ_ε	Turbulent Prandtl number in ε-transport equation
σ_k	Turbulent Prandtl number in k-transport equation
τ_{ij}	Laminar shear stress
τ_w	Wall shear stress
Φ	Variable parameter
$\overline{\Phi}$	Time-averaged value of variable Φ
Φ'	Fluctuating part of variable Φ
ϕ_{ij}	Pressure-strain term in RSM transport equation
ω_k	Angular velocity
f	Under-relaxation factor

Subscripts

a	Ambient conditions
i, j, k	Tensor notation
k	Turbulent kinetic energy
nn	Nearest neighbour
o	Reference value
P	Current point or node
t	Turbulent flow condition
W	West node of a control volume (E for east node)
w	Water, west face of a control volume (e for east face)
ε	Rate of energy dissipation

Superscripts

/	Correction
+	Non-dimensionalized on wall variables
T	Turbulent

Chapter 1

1. INTRODUCTION

1.1. Background

1.1.1. Free turbulent flows

Turbulent flows which are not directly influenced by solid walls are known as free turbulent flows. These flows are among the simplest turbulent flows of significant engineering importance. They can be divided into three main categories, namely, mixing layers, jets and wakes. Figure 1.1 shows the mean velocity profiles for these three types of free turbulent flow categories. In Figure 1.1a, the mixing layer forms at the interface of two fluids moving at different speeds in the same general direction. The region in between the two streams become unstable due to the discontinuity in the velocities, which gives rise to a turbulent mixing layer downstream of the point where the two streams first meet. As a result of the enhanced mixing process, the width of the mixing region increases with distance in the downstream direction. Such condition occurs in a number of practical situations, e.g. jets and plumes in cross flows and flow in sudden expansion ducts.

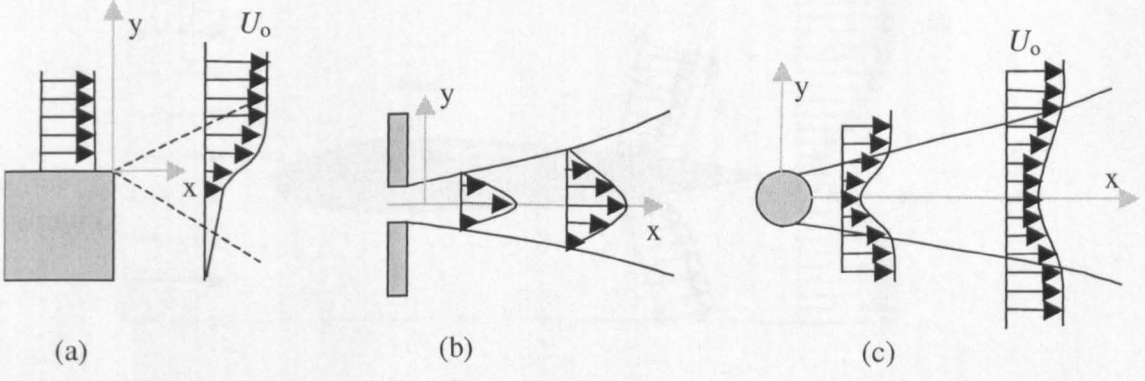

Figure 1.1: Free turbulent flows: (a) mixing layer, (b) jet, (c) wake, Schlichting (1979).

A jet (Figure 1.1b) forms when a region of high-speed flow meets a relatively low speed or stationary fluid in the surrounding region. Such condition occurs when a fluid is

discharged from a gas turbine nozzle and in flow through an orifice. In jets, the discontinuity in the velocities is greater than in the mixing layer, which causes vigorous mixing in the downstream direction. As a result, the jet becomes completely turbulent at a short distance from the point of discharge. Furthermore, the fast moving fluid of the jet becomes partially mixed with the surrounding fluid and loses its momentum to speed up the stationary or slow moving fluid in the surrounding. The process increases the mass flow in the downstream direction, but as the distance increases the jet spreads out and the mean speed of the jet decreases which leads to the conservation of momentum of the jet. The present study is concerned primarily with the wake of an airfoil, therefore, the wake of a body is discussed in more detail in following section.

1.1.2. Wake

A wake is one of the important flow regions in the fields of aerodynamics and hydrodynamics. Also, it forms in numerous practical situations, e.g. behind a solid body, such as an airfoil placed in a stream of fluid, where the boundary layers formed on the body come into contact as the sudden removal of the solid surface takes place. Therefore, the velocity in the wake region is smaller compared with the mainstream velocity as shown in Figure 1.2. However, as the distance from the body increases, the differences between the velocities in the wake and the mainstream region gradually become smaller and smaller.

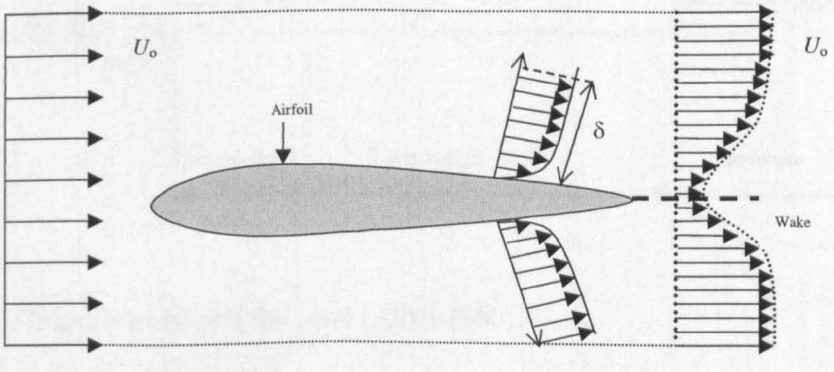

Figure 1.2: Symmetrical wake of an airfoil.

At some stage as the distance increases in the downstream direction, the wake reaches the so-called asymptotic state, where the distributions of mean and turbulence quantities

normalized with respect to characteristic length and velocity scales become fully independent of streamwise location. Ramaprian et al. (1982) states the asymptotic stage for the wake of a flat plate to be at a distance of $x/\theta \geq 350$, where x is the streamwise distance from the trailing edge and θ is the momentum thickness. Similar investigation by Alber (1980) indicates that the wake region between the trailing edge of the body and the beginning of the asymptotic stage (far-wake) can be further divided into two regions, near-wake region and intermediate-wake region as shown in Figure 1.3. In the near-wake region the laminar inner wake grows into the trailing edge laminar sublayer. According to Ramaprian et al. (1982) the near-wake extends downstream from the trailing edge to $x/\theta < 25$. Furthermore, Alber (1980) shows that the near-wake region is approximately ten initial sublayer thicknesses long measured from the wake generating body. In the intermediate-wake region ($25 < x/\theta < 350$), the turbulent inner layer grows into the initial logarithmic layer of the boundary layer on the body, where the influence of the upstream wall layer is insignificant. In this region the wake develops as a free turbulent flow with a slower rate of growth and decay of the centreline defect than either in the near-wake or in the far-wake region (Ramaprian et al., 1982). Alber (1980) reported the length of this region is approximately ten initial boundary layer thicknesses.

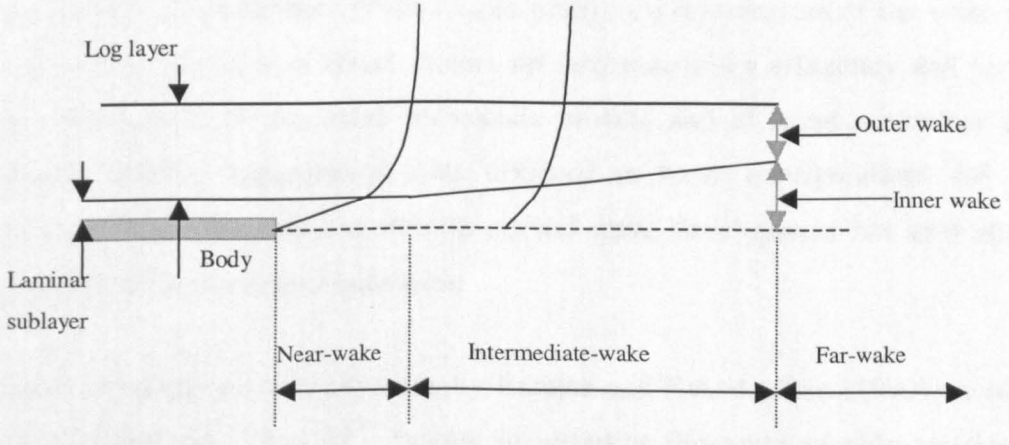

Figure 1.3: Wake regions of a flat plate (Alber 1980).

Due to practical importance of wake flows, particularly behind the streamline bodies, such as an airfoil or thin flat plate, their study have received significant attention in the past few decades. The first extensive experimental study of this flow was done by Chevray & Kovasznay (1969). Since then numerous studies of wakes have been reported

in the literature, but mainly on wakes not subjected to streamline curvature or pressure gradient. But, there are a number of practical situations where a turbulent wake is subjected to extra rates of strain due to the streamwise curvature and pressure gradient. Due to these effects, such flows are classified as complex turbulent flows (Bradshaw, 1976).

Previous studies by many investigators, like Tulapurkara et al. (1994, 1995), Ramjee and Neelakandan (1990), Starke et al. (1999) show that the mean and turbulence quantities in the wake region are significantly affected by the streamwise curvature and pressure gradient. Examples of such flows are in bends with guide vanes, heat exchangers, turbomachines, aircraft intake, and multi-element airfoil. During the high-lift condition, the wake of an airfoil wing develops under the combined influence of curvature and pressure gradient and interacts with the flow over the flaps. The prediction of such flows using turbulence models is complex. Therefore, recent experimental research on turbulent curved wakes of streamline and bluff bodies is motivated by the needs of aircraft industry for a better understanding of the flow around an airfoil in high-lift condition. Secondly, in the field of turbomachinery aerodynamics, the curved turbulent wake generated by the blade influences the boundary layer transition behaviour and the heat transfer characteristics of the blades positioned downstream of the wake (Schobeiri et al., 1996). Because of direct impact on turbomachinery efficiency and performance, the development of advanced turbulence models and efficient numerical techniques requires reliable experimental data obtained in basic configurations for validation purposes. Therefore, the research on curved wake development has also attracted the interest of turbomachinery industries.

Recent experimental investigations by Ramjee and Neelakandan (1990) on wakes have indicated that the effects of curvature in turbulent flows are roughly ten times greater than those in laminar flows. Tulapurkara et al. (1995) show that the mean and turbulence quantities of a curved wake become more and more asymmetric with the increase of streamwise distance and also the turbulence shear stress is more sensitive to the curvature than the normal stresses. According to Bradshaw (1973) even a very small value of the curvature parameter can change significantly the Reynolds stresses of turbulent flow. Tulapurkara et al. (1994) show that an additional strain due to pressure gradient makes

the asymmetric profiles of the mean and turbulence quantities due to curvature even more asymmetric and causes a slower decay of velocity defect. The flow configuration shown in Figure 1.4 is the subject of the present investigation. The wake developing in such a duct experiences the combined effects of streamline curvature and pressure gradient. Due to these effects, the half-width of the wake increases on the inner side and decreases on the outer side. The inner side and outer side regions of the wake are the regions between the centreline of the wake and the convex and concave walls, respectively.

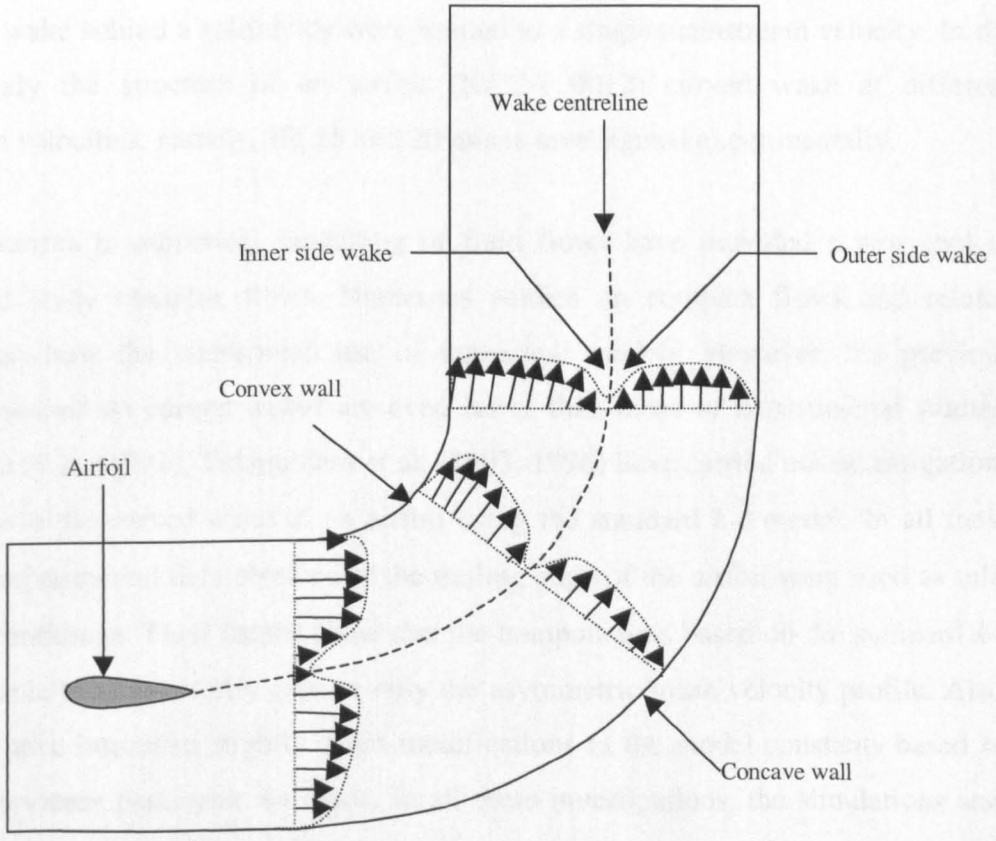

Figure 1.4: Airfoil wake developing in a bend.

Most of the research conducted on wakes deals with two-dimensional straight wakes at zero streamwise pressure gradient. Also, the experimental studies on curved wakes are much fewer than those conducted on straight wakes. The growing interest in the study of curved wakes in the past two decades is evident from the increased number of published experimental data on the curved wakes. However, most of these studies have concentrated on the wake of a cylinder, or an airfoil at zero angle of attack, where the data has always composed of single profile measurements made along the duct

centreline. Among these studies, Savil (1983) carried out the first detailed investigation of a thin cylinder wake subjected to the curvature and pressure gradient effect. Nakayama (1987) investigated the mild curvature and mild pressure gradient effects on turbulent wakes and indicated a strong influence of curvature and pressure gradient on turbulence quantities, particularly the Reynolds shear stress. Tulapurkara et al. (1996) and Schobeiri et al. (1996), Starke et al. (1999) have also reported more recent studies on curved wakes. Previous experimental studies have made a significant contribution to the present understanding of the flow structure behind an airfoil. However, in the past, the studies on the curved wake behind a solid body were limited to a single mainstream velocity. In the present study the structure of an airfoil (NACA 0012) curved wake at different mainstream velocities, namely, 10, 15 and 20 m/s is investigated experimentally.

Recent advances in numerical modelling of fluid flows have provided a new tool to predict and study complex flows. Numerous studies on complex flows and related publications show the widespread use of numerical models. However, the previous numerical studies on curved wakes are even fewer than those of experimental studies. Narasimhan et al. (1991), Tulapurkara et al. (1993, 1996) have carried out investigations of the flow in the curved wake of an airfoil using the standard k-ε model. In all these cases, the experimental data obtained at the trailing edge of the airfoil were used as inlet boundary conditions. Their results show that the computations based on the standard k-ε model are able to satisfactorily capture only the asymmetric mean velocity profile. Also, the results have improved slightly when modifications to the model constants based on the local curvature parameter are made. In all these investigations, the simulations start from the trailing edge of the airfoil (inlet to the computational domain) by assuming that the boundary layers on the wake generating body were well predicted.

The uses of turbulence models rely on the accuracy and validity of the assumptions made. Therefore, a deep understanding of the flow nature is vital in setting up reliable and accurate models. The present numerical investigation was conducted in a more realistic manner by placing the inlet to the computational domain upstream of the airfoil. This procedure allows the wake to develop from the initial boundary layers on the airfoil and thus yields more realistic information about the capability of the turbulence models to predict complex flows. The present numerical study was based on the solution of the

time-averaged conservation equations of mass and momentum for turbulent flow. The flow in the computational domain was treated as three-dimensional, turbulent, incompressible, isothermal and steady. The measured mean and turbulence quantities obtained at approximately one chord length upstream of the airfoil were used as inlet boundary conditions for the simulations.

1.2. Present work and objectives

The broad aim of this work was to improve the present understanding of an airfoil wake, which is developed in a 90° bend duct of square cross-section. This was achieved by conducting an extensive experimental investigation using hot-wire anemometry, and numerical simulations. The specific objectives were:

- Obtain experimentally the mean velocity components and turbulence quantities, such as turbulence intensities and Reynolds shear stresses in the upstream and downstream regions of an airfoil at mainstream velocities of 10, 15 and 20 m/s. Therefore, the measurements were carried out in the radial and spanwise directions at one duct height upstream of the bend, three locations within the bend section, namely, at the bend entry (0°), middle (45°) and the exit (90°) and one duct height downstream of the bend exit. In addition, the pressure measurements were carried out to obtain the static pressure distributions on the concave and convex walls of the duct, on the airfoil itself and in the radial direction at each station.

- Use a well-tested Computational Fluid Dynamics code to model the three-dimensional flow field as occurred experimentally. To fulfil this objective, the mean and turbulence quantities obtained at one duct height upstream of the bend were used as inlet boundary conditions to the computational domain.

- To compare the numerical and experimental results for the mean and turbulent quantities in the wake region of an airfoil and assess the performance of a number of turbulence models, namely, Reynolds Stress Model, standard k-ε model, Realizable k-ε model and RNG k-ε model in conjunction with the two-layer zonal model for the near wall modelling and discretisation schemes QUICK and upwind. This would

enable assessment of the capabilities of current models and numerical techniques incorporated in a CFD code to predict complex flows.

1.3. Outline of the Thesis

The thesis consists of eight Chapters. Chapter 1 presents an introduction to the present work and objectives. Chapter 2 describes the literature survey, particularly experimental and numerical works on curved wakes and others related to the current investigation. In Chapter 3, the experimental rig, instrumentation and the experimental procedures adopted are described. The governing conservation equations, turbulence models, aspects of the near wall modelling and the discretisation schemes used are described in Chapter 4. Computational details, such as boundary conditions, grid distribution of the flow domain, accuracy, computer time and memory used for the numerical work are presented in Chapter 5. The experimental results are presented in Chapter 6, whereas the numerical results are presented in Chapter 7. Finally, Chapter 8 describes the conclusions of the present work and the recommendations for further work.

Chapter 2

2. LITERATURE REVIEW

2.1. Introduction

This Chapter provides the background of the earlier work on curved wakes of streamline and bluff bodies. The review is divided into two main sections, namely, experimental investigation and numerical investigation. Although the studies on curved wakes are much fewer than those conducted on straight wakes, the number of published literature on curved wakes has increased significantly in recent years. Therefore, the present literature survey focuses on the past work, which is most relevant to the present study. Furthermore, the concentration of the review is on turbulent curved wakes generated by streamline and bluff bodies, such as airfoil, circular rod and thin / thick plates.

2.2. Curved wakes

2.2.1. Experimental investigations of wake flows

Curved wake of an airfoil

Development of an airfoil wake in curved and straight ducts were investigated by Ramjee et al. (1988). The work was carried out in two curved ducts of different radii of curvature (R), namely, R = 350 mm and R = 700 mm and a straight duct of length 600 mm. The measurements were made with mean velocity of 15 m/s. An airfoil (NACA 0012) of 100 mm chord length was kept at zero angle of attack to generate the wake. At the entry to the curved duct, the values of the curvature parameter, b/R, were 0.0286 and 0.0143 for R = 350 mm and R = 700 mm, respectively, where b is the wake width. The presented mean velocity and streamwise turbulence intensity profiles indicate that the wakes in the curved ducts are asymmetric and the curvature increases the maximum velocity defect and the average wake width. The streamwise intensity was enhanced on the inner side (region between wake centre line and convex wall) compared with the

outer side (region between wake centre line and concave wall) of the wake. The turbulence shear stresses were not measured at all in this investigation.

Ramjee and Neelakandan (1990) carried out a more extensive investigation of curved wakes. This investigation was conducted in a straight duct and two curved ducts (similar experimental set-up as their previous investigation) using an airfoil (NACA 0012, chord 100 mm), a square cylinder (side length 4 mm) and a rectangular cylinder (height 2.5 mm and length 8 mm) as the wake generating bodies. The measurements were made at a velocity of 15 m/s. The results showed a larger maximum velocity defect in the curved wake than in the straight wake. Furthermore, the streamwise intensities increased on the inner side and reduced on the outer side of the curved wake. It was also concluded that the half-width on the inner side of the curved wake was greater than the half-width on the outer side. It is clear from the results of these investigations that the turbulence shear stress is more sensitive to the curvature than the normal stresses. Comparisons were also made with their earlier work (Ramjee and Neelakandan, 1989) on bluff bodies (rectangular and square cylinders) for the turbulence shear stress. The results showed a greater peak in the cylinder wake than that in the wake of an airfoil.

The development of a wake in the presence of both curvature and pressure gradient was studied by Tulapurkara et al. (1994). The straight and curved ducts used in their investigations were similar to those used by Ramjee et al. (1988), but an additional curved diffuser with an area ratio of 1.74 and a turning angle of 60° was employed. The wake in the curved diffuser was subjected to both streamwise curvature and pressure gradient while the wake in the 90° curved duct was only subjected to streamwise curvature. The mainstream velocity in the test section was about 15 m/s. The wake was produced by an airfoil (NACA 0012) of 100 mm chord. The presented profiles of Reynolds stresses and turbulence kinetic energy became more asymmetric with increasing streamwise distance. Also, the asymmetry of these profiles enhanced further with the presence of pressure gradient. They also concluded that the wake half-width increased on the inner side and decreased on the outer side. However, their new finding showed that the presence of an adverse pressure gradient caused slower decay of the velocity defect.

Curved wake of bluff bodies

Early experimental studies of combined effects of streamline curvature and adverse pressure gradient on the wakes of bluff bodies were conducted by Savill (1983) and Koyama (1983). Savill (1983) investigated the wake of a circular cylinder formed in a 90^{o} bend. The measured profiles of mean and turbulence intensities at various downstream locations indicated a strong influence of the streamline curvature on the wake. However, the data was presented for the duct central plane only and no spanwise variations of any quantities were presented. Koyama (1983) studied the stabilising (concave side), destabilising (convex side) effects and secondary flow effects of streamline curvature on laminar and turbulent wakes behind a circular cylinder. A detailed comparison of the mean and turbulence intensity distributions and photographs of the instantaneous smoke streak-line patterns in the straight and curved wakes were presented. The results indicated that the development of a turbulent wake is promoted by the destabilising effect of streamline curvature and is suppressed by the secondary flow effects, which arise as a result of an imbalance between the pressure gradient force acting towards the centre of the curvature and the centrifugal force due to streamline curvature.

Nakayama (1987) studied the mean and turbulence quantities in the wake of a wire, which was subjected to mild pressure gradient and streamline curvature effects caused by deflection. The cylindrical wire had a diameter of 1.6 mm and, for a mainstream velocity of 15 m/s, the Reynolds number based on the wire diameter was 1550. Despite the mild pressure gradient and curvature, the measured data indicated a strong influence of curvature and pressure gradient on turbulence quantities, particularly on the Reynolds shear stresses.

Ramjee and Neelakandan (1989) investigated the wakes of a rectangular cylinder in a straight and a curved duct. A detailed comparison of the mean, turbulence quantities (normal and shear stress) and the wake parameters (half-width and maximum velocity defect) were presented for both curved and straight wakes. Their results showed that the mean velocity profile of the wake was asymmetric about the centreline of the curved duct. Also, the half-width of the wake was larger on the inner side of the curved wake than the corresponding one in the straight wake. It was concluded that the velocity defect of the curved wake was larger than in the straight wake and the shear stresses were

more sensitive to the curvature than to the normal stresses.

Development of a bluff body wake under the combined influence of curvature and pressure gradient was studied by Tulapurkara et al. (1995). This systematic investigation was conducted in four different ducts, namely, in a straight duct, a curved duct, a straight diffuser and a curved diffuser. This enabled them to investigate the effects of pressure gradient and curvature on the wake development separately. Their results show that the curvature makes the wake asymmetric and the wake half-width increases more on the inner side compared with the one the outer side. Ramjee and Neelakandan (1989) also reported this feature. Their new findings showed that the presence of adverse pressure gradient causes a greater wake growth and velocity defect but reduces the rate of decay of the velocity defect. They also concluded that the curvature enhances the Reynolds stresses and the turbulence kinetic energy, which become progressively more asymmetric with distance. The degree of asymmetry is enhanced further when the curvature and pressure gradient effects are combined.

Three-dimensional wake structure of straight and mildly curved ($b/R < 2\%$) flat plates at a relatively high Reynolds number (Re = 28000) was studied by Weygandt and Mehta (1995). Their results showed that the inner half of the wake was unstable while the outside half was stable.

Development of a cylindrical rod wake under zero streamwise pressure gradient in a curved channel was studied experimentally by Schobeiri et al. (1995, 1996). The quantities, such as the mean velocity, turbulent intensities in streamwise and normal directions and turbulence shear stress $-\overline{u'v'}$ were presented. John and Schobeiri (1996) carried out a similar work with positive streamwise pressure gradient. Their results showed strong asymmetry in the profiles of velocity and Reynolds stress components as many other investigators. Their comparisons with the wake development in a curved channel with zero streamwise pressure gradient showed that the decay rate of velocity defect was slower and the growth of wake width was faster for a positive streamwise pressure gradient. This finding was also previously reported by Tulapurkara et al. (1995).

Recently, Starke et al. (1999) investigated the turbulent near wake of a flat plate subjected to the simultaneous effects of curvature and adverse pressure gradient. A

flat plate with a chord length of 600 mm and width of 18 mm was employed. A square test section followed by a channel with adjustable sidewalls was used to obtain a zero and adverse pressure gradient wakes. Their experimental results showed mostly known wake characteristic, such as a higher spreading rate and higher Reynolds stresses on both sides (inner and outer) of the wake due to adverse pressure gradient.

2.2.2. Numerical investigations of wake flows

Narasimhan et al. (1991) reported prediction of an airfoil (NACA 0012) wake in a curved duct. Their calculation was based on the k-ε model of turbulence with standard constants and with the model constant C_μ dependent on the local curvature. The numerical solution was obtained using the finite volume method and prescribing the profiles of streamwise velocity, turbulent kinetic energy k and its rate of dissipation ε at the trailing edge of the airfoil. Their numerical results showed some of the features obtained experimentally by many investigators like Ramjee and Neelakandan (1989, 1990) and Tulapurkara et al. (1995), such as the mean velocity profile is asymmetric and the half-width of the wake on the inner side is greater than those on the outer side. Although the k-ε model captured the asymmetry in the profiles of the Reynolds shear stress and the mean velocity, the predicted peak values did not match the experimental values of Ramjee and Neelakandan (1990). It was concluded that the standard k-ε model was able to satisfactorily capture the characteristics of a curved wake. Furthermore, they showed that making C_μ dependent on the local curvature improved the agreement on the inner side but slightly worsened it on the outer side of the wake.

The development of an asymmetric wake behind an airfoil in turbulent incompressible flow was computed by Tulapurkara et al. (1993) using the finite volume method with the k-ε model of turbulence. Their numerical results were compared with the asymmetric wake developed experimentally by Ramaprian et al. (1981). Furthermore, the trailing edge of the airfoil was treated as the inlet of the region of interest. Their results showed that the computed shift of the point of minimum velocity with distance was sensitive to the prescribed value of the normal velocity component at the trailing edge of the airfoil (inlet to the flow domain). It was concluded that making C_μ as a function of streamline curvature has only marginal influence on the result, which was also stated by Narasimhan

et al. (1991).

The prediction of an airfoil (NACA 0012) wake subjected to the effects of curvature and adverse pressure gradient was studied numerically by Tulapurkara et al. (1996). The computation was based on the finite volume scheme incorporating the k-ε model of turbulence. In their investigations the initial profiles and the boundary conditions were implemented in the same way as those by Narasimhan et al. (1991), where the trailing edge of the airfoil was treated as the inlet to the flow domain. The numerical results in the wake region of the airfoil were compared with their earlier experimental work on an airfoil (Tulapurkara et al., 1994). The comparison showed that the computations based on the standard k-ε model were able to satisfactorily capture the mean velocity profiles as also indicated by Narasimhan et al. (1991). Furthermore, modifications to the model constant C_μ based on the curvature parameter and the ratio between the production of the turbulence kinetic energy and its rate of dissipation showed improvement in the velocity profiles, wake parameters and profiles of turbulence kinetic energy and Reynolds shear stresses. It was concluded that the modified model was able to capture the asymmetry in the profiles, particularly the asymmetry in the turbulence kinetic energy and shear stress profiles caused by curvature and adverse pressure gradient.

Technical specifications of previous relevant experimental and numerical investigations on curved wakes are given in Tables 2.1 and 2.2, respectively.

Investigators	Test section (mm) (H * W * L)	Centreline Radius of curvature (mm)	Duct turning angle	Reynolds number (Re)	Mainstream velocity (m/s)	Turbulence intensity (%)	Wake generating body	Body dimension (mm)	pressure gradient	Technique used
Savil (1983)	450 * 450		90°	6500 (*d*)	10.3	0.1	Thin cylinder	9.5 (*d*)	yes	Hot-wire
Koyama (1983)	280 * 50 * 210	200		1500 (*d*)	35		Cylinder	2.13 (*d*)	no	Hot-wire
Ramgee and Neelakandan (1989)	140 * 140 * 600	350	90°	2500 (*h*)	15	1	Rectangular cylinder	2.5 * 8 (*h* * *w*)		Hot-wire
Ramgee and Neela kandan (1990)	140 * 140 * 600	700	90°		15	0.5	Airfoil (NACA 0012)	100 (c)	yes	Hot-wire
Narasimhan et al. (1991)	140 * 140 * 600	350	90°		15		Airfoil (NACA 0012)	100 (c) 140 (S)	yes	Hot-wire
Tulapurkara et al. (1995)	140 * 140 * 600	700	90°	4000 (*h*)	15	0.5	Square cylinder	4 (*h*)	yes	Hot-wire
John et al. (1996)	420 * 593		90°	2600 (*d*)	20	1.25	Circular rod	1.98 (*d*)	yes	Hot-wire
Starke et al. (1999)	400 * 400			$4*10^5$ (ℓ)	10		Flat plate	18 * 600 (*h* * ℓ)	yes	LDA
Present study	457 * 457 * 457	534	90°	$1*10^5$ to $2*10^5$ (c)	10, 15, 20	0.3	Airfoil (NACA 0012)	150 (c) 457 (S)	yes	Hot-wire

Table 2.1: Technical specifications of previous and present experimental investigations on curved wakes.

Note- Most of the values are based on explicit information provided by the investigators. LDA- Laser Doppler Anemometer; *d* -diameter; c - chord; *h* - body height; *w* - body width; ℓ - body length; S - span; H - duct height; W - duct width; L - duct length.

Investigators	Turbulence model	Discretisation scheme	Grid type and size	Mainstream velocity (m/s)	Flow domain	Boundary conditions used	Position of the inlet plane	Wake generating body	Technique used
Narasimhan et al. (1991) Tulapurkara et al. (1996)	Standard k-ε model	Upwind		15	Curved duct	Profiles of U, V, k, ε	Trailing edge	Airfoil	Finite volume
Tulapurkara et al. (1993)	Standard k-ε model	Upwind	Staggered (192 86)	22.25	Curved duct	Profiles of U, V, k, ε	Trailing edge	Airfoil	Finite volume
Present study	Reynolds Stress Model, Standard k-ε model, RNG k-ε model, Realizable k-ε model	QUICK	Non-Staggered (see Chapter 5 for details of grid size used)	10 and 20	Curved duct	Profiles of U, V, k, ε, all Reynolds stresses (except $\overline{v'w'}$)	0.343H upstream of Airfoil	Airfoil	Finite volume

Table 2.2: Technical specifications of previous and present numerical investigations on curved wakes.

Note- Most of the values are based on explicit information provided by the investigators. H- duct height.

Chapter 3

3. EXPERIMENTAL INVESTIGATION

3.1. Introduction

The experimental study was conducted in the aerodynamics laboratory at Brunel University. In this study, a turbulent wake of an airfoil (NACA 0012) subjected to the combined effects of curvature and pressure gradient was investigated using constant temperature hot-wire anemometry. This technique is one of the well-established methods for fluid flow measurements, which has been used for more than 50 years. As was noted in Table 2.1, this method was employed in a number of previous experimental investigations on curved wakes, for example, by Savill (1983), Koyama (1983) and Nakayama (1987). In the present study, two cross-wire probes (types DANTEC 55P63 and 55P64) were employed to determine the mean and turbulence quantities in the upstream and downstream regions of the airfoil at 10, 15 and 20 m/s mainstream velocities. The quantities obtained at upstream region (station 1) were later used as the inlet boundary conditions for the numerical calculations. Furthermore, the data obtained in the downstream region (stations 2 to 5) were used for direct comparisons with the present CFD results. In addition to the hot-wire measurements, static pressure distributions on the airfoil, along the concave and convex walls and in the normal direction at stations 1 to 5 were measured using a manometer.

The present experimental study, therefore, extends the very limited previous studies by providing quantitative data for an airfoil curved wake subjected to the effects of curvature and pressure gradient, which can be used by other investigators to validate new or existing mathematical models. In the following sections 3.2 and 3.3, details of the experimental rig and other associated measuring and recording instrumentation used in the present work are described. This is followed by descriptions of the tunnel and the cross-wire probe calibration methods. The final part of this Chapter describes the experimental procedure adapted to estimate the error due to misalignment of the cross-wire probe. The obtained experimental data can be found in tabular and profile forms in

Appendix III and Chapter 6, respectively.

3.2. Tunnel geometry and operation

The present work was conducted in a subsonic blower tunnel of closed working-section, open return type, where the downstream tangent of the tunnel discharges directly into the laboratory. A variable speed pulley is incorporated in the motor drive system, which allows the subsonic centrifugal blower fan to run between 470 to 1170 rev/min. The maximum achievable air speed in the test section was 33 m/s. Figure 3.1 shows the wind tunnel test section and instrumentation.

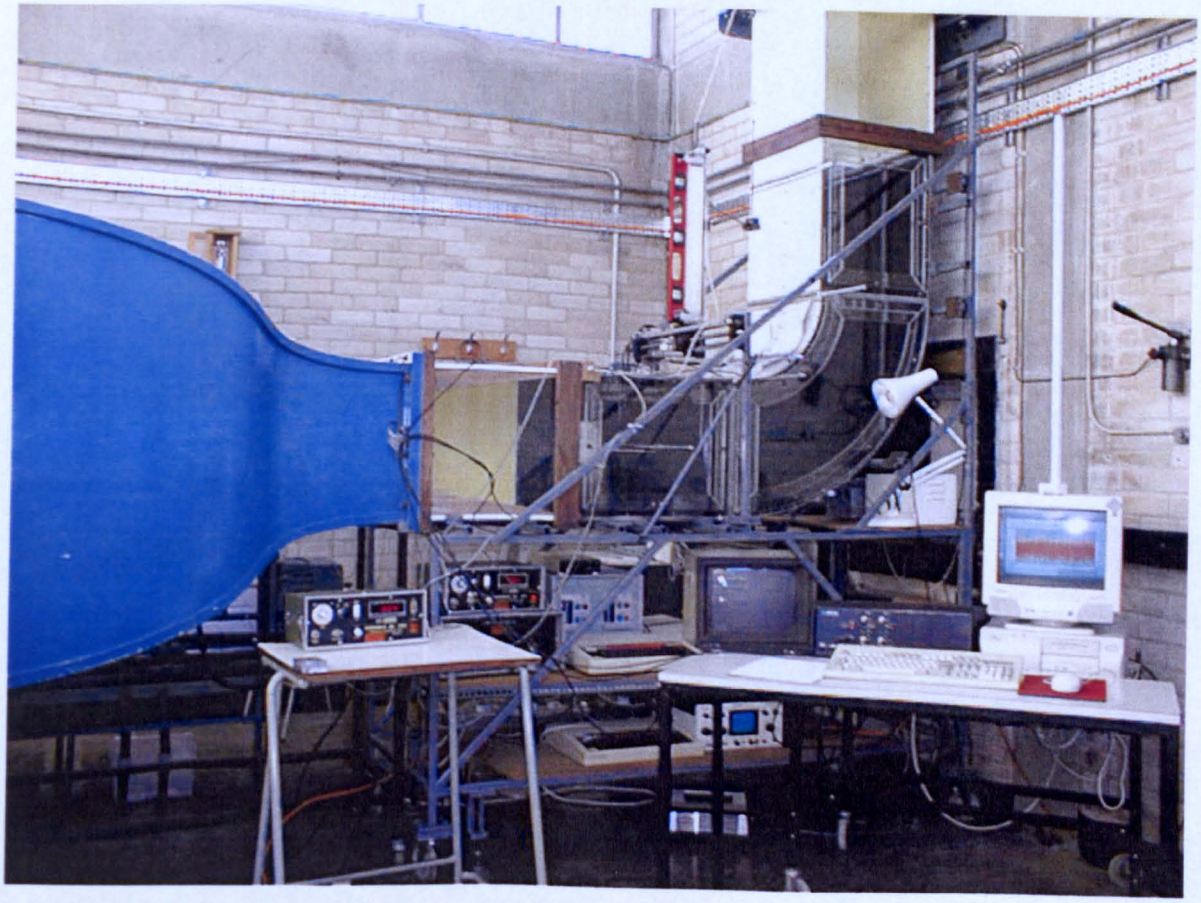

Figure 3.1: The wind tunnel test section and the hot-wire anemometry system.

(Original in colour).

3.2.1. Test section

The air is drawn into the tunnel via a bank of filters and passes to the centrifugal fan. The fan delivers the air first to a short straight section containing a honeycomb and then a short diffuser, whose cross-sectional area increases to a maximum of 1.5 m^2. Furthermore, the diffuser is fitted with three wire mesh smoothing screens. The air then enters a contraction section leading to a straight section of 0.6 m length, which provides a smooth transition to the following square test section. A schematic diagram of the test section is shown in Figure 3.2.

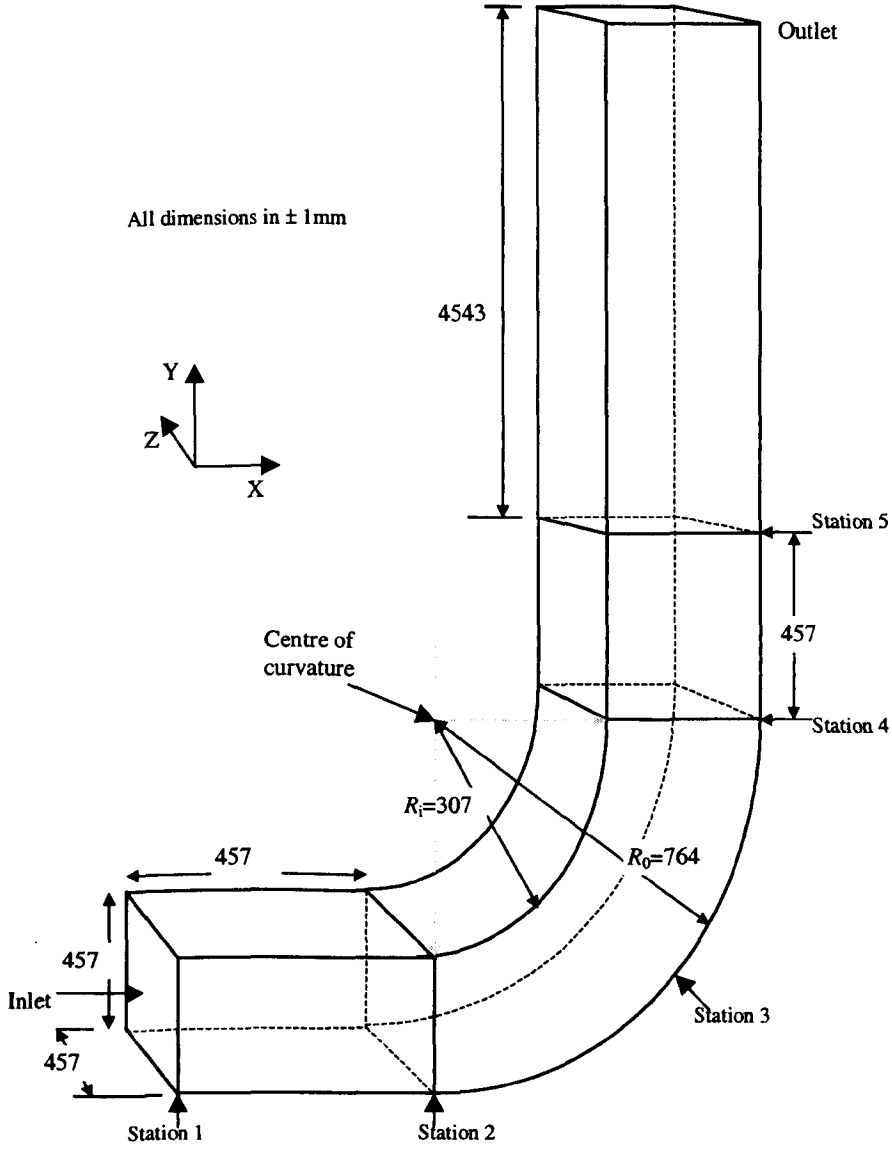

Figure 3.2: Schematic diagram of the test section (not drawn to scale).

The test section is a separate unit, consisting of three sections, namely, upstream tangent, bend and downstream tangent. The bend has a turning angle of 90° and a mean radius to height ratio of $R/H = 1.17$, which diverts the flow vertically upwards through the straight downstream tangent of 5m long into the laboratory atmosphere. Most of the tunnel and test section walls are made of 12 mm thick plywood plates except one of the sidewalls of the test section, which is made of transparent sheets of Perspex. Furthermore, the transparent wall incorporates three windows, which can be used for access and probe insertion and alignment. The concave and convex surfaces of the bend section are made of 3 mm thick plywood plates and are painted smoothly.

The experiments were carried out for the mainstream velocities of 10, 15 and 20 m/s at station 1, where the root-mean-square value of the streamwise velocity fluctuations in the central plane was less than 0.3% of the mainstream velocity, indicating low level of turbulence. All the measuring stations have slots on the convex wall along the spanwise direction of the test section, which allow the cross-wire guide tube to move in the spanwise direction as well as normal direction. The first station is located at 0.457 m upstream of the bend entry, which is 0.6 m away from the exit of the contraction cone. Stations 2 to 4 are located at the bend entry (0°), middle (45°) and the exit (90°), respectively. Station 5 is located at 0.457 m downstream of the bend exit. The static pressure values on the concave and convex walls are measured directly via the pressure tappings located along the mid-plane of these walls. Also, the pressure tappings located at the entrance and exit of the contraction section were used for tunnel calibration and to determine the mainstream velocity at station 1.

3.2.2. Traversing system

In the present investigation, an especially designed computer controlled traversing system was employed to enable the cross-wire probe and Pitot-static tube measurements within the test section. The traversing unit was a separate system mounted above the convex wall of the test section. The movements of the probe in the horizontal and vertical directions were achieved using linear bearings on both axes, powered by precision lead-screws of 1 mm pitch and precision nuts, where the lead-screws were mechanically driven by a stepping motor with 200 steps to one revolution. The stepping motors were

controlled by a BBC computer model B via an IEEE-488 interface card.

At each measuring station, the reference height, which is the distance between the centre of the probe sensor and the wall of the duct, was measured in the following manner. A thin straight metal plate was placed onto a straight thick plate and their combined thickness was measured initially using a micrometer. The two plates were then placed onto the wall of the test section and then the probe was brought gradually down towards the thin plate until the prongs of the probe touch the plate as shown in Figure 3.3. Similar technique was used to determine the gap between the probe prongs. Finally, the reference height from the wall was taken as the sum of the combined thickness of the plates and half the distance between the probe prongs. By using this technique damages to the probe can be avoided. For a cross-wire probe the closest achievable distance from the wall was 1.4 mm.

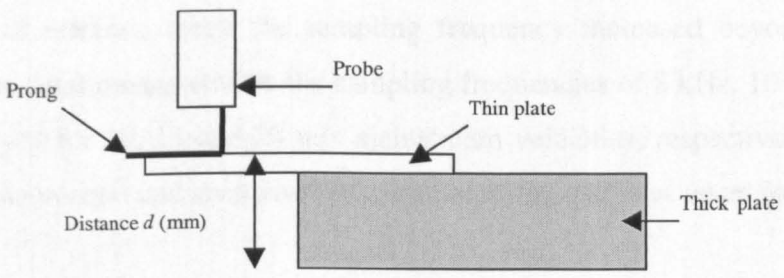

Figure 3.3: Technique adopted to determine the distance between the wall and the probe.

3.2.3. Data acquisition system

The data acquisition system consists of an analogue-to-digital (A/D) converter board and the software developed by DANTEC (StreamWare®-1.18), which were installed on a computer. The voltage signals (analogue) of the cross-wire probe were transferred through the CTA modules to the 16-channel A/D converter (National Instruments type AT-M10-E10) for simultaneous sampling. The A/D board sampling frequency ranges from 0.015 kHz to 66.67 kHz, which can produce 0 to 8.355×10^6 samples per channel. The digitized output voltage (ranges between 0 V to 10 V) signal from the A/D converter was then transferred to the computer software, where the conversion algorithm of the software converts the voltage into the mean velocity components using probe

calibration data. Furthermore, the software simultaneously calculates the turbulence quantities, such as turbulence intensities and turbulence shear stresses of the flow. The data was exported to a spreadsheet for further analysis.

In the present work, the reference frequency scale f_0 and the sampling frequency were chosen as stated by Yuan (1991). The reference frequency scale was defined as

$$f_0 = \frac{U_0}{\delta} \tag{3.1}$$

The above reference frequency scale was used to determine an optimum sampling frequency. In the present study a sampling frequency range from 8 kHz to 12 kHz was used, which was ten times the reference frequency scale. Also, a number of frequency tests were carried out at 10, 15 and 20 m/s mainstream velocities to determine the effects of the sampling frequency. But, the analysis showed no significant changes in the parameters of interest, when the sampling frequency increased beyond the optimum values. In the final measurements the sampling frequencies of 8 kHz, 10 kHz and 12 kHz were employed for 10, 15 and 20 m/s mainstream velocities, respectively. Also, at each location in the normal and spanwise measurements, the data was taken for 15 seconds.

3.3. Experimental equipment

3.3.1. Constant temperature hot-wire anemometry

There are two main modes of hot-wire anemometry, namely, Constant Current (CC) and Constant Temperature (CT). As briefly stated earlier, the constant temperature anemometry was employed in the present investigation to measure the mean velocity components, turbulence intensities and the Reynolds stresses within the test section. In a constant temperature anemometer, the probe resistance and temperature are kept constant and independent of the cooling effects of the flow medium by an error signal (voltage) across a Wheatstone bridge. Therefore, the Wheatstone bridge output voltage is always a function of the effective cooling velocity acting on the probe sensor. The DANTEC constant temperature anemometer frame type 90N10 has room for six Modules (CTA or calibration Modules) and input for a temperature probe. Also, it contains power supplies for the CTA-modules and a controller, which takes care of the communication between

the frame and the StreamWare®-1.18 application software. The application software can control up to three frames simultaneously. A schematic diagram of the present experimental set-up of the constant temperature anemometry frame with two 90C10 CTA-modules, cross-wire and temperature probes are shown in Figure 3.4. Each module was connected to each sensor of the probe via a probe cable attached to a BNC connector on the module front plate. The temperature probe was connected to the controller and the signal is directed to the PC via the serial interface.

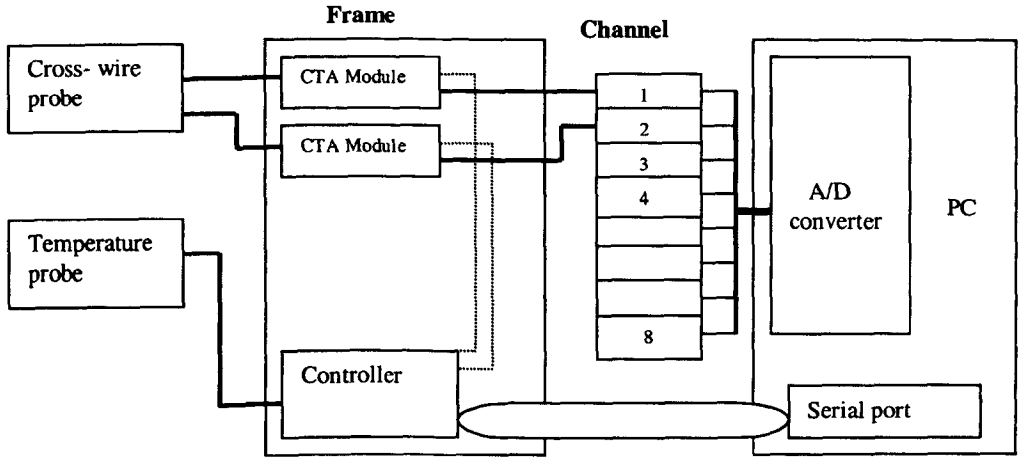

Figure 3.4: Schematic diagram of the constant temperature anemometry used in the present experimental investigation.

3.3.2. Cross-wire probe calibration system

All cross-wire probes used in the present study were calibrated by DANTEC at Bristol using a DANTEC Streamline® calibrator type 90H10. The calibrator is intended for calibration of probes in air or other gasses from 0.02 m/s up to Mach 1. The calibrator consists of a calibration module of type 90H01 and a separate flow unit connected to the calibration module via a cable. The calibration module directs set-up parameters from the StreamWare®-1.18 software to the flow unit. Also, it samples the signal from the pressure, temperature transducers of the flow unit and transmits them via the controller of the frame to the computer, where the StreamWare®-1.18 software uses them to calculate the velocity of the jet at the exit of the nozzle.

The flow unit operates from a pressurised air supply and creates a free jet using one of four different outlet diameter nozzles, namely, 5, 8.7, 12 and 42 mm (depending on the

required velocity range). Furthermore, the nozzles have elliptical contours to minimise the boundary layer development during the calibration process, which also ensures a flat jet profile. The air enters the flow unit through an external filter that filters away particles and oil droplets. During the calibration process, the probe to be calibrated is placed directly above the nozzle of 12 mm outlet diameter (in the centre of the free jet) and mounted in a probe holder of the flow unit. The calibration system was fully computer controlled, therefore, an automatic calibration procedure was adopted in the present study. The calibrated data and the cross-wire probes were subsequently employed for measurements at all stations.

3.3.3. Probes

Cross-wire probe

In the present experimental study cross-wire cylindrical type probes, namely, DANTEC 55P63 and 55P64 were employed to measure the three mean velocity components, turbulence intensities and turbulence shear stresses (except $-\overline{v'w'}$). The sensor of both probes was made of tungsten plated platinum wire with length and diameter of 1.25 mm and 5 μm, respectively, which was equivalent to a length-to-diameter ratio of 250. The wire is welded directly to the tip of the prongs and the entire wire length acts as a sensor. A typical technical specification of a cross-wire probe is given in Table 3.1.

Medium	Air, other gasses
Sensor material	Platinum-plated tungsten
Sensor dimensions	5 μm diameter, 1.25 mm long
Sensor resistance	3.5 Ω
Max sensor temperature	300 °C
Max ambient temperature	150 °C
Min velocity	0.05 m/s
Max velocity	500 m/s

Table 3.1: Technical specification of a cross-wire probe (Streamline/StreamWare®-1.18 user guide, 2000).

A cross-wire probe consists of two inclined wires placed close to each other to form an X-array, where they form an angle of 90° with each other. If the two sensors are in the x-

y plane, then sensor 1 and sensor 2 form + 45° and – 45°, respectively, with the x-axis. The X-arrays of DANTEC 55P63 probe is parallel to and of DANTEC 55P64 probe is perpendicular to the probe stem. Therefore, the DANTEC 55P63 probe can be used to measure the mean streamwise and normal velocity components, whereas the DANTEC 55P64 probe measures the mean streamwise and spanwise velocity components. The sensor number of dual and triple sensor probes is marked by dots on the probe stem, which is a 2.3 mm diameter ceramic tube designed to provide a rigid, aerodynamic mounting of the sensors as well as the sensor supports.

Temperature probe

This is a thermistor-based thermometer used to measure the ambient temperature of the fluid. The sensing element of the probe is embedded in a stainless steel tube equipped with a cable that connects to the CTA frame via a Coax cable. The temperature signal from the probe is linearized in the controller and directed to the computer via the serial interface. The probe can be used to measure temperature in a range of 0 to 150 °C with an accuracy of ± 0.5 °C. It is possible to obtain a wide range of temperatures without special modification to its cables and connectors.

3.3.4. Pitot –static tube

A Pitot-static tube provides a simple, relatively inexpensive and fairly accurate way to measure fluid speed. It consists of two concentric tubes, with the end turned through a right angle, so the tip of the tube can be faced into the airstream for measurements. The ellipsoidal nose (tip of the tube) has a single forward-facing hole to measure the stagnation pressure and a ring of side holes on the surface of the tube to measure the static pressure. In the present experiment the Pitot-static tube is used for two purposes, firstly, to measure the static and stagnation pressures during the tunnel calibration and secondly, to measure the radial (normal) static pressure distribution at each station. In the tunnel calibration process, the Pitot-static tube is mounted into the test section at station 1 with the tip facing directly into the flow. The pressure difference was determined at various tunnel speeds by connecting the static and stagnation pressure tapping to a digital manometer. The velocity of the air was calculated using the measured pressure difference between the static and stagnation pressures in conjunction with atmospheric pressure

and temperature. In the measurement of the radial static pressure, the stagnation pressure hole was blocked and the Pitot-static tube was mounted onto the traversing system to allow movement in the radial direction.

3.3.5. Airfoil geometry

In the present study a NACA 0012 symmetrical type airfoil was used. The airfoil was made of plywood and varnished smoothly. It had a chord and span lengths of 150 mm and 457 mm, respectively, and an aspect ratio of 3.046. A schematic diagram of the airfoil cross-section is shown in Appendix II. Small pressure tappings were incorporated along the centreline (streamwise direction) of the upper and lower surfaces for the purpose of measuring static pressure distribution on the airfoil. All these pressure tappings were individually connected by stainless steel tubes inside the body of the airfoil, which were then collectively brought out of the airfoil mounting on the sidewall of the test section. The airfoil was mounted horizontally at zero angle of attack between stations 1 and 2 (upstream tangent) as shown in Figure 3.5. Furthermore, the trailing edge of the airfoil was placed at a distance of one chord length from the bend entry (station 2).

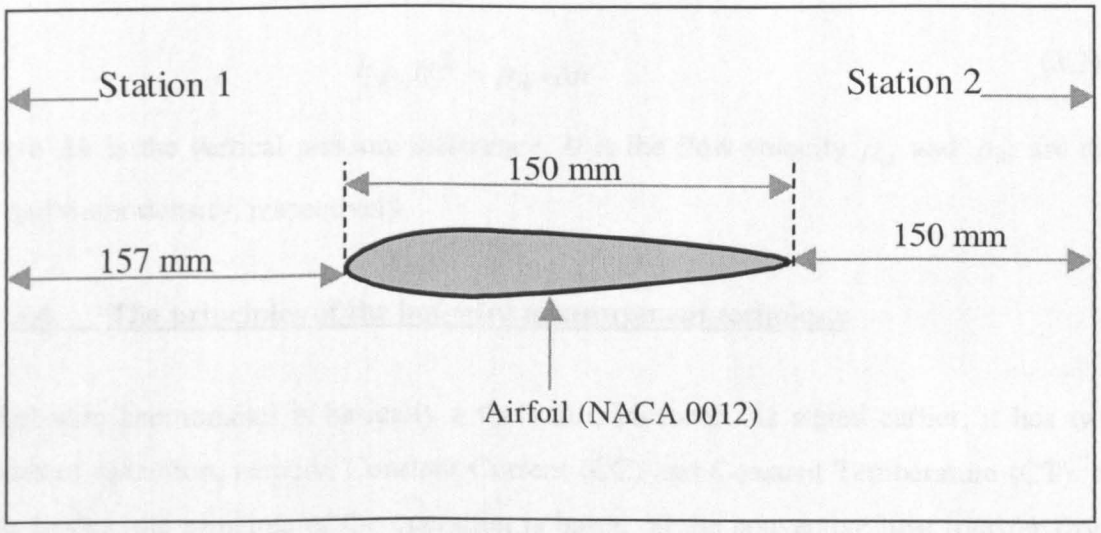

Figure 3.5: Location of the airfoil in the upstream tangent.

3.3.6. Manometers

Two different types of manometers were used in the present study, namely, an electronic

digital micro-manometer and an inclined-tube manometer. The following section describes the application of both manometers.

Digital micro-manometer

An electronic micro-manometer of type MDS FC002 manufactured by Furness control Ltd was employed in all the final pressure measurements. The static pressures along the concave and convex walls of the test section and on the airfoil surfaces were measured using 20-way single auto selection box in conjunction with the manometer. The manometer was capable of measuring the pressure from 0.01 to 199.9 mm of water with an accuracy of 0.5% as stated by the manufacturer.

Inclined-tube manometer

An inclined-tube manometer manufactured by Airflow Development Ltd was used for preliminary experimental work. The adjustable limb was used vertically for large pressure changes and at an inclined position for small pressure measurements. The relationship between the pressure difference and the flow velocity can be expressed as

$$\frac{1}{2}\rho_a U^2 = \rho_w g \Delta h \tag{3.2}$$

where Δh is the vertical pressure difference, U is the flow velocity, ρ_a and ρ_w are the air and water density, respectively.

3.4. The principles of the hot-wire measurement technique

A hot-wire anemometer is basically a thermal transducer. As stated earlier, it has two modes of operation, namely, Constant Current (CC) and Constant Temperature (CT). In both modes, the principle of the operation is based on the convective heat transfer from an electrically heated wire due to a cross flow. In the constant current mode of operation, the current in the wire is kept constant. Furthermore, as the flow rate varies the variation of the wire resistance due to the cooling effects is measured in terms of the voltage drop across the wire. However, in the constant temperature mode the wire resistance and its temperature are kept constant by a feedback circuit and the variation of the current is

measured. The principles of hot-wire anemometry have been previously discussed by many investigators, see for example, Reynolds (1974), Hinze (1975), Perry (1982), Goldstein (1983), Lomas (1986), and Bruun (1995). A relationship between the output voltage of the hot-wire anemometer bridge E and the normal velocity component U_N to an infinite length wire is written in the form

$$E^2 = A + B\,(U_N)^n \tag{3.3}$$

where A, B and n are constants. Equation (3.3) is known as the King's law.

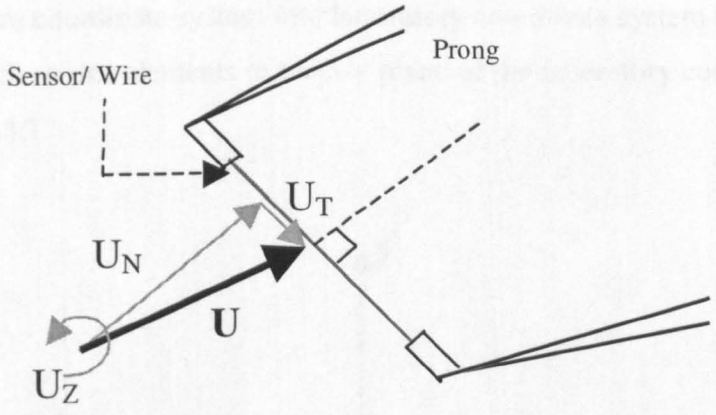

Figure 3.6: Single-wire and flow configuration.

Champagne et al. (1967a, b) found an expression for a finite length wire (see Figure 3.6), subjected to the combined cooling effects of normal velocity component U_N and tangential velocity component U_T. They defined a parameter known as effective cooling velocity U_e to take account of the effects of the tangential velocity component. This effective velocity expression can be written as

$$(U_e)^2 = (U_N)^2 + k_1^2\,(U_T)^2 \tag{3.4}$$

where the yaw coefficient $k_1 = 0.2$.

The third velocity component U_Z (in z-direction) will also affect the heat transfer from the wire. The effective velocity that takes into account the effects of this component is given by (see Goldstein 1983)

$$(U_e)^2 = (U_N)^2 + k_1^2 (U_T)^2 + h^2 U_Z^2 \tag{3.5}$$

where the pitch factor coefficient h = 1.18.

By substituting equation (3.5) into equation (3.3) Yields:

$$E^2 = A + B\{U_N^2 + k_1^2 U_T^2 + h^2 U_Z^2\}^{n/2} = A + B U_e^n \tag{3.6}$$

3.4.1. Probe velocity decomposition

The probe velocity decomposition is the process of converting the velocity components of the wire coordinate system into laboratory coordinate system (Cartesian). A cross-wire probe with sensor elements in the x-y plane of the laboratory coordinate system is shown in Figure 3.7.

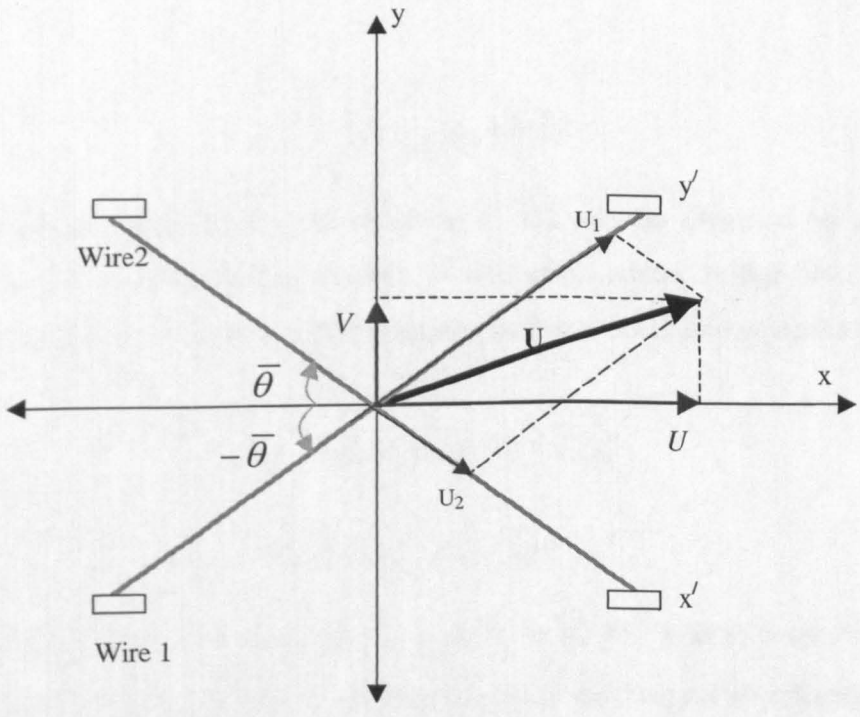

Figure 3.7: Cross-wire probe and flow configuration.

In Figure 3.7, the velocity components U_N, U_T and U_Z for the inclined wire 1 can be written as:

$$U_N = U_2 = U\cos\bar{\theta} - V\sin\bar{\theta}, \quad U_T = U_1 = U\sin\bar{\theta} + V\cos\bar{\theta}, \quad U_Z = W \tag{3.7}$$

For wire 2:

$$U_N = U_1 = U\sin\bar{\theta} + V\cos\bar{\theta}, \quad U_T = U_2 = U\cos\bar{\theta} - V\sin\bar{\theta}, \quad U_Z = W \tag{3.8}$$

Substituting the above equation (3.7) into equation (3.5) yields:

$$U_{e1} = \left[\begin{array}{l} U^2\left(\cos^2\bar{\theta} + k_1^2\sin^2\bar{\theta}\right) + V^2\left(\sin^2\bar{\theta} + k_1^2\cos^2\bar{\theta}\right) \\ -UV\left(1-k_1^2\right)\sin 2\bar{\theta} + h^2W^2 \end{array} \right]^{1/2} \tag{3.9}$$

Similarly, for the inclined wire 2 where the angle is $-\bar{\theta}$:

$$U_{e2} = \left[\begin{array}{l} U^2\left(\cos^2\bar{\theta} + k_1^2\sin^2\bar{\theta}\right) + V^2\left(\sin^2\bar{\theta} + k_1^2\cos^2\bar{\theta}\right) \\ +UV\left(1-k_1^2\right)\sin 2\bar{\theta} + h^2W^2 \end{array} \right]^{1/2} \tag{3.10}$$

For a cross-wire probe, U_{e1} and U_{e2} are the effective cooling velocities for wire 1 and wire 2, respectively. In the DANTEC StreamWare®-1.18 computer software, the effective cooling velocity U_e is replaced by the calibration velocity U_{cal}. Which can be written as:

$$U_e = \frac{1}{\sqrt{2}} U_{cal}\,(1+k^2)^{0.5} \tag{3.11}$$

The calibration velocity U_{cal} in equation (3.11) can be obtained by substituting the temperature corrected output voltage of the anemometer bridge into the calibration transfer function (polynomial). Substituting equation (3.11) into equation (3.5) yields:

$$\frac{1}{2} U_{1cal}^2 (1+k_1^2) = k_1^2\, U_1^2 + U_2^2 \tag{3.12}$$

$$\frac{1}{2} U_{2cal}^2 (1+k_2^2) = U_1^2 + k_2^2\, U_2^2 \tag{3.13}$$

If wire 1 and wire 2 form angles $\bar{\theta}_1$ and $\bar{\theta}_2$ with the x-axis, respectively. Equations (3.12) and (3.13) can be used to obtain the normal and tangential velocities U_1 and U_2 of the wire coordinate system, which then leads to the calculation of U and V in the laboratory coordinate system using:

$$U = U_1\cos\bar{\theta}_1 + U_2\cos\bar{\theta}_2 \tag{3.14}$$

$$V = U_1\sin\bar{\theta}_1 - U_2\sin\bar{\theta}_2 \tag{3.15}$$

3.5. Calibration procedure

Two different types of calibration were carried out in present work, namely, wind tunnel calibration and probe calibration.

3.5.1. Tunnel calibration

The objective of tunnel calibration was to obtain a relationship between the static pressure drop across the contraction section of the tunnel and its corresponding Pitot-static tube pressure readings at station 1. The tunnel calibration was conducted by the following procedures. Firstly, the Pitot-static tube was placed in the mid-height of the test section at station 1. The pressure tappings located at the entrance and exit of the contraction section were connected to a digital micro-manometer to obtain the static pressure difference across contraction chamber. The air velocity through the duct was gradually increased by increasing the fan speed in steps and at each incremental step the contraction chamber static pressure difference and the Pitot-static tube readings were measured simultaneously. The atmospheric pressure and temperature were also measured using a mercury manometer and a thermometer before and after the tunnel calibration to monitor any drift due to the ambient conditions. The tunnel calibration process was repeated a number of times until a linear relationship was obtained between the contraction section static pressure drop and Pitot-static tube pressure readings at station 1. The obtained linear relationship was subsequently used along with the atmospheric pressure and temperature to determine the mainstream velocity U_o at station 1, when the Pitot-static tube was removed.

In Figure 6.2(a), the contraction section static pressure drop readings were plotted against the Pitot-static tube pressure readings at various tunnel speeds. In the absence of the Pitot-static tube, the velocity of the air at station 1 was calculated using

$$U_o = \sqrt{\frac{2\rho_w g \Delta h}{\rho_{air}}}, \text{ where } \rho_{air} = \frac{P_a}{RT_a} \tag{3.16}$$

and P_a and T_a are the static atmospheric pressure and temperature, respectively, ρ_w is the water density, g = 9.81 m/s^2, Δh is the pressure difference of the Pitot-static tube obtained

using the calibration relationship (linear) and the contraction static pressure difference.

3.5.2. Cross-wire probe calibration

The DANTEC Streamline® calibration system was used to perform an automatic calibration process on probes by exposing them to a set of known flow velocities. The process was conducted in the following manner. Initially, a calibration module of type 90H01 was inserted into the slot of the anemometer frame type 90N10 and all the associated screws were firmly tightened to secure a reliable ground connection between the module and the frame. Secondly, the calibration module was connected with the flow unit using a calibration system cable type of 90B01 and then a nozzle of 12 mm diameter was placed at the outlet of the flow unit to achieve the desired velocity range of 0 to 25 m/s. In the final part of the set-up procedure, a specially designed probe clamp and mounting rod were used to place the probe into the core region of the jet with the sensor being flush with the exit plane of the nozzle. The flow of the jet, particularly in the core region was characterised as non-turbulent and straight ($V = W = 0$). The system temperature probe was used to measure the flow temperature changes during the calibration period and was placed further downstream of the jet to avoid any disturbances to the cross-wire probe.

The probe calibration was initiated by the StreamWare®-1.18 program, which generated a set of equally spaced incremental velocity points using defined velocity limits and incremental points. As the calibration proceeded through all the generated points, the velocity of the jet was automatically adjusted to the closest value of the corresponding generated point by the calibrator. Furthermore, at each generated point both sensors of the probe were calibrated simultaneously for 15 seconds. The process was repeated for all the generated points and at the end the calibration system stopped automatically. Finally, a best curve was drawn through the calibration points using polynomial curve fit. All the probes were calibrated a number of times during the whole experimental work to minimise errors associated with the probe calibration.

3.6. Uncertainty in the measurements

There are a number of factors that can affect the final output signal from a hot-wire

anemometer. This includes the probe misalignment, temperature changes, contaminated sensors, calibration drift, sensor angle, electronic noise, aerodynamics of probe and finite hot-wire length (see Perry, 1982 for more details). Since the tunnel is an open return type and it was run for a long period prior to each experimental work, the ambient temperature variation was found to be small. Furthermore, a temperature probe was used to take even these small changes into account. As stated earlier, the air is drawn into the tunnel via a bank of filters to minimise oil and dust particles entering into the tunnel, which reduces accumulating deposits on probe sensors. In both, experimental and calibration processes the entire measuring chain including probe, probe support, cables, anemometer (CTA), computer and A/D board were used, which reduces additional problems caused by variation in electronic resistance and noise.

The sensor angle can affect the final results significantly, therefore to minimise this effect the wires of probe were checked using a magnifier before and after each experimental work completion, which also ensured no deposits built-up on the sensor. During the experimental work, to minimise the effects of calibration drift and other drift caused by changes in the metallurgical properties of the wire, the probes were not only calibrated several times but also a number of them were employed. Therefore, the effects of temperature changes, accumulated deposits on sensors, electronic resistance and noise, sensor angle, and calibration drift can be taken as negligible.

The prongs, which support the wire, will have an aerodynamic effect on the filament. It appears that the aerodynamics effects, such as wake of the prongs will upset the heat transfer from the wire, particularly when the flow is at an angle. In the present study, the normal and spanwise velocity components are much smaller than the streamwise velocity component, therefore the effects of probe aerodynamics are very small and can also be assumed as negligible. As stated by the manufacturer of the probes, the effects by finite hot-wire length on heat transfer of the probe sensor is very small since it has a length-to-diameter ratio of 250. The misalignment of the probe is a perfect example of an error, which could easily occur in mounting and unmounting probes and their supports. In the present work, the effect of misalignment of the probe was investigated experimentally. The following section describes the procedures adopted to determine the effects of pitch and yaw misalignment of a cross-wire probe.

3.6.1. Analysis of yaw angle misalignment

This investigation was carried out at station 1 in the boundary layer region at a height of 9 mm from the concave wall, where the turbulence level was higher than the free-stream region. The probe was mounted onto the traversing system and allowed to rotate in the x-z plane as shown in Figure 3.8.

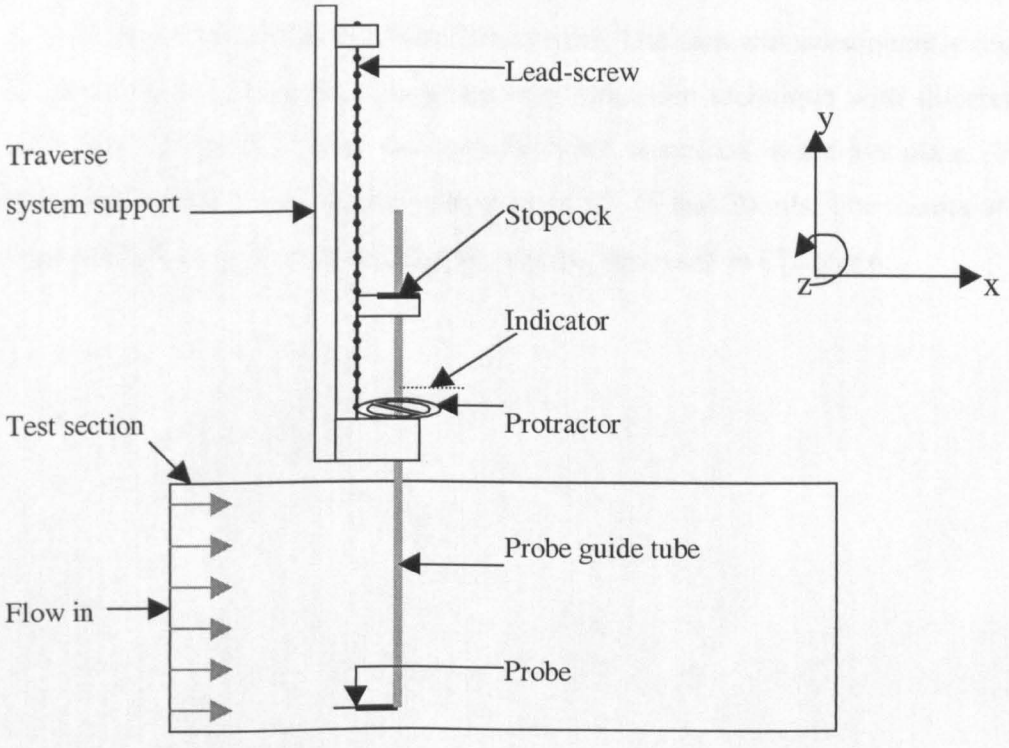

Figure 3.8: An experimental set-up for the yaw angle misalignment investigation.

To restrict rotation to the x-z plane only, a stopcock was attached to the probe guide tube to hold it firmly and stops probe movement in the vertical (y) direction. This technique helped to avoid damage to the probe and the guide tube during the investigation. A straight thin metal piece was attached on to the guide tube and used as an indicator to determine the angle of rotation from a protractor, which was placed directly below it. Finally, the probe was aligned with the flow and the indicator was set to 0^{o} as shown on the protractor. The probe was then rotated gradually from 0^{o} to 5^{o} in the clockwise and anticlockwise directions in the x-z plane and at each incremental angular position the

data was taken. The study was conducted at mainstream velocities of 10, 15 and 20 m/s.

3.6.2. Analysis of pitch angle misalignment

This particular investigation was carried out using the coordinate transformation techniques of the StreamWare®-1.18 application software, which is a process of transforming the decomposed velocities from the probe coordinate system into the laboratory coordinate system. As in the yaw angle misalignment investigation, the probe was initially aligned with the flow and a set of data was obtained for zero pitch angle in the x-y plane of the laboratory coordinate system. The data was subsequently reprocessed a number of times using the coordinate transformation technique with different angles from 0° to 5° in the clockwise and anticlockwise directions in the x-y plane. The study was also conducted at mainstream velocities of 10, 15 and 20 m/s. The results of yaw and pitch angle misalignments investigations will be presented in Chapter 6.

Chapter 4

4. NUMERICAL INVESTIGATION: Mathematical Model

4.1. Introduction

The numerical part of the present study was based on the solution of the time-averaged conservation equations of mass and momentum for three-dimensional, steady, turbulent, isothermal and incompressible flow in a 90° curved square duct. This Chapter, therefore, presents first the conservation equations, followed by a brief review of the turbulence models and the discretisation schemes. Since the FLUENT 5 CFD code was used, the general description of the equations follows the form given in the FLUENT User's Guide (1998), which also provides further details. To assess the performance of the most commonly used turbulence models, four different models were adopted, namely, the Reynolds Stress Model, standard k-ε model, RNG k-ε model and the Reliazable k-ε model.

The governing equations are discretised using the finite volume method on a non-staggered grid. To compare the effect of discretisation schemes on the results, the convection terms are discretized with either the first-order upwind scheme or the third-order scheme QUICK. The pressure is derived using the SIMPLEC algorithm, which is an iterative method by which the velocity and pressure are first guessed and then step by step corrected until the required accuracy is achieved.

4.2. Governing equations

The fluid motion can be represented by mathematical models, which are based on the conservation laws of mass, momentum and energy. These conservation laws can be expressed in mathematical forms, namely, the continuity equation, three components of momentum equation and energy equation. In the present study the flow is treated as isothermal, therefore, the energy equation is omitted. The governing equations of continuity and momentum for an incompressible flow with constant viscosity can be

written in terms of instantaneous properties as

Continuity equation

$$\frac{\partial}{\partial x_i}(\rho U_i)=0 \tag{4.1}$$

Momentum (Navier-Stokes) equation

$$\frac{\partial(\rho U_i)}{\partial t}+\frac{\partial}{\partial x_j}(\rho U_i U_j-\tau_{ij})+\frac{\partial P}{\partial x_i}-S_{ui}=0 \tag{4.2}$$

where S_{ui} is the source term.

The time-averaged form of these equations for turbulent flows can be derived by substituting the mean and fluctuating component of flow variables, e.g.

$$U=\overline{U}+u', \quad P=\overline{P}+p' \tag{4.3}$$

Equation (4.1) can rewritten in terms of the time-averaged terms as:

$$\frac{\partial}{\partial x_i}(\rho\overline{U}_i)=0 \tag{4.4}$$

and the time-averaged momentum equation can be derived as

$$\frac{\partial}{\partial x_j}(\rho\overline{U_i}\,\overline{U_j}-\overline{\tau}_{ij})+\frac{\partial \overline{p}}{\partial x_i}-\overline{S}_{u\,i}=\frac{\partial}{\partial x_j}(-\rho\overline{u_i' u_j'}) \tag{4.5}$$

4.3. Turbulence modelling

The time-averaging process of the governing equations leads to the appearance of six independent unknown correlations known as Reynolds stresses shown as $-\rho\overline{u_i' u_j'}$ in equation (4.5). In the presence of these additional unknown variables, the governing equations do not form a closed set. Thus, in order to solve these equations some form of modelling is required. The turbulence modelling is a computational procedure, which

closes the governing equations by modelling the Reynolds stresses. The models generally known as zero- (mixing length), one- and two- equation models use an eddy-viscosity hypothesis to close the governing equations, whereas, the Reynolds Stress Model uses six individual transport equations, one for each of the Reynolds stresses.

4.3.1. Eddy-viscosity hypothesis

This concept is based on an analogy between stresses in laminar flow and Reynolds stresses in turbulent flow. The laminar stresses are written as

$$\tau_{ij} = \mu e_{ij} \tag{4.6}$$

where μ is the laminar viscosity and $e_{ij} = \left(\frac{\partial U_i}{\partial x_j} + \frac{\partial U_j}{\partial x_i} \right)$ is the rate of strain tensor. Using the above analogy for turbulent flows, the turbulent stresses are expressed as

$$-\rho \overline{u_i' u_j'} = \mu_t \left(\frac{\partial \overline{U}_i}{\partial x_j} + \frac{\partial \overline{U}_j}{\partial x_i} \right) - \frac{2}{3} (\rho k \delta_{ij}) \tag{4.7}$$

where k is the turbulence kinetic energy, μ_t is the turbulent or eddy-viscosity and δ_{ij} is the Kronecker delta. At this stage the key assumption is made that the turbulent viscosity μ_t is the same in all directions at any point (isotropic condition).

The time-averaged momentum equation (4.5) can be rewritten by taking the turbulent and laminar viscosities into account as

$$\frac{\partial}{\partial x_j} (\rho \overline{U}_i \overline{U}_j) + \frac{\partial \overline{p}}{\partial x_i} - \overline{S}_{ui} = \frac{\partial}{\partial x_j} \left(\mu_{eff} \frac{\partial \overline{U_i}}{\partial x_j} \right) \tag{4.8}$$

where $\mu_{eff} = \mu_t + \mu$

Those turbulence models that take this approach are known as eddy-viscosity closure models. Based on the above analogy, the eddy-viscosity can be written in terms of a length scale ℓ and a velocity scale ϑ, which characterise the turbulent motion. The relationship can be written as

$$\frac{\mu_t}{\rho} \propto \vartheta \ell \tag{4.9}$$

hence

$$\mu_t = \rho C \vartheta \ell \tag{4.10}$$

where C is a dimensionless constant.

The k-ε model uses the eddy-viscosity concept and thus the isotropic assumption for μ_t. The eddy-viscosity μ_t is evaluated from k and ε computed from the solution of two differential equations, one for k and the other for ε (rate of dissipation of k). The relationship can be written as

$$\mu_t = C_\mu \rho \frac{k^2}{\varepsilon} \tag{4.11}$$

where C_μ is a coefficient taken as a constant in the standard k-ε model and ρ is the density.

The turbulent viscosity μ_t is not a fluid property and it depends on the state of turbulence, which may vary from flow to flow and even within the flow from one point to another. The following sections describe the main features of the turbulence models and their governing equations adopted in the present study. The detailed description of these models are given in many sources, see for example Launder and Spalding (1972a-b, 1974), Patel et al. (1985), Patankar (1988) and Versteeg and Malalasekera (1995).

4.3.2. Standard k-ε model

The standard k-ε model (Launder and Spalding, 1974) is a semi-empirical model that has been proven to yield good predictions for practical engineering purposes. As stated earlier, the model is based on the solution of two transport equations, namely, one equation for the turbulence kinetic energy k and one for the rate of dissipation of turbulence energy ε. These equations are solved simultaneously with other governing equations of fluid motion. The standard form of the model is applicable to high Reynolds number flows where the effect of molecular viscosity is negligible. This model is robust, provides good economy and reasonable accuracy for a wide rage of turbulence flows.

The equations for k and ε are written as

k - equation

$$\rho\frac{Dk}{Dt}=\frac{\partial}{\partial x_i}\left[\left(\mu+\frac{\mu_t}{\sigma_k}\right)\frac{\partial k}{\partial x_i}\right]+\mathbf{P}_k-\rho\varepsilon \tag{4.12}$$

ε - equation

$$\rho\frac{D\varepsilon}{Dt}=\frac{\partial}{\partial x_i}\left[\left(\mu+\frac{\mu_t}{\sigma_\varepsilon}\right)\frac{\partial \varepsilon}{\partial x_i}\right]+C_1\frac{\varepsilon}{k}\mathbf{P}_k-C_2\rho\frac{\varepsilon^2}{k} \tag{4.13}$$

where C_1, C_2, σ_k and σ_ε are constants. The term $\mathbf{P}_k$ is the generation of turbulence kinetic energy k due to the interaction between the Reynolds stresses and mean velocity gradients, which can be written as

$$\mathbf{P}_k=-\rho\overline{u_i'u_j'}\frac{\partial U_i}{\partial x_j} \tag{4.14}$$

Substituting equation (4.7) into equation (4.14), yields

$$\mathbf{P}_k=\mu_t\frac{\partial U_i}{\partial x_j}\left(\frac{\partial U_i}{\partial x_j}+\frac{\partial U_j}{\partial x_i}\right) \tag{4.15}$$

The model uses equation (4.11) to determine the eddy-viscosity. The values of constants used in this model are shown in Table 4.1:

C_μ	0.09
C_1	1.44
C_2	1.92
σ_k	1.0
σ_ε	1.217

Table 4.1: Constants in the standard k-ε model.

4.3.3. Reynolds Stress Model

The Reynolds Stress Model (Rodi, 1980) does not require the eddy-viscosity assumption, instead the transport equations of individual stresses are solved in conjunction with the transport equation for the rate of dissipation of turbulence kinetic energy ε. The numerical prediction based on the RSM is significantly influenced by the closure assumptions employed to model various terms in the transport equations for Reynolds stresses. Since the RSM enables to capture the anisotropy effects, such as due to streamline curvature, rotation and swirl of the flow, the prediction of complex flows is generally far superior to other one- or two- equation models. The exact equation for the transport of Reynolds stress takes the following form

$$\frac{\partial}{\partial t}(\rho\overline{u_i'u_j'}) + \frac{\partial}{\partial x_k}(\rho U_k \overline{u_i'u_j'}) = \text{Stress production}\,(P_{ij}) + \text{Turbulent diffusion}\,(D_{ij}^T) - \text{Dissipation}\,(\varepsilon_{ij}) + \text{Pressure} - \text{strain}\,(\phi_{ij}) + \text{Rotation}\,(O_{ij}) \tag{4.16}$$

where

$$P_{ij} = -\rho\left[\overline{u_i'u_k'}\frac{\partial U_j}{\partial x_k} + \overline{u_j'u_k'}\frac{\partial U_i}{\partial x_k}\right] \tag{4.17}$$

In order to solve equation (4.16), the diffusion, dissipation and pressure-strain terms on the right hand side need to be modelled. These terms for an incompressible flow are modelled in the following form.

The turbulent diffusion term (D_{ij}^T) can be modelled by assuming that the rate of transport of Reynolds stresses by diffusion is proportional to the gradients of Reynolds stresses. Thus this term can be written as

$$D_{ij}^T = \frac{\partial}{\partial x_k}\left(\frac{\mu_t}{\sigma_k}\frac{\partial \overline{u_i'u_j'}}{\partial x_k}\right) \tag{4.18}$$

The dissipation rate (ε_{ij}) can be modelled by assuming isotropy of small dissipative eddies, thus

$$\varepsilon_{ij} = \frac{2}{3}\rho\varepsilon\delta_{ij} \tag{4.19}$$

In equation (4.19), the scalar dissipation rate ε is computed from the transport equation (4.13) in the standard k-ε model.

The pressure-strain term (ϕ_{ij}) can be expressed as

$$\phi_{ij} = -C_3\rho\frac{\varepsilon}{k}\left(\overline{u_i'u_j'} - \frac{2}{3}k\delta_{ij}\right) - C_4\left((P_{ij} + O_{ij} - C_{ij}) - \frac{2}{3}\delta_{ij}(P - C)\right) \tag{4.20}$$

where $C_{ij} = convection\ term = \frac{\partial}{\partial x_k}(\rho U_k \overline{u_i'u_j'})$ and $P = \frac{1}{2}P_{kk}$, $C = \frac{1}{2}C_{kk}$

The rotation term is given by

$$O_{ij} = -2\rho\omega_k\left(\overline{u_j'u_m'}e_{ijm} + \overline{u_i'u_m'}e_{jkm}\right) \tag{4.21}$$

where ω_k is the rotation vector. The symbol e_{ijk} = 1, when i, j and k are different and in cyclic order, e_{ijk} = -1, when i, j and k are different and in anti-cyclic order and e_{ijk} = 0, if any two indices are the same.

The turbulence kinetic energy can be found by adding the three normal stresses as

$$k = \frac{1}{2}(\overline{u_i'u_i'}) \tag{4.22}$$

The values of constants used in this model are shown in Table 4.2:

C_μ	0.09
C_1	1.44
C_2	1.92
C_3	1.80
C_4	0.60
σ_k	0.82
σ_ε	1.30

Table 4.2: Constants in the Reynolds Stress Model

4.3.4. RNG k-ε model

The RNG (Renormalization Group Method) k-ε model (Yakhot et al., 1992) was derived from the application of a statistical method to the Navier-Stokes equations. It significantly improves the accuracy for rapidly strained flows. The transport equations for k and ε are similar in form to the standard k-ε model but differ by additional terms and functions, particularly in the transport equation for ε. In the present investigation, the RNG model is used in conjunction with an analytically derived differential formula for the effective viscosity, which takes the low Reynolds number effects into account. The transport equations of this model are

k - equation

$$\rho\frac{Dk}{Dt}=\frac{\partial}{\partial x_i}\left[\alpha_k\mu_{eff}\frac{\partial k}{\partial x_i}\right]+\mathbf{P}_k-\rho\varepsilon \tag{4.23}$$

ε - equation

$$\rho\frac{D\varepsilon}{Dt}=\frac{\partial}{\partial x_i}\left[\alpha_\varepsilon\mu_{eff}\frac{\partial \varepsilon}{\partial x_i}\right]+C_{1\varepsilon}\frac{\varepsilon}{k}\mathbf{P}_k-C_{2\varepsilon}^{*}\rho\frac{\varepsilon^2}{k} \tag{4.24}$$

The turbulent viscosity is given by

$$d\left(\frac{\rho^2 k}{\sqrt{\varepsilon\mu}}\right)=\frac{1.72\Theta}{\sqrt{\Theta^3-1+C_\Theta}}d\Theta \tag{4.25}$$

where $\Theta=\dfrac{\mu_{eff}}{\mu}$ and $C_\Theta=100$.

The use of equation (4.25) allows the model to handle better the effects of low Reynolds number and near wall flows into account. For high Reynolds number cases, the model uses equation (4.11). The significant difference between the RNG model and the standard k-ε model is the last term in the ε equation, which can be evaluated as

$$C_{2\varepsilon}^{*}=C_{2\varepsilon}+\frac{C_\mu\rho\eta^3(1-\eta/\eta_0)}{1+\beta\eta^3} \tag{4.26}$$

where $\eta \equiv \frac{Sk}{\varepsilon}$, $\eta_0 = 4.38$, $\beta = 0.012$, $S = (2S_{ij}S_{ij})^{\frac{1}{2}}$ and $S_{ij} = \frac{1}{2}\left(\frac{\partial U_i}{\partial x_j} + \frac{\partial U_j}{\partial x_i}\right)$.

The constants α_k , α_ε, $C_{1\varepsilon}$, $C_{2\varepsilon}$ were obtained as part of the derivation of the equations and have different values than those used in the standard k-ε model. The values of constants used in this model are shown in Table 4.3.

α_k , α_ε	1.39
C_μ	0.0845
$C_{1\varepsilon}$	1.42
$C_{2\varepsilon}$	1.68

Table 4.3: Constants in the RNG k-ε model.

4.3.5. Realizable k-ε model

The Realizable k-ε model (Shih et al. 1995) is a relatively recent development to provide superior performance for flows subjected to strong adverse pressure gradient, rotation, separation and recirculation. The model differs from the standard k-ε model by a new formula for turbulent viscosity and a new transport equation for ε. The model has been validated recently by investigators like Shih et al. (1995), Kim et al. (1997) for a wide range of flows, such as jets and mixing layers, channel and boundary layer flows, and separated flows. In all these cases the prediction by the model is substantially better than the standard k-ε model. The transport equations and the new formula for the turbulent viscosity of this model can be written as

k - equation

$$\rho\frac{Dk}{Dt} = \frac{\partial}{\partial x_i}\left[\left(\mu + \frac{\mu_t}{\sigma_k}\right)\frac{\partial k}{\partial x_i}\right] + \mathbf{P}_k - \rho\varepsilon \tag{4.27}$$

ε - equation

$$\rho\frac{D\varepsilon}{Dt} = \frac{\partial}{\partial x_i}\left[\left(\mu + \frac{\mu_t}{\sigma_\varepsilon}\right)\frac{\partial \varepsilon}{\partial x_i}\right] + \rho C_1 S\varepsilon - \rho C_2 \frac{\varepsilon^2}{k + \sqrt{\nu\varepsilon}} \tag{4.28}$$

The Realizable k-ε model also uses equation (4.11) to compute the eddy-viscosity. But the model coefficient C_μ is not constant and is related to the mean strain rate to ensure realizability (positive normal stresses). Shih et al. (1995) proposed the following formulation to compute the coefficient C_μ.

$$C_\mu = \frac{1}{A_0 + A_s U^* \frac{k}{\varepsilon}} \tag{4.29}$$

where A_s and U^* are functions of velocity gradient (see Shih et al., 1995 for details). The coefficient C_1 in the equation (4.28) is obtained from

$$C_1 = \max\left[0.43, \frac{\eta}{\eta+5}\right] \tag{4.30}$$

The values of constants used in the Realizable k-ε model are shown in Table 4.4.

C_2	1.90
σ_k	1.0
σ_ε	1.20
A_0	4.04

Table 4.4: Constants in the Realizable k-ε model.

4.4. Discretisation of the governing equations

The solution of the governing transport equations cannot be achieved analytically, thus a numerical method should be adopted. Adopting a numerical solution means that we restrict the solution to a finite number of discrete locations defined by the grid within the flow domain. The discretisation process of the governing equations is covered below.

4.4.1. Discretisation procedure

The principles of the discretisation procedure may be introduced by considering the simple case of a steady, one-dimensional flow involving convection and diffusion through the boundaries of the control volume surrounding the node P as shown in Figure

4.1 (a). But, in three-dimensional flows, the node P has six neighbouring nodes on west, east, north, south, top and bottom sides indicated as (W, E, N, S, T, B), respectively, as shown in Figure 4.1 (b).

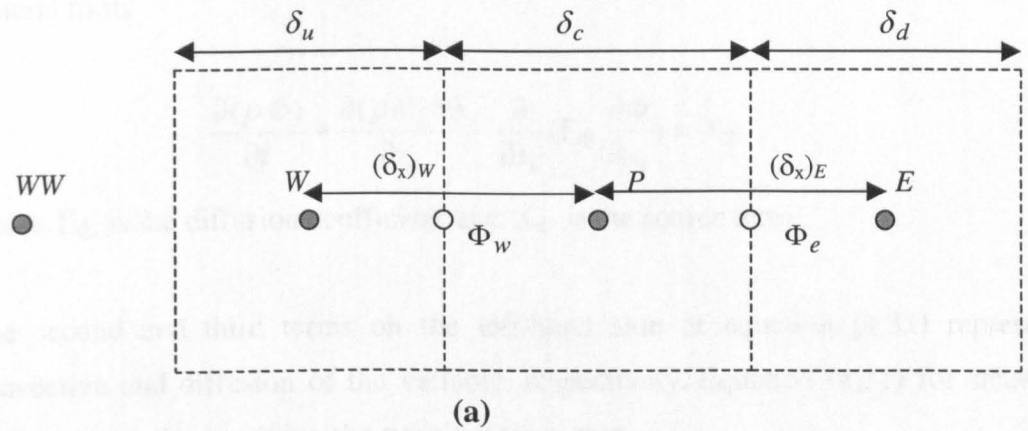

(a)

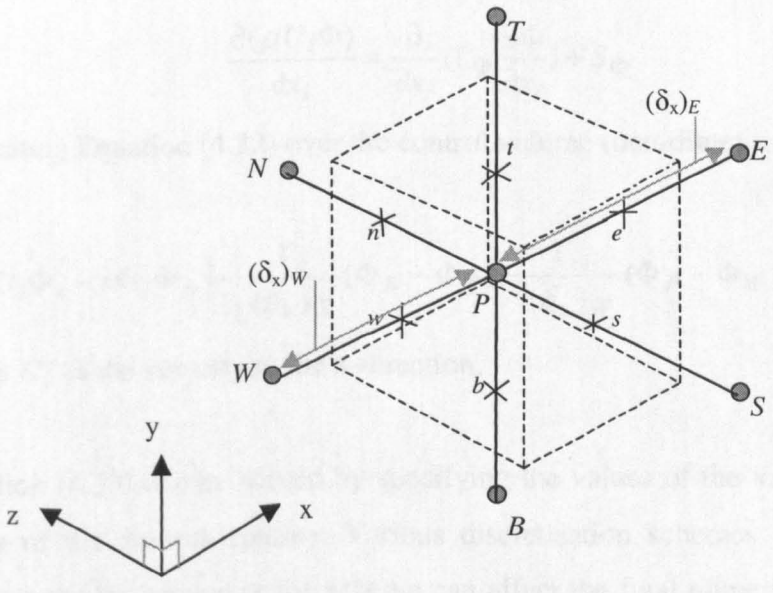

(b)

Figure 4.1: Control volume notation and neighbouring nodes: (a) one-dimensional cell, (b) three-dimensional cell.

The notation (w, e, n, s, t and b) in Figure 4.1 (b) are used to refer to the faces of the control volume located between node P and the neighbouring nodes. The distance between the nodes W and P, and between nodes P and E, are identified by $(\delta_x)_W$ and $(\delta_x)_E$, respectively. In the following section a lower case subscript (w, e, n, s) is used to

indicate the values at the face of the control volume, whereas an upper subscript (*W, E, N, S*) refers to values at the node.

The governing differential equations for a variable Φ can be written in the following general form:

$$\frac{\partial(\rho\Phi)}{\partial t}+\frac{\partial(\rho U_i\Phi)}{\partial x_i}-\frac{\partial}{\partial x_i}(\Gamma_\Phi\frac{\partial\Phi}{\partial x_i})=S_\Phi \tag{4.31}$$

where Γ_Φ is the diffusion coefficient and S_Φ is the source term.

The second and third terms on the left-hand side of equation (4.31) represent the convection and diffusion of the variable, respectively. Equation (4.31) for steady flow can be obtained by omitting the transient term, thus

$$\frac{\partial(\rho U_i\Phi)}{\partial x_i}=\frac{\partial}{\partial x_i}(\Gamma_\Phi\frac{\partial\Phi}{\partial x_i})+S_\Phi \tag{4.32}$$

Integrating Equation (4.32) over the control volume (one-dimensional) we obtain

$$[\rho U_i\Phi_e-\rho U_i\Phi_w]-\left[\frac{\Gamma_e}{(\delta_x)_E}(\Phi_E-\Phi_P)-\frac{\Gamma_w}{(\delta_x)_W}(\Phi_P-\Phi_W)\right]=\int S_\Phi dV \tag{4.33}$$

where U_i is the velocity in the x-direction.

Equation (4.33) can be solved by specifying the values of the variable Φ at the faces w and e of the control volume. Various discretisation schemes can be chosen for this purpose and the choice of the scheme can affect the final numerical results. The general form of the discretised equation for a control volume can be written as

$$a_P\Phi_P=\sum_{nn}a_{nn}\Phi_{nn}+S \tag{4.34}$$

where

$$a_P=\sum_{nn}a_{nn} \tag{4.35}$$

and a_{nn} are the neighbouring coefficients $a_W, a_E, a_S, a_N, a_B, a_T$ describing combined convection and diffusion at the cell boundaries, whereas Φ_{nn} are the values of

the variable Φ at each neighbouring nodes.

4.4.2. Discretisation of the diffusion term

The diffusion term is the simplest to discretise. If we consider the west face of the control volume, the diffusion flux at the face can be written as:

$$\int \Gamma \frac{\partial \Phi}{\partial x_j} \cdot \mathbf{n}\, dA = \frac{\Gamma A_w}{(\delta_x)_W}(\Phi_P - \Phi_W) = D_w(\Phi_P - \Phi_W) \tag{4.36}$$

where the area of the west face is denoted by A_w and D_w is the west face diffusion coefficient. In the formulation of the discretised equations, the value of the property at the required face of the control volume is obtained using a linear profile between the two adjacent nodes.

4.4.3. Discretisation of the convection terms

The treatment of the convection terms determines the accuracy of the solution. The problem in the discretisation of the convection terms is the determination of the value of the variable Φ at the control volume faces and its convective flux across these boundaries. A variety of schemes is used to achieve this, which range from first-order accurate to higher-order accurate schemes. The more accurate higher-order discretisation schemes lead to less robust or slower solution process. In the present study, two discretisation schemes, namely, upwind and QUICK were adopted to discretise the convective terms.

The upwind scheme

In a strongly convective flow, say from west to east direction, the west cell face receives much stronger effects from node W than node P. The upwind differencing scheme takes the flow direction into account when determining the value at a cell face. In this scheme, the values of the variable Φ at the faces of the control volume are taken to be equal to the values at the upstream nodes.

When the flow is in the positive direction, say from "west to east", then the variable takes

the value on the cell boundary as

$$\Phi_w = \Phi_W \text{ and } \Phi_e = \Phi_P \tag{4.37}$$

Similarly, for the flow in the opposite direction, say from east to west:

$$\Phi_w = \Phi_P \text{ and } \Phi_e = \Phi_E \tag{4.38}$$

Subsituting equations (4.37) and (4.38) in equation (4.33), the coefficients of a_W and a_E (see equation (4.34)) are given by

a_W	a_E
$D_w + \max(C_w, 0)$	$D_e + \max(0 - C_e)$

Table 4.5: Neighbour coefficients of upwind differencing scheme, (Versteeg and Malalasekera, 1995).

In Table 4.5, $C_e = (\rho U)_e$ and $C_w = (\rho U)_w$ are the convective mass flux per unit area at the east face and west face, respectively. The upwind scheme is a first order accurate scheme.

Quadratic Upwind Differencing (QUICK)

Higher order schemes bring in the influence of a greater number of surrounding nodes. The Quadratic Upstream Interpolation for Convective Kinetics (QUICK) scheme of Leonard (1979) is a third order accurate differencing scheme for convection terms. It uses two upstream and one downstream nodes to determine the value of the variable at a cell face. If the flow is from west to east, the value of variable Φ at the east cell face between the two nodes P and E in Figure 4.1 (a) can be written as

$$\Phi_e = \theta\left[\frac{\delta_d}{\delta_c + \delta_d}\Phi_P + \frac{\delta_c}{\delta_c + \delta_d}\Phi_E\right] + (1-\theta)\left[\frac{\delta_u + 2\delta_c}{\delta_u + \delta_c}\Phi_P - \frac{\delta_c}{\delta_u + \delta_c}\Phi_W\right] \tag{4.39}$$

The traditional QUICK scheme can be obtained by setting $\theta = \frac{1}{8}$. However, in FLUENT a variable, solution dependent value of θ is implemented.

4.5. Derivation of pressure

All the variables in the governing equations except pressure have their own equations. Methods, such as SIMPLE (Semi-Implicit Method for Pressure Linked Equations) of Patankar and Spalding (1972) were developed to derive the pressure by an iterative method. The procedure is as follows.

The discretised momentum equation for the west face of the control volume can be written in terms of the guessed pressure P^* and velocity U^* as

$$a_P U_w^* = \sum_{nn} a_{nn} U_{nn}^* + A_w (P_W^* - P_P^*) + S_w \tag{4.40}$$

If the pressure field in equation (4.40) is correct then the resulting velocity field will satisfy the continuity equation. If not, then improved pressure and velocity fields are required. If we define the required correction P' as the difference between the correct pressure field P^{**} and the guessed pressure P^*, then

$$P^{**} = P^* + P' \tag{4.41}$$

Similarly for the velocity correction U' we can write

$$U^{**} = U^* + U' \tag{4.42}$$

Substituting the correct pressure field P^{**} into the discretised momentum equation (4.40) yields the correct velocity field U^{**} as

$$a_P U_w^{**} = \sum_{nn} a_{nn} U_{nn}^{**} + A_w (P_W^{**} - P_P^{**}) + S_w \tag{4.43}$$

By subtraction of equation (4.43) from equation (4.40), we obtain

$$a_P U_w' = \sum_{nn} a_{nn} U_{nn}' + A_w (P_W' - P_P') \tag{4.44}$$

At this stage the SIMPLE algorithm applies an approximation to simplify the equation (4.44) by omitting $\sum a_{nn} U_{nn}'$. But, the SIMPLEC (SIMPLE-Consistent) algorithm does

not omit $\sum a_{nn}U'_{nn}$. From equation (4.44), the velocity correction required can be written as

$$U'_w = \frac{A_w}{a_P}(P'_W - P'_P) \tag{4.45}$$

The SIMPLE algorithm substitutes equations (4.42) and (4.45) into the continuity equation to obtain an equation for the pressure correction P' as

$$a_P P' = \sum_{nn} a_{nn} P'_{nn} + b \tag{4.46}$$

where the source term b is the mass flow into the cell can be written as

$$b = \sum_{nn} \rho A_{nn} U^*_{nn} \tag{4.47}$$

Once the pressure correction is obtained from the solution of the pressure correction equation (4.46), the corrected pressure field can be calculated using equation (4.41). Hence, the corrected velocity field can be calculated using equations (4.45) and (4.42). In order to stabilise the solution during the iterative process the pressure is under-relaxed as

$$P^{**} = P^* + f P' \tag{4.48}$$

The term f is called an under-relaxation factor and takes value between 0 to 1.

Chapter 5

5. NUMERICAL INVESTIGATION: Computational Details

5.1. Introduction

This Chapter presents detailed description of computational details, such as boundary conditions, grid distribution of the flow domain and solution procedures adopted in the present investigation. The first part of this Chapter describes the boundary conditions. This is followed by detailed description of the full-scale three-dimensional flow domain, within which the numerical equations are solved. Description of the grid used and the process employed to determine an optimum grid size are also presented. The final part involves details of the solution procedures incorporated in a commercial CFD software code known as FLUENT 5, hereafter referred to as FLUENT.

5.2. Incorporation of the boundary conditions

This section is concerned with setting of real information on boundary surfaces, such as the walls, inlet, and outlet of the flow domain. The boundary conditions therefore have a significant influence on the final solution. In the present study the FLUENT mesh generator known as GAMBIT 1.2 is used to create the 3-D structured grid of the flow domain. Furthermore, the inlet and outlet boundary surfaces of the flow domain are specifically defined during the mesh generating process. The final grid is then directly imported into FLUENT for the solution process. The boundary conditions used in this investigation are described in the following sections.

5.2.1. Inlet boundary

An inlet is an edge boundary of the flow domain where the values of the variables are specified. In the present study, experimentally measured profiles of the mean, turbulence quantities and turbulence kinetic energy at station 1, and calculated turbulence kinetic energy dissipation rate are set at the inlet. The so-called "point profile" type of boundary

profile is employed for this purpose, where FLUENT uses an interpolation method to obtain the variable values at the cell boundary faces. The turbulence kinetic energy and its dissipation rate are calculated using the following equations (5.1) and (5.2), respectively.

$$k = \frac{1}{2}(\overline{u'^2} + \overline{v'^2} + \overline{w'^2}) \tag{5.1}$$

$$\varepsilon = \frac{k^{\frac{3}{2}}}{\ell}, \text{ where } \ell = c\frac{H}{2} \tag{5.2}$$

where c is a constant and H is the duct height.

In order to calculate the dissipation rate of turbulence energy ε, the unknown length scale ℓ in equation (5.2) had to be determined. Numerous sensitivity tests were carried out with different values of length scale for the region outside the boundary layers on the duct walls. Furthermore, the length scale within the boundary layer region was taken to be equal to 0.41y, where y is the normal distance from the wall. In each test, the profile of the predicted kinetic energy at the bend entry (station 2) was compared with its corresponding measured profiles to obtain best agreement. For the two mainstream velocities, namely, 10 m/s and 20 m/s the length scales which led to the best agreement were chosen. Thus, the constant c in the equation (5.2) was taken as 0.25 and 0.20 for 10 m/s and 20 m/s mainstream velocities, respectively.

5.2.2. Outlet boundary

The outlet boundary plane of the flow domain consisted of five individual block faces, which were combined together and treated as a single face. It was placed at 6H downstream of station 4 (exit of the bend), where the Neuman boundary conditions were applied, which sets the gradients of all transported quantities except velocity to zero. This type of boundary condition is equivalent to a fully developed condition. The normal and spanwise velocity components are set to zero and the value of streamwise velocity component is obtained using the upstream value such that the global mass conservation for the whole flow domain is satisfied. The pressure is obtained by extrapolation from the upstream value.

5.2.3. Wall boundary and near wall treatment

The wall boundary conditions are the most common boundary conditions encountered in fluid flow problems, where the mean velocity is mainly affected by the no-slip condition, which forces the mean velocity to satisfy a zero magnitude condition at stationary walls. The turbulence quantities are also significantly affected by this condition. Therefore, an accurate modelling of the flow in the near wall region is required. In the present study, two different methods were employed to model the near wall region, namely, wall functions method and a two-layer zonal model. The following section describes these two approaches and their capabilities to predict the flow field in the near wall region.

Wall functions method

The wall function method is an economical, robust and reasonably accurate method to resolve the turbulent flow near the wall. In this method, well-established formulas of turbulent boundary layers referred to as "wall functions" are used to avoid the solution of the governing equations required to predict the steep variations of fluid properties in this region. Thus, the solution in the close proximity of the wall is by-passed by starting the solution from a distance, d, from the wall (determined by the first grid line) where the wall functions can be applied. The distance d can be chosen such that it places the first grid line in the viscous sublayer or the turbulent layer of the boundary layer. In the former case the relationships for the viscous sublayer are used and in the latter case the relationships such as the logarithmic law of the wall are applied. The full governing equations are then solved from the next grid line.

The logarithmic law of the wall can be written in terms of the non-dimensional parameters of u^+ and y^+ as

$$u^+ = \frac{1}{\kappa} \ln(E\, y^+) \tag{5.3}$$

where the constants E and κ have the values of 9.793 and 0.41, respectively.

The non-dimensional parameters of u^+ and y^+ can be written as

$$y^+ = \frac{\rho (\tau_w/\rho)^{\frac{1}{2}} y}{\mu} \tag{5.4}$$

and

$$u^+ = \frac{U}{(\tau_w/\rho)^{\frac{1}{2}}} \tag{5.5}$$

where y is the normal distance from the wall and τ_w is the wall shear stress. Equation (5.3) is applied for y^+ values greater than 11.225 and less than 500.

The kinetic energy equation is reduced to a simpler form based on the local equilibrium assumption, leading to the wall shear stress τ_w, which can be written as

$$\tau_w = \rho C_\mu^{\frac{1}{2}} k = \frac{\rho \kappa C_\mu^{\frac{1}{4}} k^{\frac{1}{2}} U}{\ln(E y^+)} \tag{5.6}$$

The energy dissipation rate ε is computed using

$$\varepsilon = \frac{C_\mu^{3/4} k^{3/2}}{\kappa y} \tag{5.7}$$

The initial simulations with the wall functions showed that the use of wall functions were not suitable for the modelling of the boundary layers on the airfoil and consequently the wake region.

Two-layer zonal model

In the two-layer zonal model (Wolfstein, 1969), the wall functions are not used. The flow adjacent to the wall is divided into the near wall region and the outer region, where the near wall region includes viscous sublayer, buffer layer and a part of fully turbulent layer and the outer region includes the rest of the flow. The boundary between these two regions is determined by the wall distance based on turbulence Reynolds number (Re_y), given by

$$Re_y = \frac{\rho \sqrt{k}\, y}{\mu} \tag{5.8}$$

where y is the normal distance from the wall.

In the outer region (Re_y > 200), the k-ε model or the Reynolds Stress Model is employed. But, when Re_y is below 200, the region is considered as the near wall region and the one-equation turbulence model is employed, which requires the solution of the equation for turbulence kinetic energy and a length scale. The eddy-viscosity is obtained from

$$\mu_t = \rho C_\mu \ell_t \sqrt{k} \tag{5.9}$$

where length scale ℓ_t is given by (Chan and Patel, 1988)

$$\ell_t = C_1 y \left[1 - \exp\left(-\frac{Re_y}{A_t}\right)\right] \tag{5.10}$$

The dissipation of turbulence energy is calculated from

$$\varepsilon = \frac{k^{1.5}}{\ell_d} \tag{5.11}$$

where length scale ℓ_d is given by (Chan and Patel, 1988)

$$\ell_d = C_1 y \left[1 - \exp\left(-\frac{Re_y}{A_d}\right)\right] \tag{5.12}$$

In equations (5.10) and (5.12), both ℓ_t and ℓ_d become linear and approach $C_1 y$ with increasing distance from the wall.

The constants C_1, A_t and A_d are given by

$$C_1 = \kappa C_\mu^{-\frac{3}{4}}, \quad A_t = 70, \quad A_d = 2C_1 \tag{5.13}$$

When the two-layer zonal model is employed, the y^+ value at the cell adjacent to the wall should be ideally about 1, however a higher y^+ value is also acceptable as long as it is less than 5 (the upper limit of the viscous sublayer).

5.3. Computational flow domain

5.3.1. Geometry

During the preliminary investigations using the CFD code CFX- 4.3, difficulties were encountered in both solution and convergence of a half-size flow domain. Therefore, in the present investigation a full-scale model was adopted. The geometry of the full-scale computational domain was constructed using the FLUENT mesh generator (pre-processor) known as GAMBIT 1.2. A multiblock approach was employed by which the geometry is broken down into many smaller blocks. Each of these blocks are created by specifying their coordinates in the physical space of the flow domain and the blocks are connected to each other by sharing common faces between their neighbouring blocks. An advantage of using a multiblock structure is that finer grids can be placed in regions with high gradients while relatively coarser grids can be placed elsewhere thus reducing the CPU time and the memory needed.

The entire flow domain is consisted of twenty-five blocks. For the purposes of discussion, the geometry is divided into three sections as the experimental test section, namely, upstream tangent, the bend and downstream tangent. The upstream tangent is constructed with fifteen blocks, where most of these blocks are located in the central part of the section, particularly around the airfoil. The walls of the airfoil are connected with the surrounding blocks of the flow domain, which enabled the creation of a so-called C-type quadrilateral grid around the airfoil. The original coordinates of the airfoil were obtained from UIUC-airfoil coordinate database (http://amber.aae.uiuc.edu/~m-selig/ads/coord/n0012.dat), which had a chord length of 1.0 m. These coordinates are later scaled down to obtain the desired coordinates of the experimental airfoil, which has a chord length of 0.150 m. As in the case of the experimental set-up, the airfoil has a zero angle of attack and is placed such that the distance between the trailing edge and the bend entry plane is equal to one chord length.

The second group of the flow domain is the bend, which connects the upstream tangent to the downstream tangent. The bend is constructed with five curved blocks and has the turning angle of 90°. The final part of the flow domain is the downstream tangent, which is an extended section of the bend outlet. Therefore, the downstream tangent is also

consisted of five rectangular blocks, where each block has identical cross-section in the y-z plane as their adjacent block of the bend section.

5.3.2. Grid distribution

The grid distribution in the streamwise and spanwise planes of the flow domain is shown in Appendix V. As can be seen, the blocks of the flow domain are constructed in such a way to allocate sufficient number of grid cells to those regions where steep variations are most likely to occur, e.g. in near walls and in the wake regions. The blocks structure in the upstream tangent are complex due to the presence of the airfoil and, therefore, two different types of grids, namely, C-type and H-type were employed to allocate sufficient number of grid cells to the near wall regions to satisfy the wall boundary conditions. Also, the structured quadrilateral cells were used to mesh the entire flow domain because they can be compressed or expanded easily to account for different gradients in different directions.

The use of the two-layer model requires very fine grid distribution near the walls. Once the two-layer model is invoked within the FLUENT code (version 5), it is applied to all the walls and impossible to restrict the model to particular walls, such as the airfoil as was ideally needed. This meant that very fine grid was also required on all four walls of the duct which imposed heavy demand on computer resources. For this reason, a very fine grid was used only around the airfoil with the nodes adjacent to the walls placed within the viscous sublayer ($y^+ < 2$), so that details of the boundary layer could be predicted more accurately. The grid nodes nearest to the walls of the duct were placed at y^+ of 40 to 60. However, comparisons with the results obtained using the wall functions method did not show any significant differences in the vicinity of the duct walls. The near wall grid density was relaxed in a geometric progression with increasing distance from the walls. But, in the wake region steep changes were expected and therefore, a uniformly distributed fine grid was used. The grid distribution in the spanwise direction was kept uniform.

Within the bend, as in the upstream tangent, a fine grid was used close to the concave and convex wall regions to capture the steep variations. Furthermore, the grid density of the near wall regions was decreased progressively with the normal distance from the wall,

but in the wake region it was kept uniform with greater number of cells. The grid in the spanwise direction was kept uniform as in the upstream tangent. The final part of the flow domain is the downstream tangent, which had the same grid distribution in the normal and spanwise directions as in the bend. However, in the streamwise direction the grid density was decreased progressively with the streamwise distance. The total number of grid cells used in various regions of the flow domain is presented in Table 5.1.

H-Type grid distribution				
Section	**x-direction** (Streamwise)	**y-direction** (Normal)	**z-direction** (Spanwise)	**Total grid number**
Upstream tangent	40	40	40	64,000
Bend	35	80	40	112,000
Downstream tangent	60	80	40	192,000
C-Type grid distribution				
Section	**Tangential** (Streamwise)	**Radial** (Normal)	**Axial** (Spanwise)	**Total grid number**
Upstream tangent	140	55	40	308,000

Table 5.1: The H- and C-types grid cells used in the geometry of the flow domain.

5.3.3. Grid sensitivity tests

The accuracy and economy of the numerical calculation are strongly influenced by the total number of grid cells. Generally, finer grids can produce more accurate results but they require larger computer memory and longer processing time. The purpose of grid sensitivity test is to determine an optimum grid number, which could predict the numerical results accurately with least computational time and memory. Because of the complex structure of the flow domain, the grid sensitivity tests were conducted on both global and local basis. The global investigation was initiated using a uniformly distributed coarse grid and the standard wall functions as the near wall treatment to obtain the overall features of the flow. Subsequently the grid was refined by gradually increasing the grid cells of each block in the x-, y- and z-directions until no significant differences of the parameters of interest were observed, particularly in the free-stream region and the near wall region of the duct.

In order to implement the two-layer zonal model further sensitivity tests were carried out, particularly in the wake region. The computations were performed using the two-layer zonal model and a fine grid around the airfoil, where the nearest grid cells to the airfoil were kept within the viscous sublayer ($y^+ < 2$) and the grid distribution around the airfoil was refined until no significant differences of the parameters of interest were resulted.

5.4. Solution of discretised equations

5.4.1. Introduction

The complexity and size of the set of linear algebraic equations depend on the number of total grid nodes, the dimension of the problem and the discretisation procedure adopted. There are two types of solution techniques, namely, direct method and indirect or iterative method, which can be used to solve the discretised algebraic equations. In the direct method the complete set of equations are solved simultaneously, which requires enormous computational effort. The iterative methods are based on repeated application of a relatively simple algorithm, which leads to convergence after a number of repetitions. In FLUENT, the direct and indirect numerical methods are known as coupled solver and segregated solver, respectively. In the present study, the iterative method or segregated solver was used. The process of solving the discretised equations is described in the following section.

5.4.2. Segregated solution method

The segregated solver solves the governing equations sequentially (i.e. each variable is taken in sequence). Because the non-linearity of the governing equations, a number of iterations must be performed until a converged solution is obtained. The iteration process begins by solving the momentum equations for U, V and W in turn using the guessed values of the variables, including pressure, over the entire domain. The solutions of the momentum equations would yield a new velocity field. The pressure-correction equation (in the SIMPLEC algorithm) is then solved to obtain improved values of pressure and velocity fields. The solving process then continues by solving the scalar equations, such as turbulence kinetic energy and energy dissipation rate. The iteration process is repeated

a number of times until the converged solution is obtained. The segregated solution process is shown in Figure 5.1.

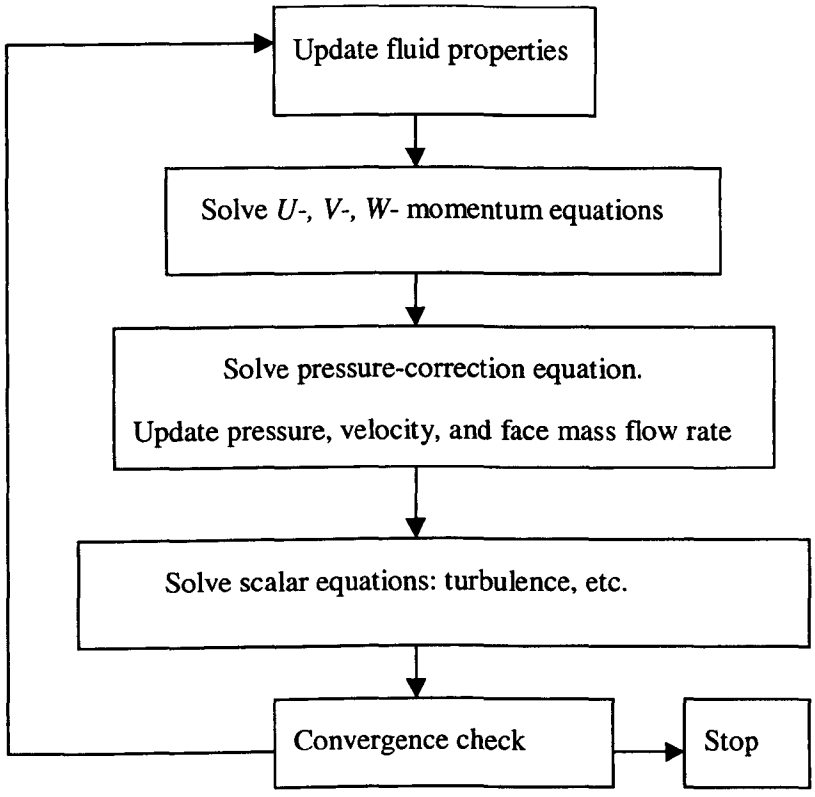

Figure 5.1: Segregated solution method block diagram, (FLUENT 5 User's guide).

5.4.3. Under-relaxation factors

In order to stabilise the solution procedure, the computed parameters were relaxed using the under-relaxation factors (URF). The under-relaxation process for a variable can be expressed as

$$\Phi_n = \Phi_o + f(\Phi_c - \Phi_o) \tag{5.14}$$

where f is the under-relaxation factor, which takes a value between 0.0 and 1.0. The variables Φ_n, Φ_c, Φ_o are the new, current and old values, respectively.

A smaller under-relaxation factor means more under-relaxation is implemented, and therefore the solution process is slowed down with only a fraction of the difference is

added to the previous value. The under-relaxation factor values used for each variable are given in Table 5.2.

VARIABLE	URF (default)	URF (used)
U, V, W	0.7	0.5
P	0.3	0.3
k, ε	0.8	0.4
All Reynolds stresses	0.5	0.4

Table 5.2: Details of under-relaxation factors used in the present study.

5.5. Other computational details

5.5.1. Convergence criterion

Until a converged solution is obtained, the computed variable Φ does not satisfy equation 4.34. Hence, the residual (imbalance) for a cell can be written as

$$R_\Phi = \sum_{nn} a_{nn}\Phi_{nn} + S - a_P\Phi_P \tag{5.15}$$

The global (total) residual can be obtained by summing the residuals for all the cells. As the solution process progresses, the sum of residuals is decreased. Since no scaling is employed, it is difficult to determine the level of convergence based on the global residual values. In FLUENT, the "scaled" residual is employed, which can be defined as

$$R_\Phi = \frac{\sum_{cells}\left|\sum_{nn} a_{nn}\Phi_{nn} + S - a_P\Phi_P\right|}{\sum_{cells}\left|a_P\Phi_P\right|} \tag{5.16}$$

Also, for the continuity equation, the unscaled residual can be defined as

$$R_c = \sum_{cells}\left|\,Rate\ of\ mass\ creation\ in\ cell\right| \tag{5.17}$$

The scaled residual for the continuity equation is obtained by dividing the unscaled residual in equation (5.17) with the largest absolute value of the continuity residual in the

first five iterations. The convergence is achieved when the scaled residuals for all the variables have reduced to an acceptable small value. In the present study, the solution is treated as converged when the scaled residual for all the variables attained 0.001.

5.5.2. Computational effort

The processing time depends on a number of factors, such as the size of the problem, computer memory and speed, the under-relaxation factors employed, the turbulence model used, and the type of solution techniques. In the present study the calculations were performed on a sun® Sparc Ultra-60 machine, with a Solaris® 7 environment. The total CPU time required for different turbulence models varied significantly. It was noticed that the standard k-ε model used the least computational effort. Furthermore, the Realizable k-ε model required very little more computational effort than the standard k-ε model. The RNG- k-ε model generally took 10 to 15% more CPU than the standard k-ε model due to the presence of the terms, functions and a greater degree of non-linearity of the equations. As expected, the Reynolds Stress Model was an expensive model, which required additional memory and CPU time due to increased number of transport equations (one equation for each of the six Reynolds stresses). However, restarting from previous solutions reduced the CPU time significantly, which also provided better initial conditions. Generally, the Reynolds Stress Model required more iterations than the k-ε based models to obtain a converged solution.

5.5.3. Accuracy

The accuracy of the numerical calculation is influenced by several factors.

- Boundary conditions- The boundary conditions are the critical components in flow simulations and it is important to specify them correctly as well as appropriately. The numerical results obtained by setting the measured profiles as inlet boundary conditions resulted in good agreement with experimental results, particularly in the near wall region of the duct.

- Turbulence model- This can have significant effects on the accuracy of the numerical calculation. In the present study, the effects of turbulence models on numerical

prediction are one of the areas of interest.

- Grid density- The size of the grid and the distribution of the cells can affect the numerical results significantly. Grid independence tests are therefore necessary as was mentioned earlier.

- Discretisation scheme- The use of discretisation schemes, such as QUICK or upwind, can affect the accuracy of the solution. Generally, higher order schemes like QUICK can produce more accurate results compared with the low order schemes (i.e. upwind). In the present study a fine grid and higher order scheme (QUICK) were used, therefore the error due to discretisation scheme can be taken to be small.

- Near-wall modelling- In the present study the near wall modelling, particularly in the near wall region of the airfoil had significant effects on the results of the mean and turbulence quantities in the wake region. The results showed that the flow of this type was very difficult to model using the standard wall functions. However, the use of the two-layer zonal model on the airfoil was found to be superior to the standard wall functions method, which led to improved results, particularly in the wake region.

- Level of convergence- It is important to achieve a good degree of convergence of the governing equations. In the present study, the solution is treated as converged when the scaled residuals for all the variables attained about 0.001. Therefore, the error due to level of convergence was considered to be very small.

5.5.4. The computer program

The numerical results of the present study were obtained by employing the CFD software code known as FLUENT 5, which is suitable for prediction of variety of flows, such as laminar flow, turbulent flows, heat transfer and multi-phase flows. The FLUENT 5 program consists of a pre-processor, a solver and a post-processor. The structure of the FLUENT 5 code is shown in Figure 5.2. The geometry of a flow domain and the grid can be created using the pre-processor known as GAMBIT. Also, the pre-processor TGrid can be used to generate mesh from existing boundaries created by GAMBIT or a third party CAD/CAE package. As stated earlier, the solution of the governing equation can be

obtained using the two types of solver, namely, segregated solver and coupled solver. Once the solution is achieved, the numerical results can be obtained in the forms of vector and contour plots, and distribution profiles using the post-processor

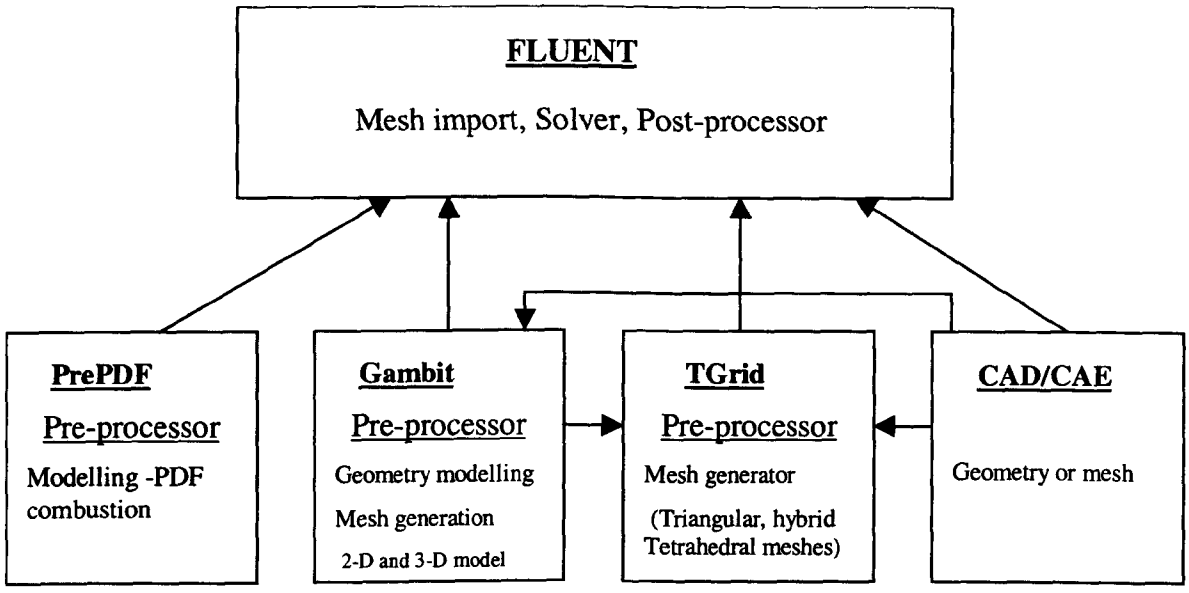

Figure 5.2: Basic program structure, (FLUENT 5 User's guide).

Chapter 6

6. THE EXPERIMENTAL RESULTS AND DISCUSSION

6.1. Introduction

This Chapter presents the results of experimental measurements of static pressure, mean velocity components and turbulence quantities. The structure of the presented results is shown in Figure 6.1. The normalized form of the results are divided into static pressure distribution, calibration data, hot-wire measurements at station 1, error analysis and hot-wire measurements at stations 2 to 5. The experimental data obtained along the duct centreline (z/H = 0.5) at a mainstream velocity of 10 m/s are the only set of data that are presented in tabular form, which can be found in Appendix III.

The hot-wire measurements obtained at each measuring station are divided further into two sets. In the first set, for fixed values of the normal distance (y) the spanwise measurements obtained with increasing distances (z) from the sidewall are plotted. In the second set, the measured quantities in the direction normal to the lower wall or upper wall are presented. Thus, for fixed values of the spanwise distance, the parameters were measured with increasing distance from the lower wall or upper wall. At station 1, several profiles of the mean and turbulence quantities were measured in the normal and spanwise directions at three mainstream velocities, namely, 10, 15 and 20 m/s to determine the characteristics of the flow field. Due to the general similarity and consistency of the spanwise profiles at different speeds, the profiles for the mainstream velocity of 10 m/s are presented. However, the normal profiles for all three mainstream velocities are presented.

In the downstream direction (stations 2 to 5), both normal and spanwise profiles were measured at three mainstream velocities. The spanwise measurements were only obtained at the wake centreline, whereas the normal profiles were measured at two different spanwise locations, namely, z/H = 0.5 and 0.6 at each station. The results obtained in the absence of the airfoil are also included for comparison. The following sections describe

the results in detail.

6.2. Normalized form of the experimental results

The mean velocity components, turbulence intensities and Reynolds shear stresses are normalized with respect to the mainstream velocity at station 1, whereas the pressure coefficients were calculated using the static pressure (P_o) and mainstream velocity (U_o) of station 1 according to

$$C_p = \frac{P - P_o}{\frac{1}{2}\rho U_o^2} \tag{6.1}$$

6.2.1. Calibration profiles

Both tunnel calibration and cross-wire probe calibration are presented in Figure 6.2 (a) and (b), respectively. As expected, there exists a linear relationship between the static pressure difference across the contraction section and the Pitot-static tube as can be seen in Figure 6.2 (a). The linear equation shown on the graph was obtained by least squares fitting, which was used to determine the mainstream velocity at station 1. The cross-wire probe calibration data seen in Figure 6.2 (b) shows the variations of the anemometer voltage against jet velocity in the range of 0 to 25 m/s for the two hot-wire sensors. The upper range exceeds the maximum speed of 20 m/s used in the present study. Fourth order polynomial curves fitted to this data are also shown in this Figure as solid lines. Both fitted curves show identical trends and closely agreed values, which confirm that the two wires were experiencing similar effective cooling velocities. During the calibration, the estimated error between the measured air velocity and the calculated air velocity based on this curve fit was less than ± 0.7%.

6.2.2. Static pressure distributions

The concave wall and convex wall static pressure distributions measured in the presence and absence of the airfoil are presented in Figure 6.3 (a) and (b), respectively. The reference points for the pressure coefficient were taken to be the first static pressure tappings located at x/H = 0.109 and 0.11 from station 1 on the concave wall and convex

wall, respectively. The measurements were taken at three nominal mainstream velocities, namely, 10, 15 and 20 m/s. The presented results indicate that the static pressure on the concave wall increases from station 1 to 2 and then remains constant over most part of the bend while the static pressure on the convex wall decreases between stations 1 and 2 followed by an increase in between stations 3 and 4. The profiles therefore show an adverse (positive) pressure gradient on the concave surface and favourable (negative) pressure gradient on the convex surface of the bend between stations 1 and 2. But, in between stations 3 and 4 the pressure gradient on the concave wall gradually becomes favourable while the pressure gradient on the convex wall becomes adverse. In the downstream tangent, the static pressure on the concave wall gradually drops towards the exit of the bend and approaches a constant value, which is approximately equal to the measured value on the convex wall in the same region. In the close proximity of station 4, the flow is close to separation. It was reported by Ondore (1999) that the flow separated and then reattached, further downstream before station 5, intermittently. The flattening of the static pressure profile at the bend exit, on the convex wall ($x/H = 2.0$), is as a result of this flow phenomenon. The general pattern seen in this Figure is consistent with an investigation by Ward-smith (1971) and Kotb (1988) on a square bend of the same radius to height ratio and radii of curvature. However, a comparison between the pressure coefficients obtained in the presence and absence of the airfoil shows a small difference in the profiles in the downstream tangent, particularly beyond $x/H > 4.0$. This is due to the change in the reference static pressure as result of the presence of the airfoil.

The effect of the airfoil on the static pressure distribution on the concave and convex walls can be seen in Figure 6.4 (a-c). The comparison of the profiles shows that the static pressure distributions on both upper (convex) and lower (concave) walls of the upstream tangent (between stations 1 to 2) and on the entire concave wall of the bend are affected by the presence of the airfoil. However, the static pressure distributions on the convex wall of the bend and on both walls of the downstream tangent are virtually unaffected. It is noted that the static pressure on the concave wall of the upstream tangent is increased slightly and on the convex wall is decreased due to the presence of the airfoil.

The distributions of static pressure over the upper and lower surfaces of the airfoil at various angles of attack ($+5^{o}$ to -5^{o}) are presented in Figure 6.5 (a-e), where the

anticlockwise rotation of the airfoil was taken as positive. The angle of attack (α) is the angle between the chord of the airfoil and the horizontal axis (x-axis). The distance x was measured from the leading edge along the chord length (c) of the airfoil. The pressure coefficient on the airfoil was calculated using the static pressure (P_0) and mainstream velocity (U_0) of station 1 according to equation (6.1). It can be seen that for +5° angle of attack (nose downward) the static pressure on the lower surface is smaller than the upper surface resulting a downward force on the airfoil. As the angle of attack gradually becomes smaller and smaller (clockwise rotation), the static pressure on the lower surface increases, while the static pressure on the upper surface decreases. When the airfoil is at zero angle of attack, the static pressure on the upper surface is smaller than the static pressure on the lower surface, which indicates a lift force on the airfoil. But, as the angle of attack becomes more and more negative (nose upward), the lift on the airfoil gradually increases.

The measured static pressure distributions in the normal (radial) direction at each measuring station are presented in Figure 6.6 (a-e). The profiles shown in this Figure are normalized with respect to the mainstream dynamic pressure at station 1. The results show a uniform static pressure distribution between the concave and convex walls at station 1. But, as the streamwise distance increases between stations 1 and 3, the static pressure gradually increases on the concave side while decreases on the convex side, which shows the presence of adverse (positive) and favourable (negative) pressure gradients on the concave and convex sides of the bend, respectively. However, in between stations 3 and 4, the adverse pressure gradient on the concave wall becomes favourable, whereas the near wall region on the convex side (beyond y/H = 0.82) becomes adverse. It is noted that the flow in the near wall region experiences greater static pressure changes on the convex side than on the concave side. In order to show the extent to which the airfoil wake is affected by these pressure variations, the wake width at stations 2 to 4 is indicated in Figure 6.6 (e). The inner side and outer side wake regions at station 3 are subjected to pressure gradients of opposite signs, namely, favourable and adverse pressure gradients, respectively, while both sides of the wake region at station 2 and 4 are influenced by favourable pressure gradients. Also, it can be noted in this Figure that the static pressure over a larger area (about 77%) of the cross-section at station 2,

68% at station 3 and 58% at station 4 is positive.

6.2.3. Profiles of mean and turbulence quantities at station 1

In the initial part of the present experimental study, several spanwise (z) measurements were taken at station 1, particularly in the boundary layer region of the duct to determine the optimum number of normal (y) profiles needed to capture the features of the flow field. Therefore, the following discussion starts by examining the flow development in the spanwise direction followed by the normal direction.

6.2.3.1. Results of measurements in spanwise direction

The quantities measured at the mainstream velocity of 10 m/s in the spanwise direction for the upper and lower near wall regions are presented next to each other for easier interpretation.

Mean velocity profiles

The mean velocity components measured in the spanwise direction at station 1 are presented in Figure 6.7 (a-c). As expected, the streamwise velocity components (U) in the near wall regions (concave and convex walls) increase with the normal (y) distance from the wall, which indicates the boundary layer formation on both walls. Furthermore, the spanwise profiles obtained at y = 15 mm and at the centre of the duct (y = 228 mm) agree closely to a large extent, which indicates that the thickness of the boundary layers on the upper and lower walls of station 1 is approximately 15 mm. Small variations of somewhat wavy pattern can be seen in the boundary layer region which becomes smaller as the normal distance from the wall increases. The repeatability and consistency of these results showed that these variations are a permanent feature of the present set-up. The measurements at the centre of the duct show the formation of two boundary layers on both sidewalls of the duct, which are separated by a large inviscid region of about 93 to 94% of the total duct width. All the presented profiles, particularly those obtained at the centre of the duct indicate a symmetry condition about the central plane of the duct (z/H = 0.5).

The profiles of mean normal velocity component (Figure 6.7 b) show generally positive but small values over the whole cross-section. In the centre of the duct, in particular, normal velocities of only about 2% of the streamwise velocity had been measured. A small value of spanwise velocity component was also measured. As seen in the results of streamwise velocity component, the small variations in the boundary layer region can also be noted in the profiles of both normal and spanwise velocity components. However, considering the small values of the normal and spanwise velocity components, especially at the centre of the duct where the airfoil is located, the flow at station 1 can be taken to be uniform and straight.

Turbulence quantities

The spanwise profiles of streamwise and normal intensities are shown in Figure 6.7 (d) and (e), respectively. The wavy pattern of variations in the spanwise profiles of mean velocity noted earlier can also be seen in the profiles of the turbulence intensities. But, the variations within the boundary layer increase with normal distance from the wall. Comparing the results of streamwise intensity with their corresponding results for the streamwise velocity component shows that a decrease in the turbulence intensity coincides with an increase in the streamwise velocity, and vice versa. This is in agreement with the findings of Mokhtarzadeh-Dehghan and Yuan (2002) who reported such variations and attributed them to the formation of streamwise vortices, which were enhanced in the flow direction on the concave wall. The results in the boundary layer region (up to 10 mm) of both upper and lower walls show higher streamwise intensity values than the normal intensity values at each corresponding location. Also, both parameters in these regions decrease as the distance from the wall increases, which indicate similar characteristics to that of a flat plate turbulent boundary layer. The small value (close to zero) of both parameters and their smooth profiles in the centre of the duct confirm the presence of a large inviscid region at station 1. Also, the profiles indicate a symmetry condition about the central plane of the duct (z/H = 0.5). The profiles of the spanwise intensity in Figure 6.7 (f) show similar characteristics to the streamwise and normal intensities. The values of spanwise intensity in the near wall region (up to 10 mm) of both upper and lower walls fall in between the (higher) streamwise intensity and the (lower) normal intensity at each corresponding location. This is expected and

consistent with the results for a flat plate turbulent boundary layer.

Due to change of sign at about the centre of the duct, the turbulence shear stresses $-\overline{u'v'}$ in Figure 6.7 (g) takes a positive value on the lower wall and a negative value on the upper wall. Also, the magnitudes of the turbulence shear stresses decrease to zero as the distance from the wall increases.

6.2.3.2. Results of measurements in normal direction

The spanwise results presented above indicated that the flow was symmetrical about the centre of the duct (z/H = 0.5), and therefore, the normal profile measurements were confined to one-half of the cross-section. The measurements in the normal direction (y) were taken at four spanwise locations, namely, z/H = 0.5, 0.6, 0.7 and 0.8. The following section presents the results of mean and turbulence quantities measured in the normal direction at station 1.

Mean velocity profiles

The velocity profiles measured on the upper (concave) and lower (convex) walls at spanwise locations of z/H = 0.5, 0.6 and 0.7 are presented in Figure 6.8 (a-c). The results indicate a general agreement with the log-law profile of flat plate turbulent boundary layers with constants of A = 2.44, B = 5.0. On the lower wall, the log-law applies between y^+ = 40 to 300. But, on the upper wall, the log-law applies to relatively larger region of y^+ = 40 to 400. The upward deviation of the outer layer on the lower wall, compared with the downward deviation on the upper wall shows the different effects of the bend on the boundary layers at this upstream location. In the present study, the friction coefficient was obtained using the Clauser-chart method from which the friction velocity was calculated. The differences seen between the values of u^+ in the inviscid region are therefore attributed to the differences in the mainstream velocity and friction velocity.

The normal profiles of mean streamwise velocity component and its intensity are presented in Figure 6.9 (a-c). The results show the formation of a turbulent boundary layer with a steep increase near the walls and fairly uniform velocity in the central

part of the duct. The root-mean square value of the streamwise velocity fluctuations at the central part of the duct are less that 0.3% of the mainstream velocity. The profiles of both parameters show that a large inviscid region spanning approximately 90% of the duct height separates the two boundary layers on the upper and lower walls. In the present study, the airfoil is located at y/H = 0.5, which is in the centre of this inviscid region, where the effects of the walls are negligible and the turbulence intensities remain at low values. The overall size of this inviscid region, particularly in the x-y plane, is in close agreement with the results of previous investigations by Kotb (1988) and Ondore (1999). If the boundary layer thickness is defined as the normal distance (y) at which the boundary layer flow velocity achieved 99% of the mainstream velocity, then the measurements obtained at all four spanwise locations show that the boundary layer thicknesses on the upper and lower walls are approximately 14 mm and 17 mm, respectively. As seen earlier in the spanwise results, the streamwise intensity is greater than its corresponding normal and spanwise intensities in both upper and lower walls boundary layer region.

The profiles of mean normal velocity component and its intensity at three mainstream velocities are presented in Figure 6.10 (a-c). Both parameters show variations in the inviscid flow region, where the flow angle is in the range of $\pm$ 1°. The mean spanwise velocity component and its intensity are presented in Figure 6.11 (a-c). As was noted earlier, in the upper and lower wall boundary layers, the spanwise intensity attains higher values than those of normal intensity. Furthermore, the spanwise intensity becomes almost equal to the streamwise and normal intensities at distances far from the wall indicating the isotropic nature of the turbulence.

The normal profiles of two turbulence shear stresses, namely, $-\overline{u'v'}$ and $-\overline{u'w'}$ are presented in Figure 6.12 (a-c). These turbulence stresses remain close to zero over much of the duct height in the inviscid region and take different signs in the boundary layer regions. Also, both turbulence stresses take a maximum value near the wall as expected for turbulent boundary layers on a flat plate.

6.2.3.3. Effects of airfoil angle of attack at station 1

The effects of airfoil presence on the mean and turbulence parameters at station 1 for various angles of attack in the range of $\pm 5^{o}$ are presented in Figure 6.13 (a-e). As was in the case of the static pressure measurements on the surfaces of the airfoil, the anticlockwise rotation of the airfoil was taken as positive. The results show that the mean velocity components, particularly the normal velocity component are significantly affected by the angle of attack of the airfoil. When the angle of attack changes in the clockwise direction, say from $+5^{o}$ to -5^{o}, the mean streamwise velocity component gradually increases in the lower half region of the duct at station 1 while decreases in the upper half region due to the deflection of the flow by the airfoil. Furthermore, the mean normal velocity component in the inviscid region becomes smaller and smaller as the angle of attack gradually changes in the clockwise direction, which indicates that the flow at station 1 is straightened by the airfoil. The presented results for the streamwise and normal intensities and the turbulence shear stress ($-\overline{u'v'}$) show no significant effects due to either the presence or the angle of attack of the airfoil.

6.2.4. Experimental error analysis

The results of three error analyses, namely, probe pitch and yaw angles misalignment error analysis, hot-wire sampling frequency error analysis and probe calibration error analysis conducted experimentally are described in the following section.

6.2.4.1. Probe pitch and yaw angles misalignment error analysis

The mean and turbulence quantities measured at different pitch and yaw angles of both *UV* (DANTEC 55p63) and *UW* (DANTEC 55p64) cross-wire probes are presented in Figure 6.14 (a-h). In the yaw angle misalignment investigation, the clockwise rotation of the sensor about the probe stem was taken as positive. Similarly, for the pitch angle misalignment investigation the anticlockwise rotation about the z-axis was taken as positive. It is apparent in Figure 6.14 that neither pitch nor yaw misalignment angle affects the streamwise velocity component significantly. But, the results of normal and spanwise velocity components indicate that they are affected by even a small misalignment angle. Furthermore, the normal velocity component profiles

indicate that this parameter is more sensitive to the pitch angle than the yaw angle. The profiles of Reynolds stresses show very small variations for both pitch and yaw misaligned angles, which can be assumed as negligible.

6.2.4.2. Hot-wire sampling frequency error analysis

Figure 6.15 (a-e) shows the effect of the sampling frequency on mean and turbulence quantities. For the three different sampling frequencies, namely, 4, 6 and 8 kHz, the sampling period was kept at 15 seconds by obtaining 60k, 90k and 120k samples, respectively. It is apparent in this Figure that the sampling frequency does not affect the mean and turbulence quantities significantly.

6.2.4.3. Probe calibration error analysis

The effects of cross-wire probe calibration on the mean and turbulence quantities are presented in Figure 6.16 (a-d). Two calibration data of a DANTEC 55P63 probe were chosen to reduce a single set of raw data to evaluate the differences between them. The results show that the mean velocity components, particularly the mean normal velocity component, are significantly affected by the probe calibration. Furthermore, the mean streamwise and normal velocity components obtained using one calibration (1^{st} calibration) always show higher values of about 2% and 11%, respectively, than the other calibration (2^{nd} calibration). Part of the variation seen in the normal velocity profiles could be related to the probe alignment during the two calibration processes. However, the turbulence intensities and turbulence shear stress $-\overline{u'v'}$ (not presented here) showed virtually no differences between these two calibrations.

6.2.5. Profiles of mean and turbulence quantities at stations 2 to 5

In the following sections the spanwise and normal profiles obtained at stations 2 to 5 are presented. For three mainstream velocities, the spanwise variations of each parameter at the wake centreline are presented on the same graph. But, the normal profiles of each parameter measured at two different spanwise locations, namely, z/H = 0.5 and z/H = 0.6 are presented together on the same graph with those obtained in the absence of the airfoil

at z/H = 0.5.

6.2.5.1. Results of measurements in the spanwise direction

The spanwise measurements of the mean and turbulence quantities obtained at stations 2 to 5 are presented in Figure 6.17 (a-h). The results of the mean streamwise velocity component show a large region in the central part of each station over which the velocity remains uniform. But, due to the formation of boundary layers on the sidewalls of the flow domain, the values of streamwise velocity component decrease as the spanwise distance reaches the near wall region. The results of the normal velocity component show an increase in the near wall region while a decrease in the central parts of stations 3 and 4, which can be attributed to the secondary flow effects. As seen earlier in the spanwise variations at station 1, a small value of spanwise velocity component was also measured at stations 2 to 5, especially in the central part of the duct. The results, therefore, indicate that the flow throughout the central part of the regions of interest can be considered as uniform in the spanwise direction, experiencing a small spanwise component.

The presented turbulence intensities also show a large uniform region in the central part of each station, where the quantities remain constant. A distinguishing feature of these intensity profiles at each station is that the flow region affected by the sidewalls increases in the streamwise direction due to the growth of boundary layers, which reduces the width of the uniform flow region significantly. Also, due to the presence of a minimum in the velocity profile at the centre of the wake, both turbulence shear stresses show insignificant values at each station. All the presented profiles indicate a very good degree of symmetry with respect to the plane at z/H = 0.5 of the duct, except the turbulence shear stresses for which a change of sign occurs in the near wall region.

6.2.5.2. Results of measurements in the normal direction

The variations of mean streamwise velocity component in the normal direction at stations 2 to 5 are presented in Figure 6.18 (a-f). The results indicate that the wake of the airfoil in the curved duct is asymmetric with respect to the wake centre due to the combined effects of the curvature and pressure gradient. The comparison of the streamwise velocity profiles obtained at stations 2 to 4 in Figure 6.18 (e) shows that the inner side wake width

is always larger than its corresponding outer side wake width. Also, as the distance from the airfoil increases the spread of both inner and outer side wake widths increases while the differences between the velocity in the wake region and the mainstream velocity gradually decrease. The streamwise velocity component in the wake region in Figure 6.18 (f) indicates a shift of about 11 mm and 24 mm from the duct centreline towards the convex side at stations 2 and 3, respectively. However, at stations 4 and 5, the wake region is shifted towards the concave wall by about 20 mm and 56 mm, respectively. The mean streamwise velocity profiles obtained in the absence of the airfoil show a linear profile across the wake region.

At each station, majority of the profiles obtained at the two spanwise locations collapse, which indicates that the variations in the spanwise direction are small as was observed earlier in Figure 6.17 (a). The profiles obtained across the whole cross-section at stations 2 and 3 show the flow acceleration on the convex side and its deceleration on the concave side. This feature confirms the presence of favourable and adverse pressure gradients on the convex and concave wall regions at these stations, respectively, as shown earlier in Figure 6.6. It is noted that the magnitude of streamwise velocity component at the edge of the boundary layer of station 2 has increased by 21% on the convex side and reduced by 12% on the concave side in comparison with the station 1 values. Compared with station 2, the streamwise velocity component on the convex side (edge of the boundary layer) has increased further by 21% at station 3, while on the concave side a further decrease of 11% has occurred. Despite these significant variations, the general pattern of the streamwise velocity component at station 3 is similar to the corresponding ones at station 2. However, the profiles change significantly at stations 4 and 5. Compared with station 3, the streamwise velocity component on the convex side has now decreased at station 4, while increased on the concave side due to the changes in the pressure gradient, which is consistent with the radial static pressure distributions results in Figure 6.6. These changes are further enhanced at station 5. The profiles also show that the wake development in the large central core region takes place without direct interference of the convex and concave wall boundary layers.

The variation of wake parameters, such as the wake half-width and maximum velocity defect for three mainstream velocities are presented in Figure 6.19 (a-d). It is noted that

the maximum velocity defect occurs near the wake centreline at each station of the bend. The half-width of the wake was taken as the normal distance between the maximum velocity defect and a point at which the wake defect equals half of the maximum velocity defect value. The results show that the half-width of both sides of the wake region decreases with increasing mainstream velocity. Furthermore, it increases as the streamwise distance from the airfoil trailing edge increases. As noted in the streamwise velocity profiles, the calculated half-width of the wake region at stations 2 to 4 confirms that its value on the inner side is always greater than that on the outer side. The maximum velocity defect increases as the mainstream velocity increases. However, its values decrease as the distance from the airfoil increases, which indicates that the differences between the velocities in the wake region and the mainstream become smaller.

The streamwise intensities at stations 2 to 5 are presented in Figure 6.20 (a-f). A distinguishing feature of these profiles is the existence of a double peak, particularly at stations 2 to 4, where the peak on the inner side is larger than its corresponding one on the outer side. Furthermore, as the streamwise distance increases between these stations, both peaks shift further away from the wake centreline and flatten, which is more pronounced on the inner side of the wake region. These features could be attributed to the effects of curvature and pressure gradient which, as pointed out by Tulapurkara et al. (1994), enhance the streamwise intensities on the inner side and suppress it on the outer side of a curved wake region. The comparison of the wake region in Figure 6.20 (e) indicates significant reduction in the streamwise intensity values between stations 2 to 4. Furthermore, at the wake centreline between stations 2 and 3, the streamwise intensity has reduced by about 47%, and further 12% reduction has occurred between stations 3 and 4. It is noted that the streamwise velocity fluctuations increase in the wake region with increasing mainstream velocity, but the intensity profiles seen here do not represent this feature due to the normalisation with respect to mainstream velocities. As expected, in the absence of the airfoil, the streamwise intensity follows a linear profile across the wake region in the curved section.

The profiles obtained across the whole cross-section in Figure 6.20 (f) indicate that the streamwise turbulence intensity of the boundary layers on the concave and convex walls

are unaffected by the presence of the airfoil. Also, at station 2, the profiles indicate small values (close to zero) in the central core region as in station 1, whereas on the concave wall, the region confined by the boundary layer is larger (approx. y/H = 0.1) and within which the streamwise intensity values are generally higher than its corresponding region at station 1. Compared with station 2, the streamwise intensity enhanced further in the region affected by the concave wall (approx. y/H = 0.28) at station 3, whereas insignificant variations occurred in the central core region and convex wall region. Furthermore, the increase in the streamwise intensity and the appearance of a wide bulge in the profiles of the concave wall could be attributed to the effects of curvature and pressure gradient. However, the profiles change significantly between stations 4 and 5, where the magnitude of the bulge in the profiles is decreasing with increasing streamwise distance. But, at these stations, the regions affected by both the boundary layers on the concave and convex walls are significantly larger compared with stations 2 and 3. On the convex wall at station 4, the flow is subjected to a strong adverse pressure gradient (see Figure 6.6) and is close to separation, thus increase in the streamwise intensity at this station could be attributed to this effect.

The distributions of normal intensity at stations 2 to 5 are presented in Figure 6.21 (a-f). In contrast to the results presented for the streamwise intensity, the profiles show a single peak, which is located on the outer side of the wake at station 2 and then shifted to the inner side as the streamwise distance increases in the downstream direction. These changes are more pronounced at higher mainstream velocities at stations 2 to 4. As noted in the streamwise intensity profiles, the normal intensity profiles in the wake region also show an asymmetric structure with respect to the wake centreline, and a larger wake width on the inner side compared with the outer side of the wake region. But, the comparison of the normal intensity profiles obtained at stations 2 to 4 (Figure 6.21 e) indicates that the value at the wake centreline at station 2 has reduced approximately by half at station 3, whereas an insignificant reduction occurred between stations 3 and 4. The normal intensity profiles obtained at the two spanwise locations (z/H = 0.5 and 0.6) agree closely, particularly in the wake region, where the profiles collapse to a large extent. However, the profiles obtained at z/H = 0.5, particularly in the flow region confined by the edge of inner side wake region and the edge of the boundary layer on the convex wall show slightly larger values compared with their corresponding values

obtained at z/H = 0.6. Furthermore, due to similar differences occurred at station 1 (Figure 6.10), it is concluded that the spanwise variations seen in this Figure are enhanced in the flow direction. At stations 2 and 3, the normal intensity profiles obtained across the whole cross-section show similar patterns to the streamwise intensity profiles, including the appearance of a wide bulge structure in the region confined by the concave wall boundary layer. But, unlike the streamwise intensity profiles on the concave wall at station 4, the bulge in the normal intensity profiles seems enlarging, which indicate that the normal intensity responds slower to the removal of curvature than streamwise intensity. However, at station 5, the bulge in the profiles is flatter and the normal turbulence level is lower than the level achieved at station 4. But, on the convex wall at this station, the normal intensity is much larger than the values achieved on the concave wall.

The distributions of spanwise intensity at stations 2 to 5 are presented in Figure 6.22 (a-f). At station 2, the profiles obtained at higher mainstream velocities show two peaks of approximately the same magnitude, which are located on each side of the wake region. But, as the streamwise distance increases in the downstream direction the double peak disappears, which led to a single peak on the inner side of the wake region at stations 3 and 4. As seen in the normal intensity profiles, the discrepancies occurred between the spanwise intensity profiles obtained at different spanwise locations in this Figure, particularly outside the wake region, are mainly attributed to their upstream differences. However, the profiles collapse in the wake region at station 2, which indicates that the wake region near the body is mainly influenced by the boundary layers forming on the body. The comparison of spanwise intensity profiles at stations 2 and 3 indicates that the value at the wake centreline has reduced by about 47%, whereas further 13% reduction occurred between stations 3 and 4. The profiles obtained across the whole cross-section at stations 2 and 3 in Figure 6.22 (f) show similar pattern as the normal and streamwise intensity profiles. But, at stations 4 and 5, the bulge seen on the concave wall profile at station 3 is flattened. Also, the profiles obtained with and without the airfoil shows insignificant effects on the concave and convex wall boundary layers by the presence of the airfoil.

Figure 6.23 (a-f) and Figure 6.24 (a-f) show the variations of turbulence shear stresses

$-\overline{u'v'}$ and $-\overline{u'w'}$, respectively, in the normal direction at stations 2 to 5. The profiles obtained at stations 2 to 4 show that the turbulence shear stresses become zero and change sign at the wake centre, where the velocity takes a minimum. At station 2, both turbulence shear stresses show positive peak on the inner side and negative peak on the outer side of the wake region. Furthermore, it is noted that the magnitude of the positive peak is larger than its corresponding negative peak at station 2 and the difference between their magnitudes increases further as the streamwise distance increases and thus causes an asymmetric structure. As noted earlier in the mean and intensity profiles, the profiles of both turbulence shear stresses at station 2 to 4 also indicate that the inner side of the wake region is larger than their corresponding outer side wake region. As reported by many investigators, e.g. Tulapurkara et al. (1995), these differences can be attributed to the combined effects of curvature and pressure gradient, which enhances turbulence shear stresses on the inner side of the wake region while suppresses it on the outer side. Also, these extra rates of strain effects seem to be affecting the turbulence shear stresses more than the normal stresses. The profiles of both turbulence shear stresses at different spanwise locations (z/H = 0.5 and 0.6) at each measuring station collapse in the wake region.

The profiles obtained across the whole cross-section at stations 2 and 3 also show the bulge structure on the concave wall, whereas the values remain close to zero over the central core region and take different sign on the convex wall. But, both quantities change significantly at station 4, particularly near the concave and convex wall regions, where the bulge structure on the concave wall and the values on the convex wall are greatly reduced. At station 5, on the concave wall, the overall behaviour of the profiles is the same as in station 4, but the bulge structure is further reduced. On the convex wall at this station, a distinguishing feature of the turbulence shear stress $-\overline{u'v'}$ profiles is the sharp drop to a trough followed by an increase to a peak as the distance approaches the wall. Also, in this region, the profiles of turbulence shear stress $-\overline{u'w'}$ indicate positive values.

The variations of turbulence kinetic energy (k) at stations 2 to 5 are presented in Figure 6.25 (a-f). The turbulence kinetic energy, which is obtained from the three intensities, show double peak about the wake centreline at station 2 and a single peak on the inner

side of the wake region at station 3 to 5.

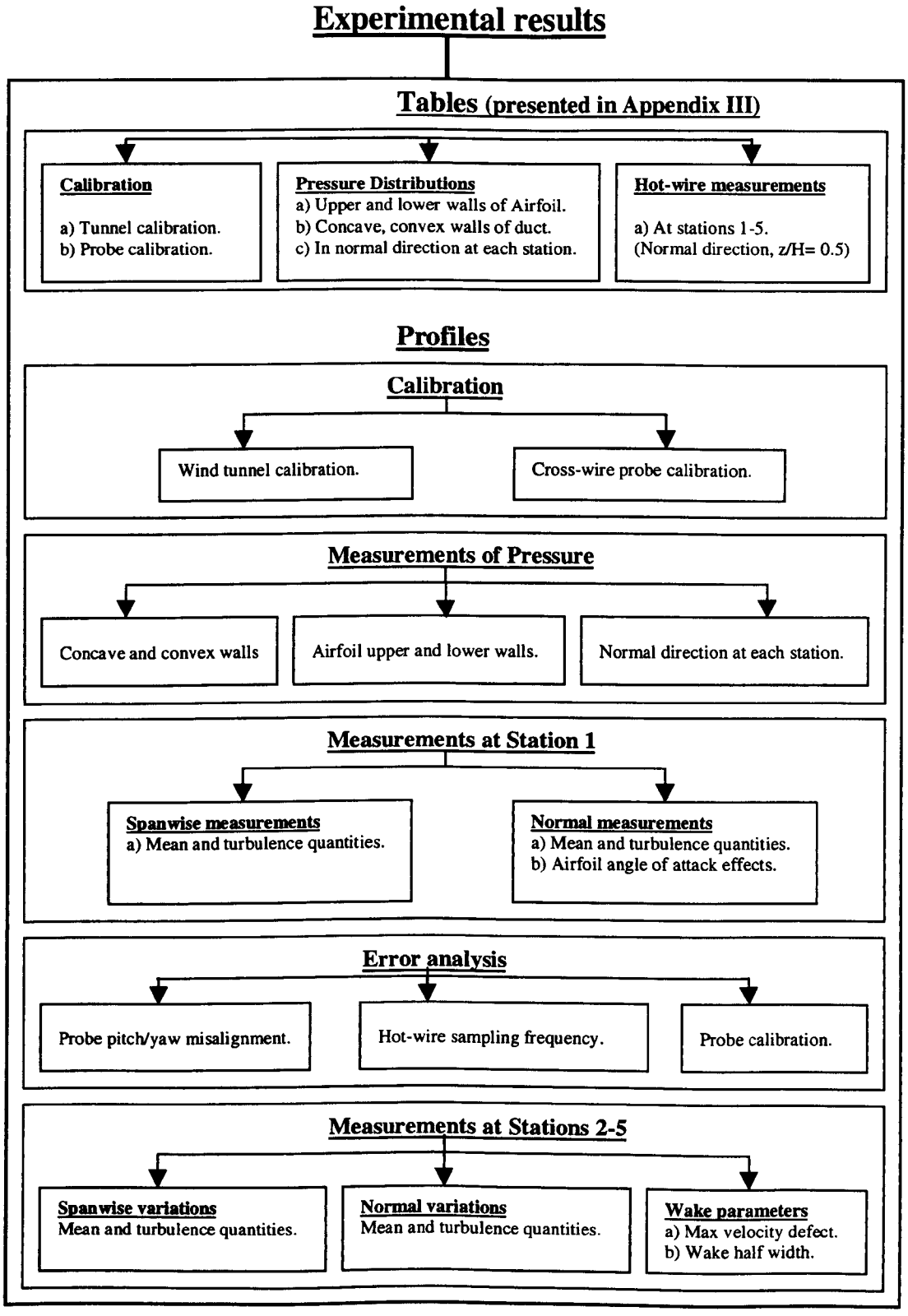

Figure 6.1: The structure of presented experimental results.

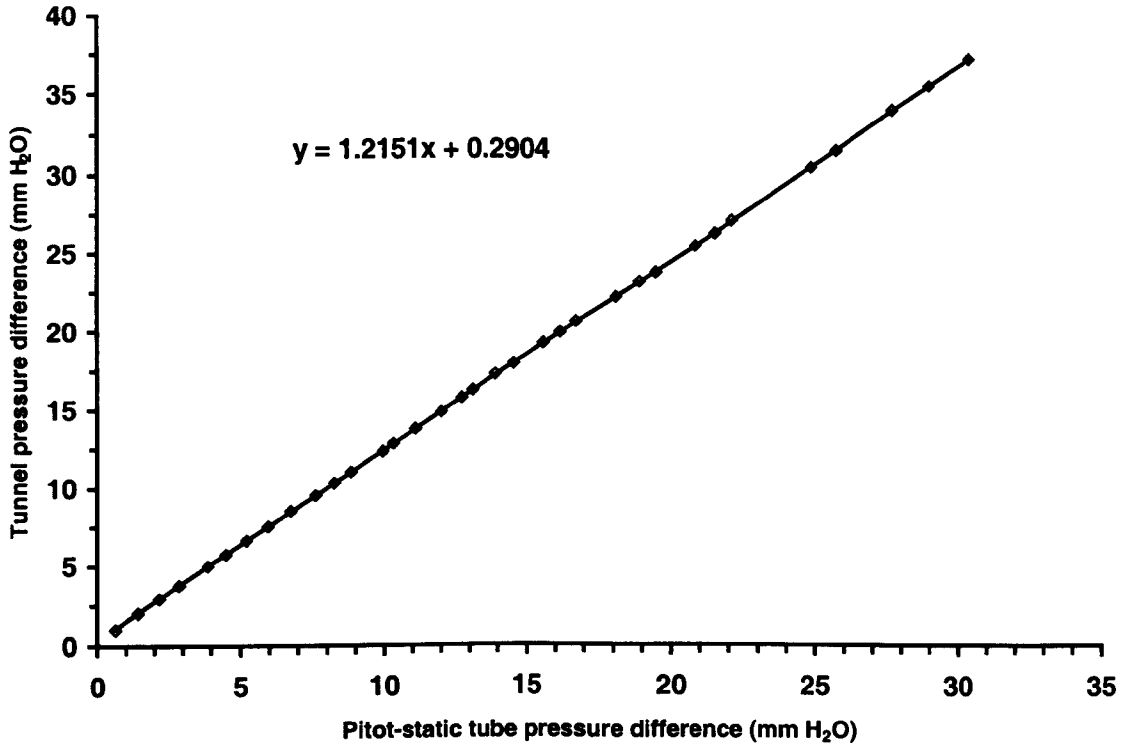

(a)

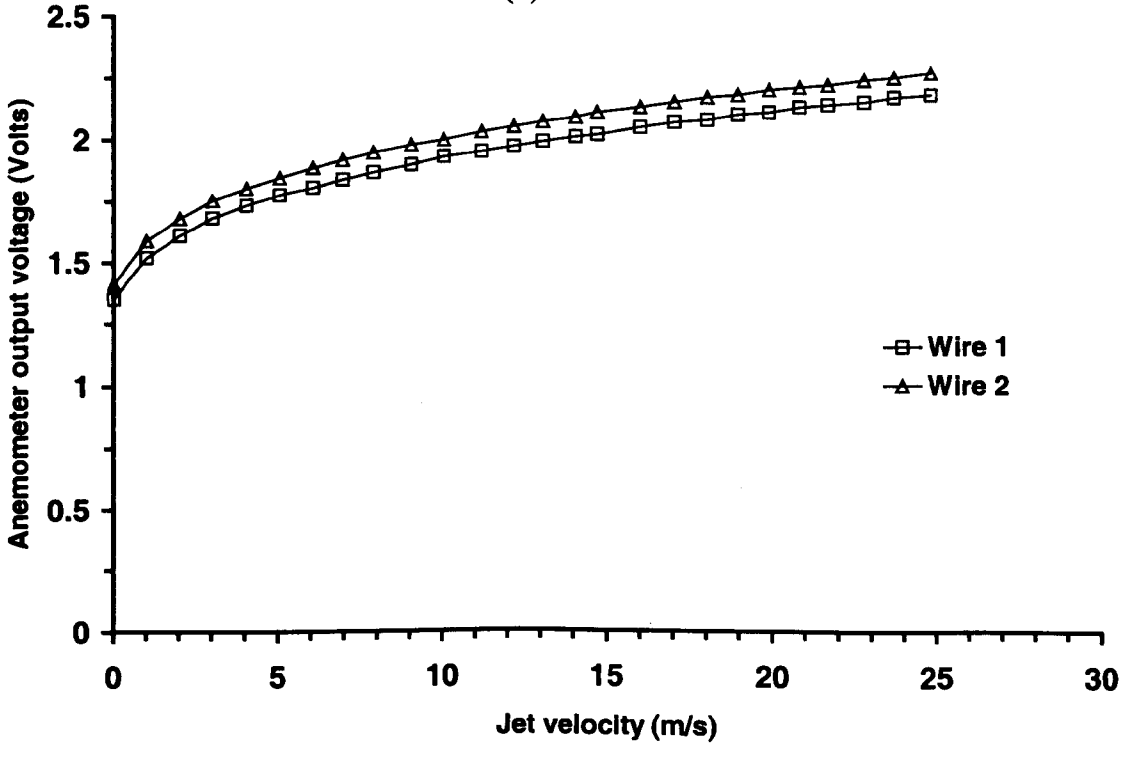

(b)

Figure 6.2: Tunnel and cross-wire probe calibrations: (a) Tunnel, (b) Cross-wire.

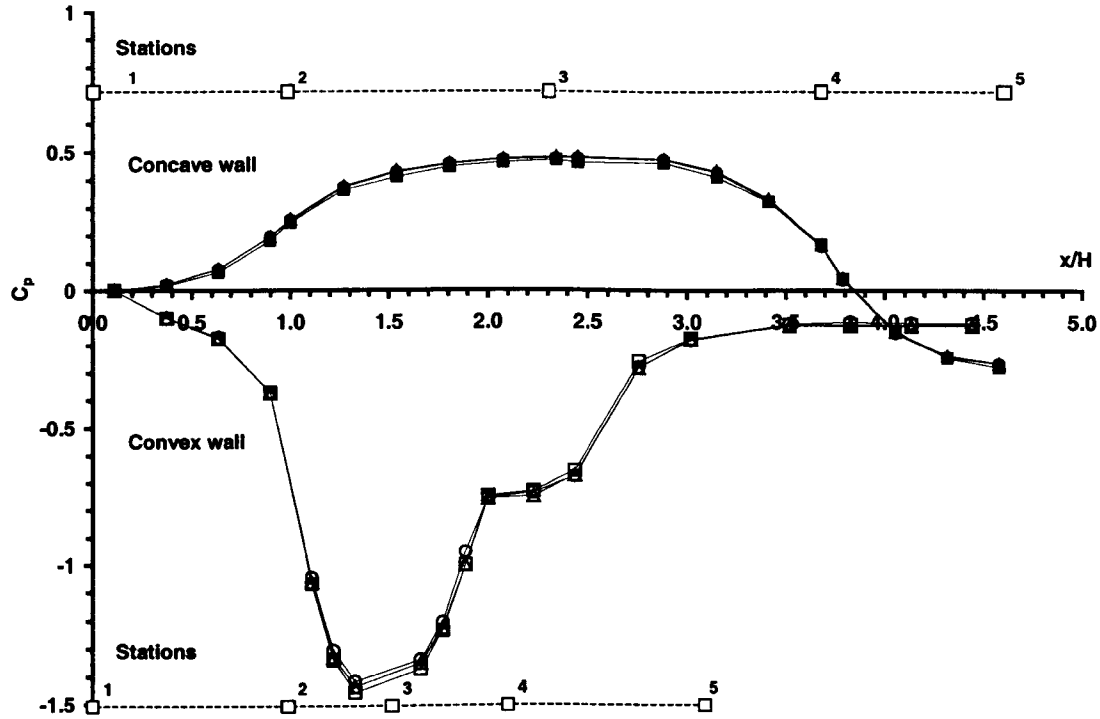

(a)

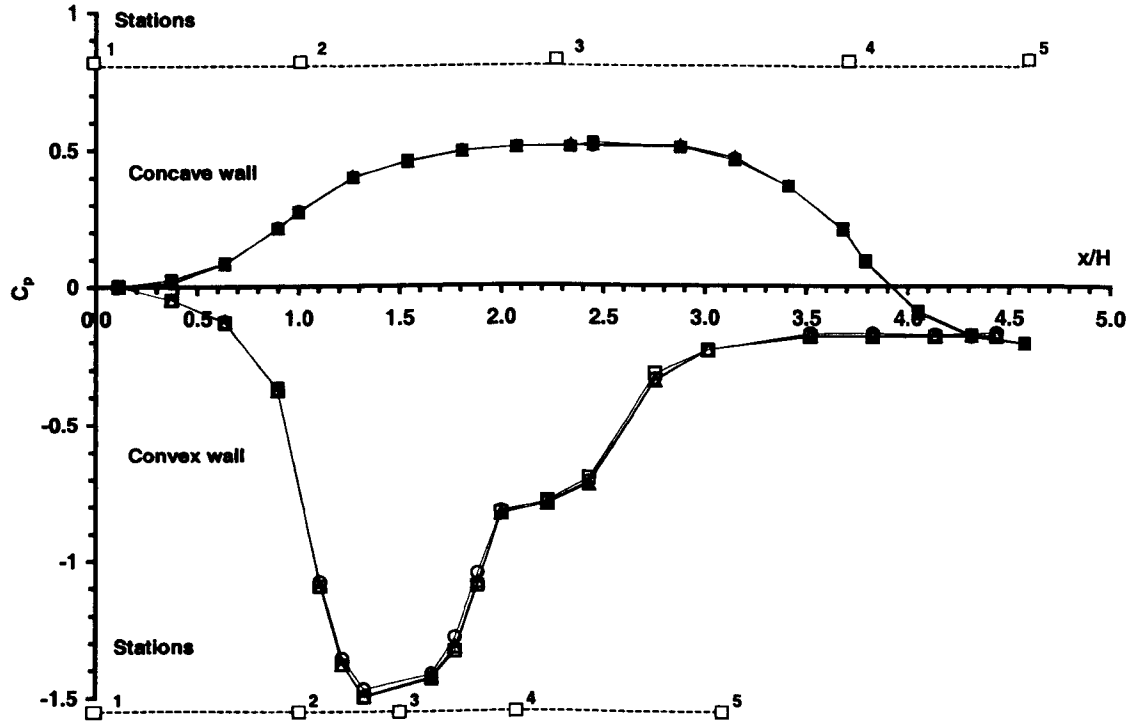

(b)

Figure 6.3: Pressure coefficient along the concave and convex walls of the duct: (a) with airfoil, (b) without airfoil.

Convex wall: □, nominal U_o = 10 m/s; Δ, nominal U_o = 15 m/s; O, nominal U_o = 20 m/s.

Concave wall: ■, nominal U_o = 10 m/s; ▲, nominal U_o = 15 m/s; ●, nominal U_o = 20 m/s.

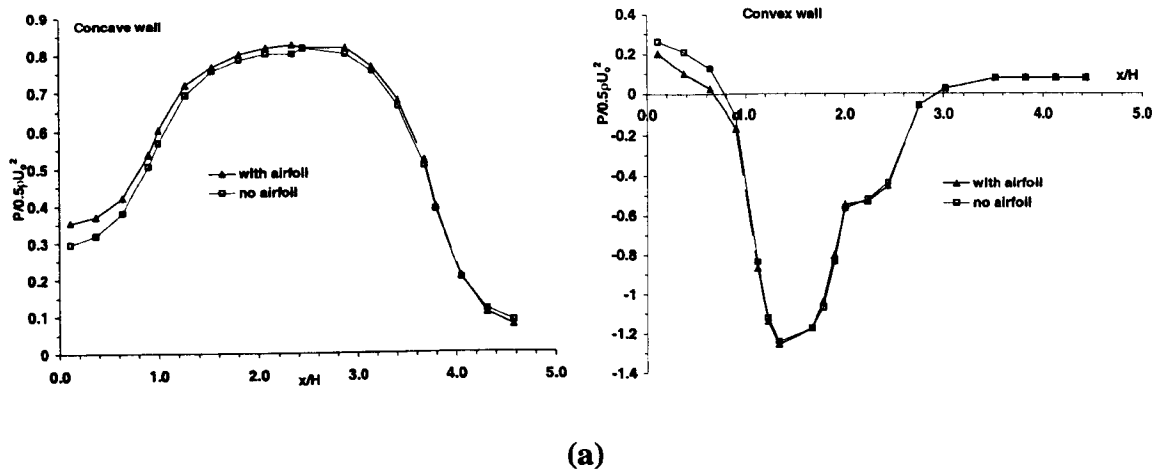

(a)

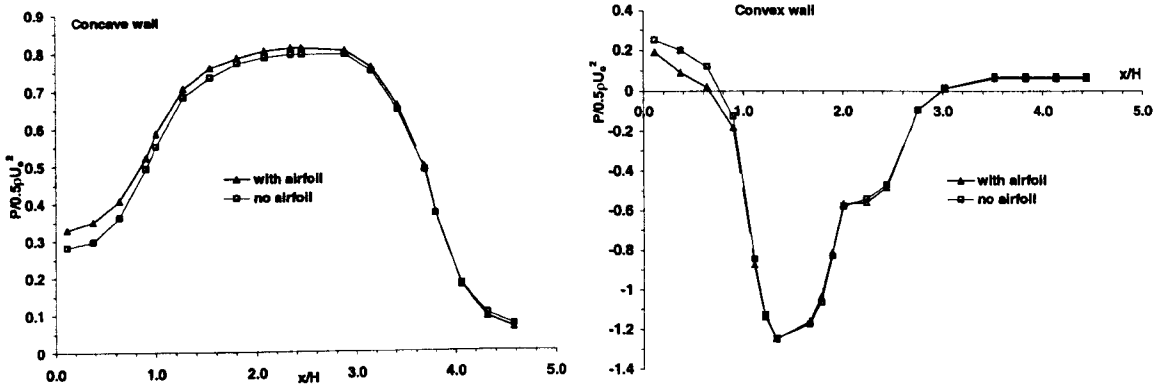

(b)

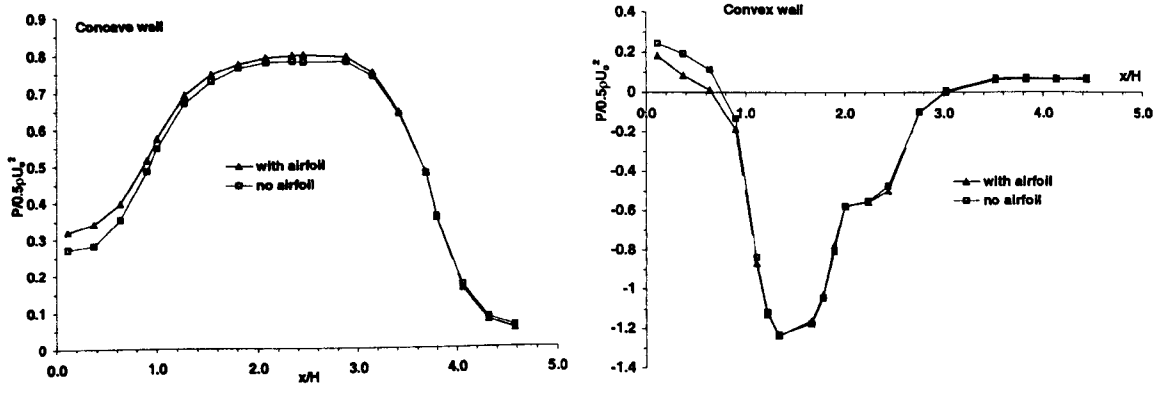

(c)

Figure 6.4: Comparison of concave and convex walls pressure distribution obtained with and without of the airfoil: normalized with the mainstream dynamic pressure at station 1, (a) nominal U_o = 10 m/s; (b) nominal U_o = 15 m/s; (c) nominal U_o = 20 m/s.

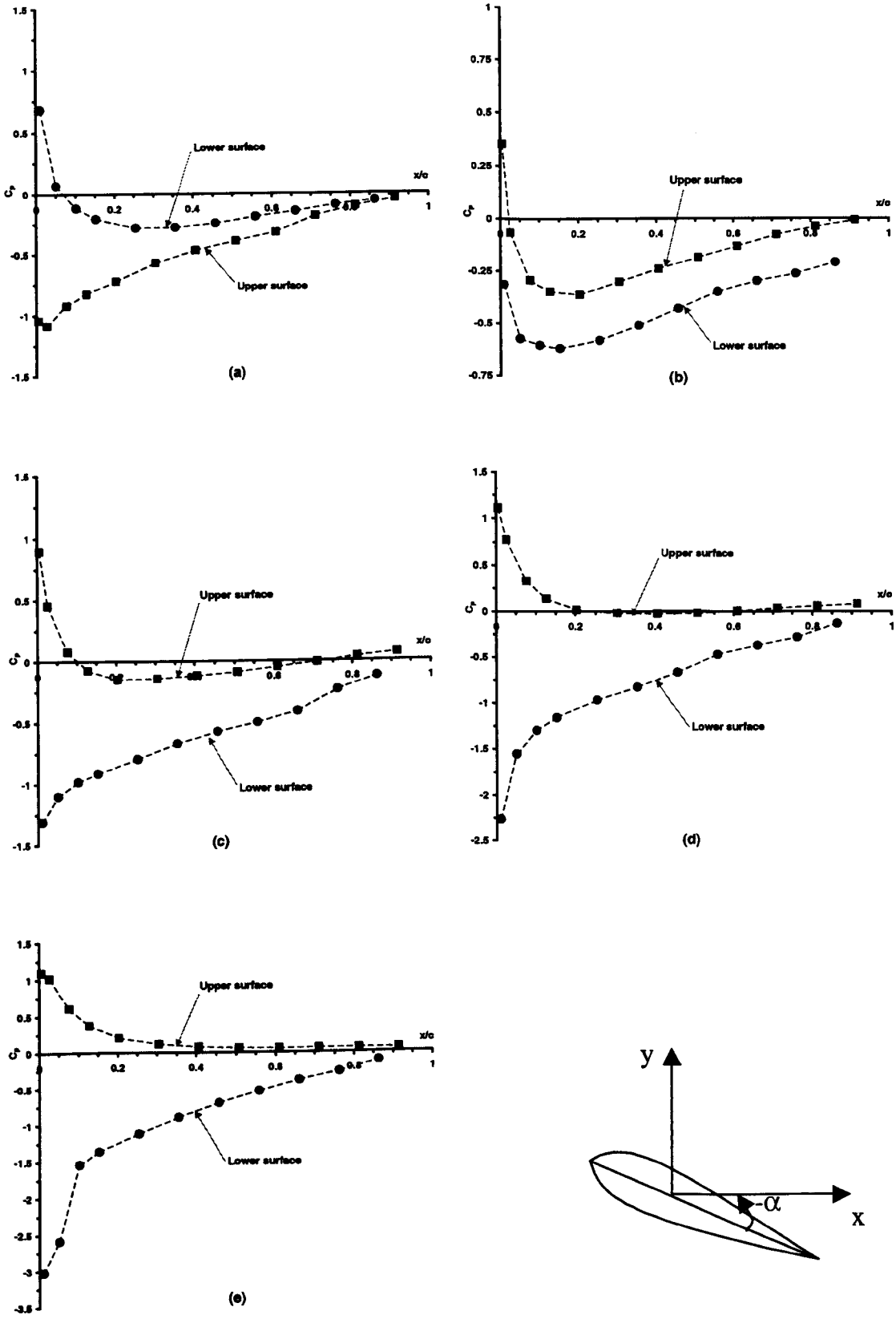

Figure 6.5: Pressure coefficient on the airfoil (z/H = 0.5) at various angles of attack: (a) $\alpha = +5^{o}$, (b) $\alpha = +2^{o}$, (c) $\alpha = 0^{o}$, (d) $\alpha = -2^{o}$, (e) $\alpha = -5^{o}$.

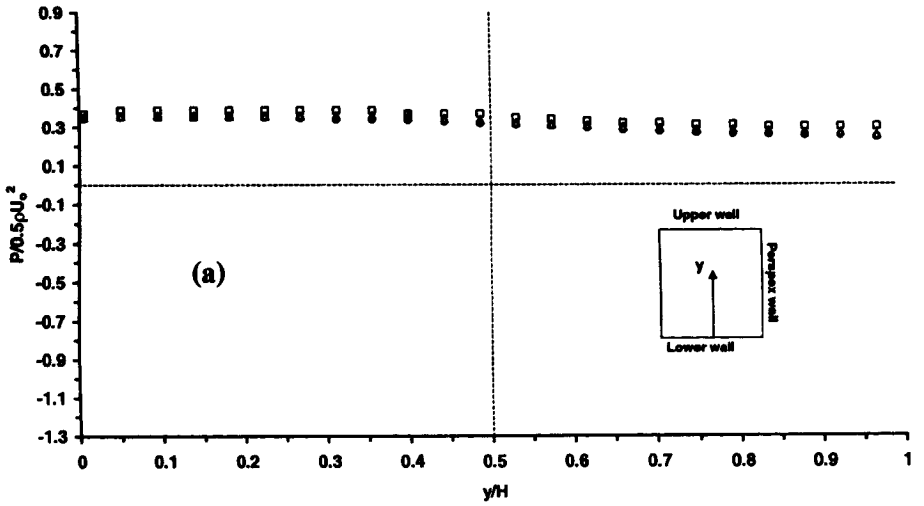
(a)
P/0.5ρU$_o^2$
y/H
Upper wall
Perspex wall
Lower wall
y

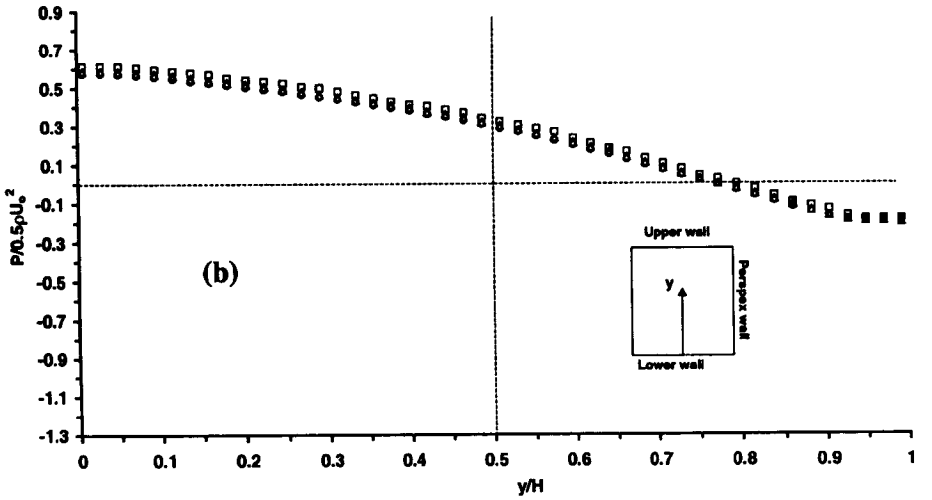
(b)
P/0.5ρU$_o^2$
y/H
Upper wall
Perspex wall
Lower wall
y

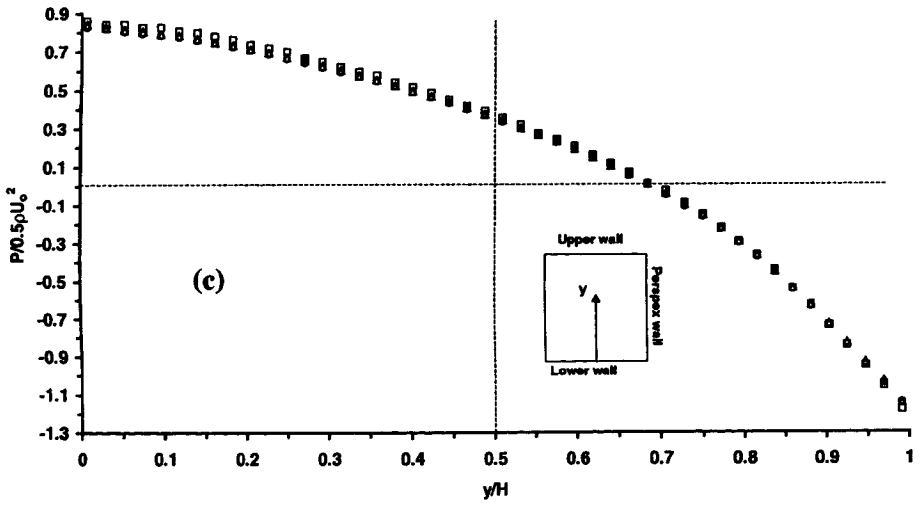
(c)
P/0.5ρU$_o^2$
y/H
Upper wall
Perspex wall
Lower wall
y

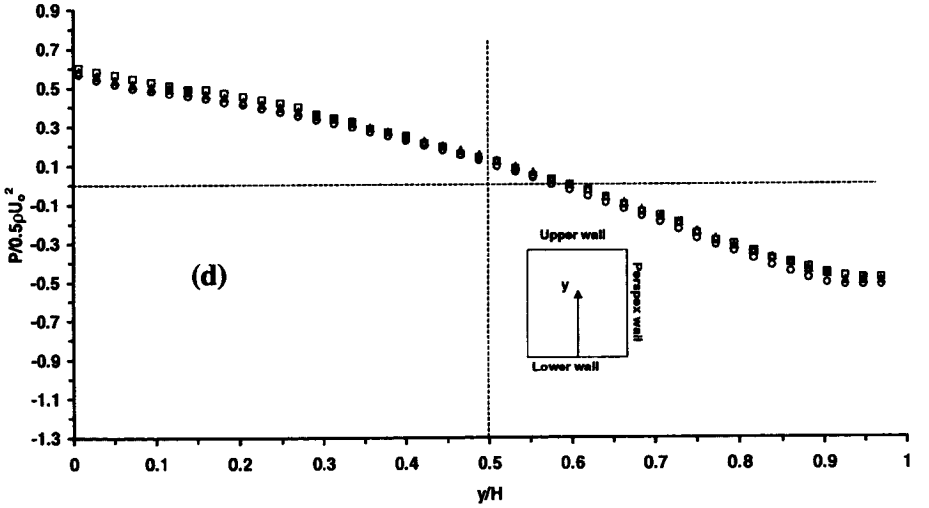
(d)
P/0.5ρU$_o^2$
y/H
Upper wall
Perspex wall
Lower wall
y

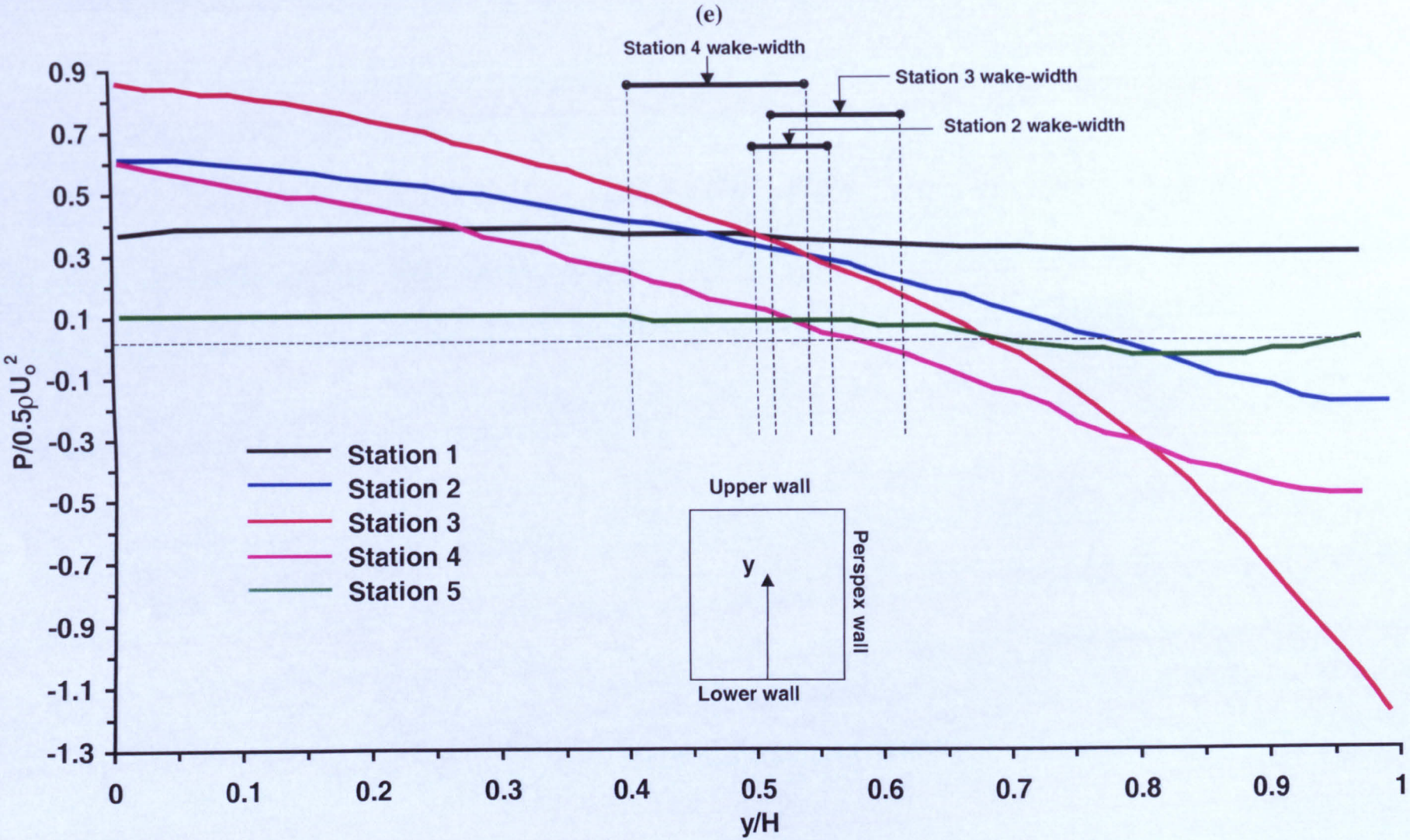

Figure 6.6: Static pressure relative to atmospheric pressure in the normal direction: (a) station 1; (b) station 2; (c) station 3; (d) station 4; (e) comparison of the profiles obtained at stations 1 to 5 at nominal velocity of 10 m/s.
□, nominal U_o = 10 m/s; Δ, nominal U_o = 15 m/s; ○, nominal U_o = 20 m/s. (Original in colour).

(a)

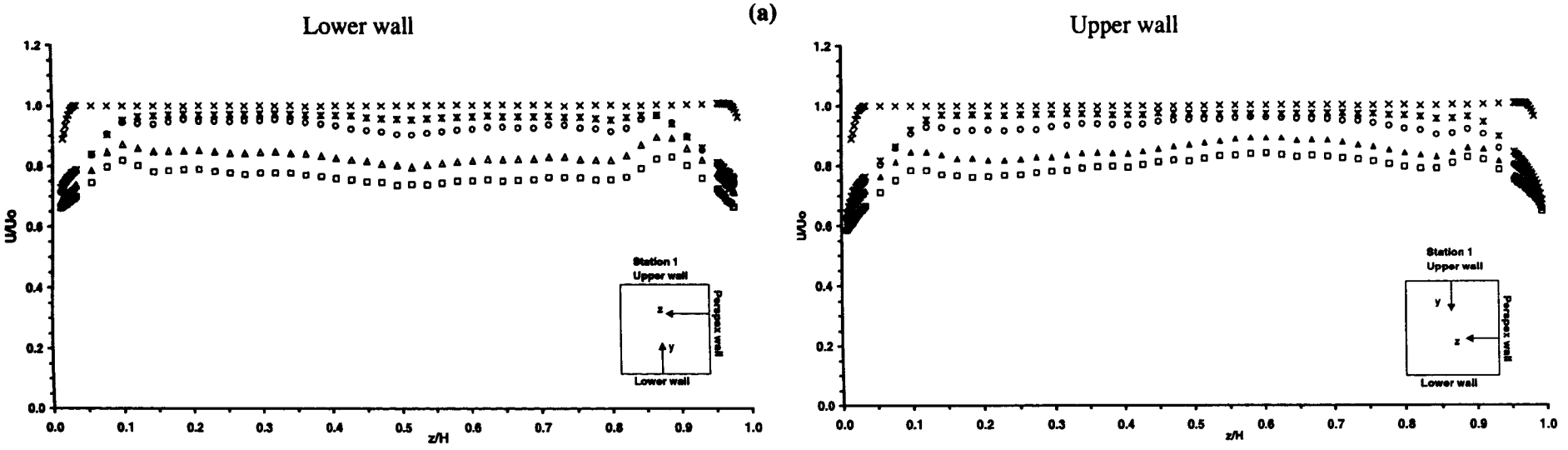
Lower wall
U/Uo
z/H
Station 1
Upper wall
Perspex wall
Lower wall
Upper wall
U/Uo
z/H
Station 1
Upper wall
Perspex wall
Lower wall

(b)

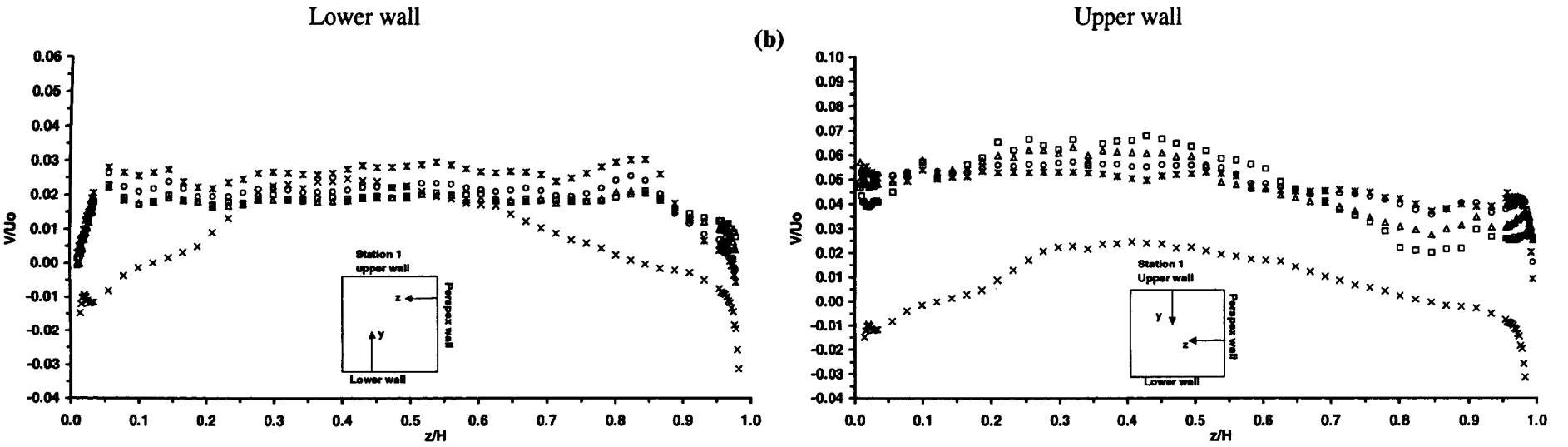
Lower wall
V/Uo
z/H
Station 1
upper wall
Perspex wall
Lower wall
Upper wall
V/Uo
z/H
Station 1
Upper wall
Perspex wall
Lower wall

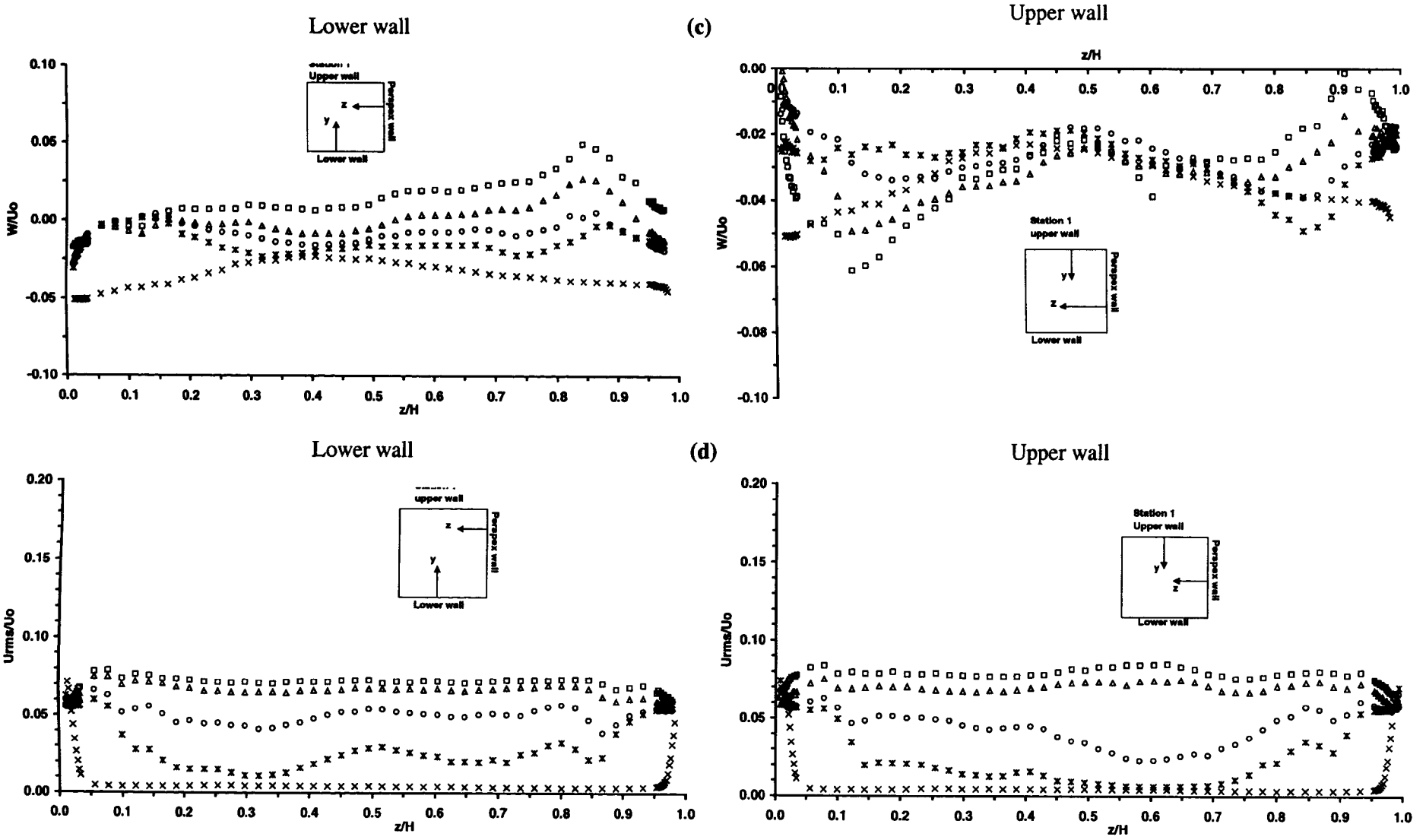
Lower wall
(c)
Upper wall
W/Uo
z/H
Station 1
Upper wall
Perspex wall
Lower wall
Lower wall
(d)
Upper wall
Urms/Uo
z/H
upper wall
Perspex wall
Lower wall
Station 1
Upper wall
Perspex wall
Lower wall

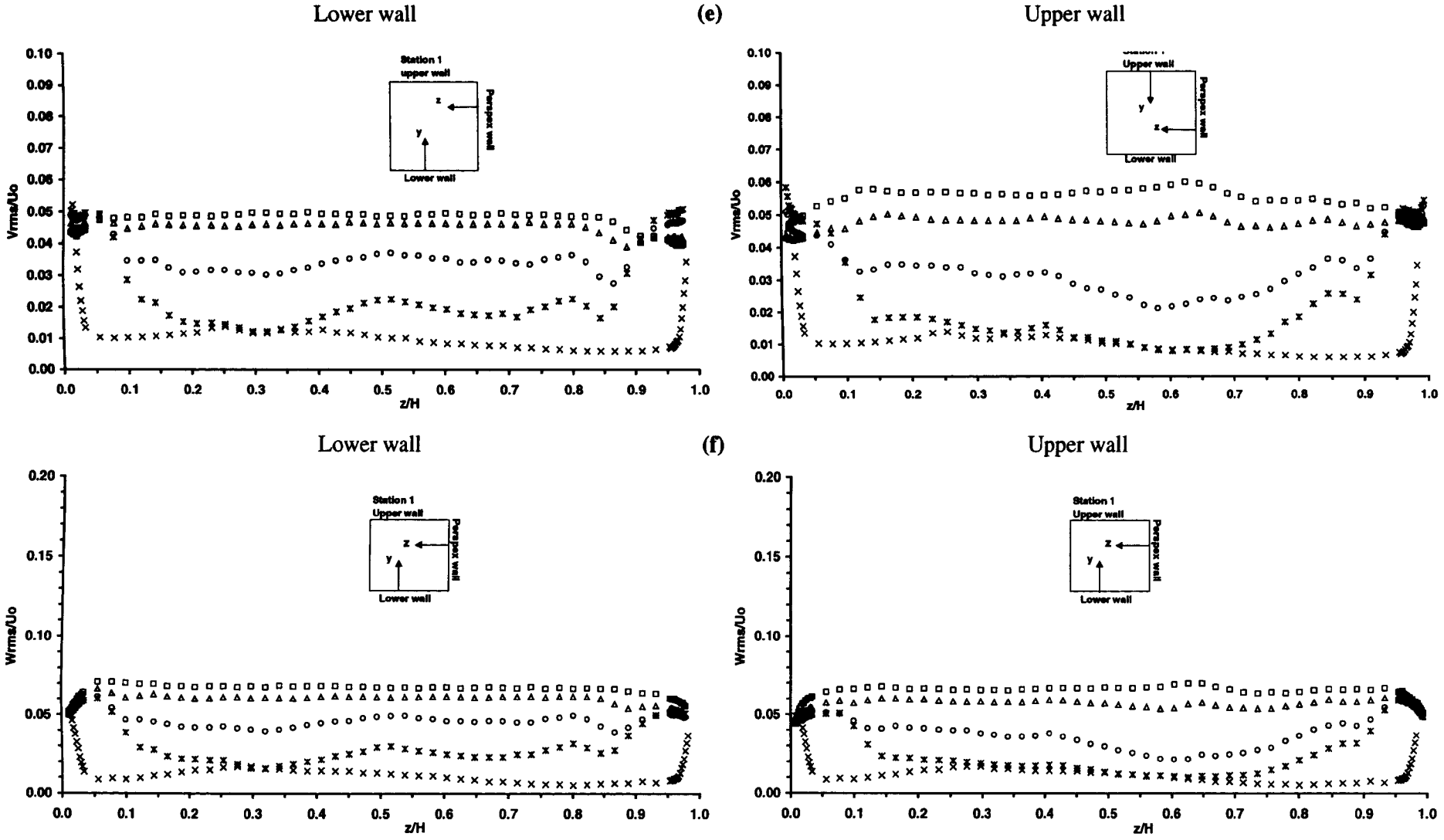
Lower wall
(e)
Upper wall
Vrms/Uo
z/H
Station 1
upper wall
Perspex wall
Lower wall
Upper wall
(f)
Wrms/Uo

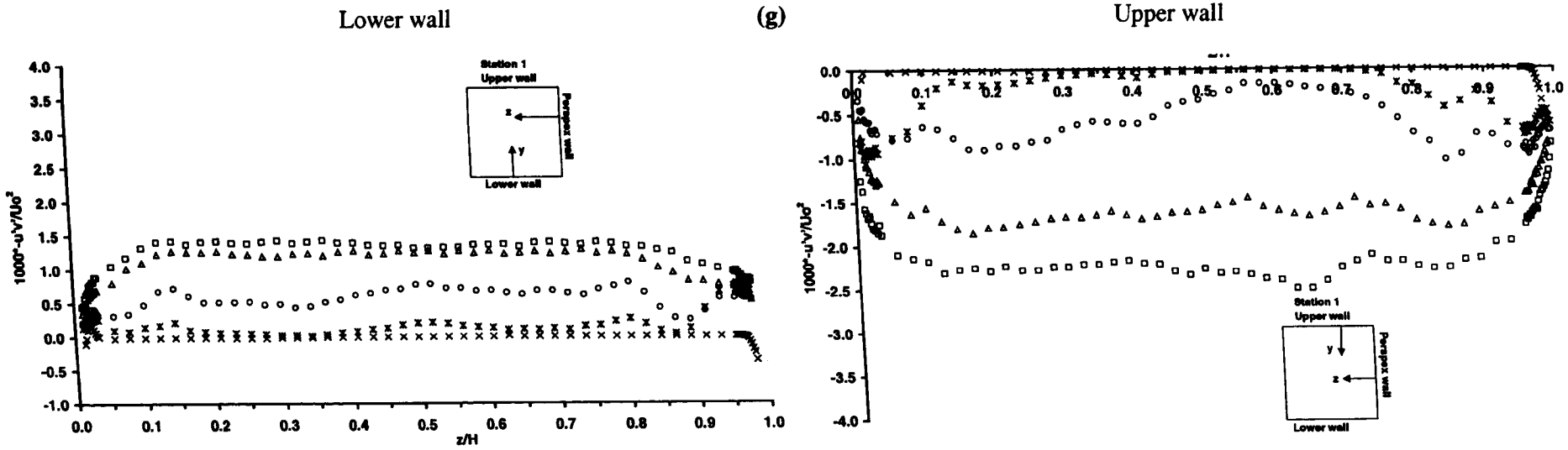

Figure 6.7: Profiles of mean and turbulence quantities obtained at nominal mainstream velocity U_o of 10 m/s in the spanwise direction at station 1: (a) mean streamwise velocity component; (b) mean normal velocity component; (c) mean spanwise velocity component; (d) streamwise intensity; (e) normal intensity; (f) spanwise intensity; (g) turbulence shear stress $-\overline{u'v'}$.

□, y = 2.5 mm; Δ, y = 5.0 mm; ○, y = 10.0 mm; ✳, y = 15.0 mm; ×, y = 228.0 mm.

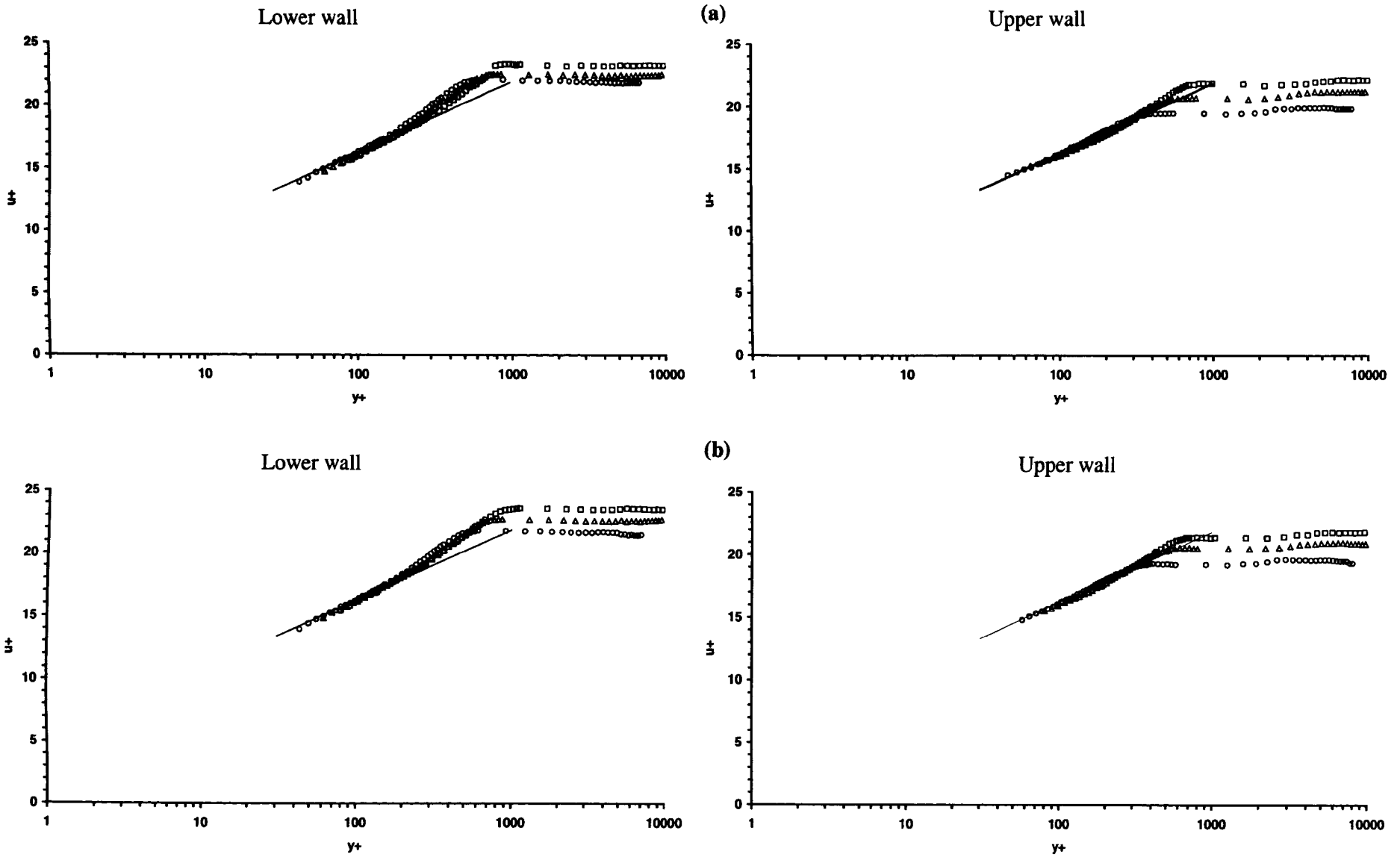
(a)
Lower wall
Upper wall
(b)
Lower wall
Upper wall
u+
y+
0
5
10
15
20
25
1
10
100
1000
10000

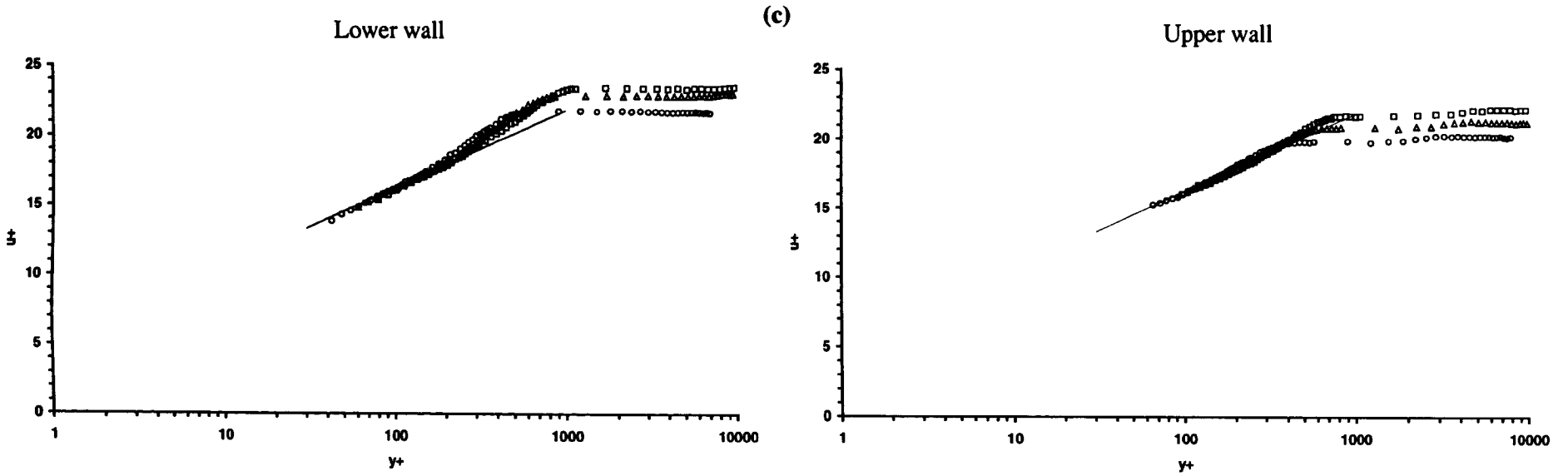

Figure 6.8: Velocity distribution near the lower and upper walls at station 1: (a) z/H = 0.5; (b) z/H = 0.6; (c) z/H = 0.7.

○, U_0 = 10 m/s; △, U_0 = 15 m/s; □, U_0 = 20 m/s; solid line is the logarithmic law of the wall with constants A = 2.44, B = 5.0.

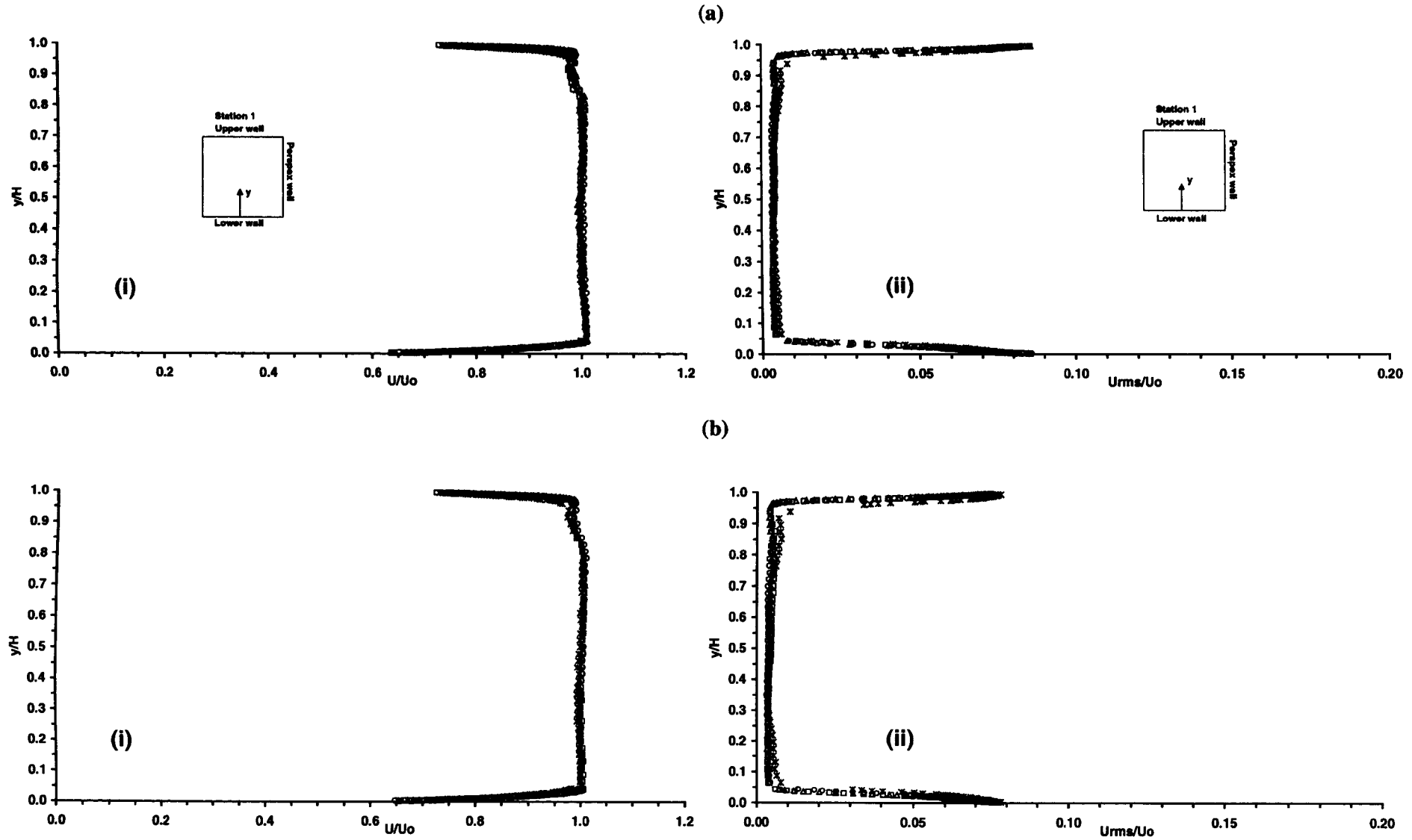
(a)
Station 1
Upper wall
Perspex wall
Lower wall
y
y/H
U/Uo
Urms/Uo
(i)
(ii)
(b)

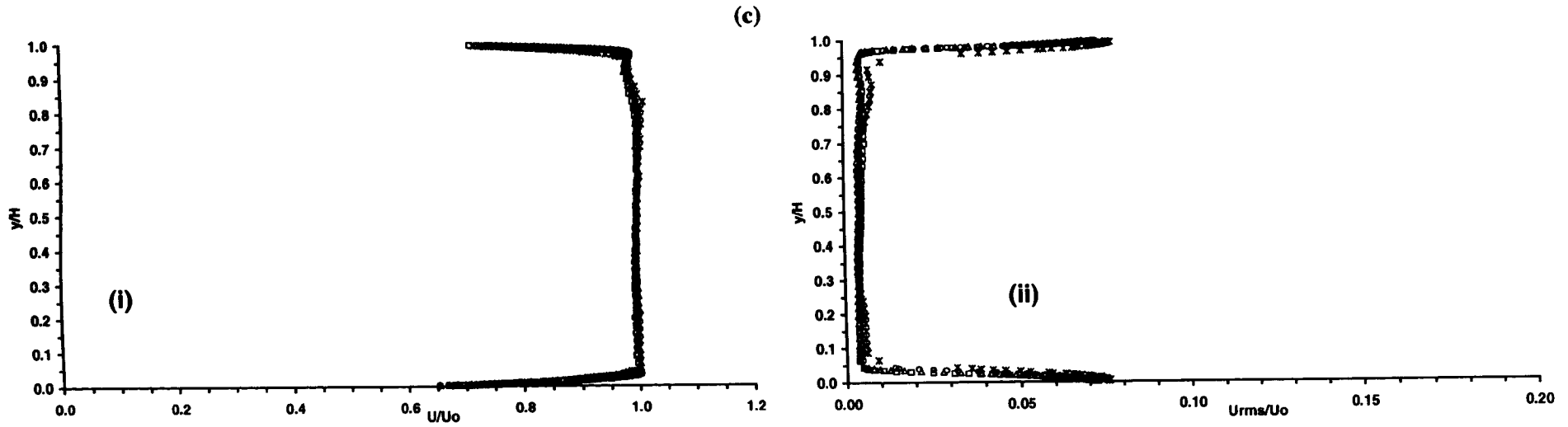

Figure 6.9: Profiles of mean and turbulence intensity in the normal direction at station 1, (i) streamwise mean velocity component; (ii) streamwise turbulence intensity: (a) U_o = 10 m/s; (b) U_o = 15 m/s; (c) U_o = 20 m/s.

□, z/H = 0.5; Δ, z/H = 0.6; ○, z/H = 0.7; ✳, z/H = 0.8.

(a)

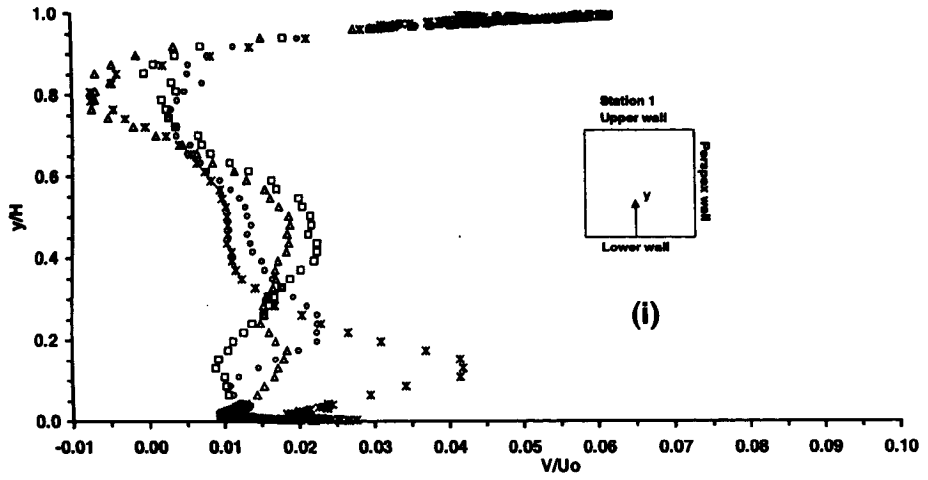
y/H
V/Uo
Station 1
Upper wall
Perspex wall
Lower wall
y
(i)

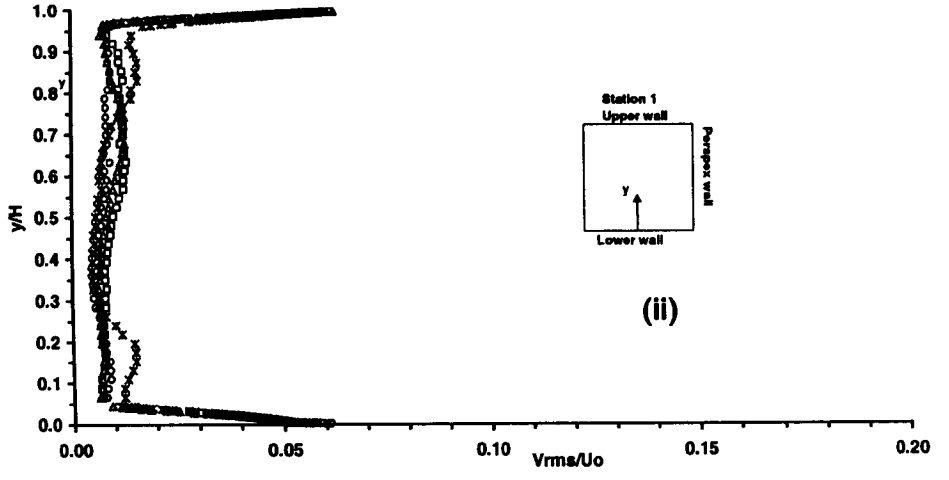
y/H
Vrms/Uo
Station 1
Upper wall
Perspex wall
Lower wall
y
(ii)

(b)

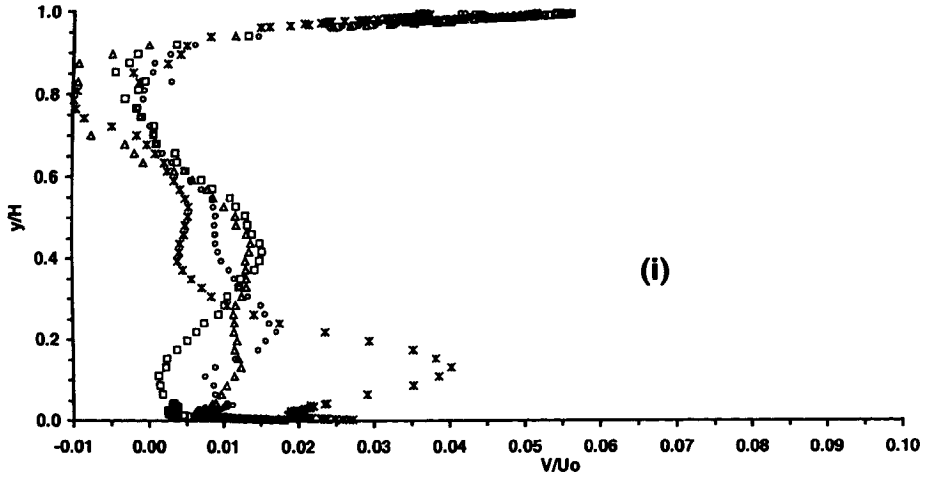
y/H
V/Uo
(i)

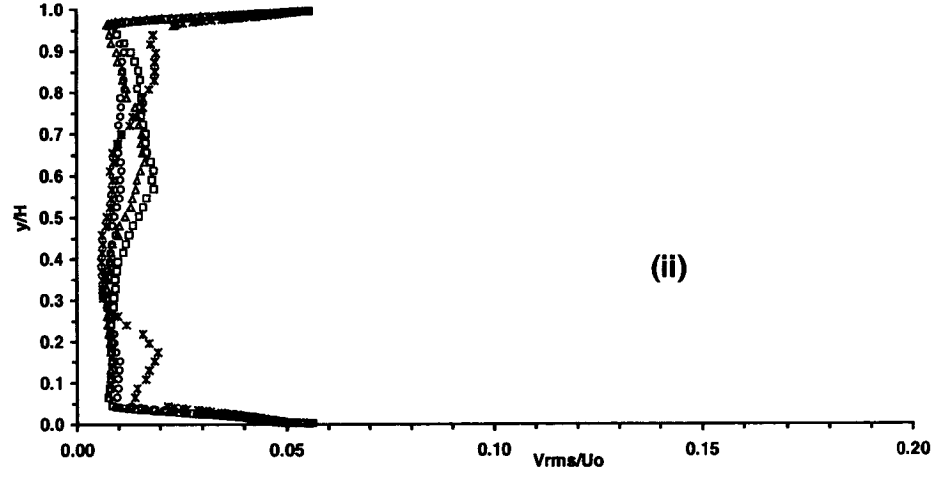
y/H
Vrms/Uo
(ii)

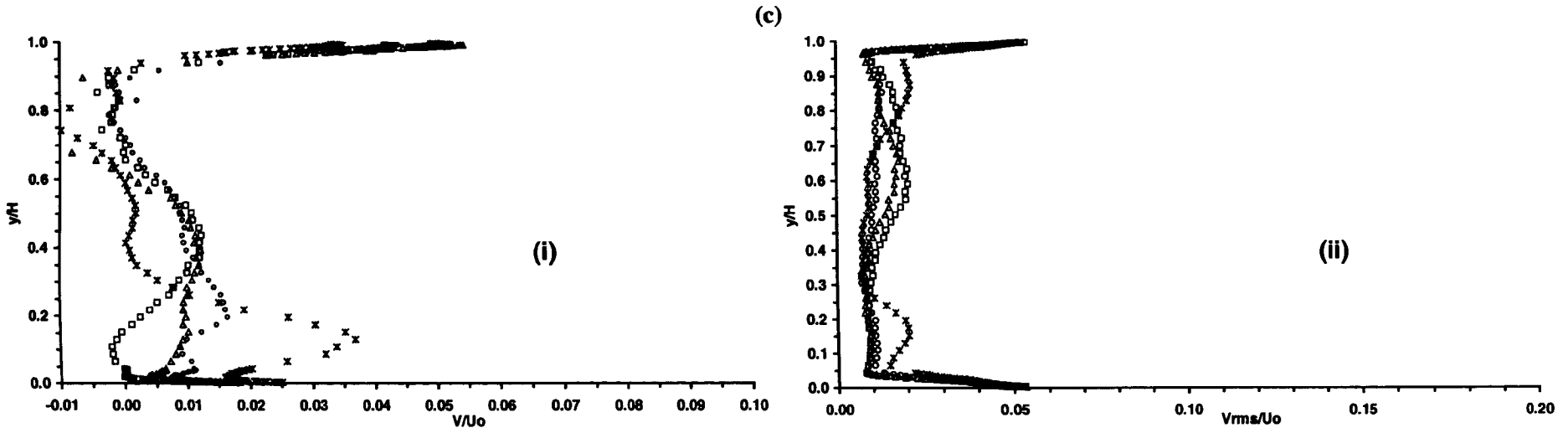

Figure 6.10: Profiles of mean and turbulence intensity in the normal direction at station 1, (i) mean normal velocity component; (ii) normal turbulence intensity: (a) U_o = 10 m/s; (b) U_o = 15 m/s; (c) U_o = 20 m/s.

□, z/H = 0.5; △, z/H = 0.6; ○, z/H = 0.7; ✳, z/H = 0.8.

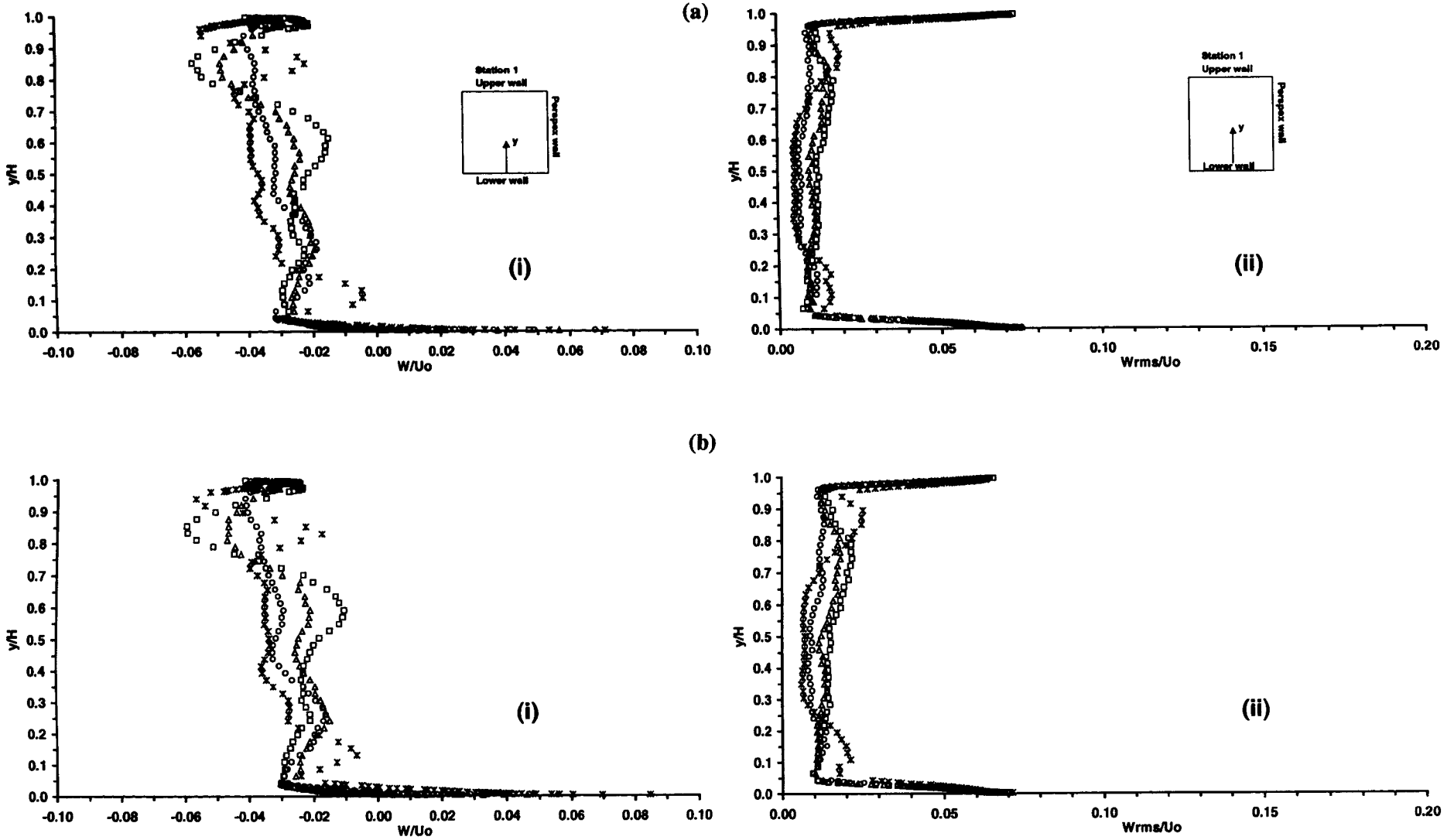
(a)
y/H
W/Uo
Station 1
Upper wall
Perspex wall
Lower wall
y
(i)
Wrms/Uo
(ii)
(b)
(i)
(ii)

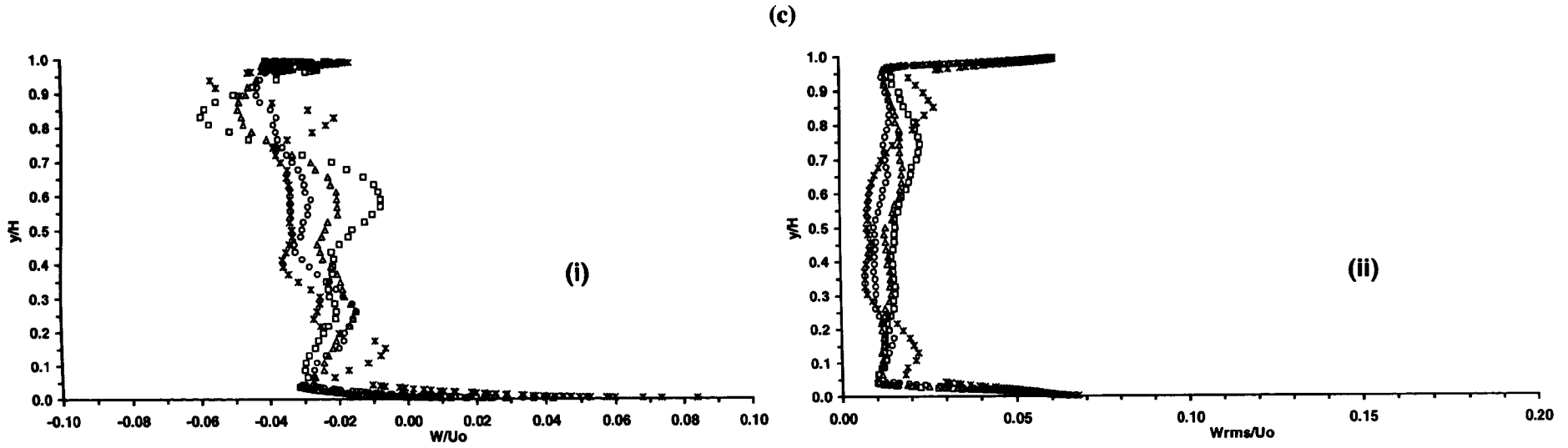

Figure 6.11: Profiles of mean and turbulence intensity in the normal direction at station 1, (i) spanwise mean velocity component; (ii) spanwise intensity: (a) $U_o = 10$ m/s; (b) $U_o = 15$ m/s; (c) $U_o = 20$ m/s.

□, z/H = 0.5; △, z/H = 0.6; ○, z/H = 0.7; ✳, z/H = 0.8.

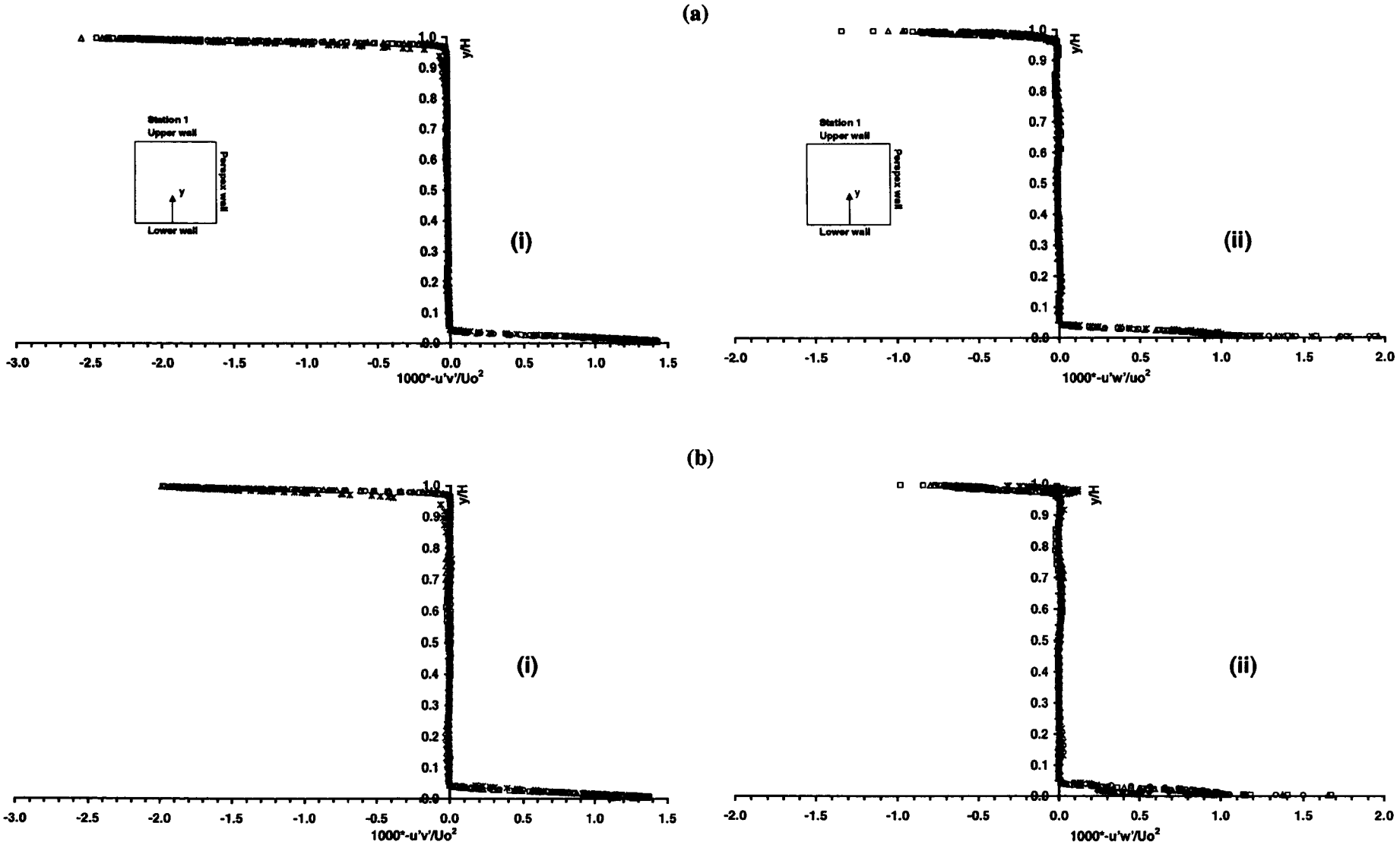
(a)
Station 1
Upper wall
Perspex wall
Lower wall
y
(i)
y/H
1000*-u'v'/Uo²
(ii)
1000*-u'w'/uo²
(b)
(i)
(ii)

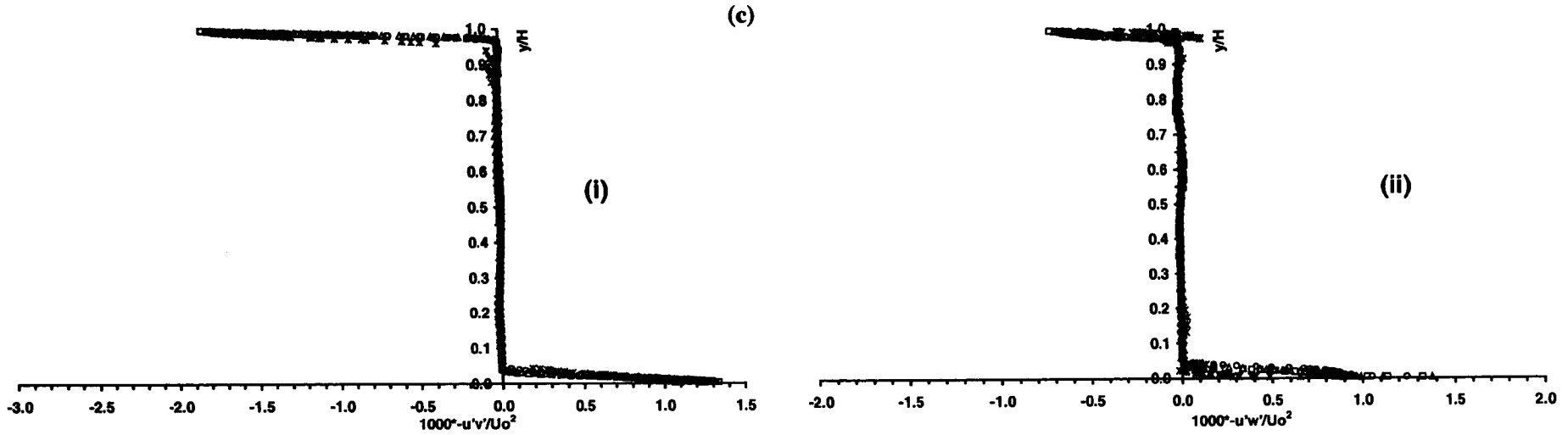

Figure 6.12: Profiles of turbulence shear stresses in the normal direction at station 1, (i) turbulence shear stress $-\overline{u'v'}$; (ii) turbulence shear stress $-\overline{u'w'}$: (a) U_o = 10 m/s; (b) U_o = 15 m/s; (c) U_o = 20 m/s.

□, z/H = 0.5; Δ, z/H = 0.6; ○, z/H = 0.7; ✱, z/H = 0.8.

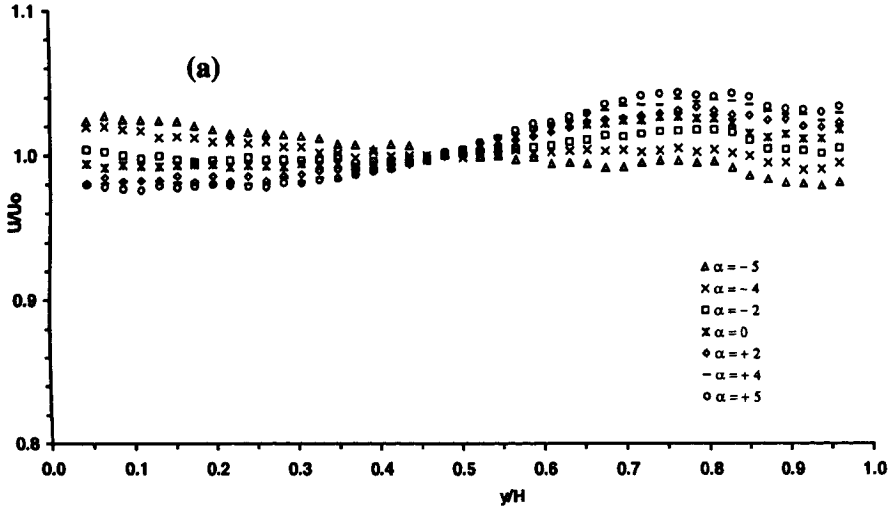
(a)
U/Uo
y/H
α = −5
α = −4
α = −2
α = 0
α = +2
α = +4
α = +5

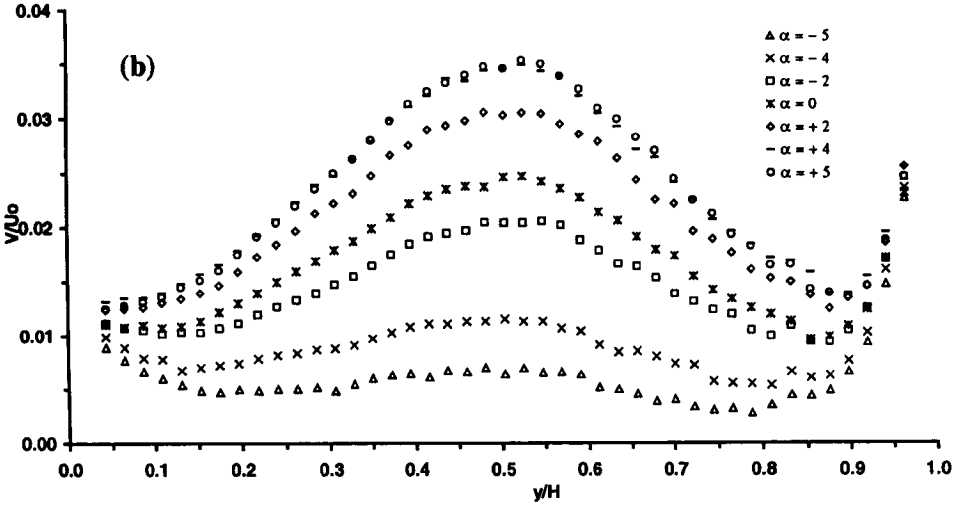
(b)
V/Uo
y/H
α = −5
α = −4
α = −2
α = 0
α = +2
α = +4
α = +5

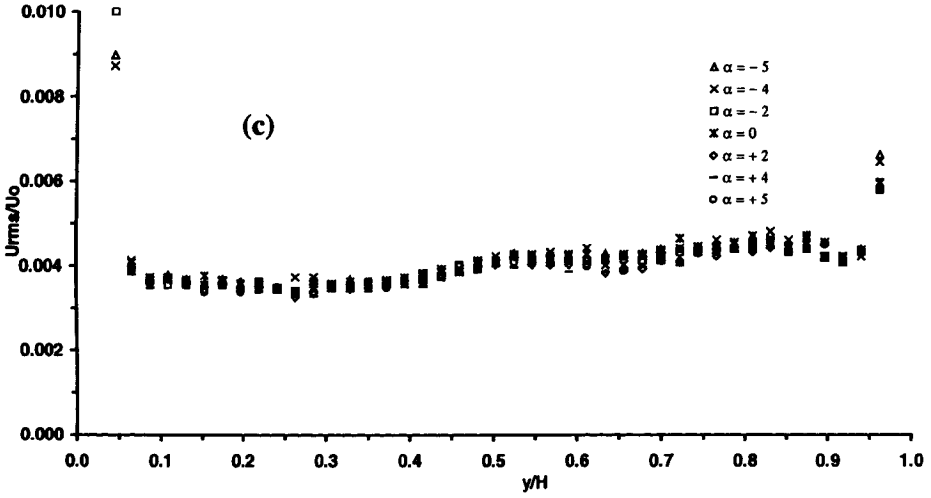
(c)
Urms/Uo
y/H
α = −5
α = −4
α = −2
α = 0
α = +2
α = +4
α = +5

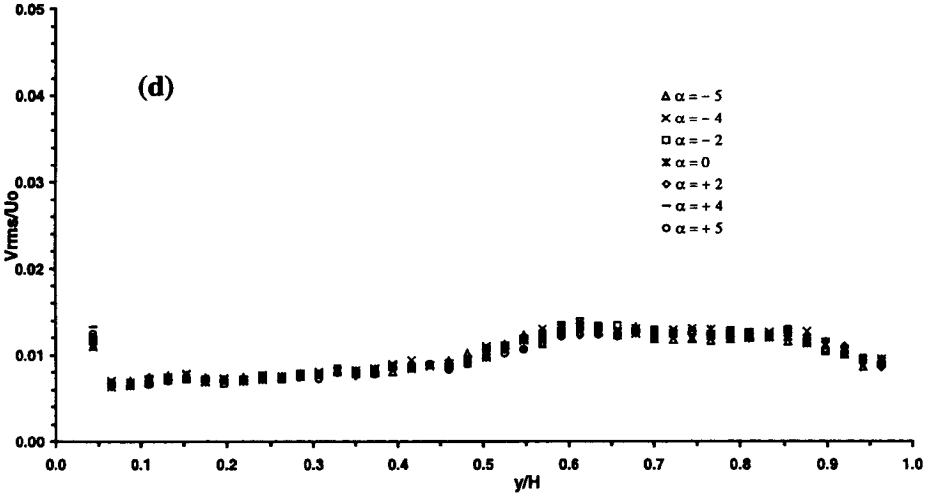
(d)
Vrms/Uo
y/H
α = −5
α = −4
α = −2
α = 0
α = +2
α = +4
α = +5

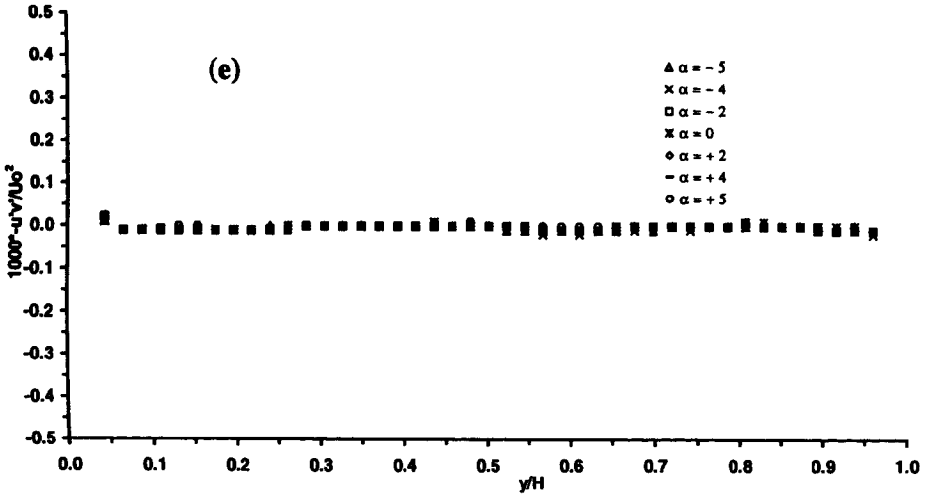

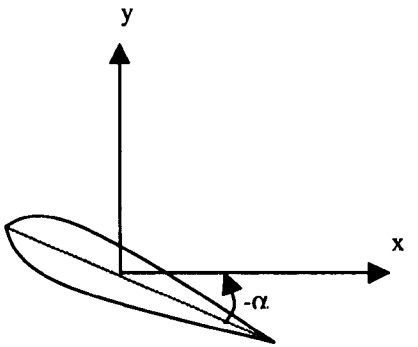

Figure 6.13: Airfoil angle of attack effects on the mean and turbulence quantities at station 1 (z/H = 0.5): (a) mean streamwise velocity component; (b) mean normal velocity component; (c) streamwise turbulence intensity; (d) normal turbulence intensity; (e) turbulence shear stress ($-\overline{u'v'}$).

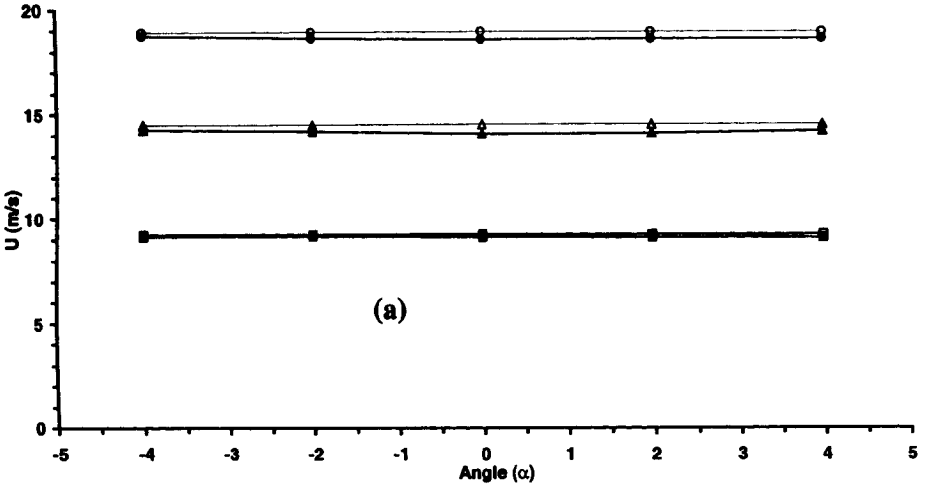
U (m/s)
Angle (α)
(a)

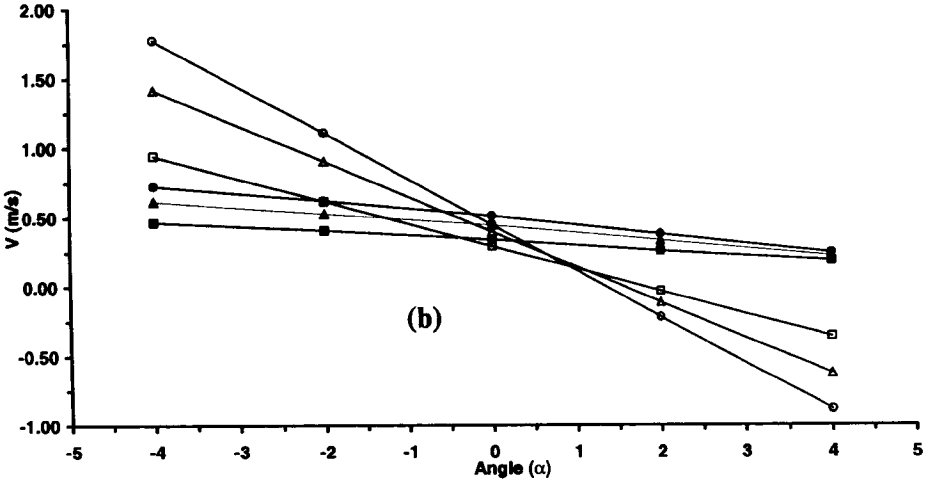
V (m/s)
Angle (α)
(b)

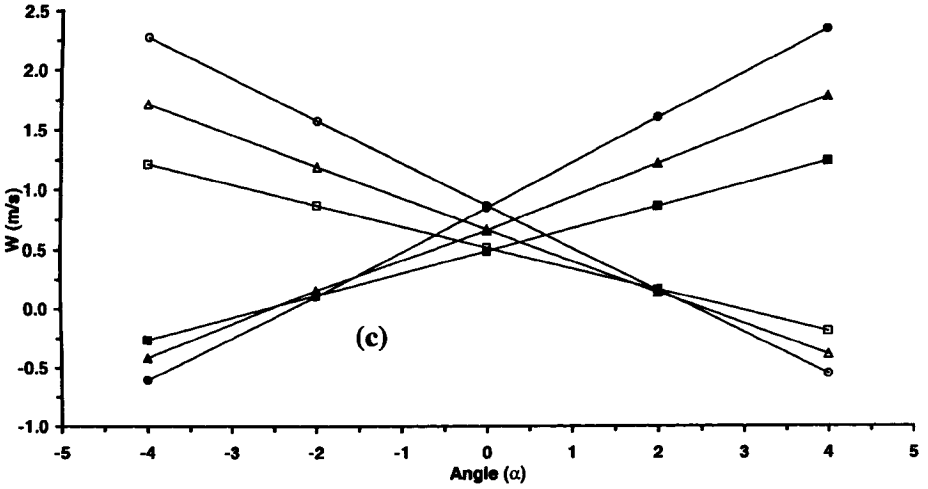
W (m/s)
Angle (α)
(c)

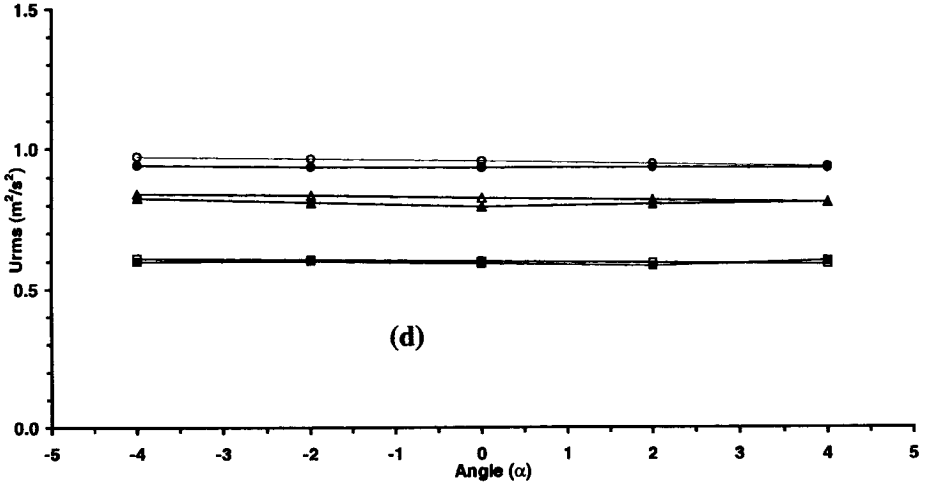
Urms (m²/s²)
Angle (α)
(d)

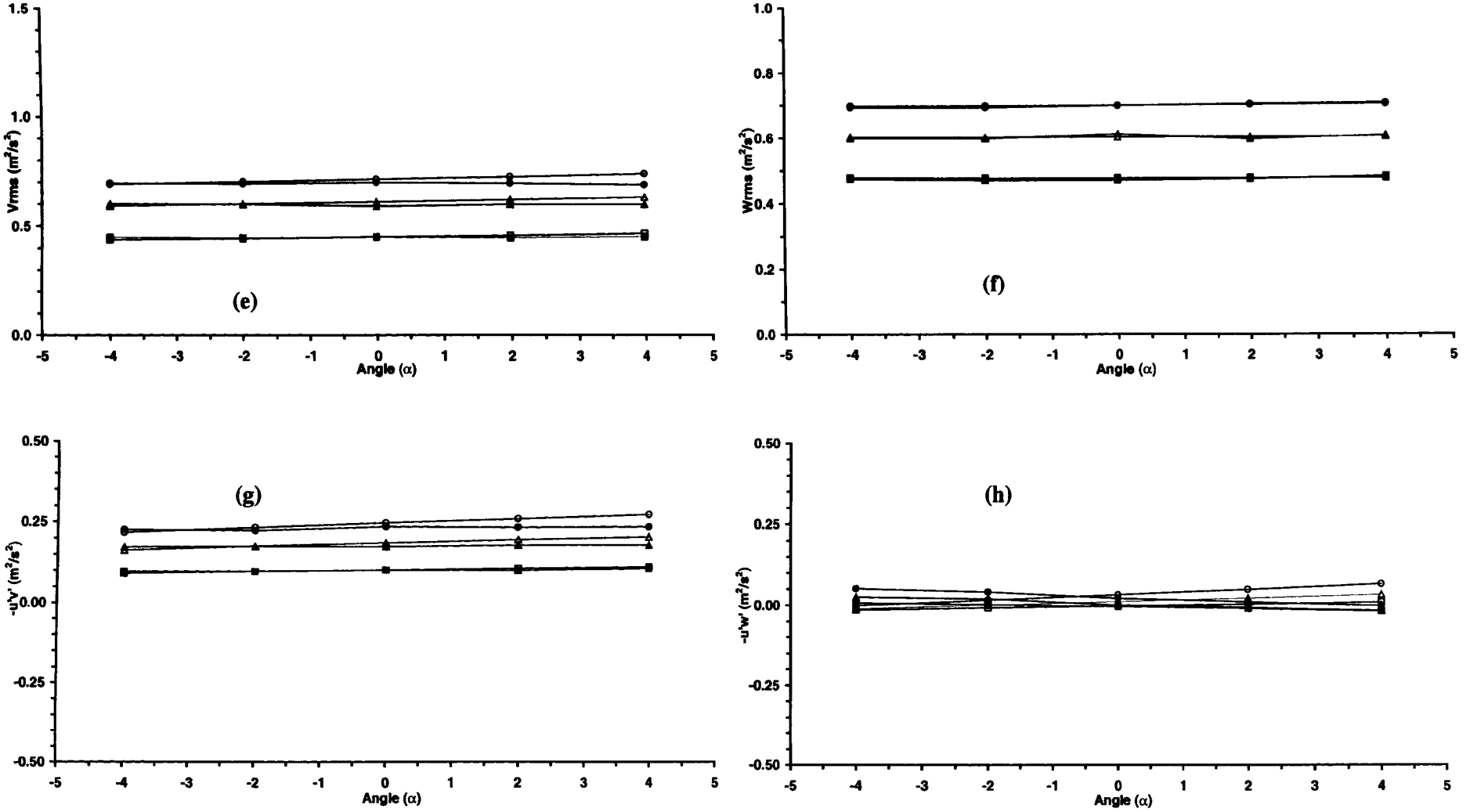

Figure 6.14: The effects of pitch angle and yaw angle misalignment on mean and turbulence quantities: (a) mean streamwise velocity component; (b) mean normal velocity component; (c) mean spanwise velocity component; (d) streamwise velocity fluctuation; (e) normal velocity fluctuation; (f) spanwise velocity fluctuation; (g) turbulence shear stress $(-\overline{u'v'})$; (h) turbulence shear stress $(-\overline{u'w'})$.

Pitch angle: □, U_o = 10 m/s; △, U_o = 15 m/s; ○, U_o = 20 m/s. Yaw angle: ■, U_o = 10 m/s; ▲, U_o = 15 m/s; ●, U_o = 20 m/s.

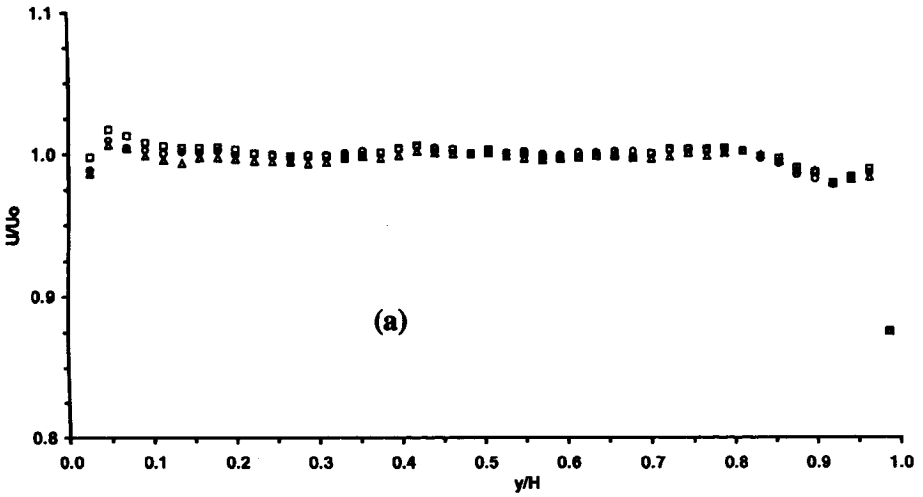
U/Uo
y/H
(a)

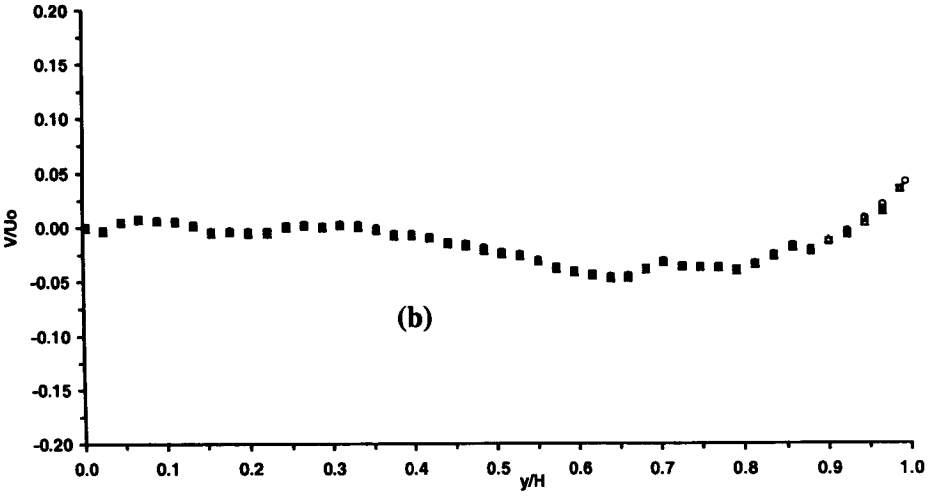
V/Uo
y/H
(b)

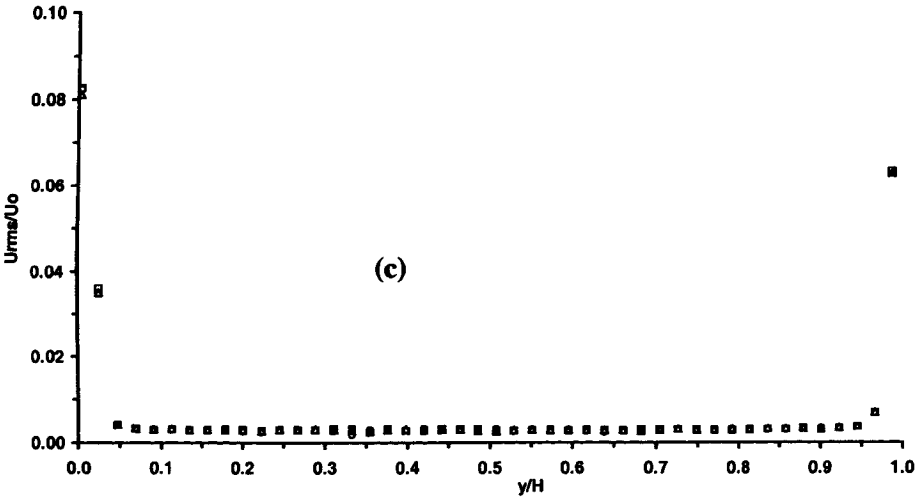
Urms/Uo
y/H
(c)

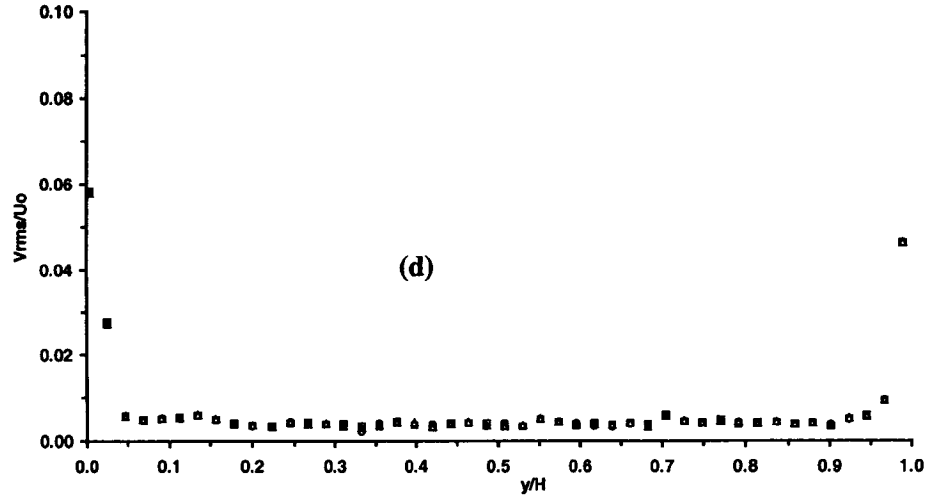
Vrms/Uo
y/H
(d)

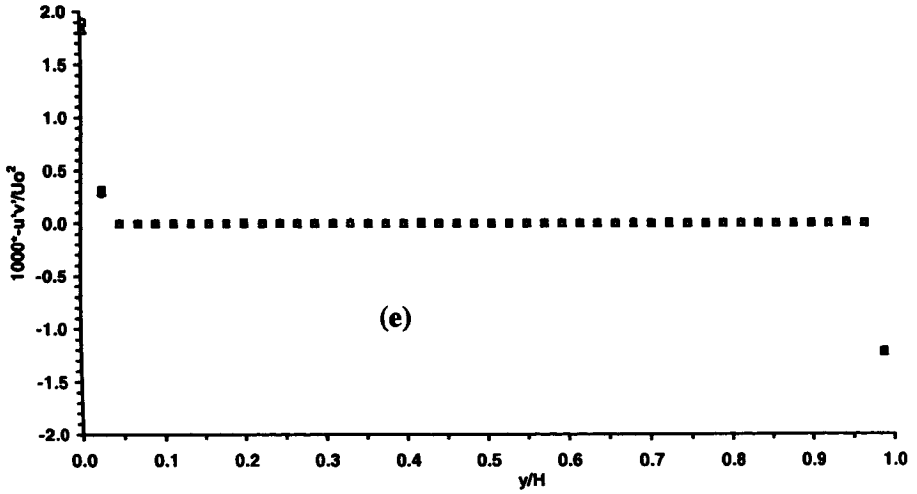

Figure 6.15: The effects of sampling frequency on mean and turbulence quantities: (a) mean streamwise velocity component; (b) mean normal velocity component; (c) streamwise turbulence intensity; (d) normal turbulence intensity; (e) turbulence shear stress $(-\overline{u'v'})$.

O, 4kHz; □, 6kHz; Δ, 8kHz.

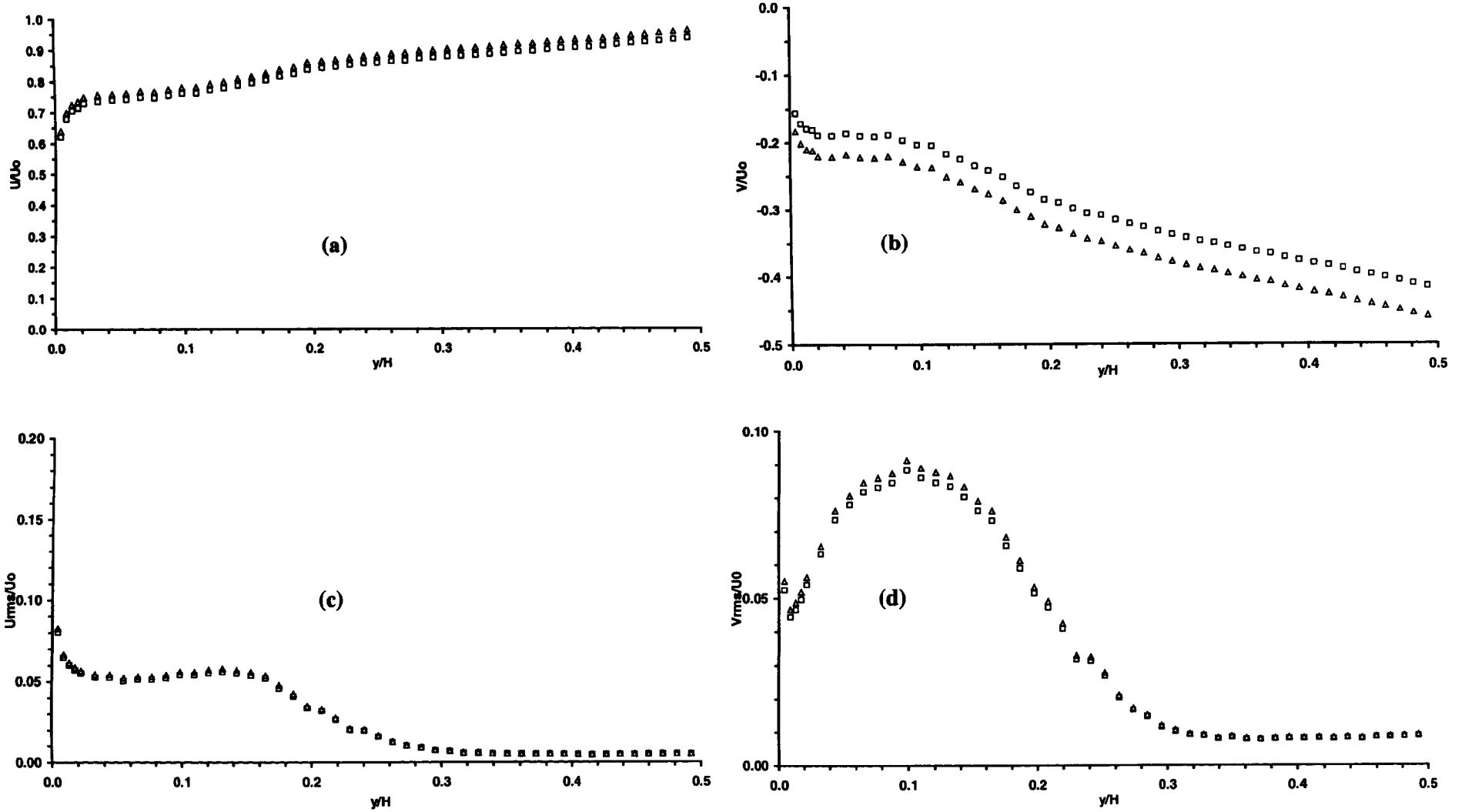

Figure 6.16: The effects of cross-wire probe calibration on the mean and turbulence quantities at station 4: (a) mean streamwise velocity component; (b) mean normal velocity component; (c) streamwise turbulence intensity; (d) normal turbulence intensity.

Δ, 1st calibration; □, 2nd calibration.

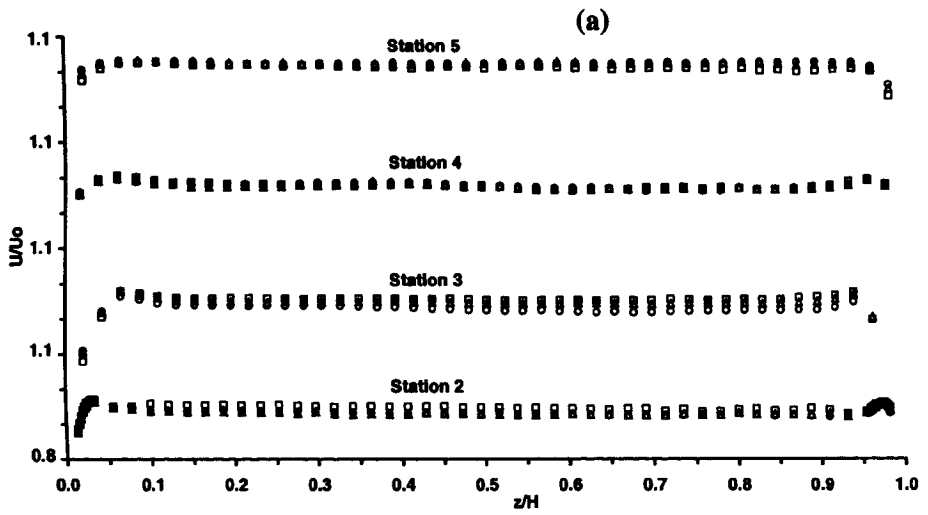
(a)
Station 5
Station 4
Station 3
Station 2
U/Uo
z/H

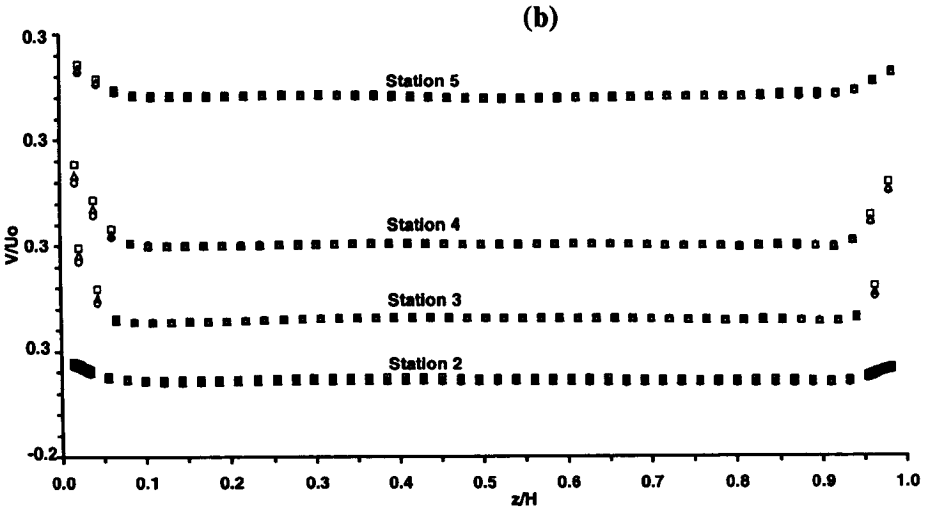
(b)
Station 5
Station 4
Station 3
Station 2
V/Uo
z/H

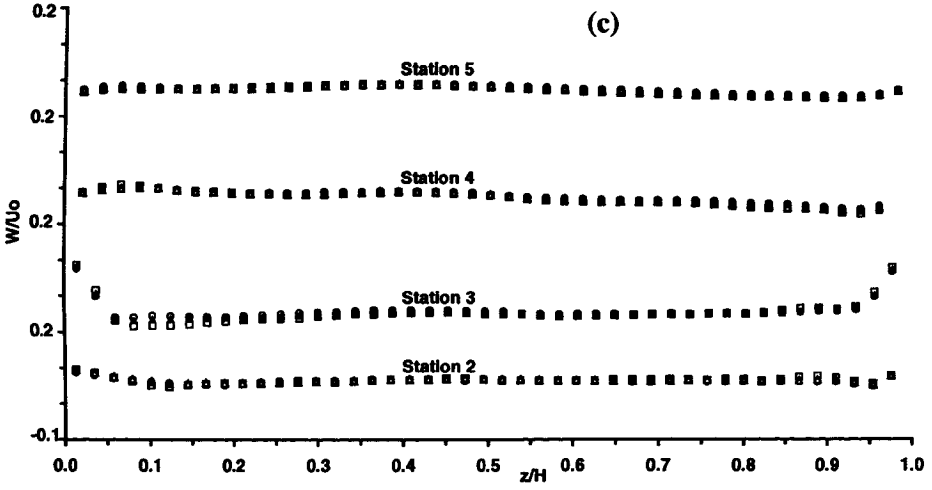
(c)
Station 5
Station 4
Station 3
Station 2
W/Uo
z/H

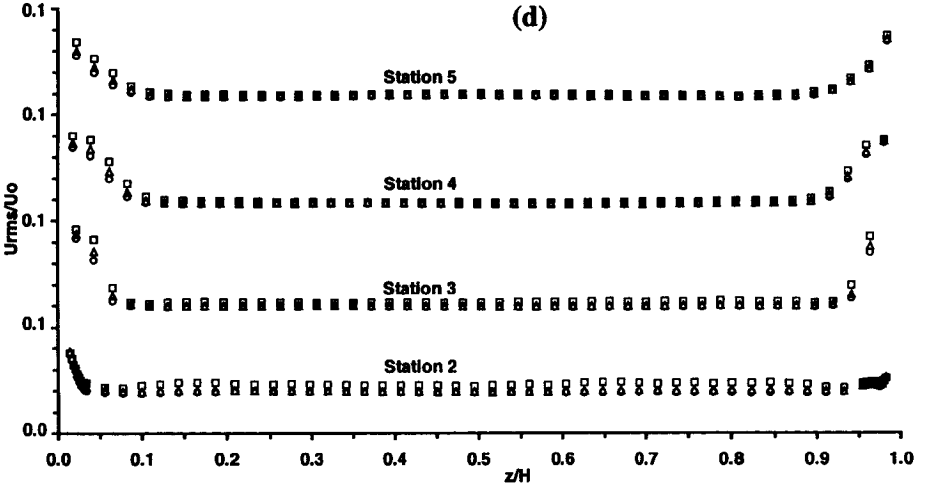
(d)
Station 5
Station 4
Station 3
Station 2
Urms/Uo
z/H

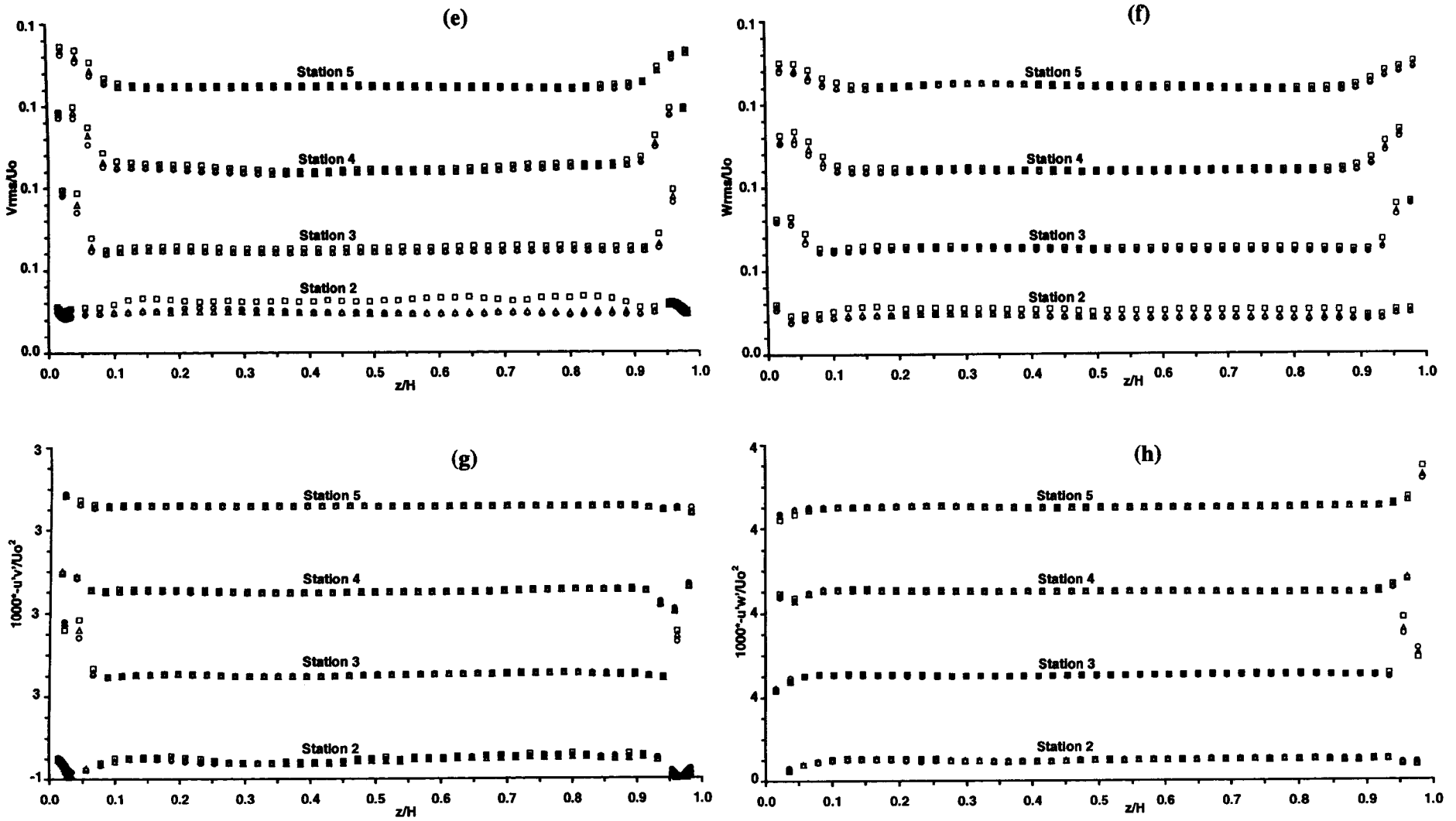

Figure 6.17: Profiles of mean velocity components and turbulence quantities in the spanwise direction (wake centreline) at stations 2 to 5: (a) mean streamwise velocity component; (b) mean normal velocity component; (c) mean spanwise velocity component; (d) streamwise turbulence intensity; (e) normal turbulence intensity; (f) spanwise turbulence intensity; (g) shear stress $(-\overline{u'v'})$; (h) shear stress $(-\overline{u'w'})$.

□, U_o = 10 m/s ; Δ, U_o = 15 m/s; ○, U_o = 20 m/s.

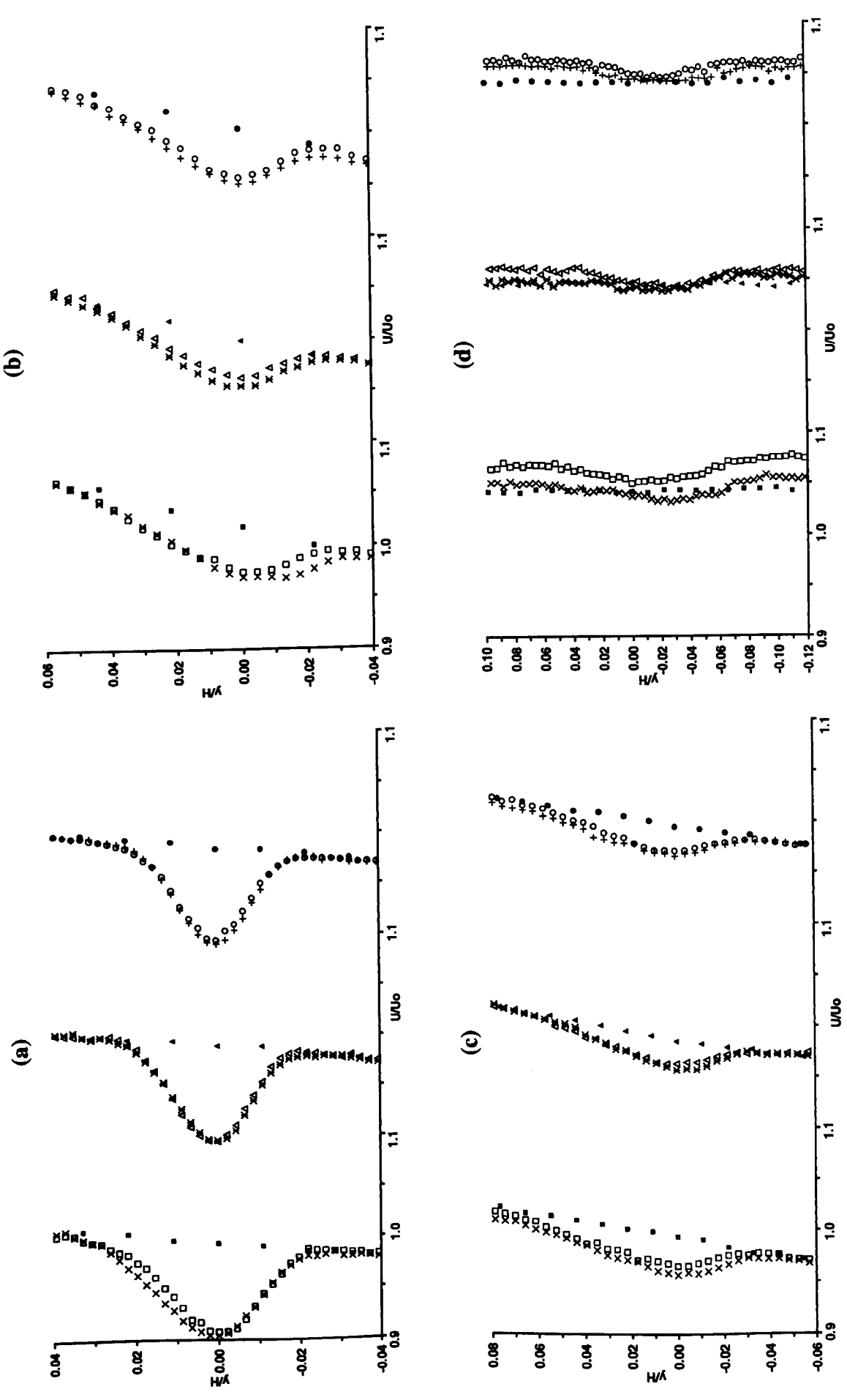
(a)
(b)
(c)
(d)
U/Uo
y/H

(e)

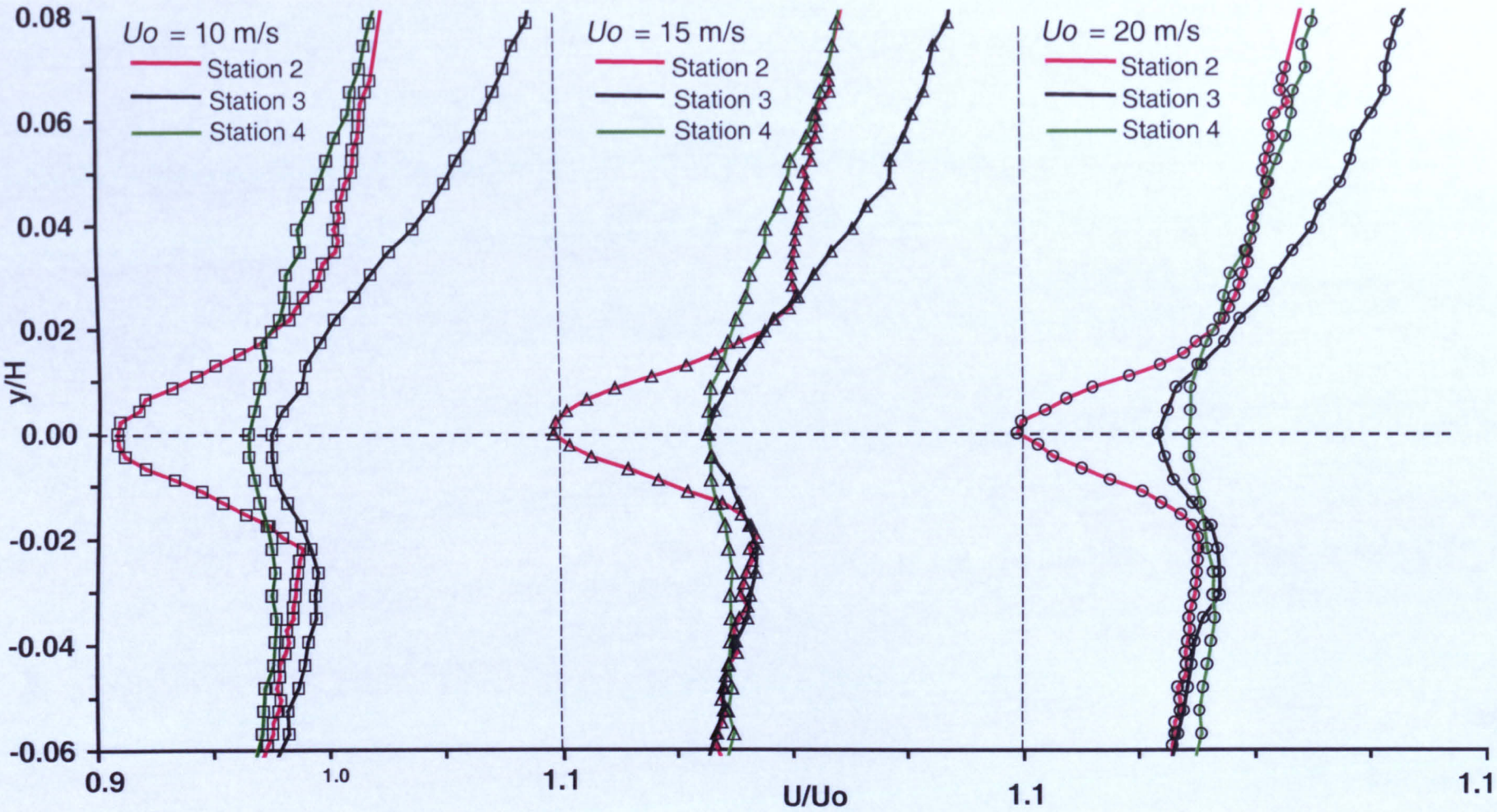

(Original in colour)

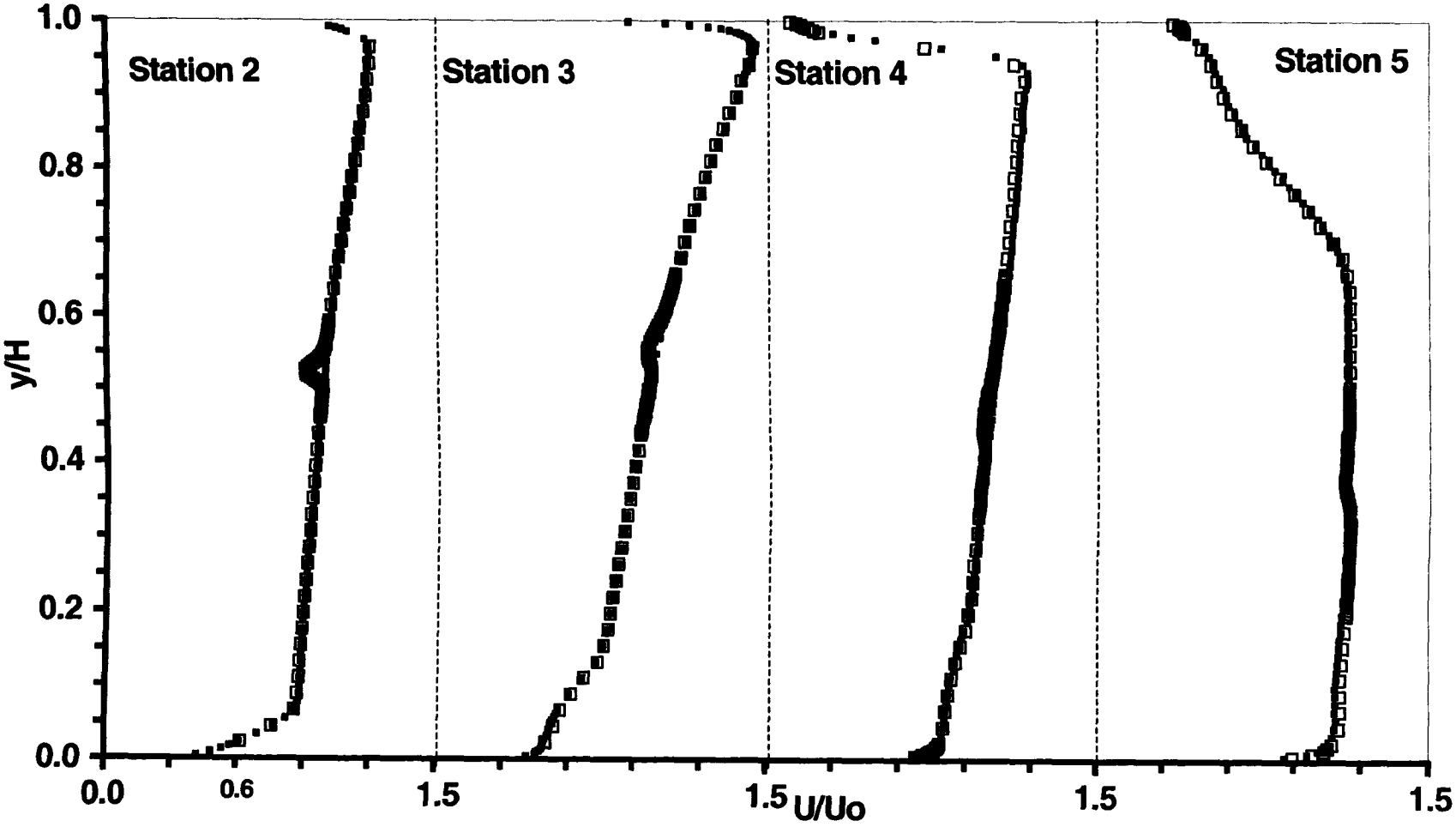

Figure 6.18: Profiles of mean streamwise velocity component in normal direction: (a) wake at station 2; (b) wake at station 3; (c) wake at station 4; (d) wake at station 5; (e) comparison of profiles in the wake at stations 2 to 4; (f) profiles obtained across the whole cross-section at stations 2 to 5.

□, U_o = 10 m/s, z/H = 0.5; ×, U_o =10 m/s, z/H = 0.7; ■, U_o = 10 m/s, z/H = 0.5, without airfoil;
△, U_o = 15 m/s, z/H = 0.5; ✱, U_o =15 m/s, z/H = 0.7; ▲, U_o = 15 m/s, z/H = 0.5, without airfoil;
○, U_o = 20 m/s, z/H = 0.5; +, U_o =20 m/s, z/H = 0.7; ●, U_o = 20 m/s, z/H = 0.5, without airfoil.

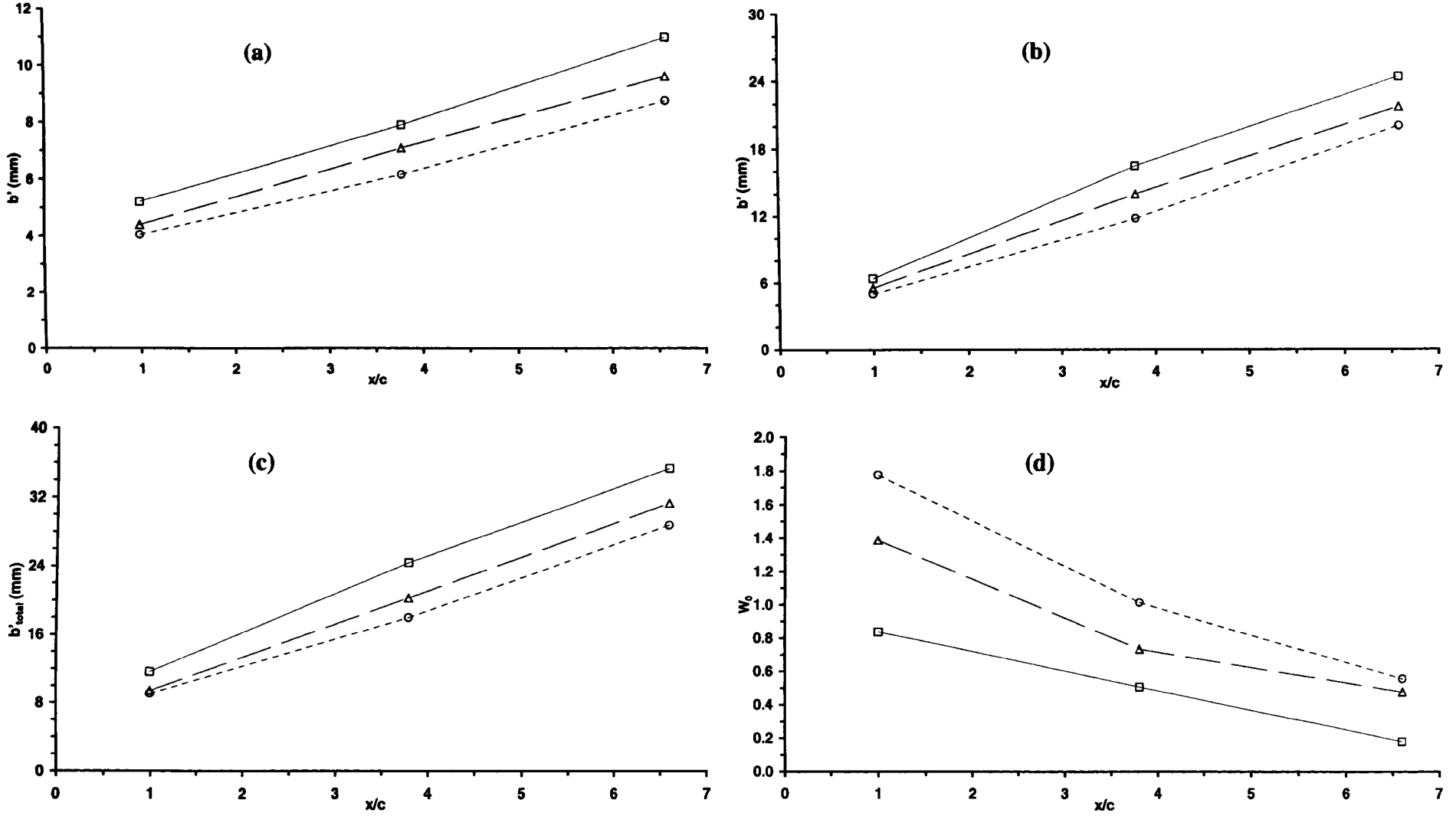

Figure 6.19: Profiles of wake parameters: (a) variation of wake half-width on the outer side; (b) variation of wake half-width on the inner side; (c) variation of total wake half-width; (d) variation of maximum velocity defect. □, U_o = 10 m/s; Δ, U_o =15 m/s; ○, U_o = 20 m/s.

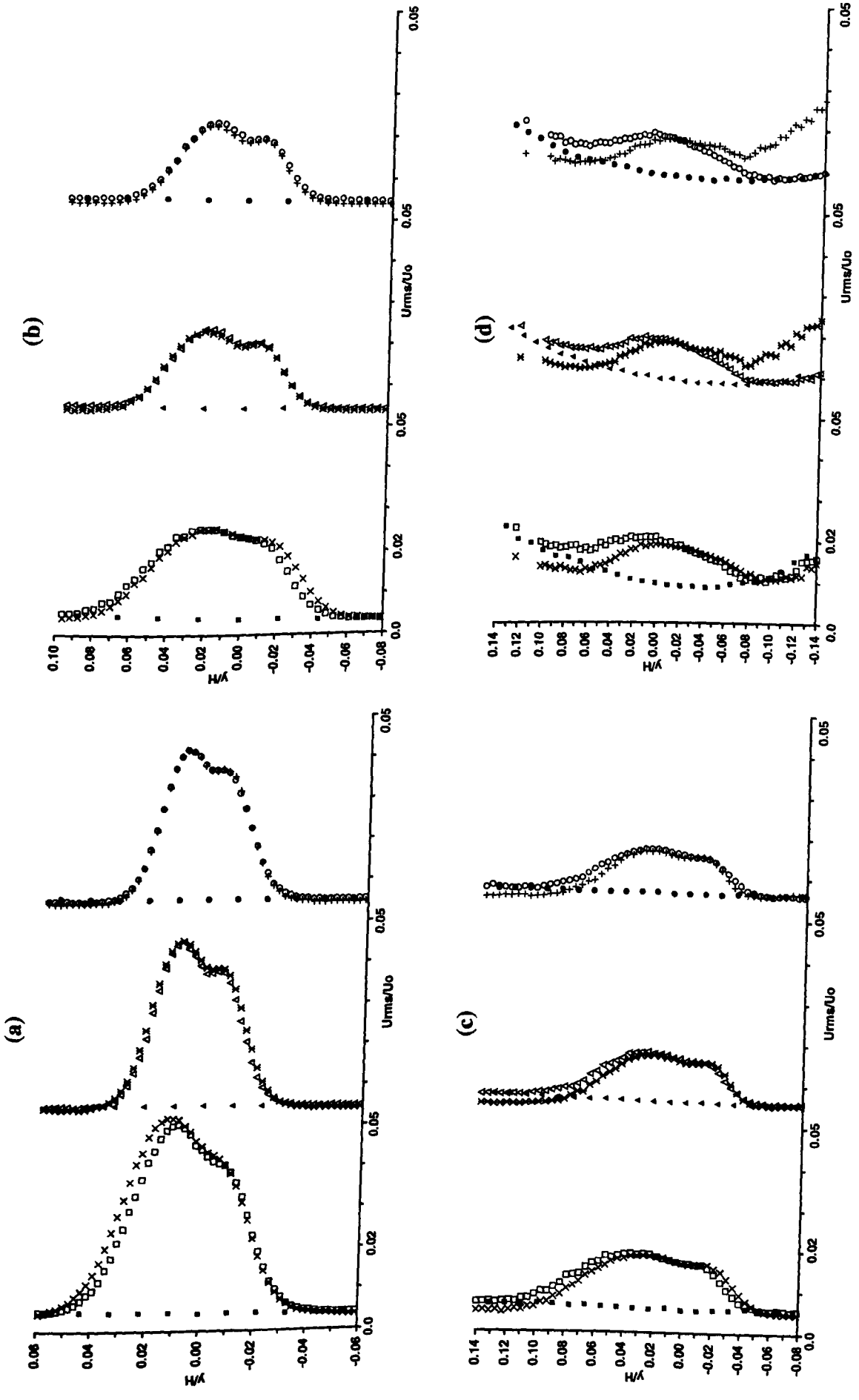
(a)
(b)
(c)
(d)
y/H
Urms/Uo

(e)

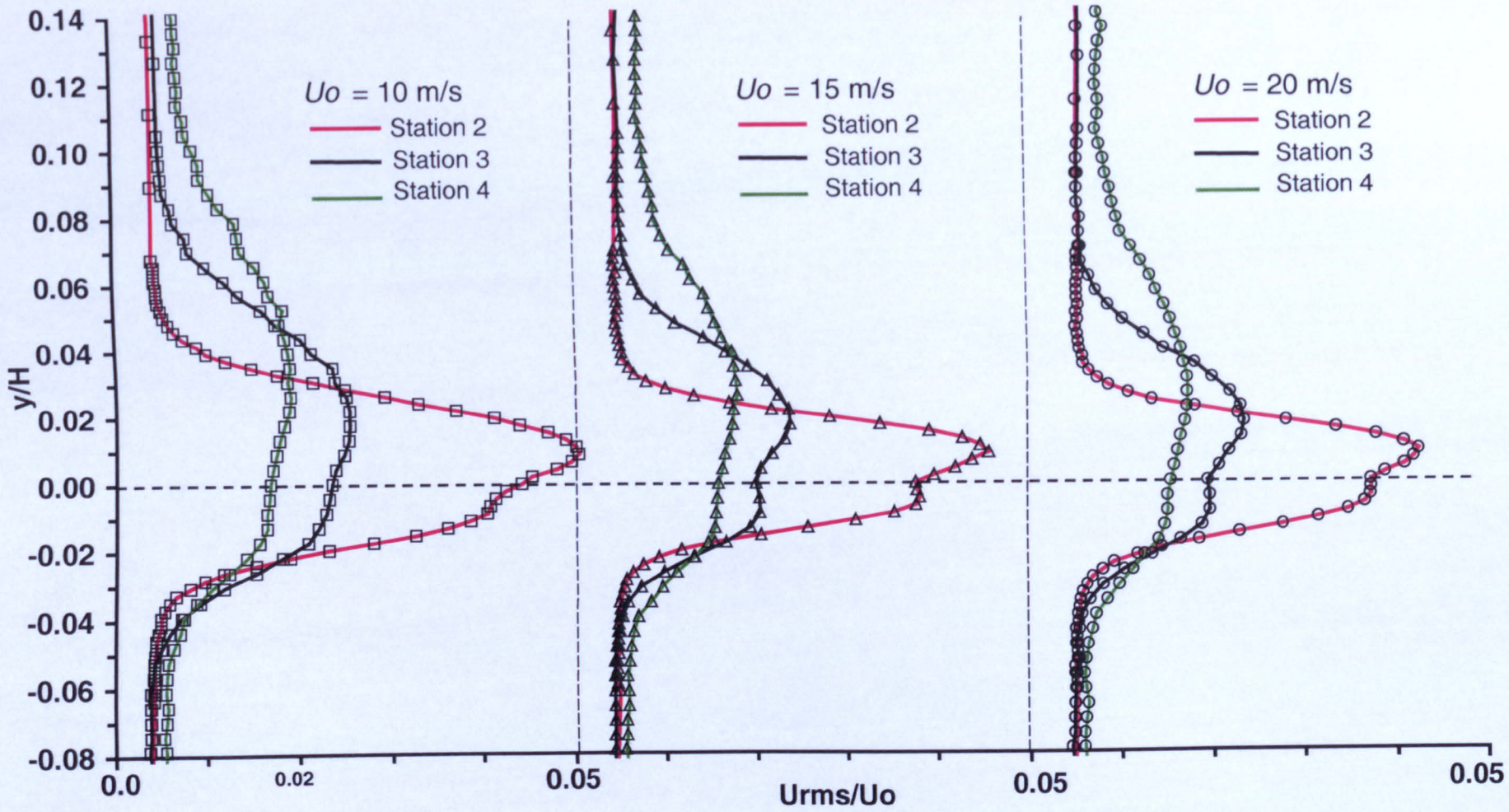

(Original in colour)

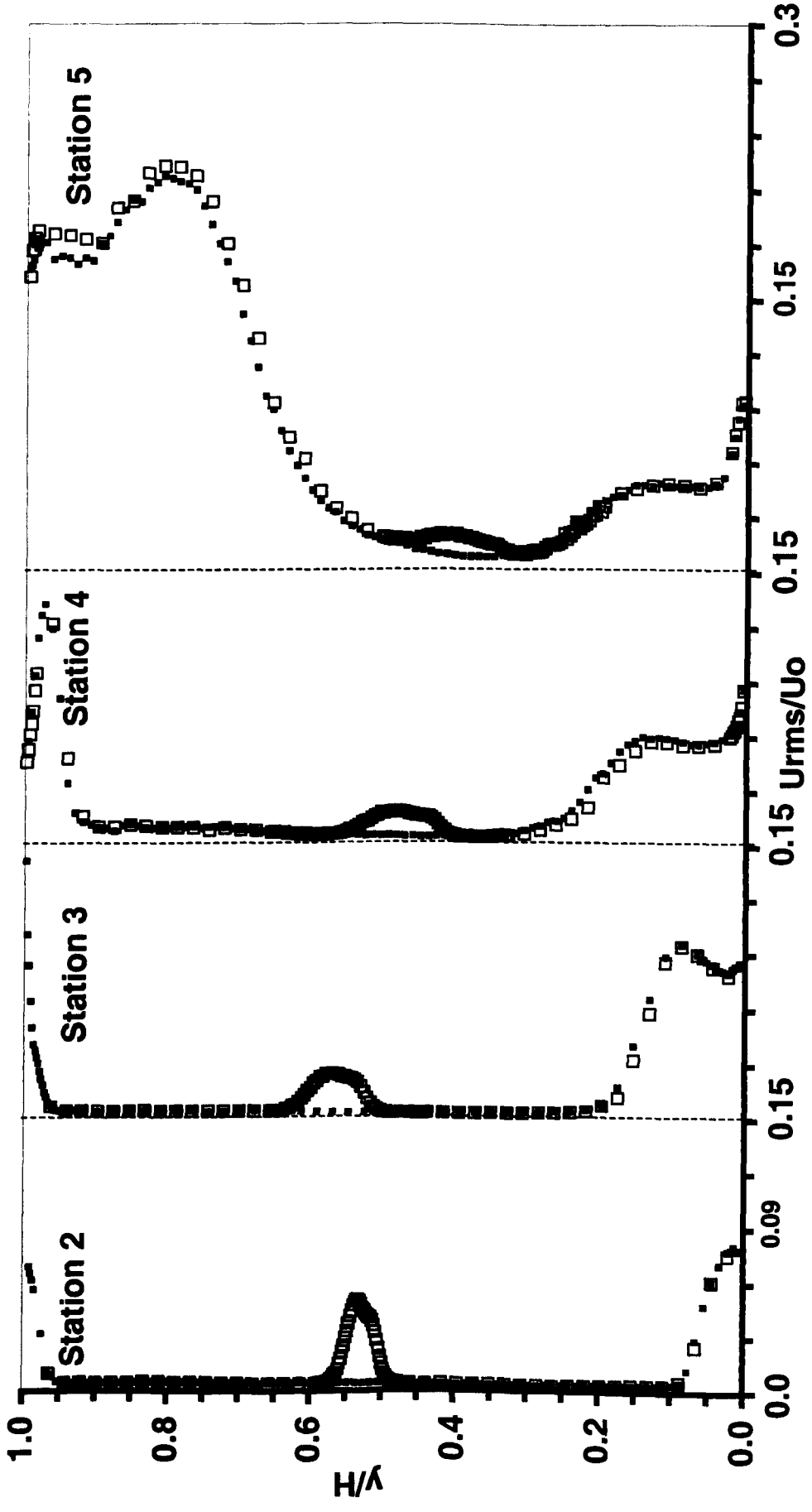

Figure 6.20: Profiles of streamwise turbulence intensity in the normal direction: (a) wake at station 2; (b) wake at station 3; (c) wake at station 4; (d) wake at station 5; (e) comparison of profiles in the wake at stations 2 to 4; (f) profiles obtained across the whole cross-section at stations 2 to 5. For definition of symbols see Figure 6.18.

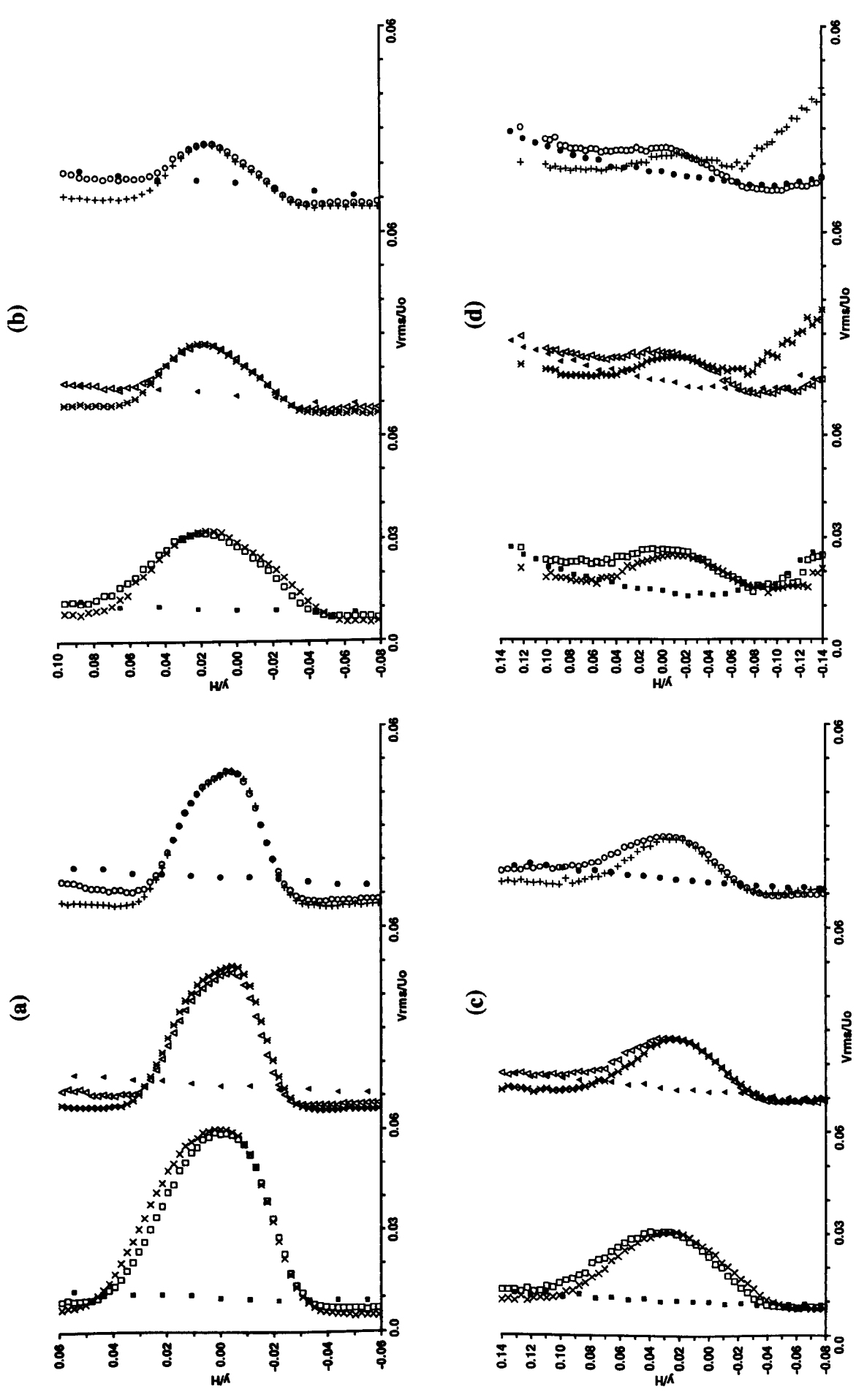
(a)
(b)
(c)
(d)
Vrms/Uo
y/H

(e)

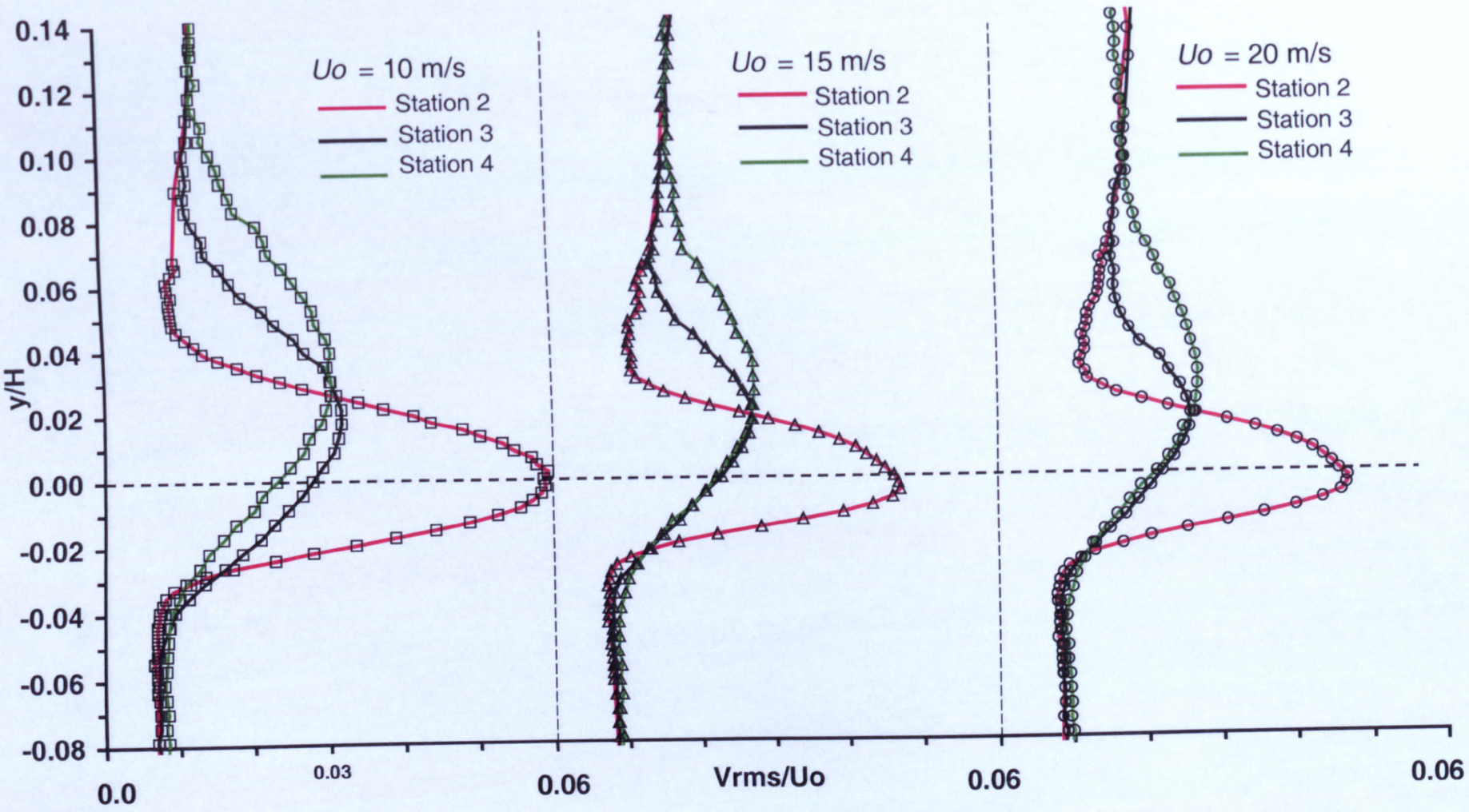

(Original in colour)

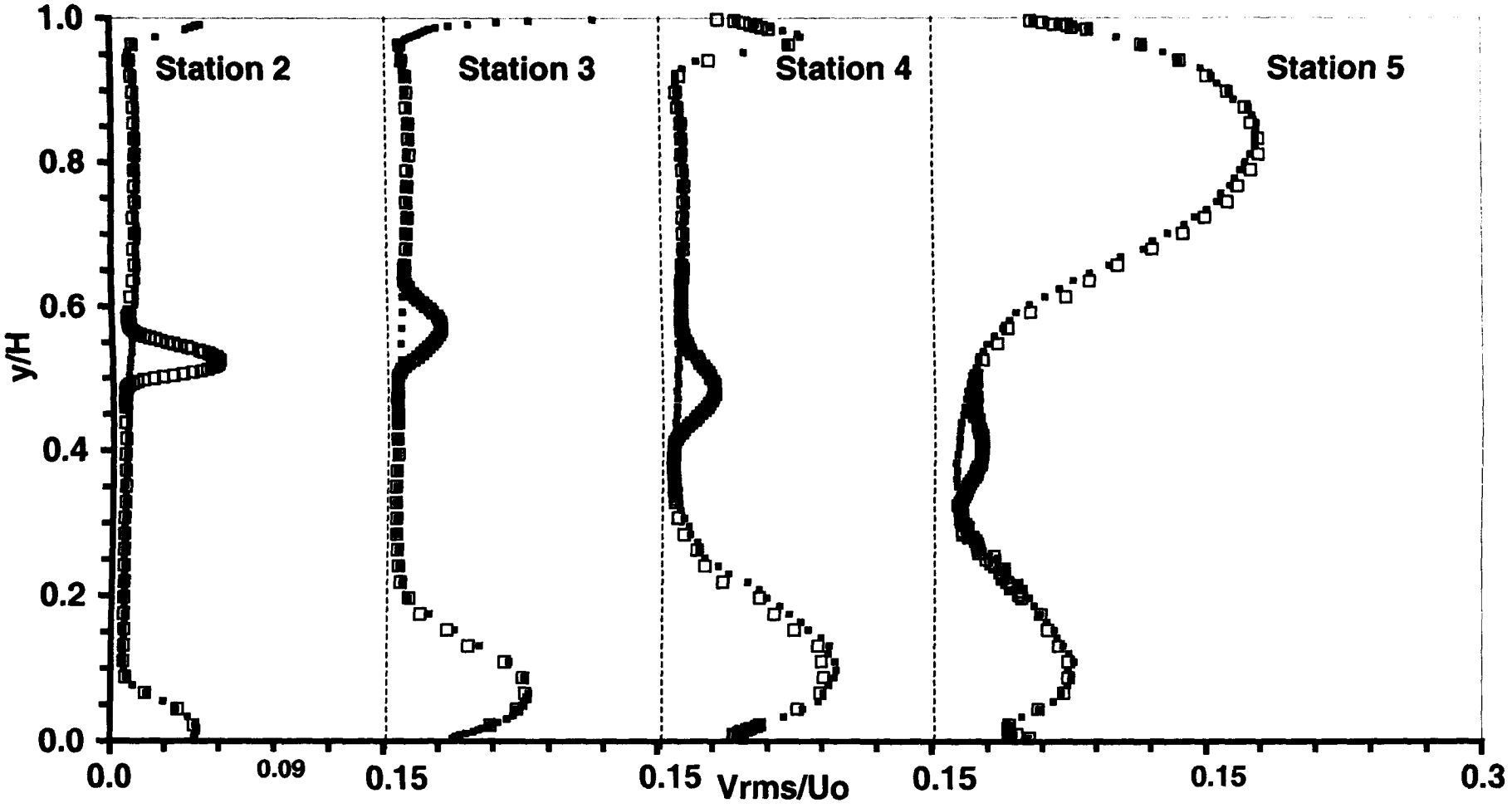

Figure 6.21: Profiles of normal turbulence intensity in the normal direction: (a) wake at station 2; (b) wake at station 3; (c) wake at station 4; (d) wake at station 5; (e) comparison of profiles in the wake at stations 2 to 4; (f) profiles obtained across the whole cross-section at stations 2 to 5. For definition of symbols see Figure 6.18.

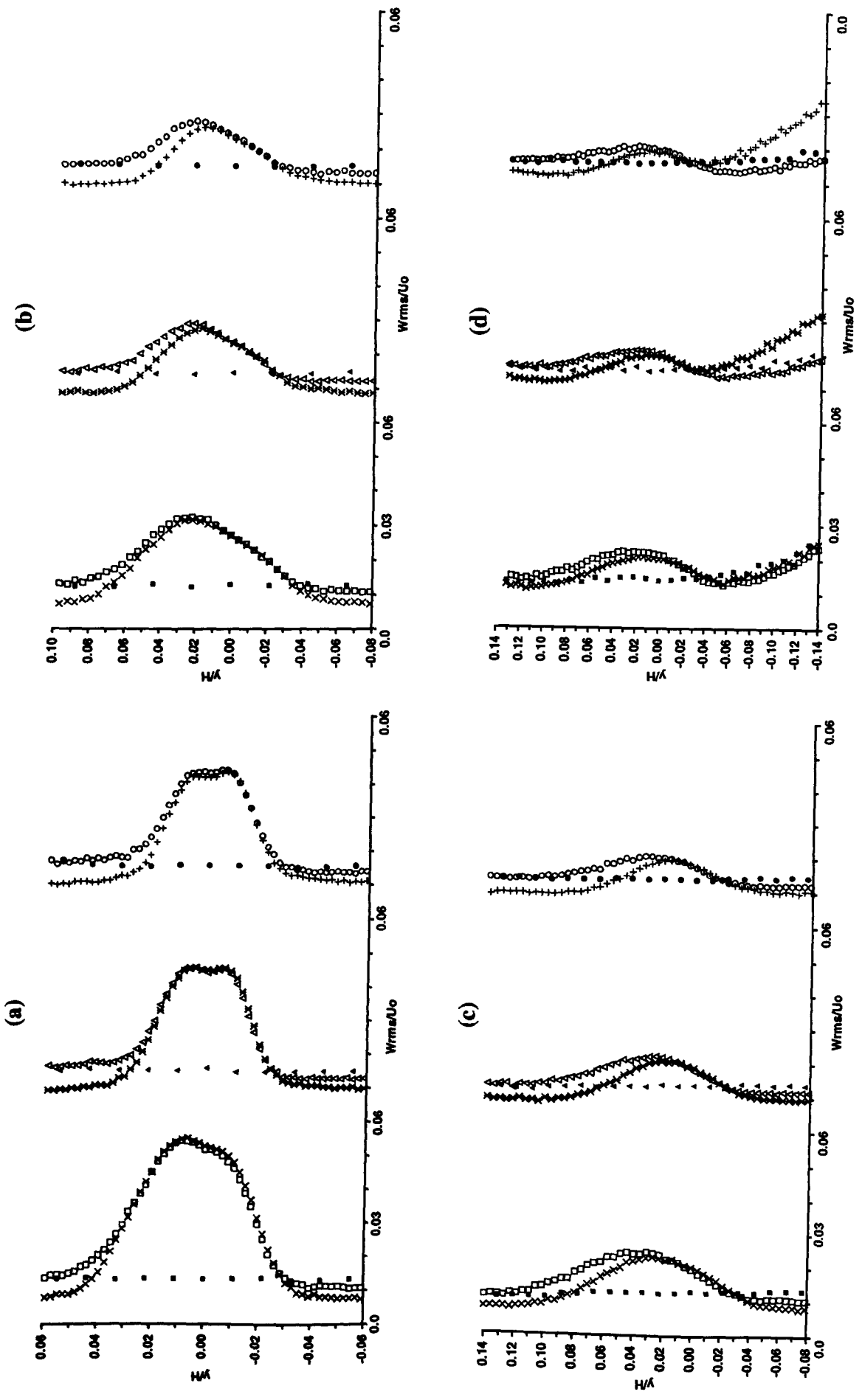
(a)
(b)
(c)
(d)
Wrms/Uo
y/H

(e)

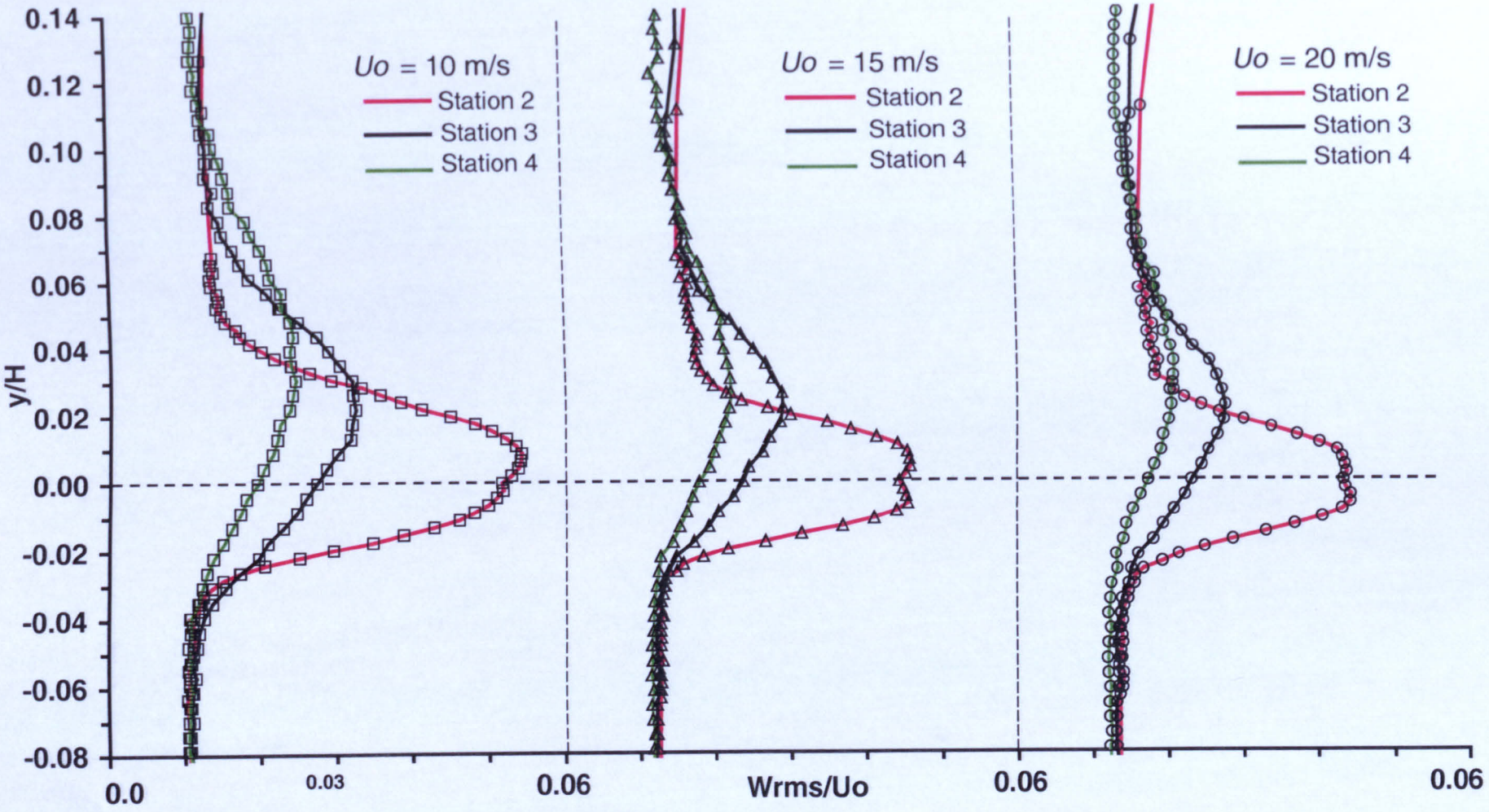

(Original in colour)

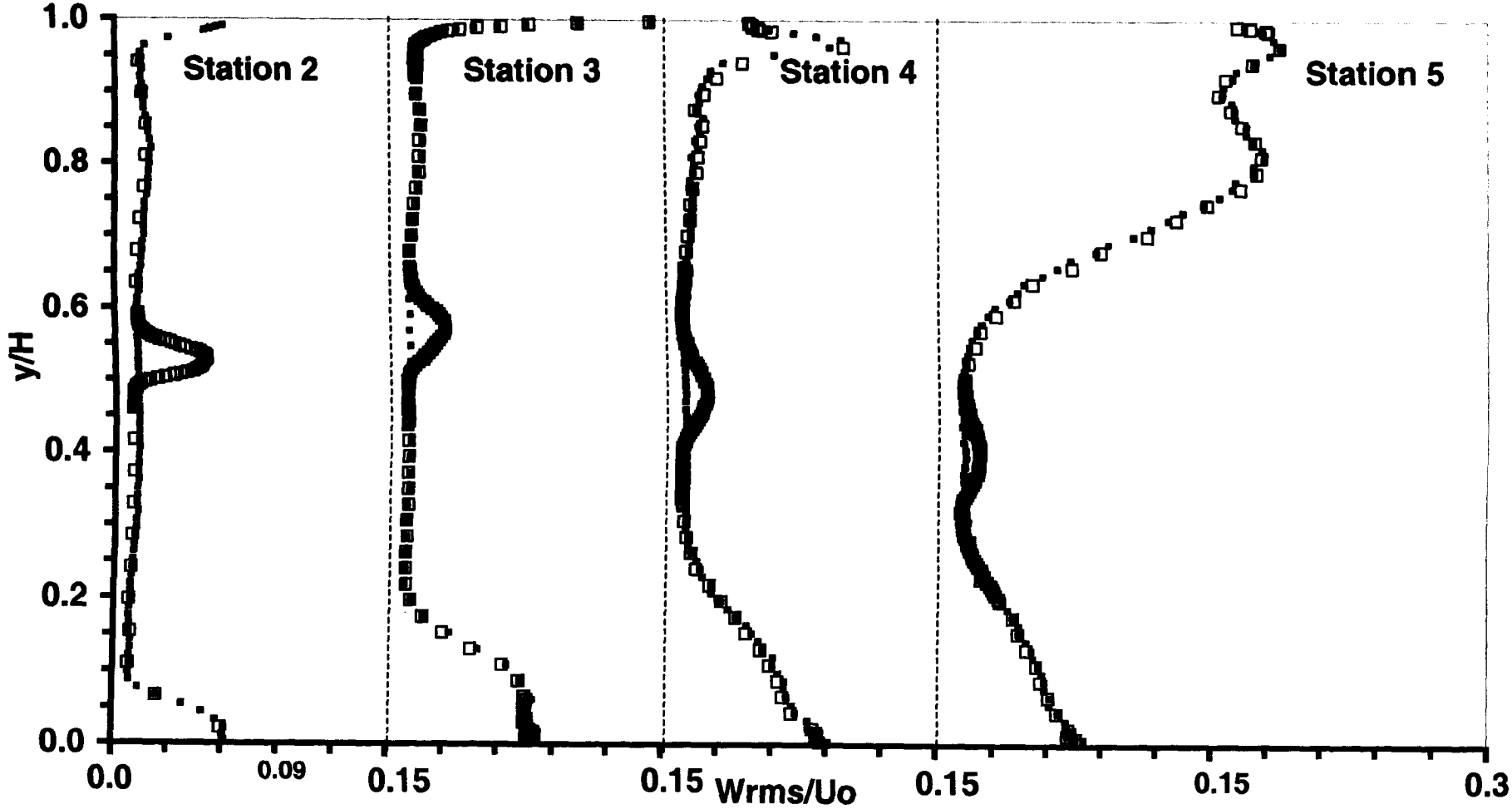

Figure 6.22: Profiles of spanwise turbulence intensity in the normal direction: (a) wake at station 2; (b) wake at station 3; (c) wake at station 4; (d) wake at station 5; (e) comparison of profiles in the wake at stations 2 to 4; (f) profiles obtained across the whole cross-section at stations 2 to 5. For definition of symbols see Figure 6.18.

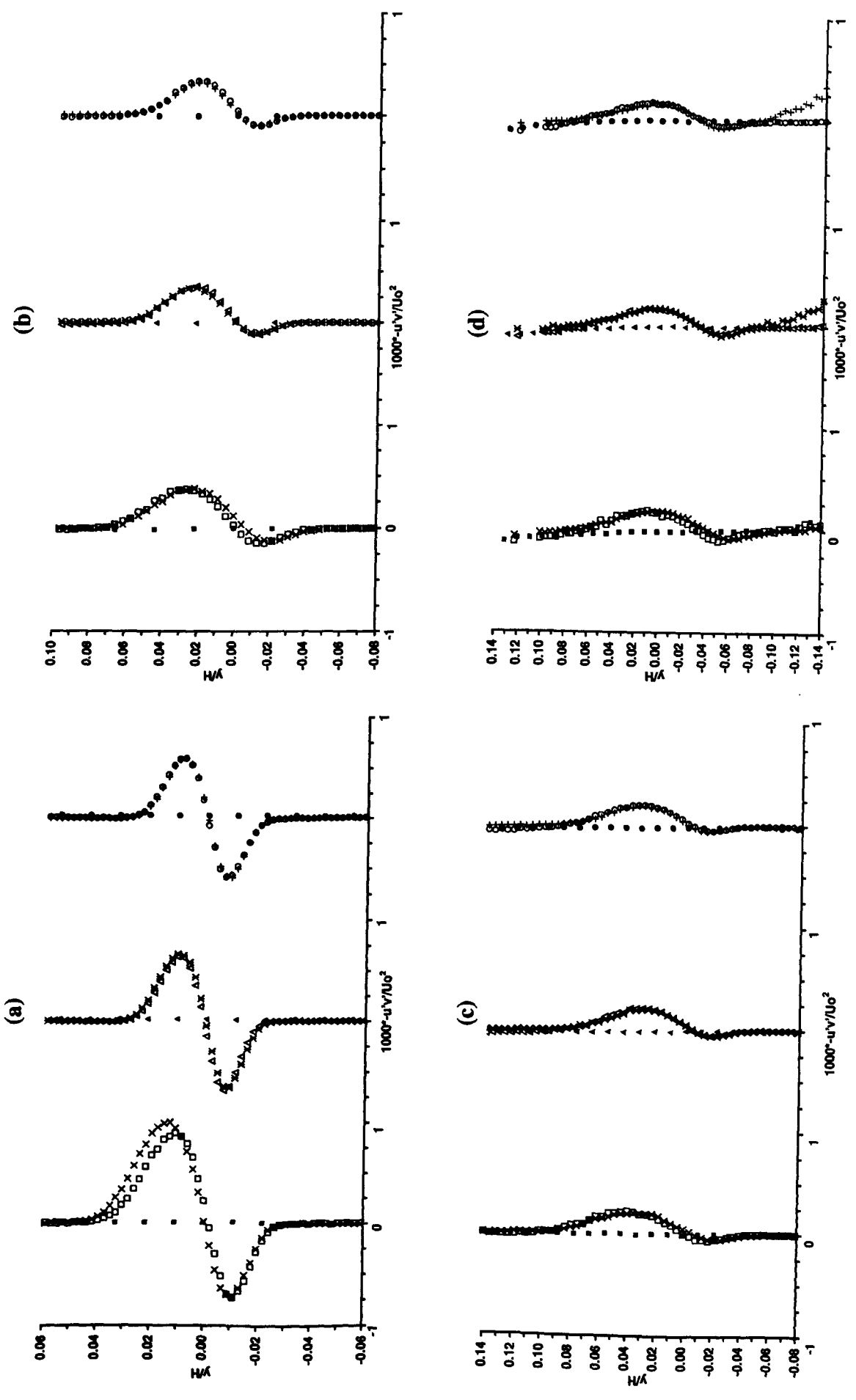
(a)
(b)
(c)
(d)
y/H
1000*-u'v'/Uo²

(e)

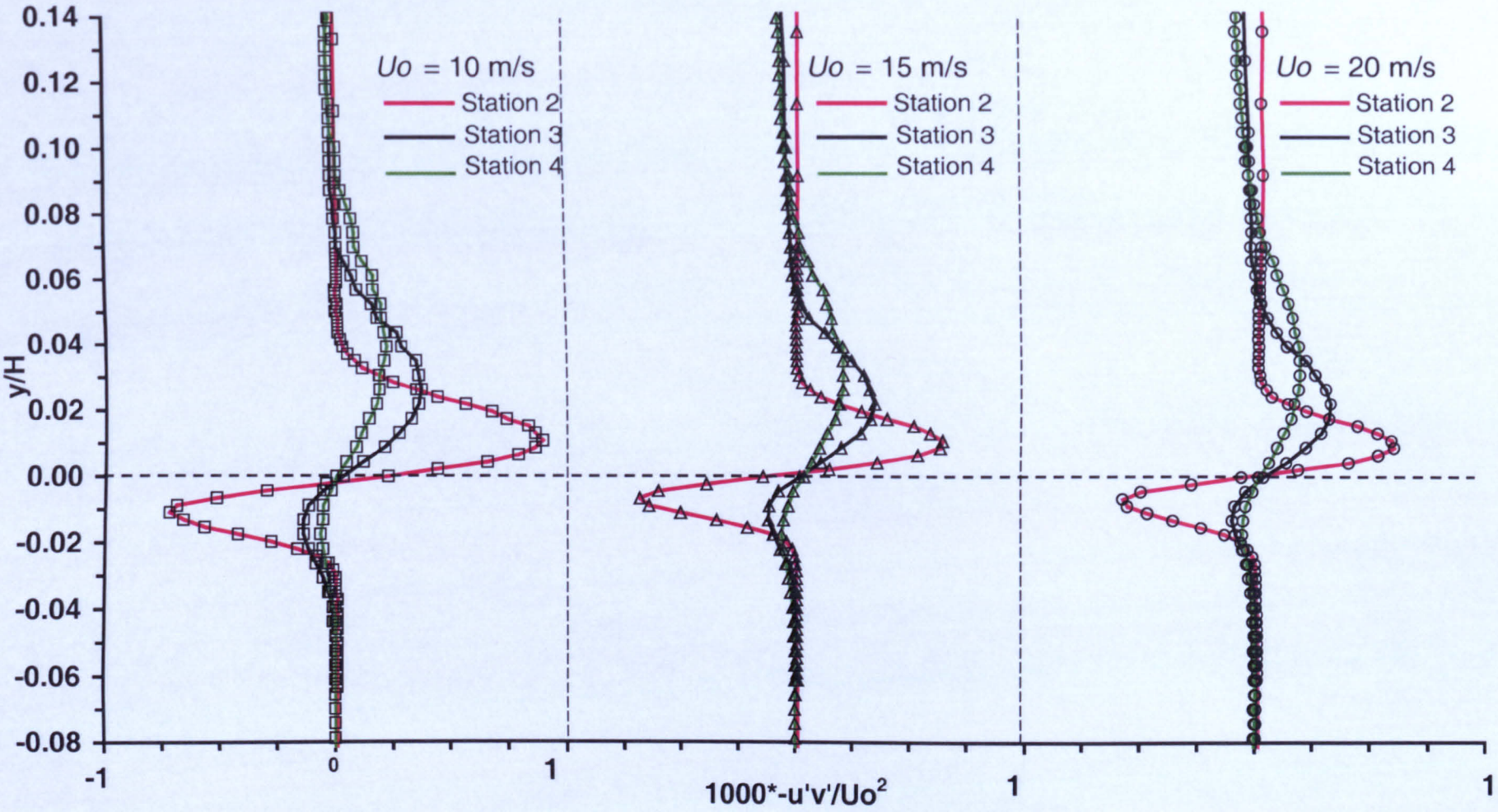

(Original in colour)

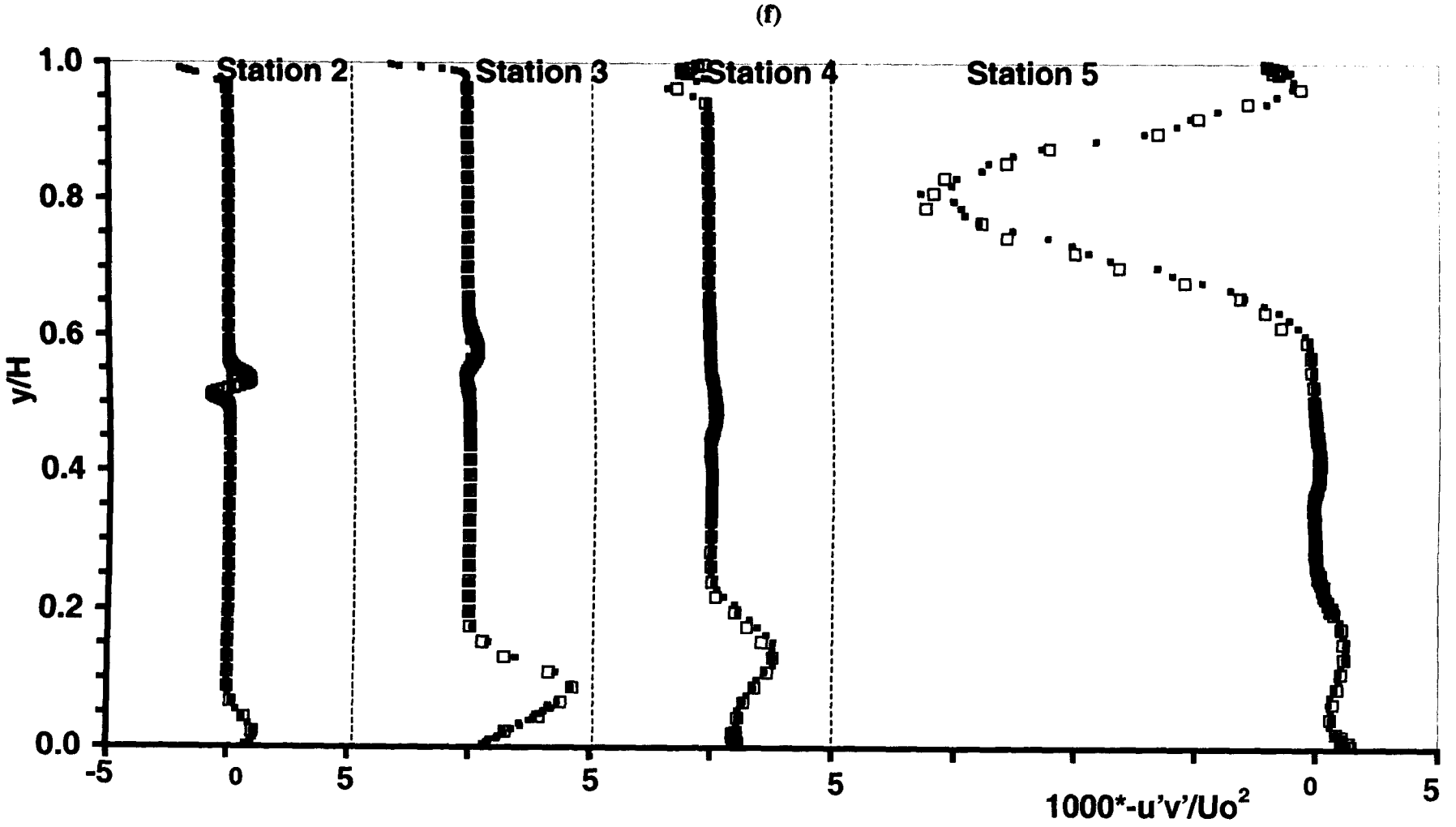

Figure 6.23: Profiles of turbulence shear stress $(-\overline{u'v'})$ in the normal direction: (a) wake at station 2; (b) wake at station 3; (c) wake at station 4; (d) wake at station 5; (e) comparison of profiles in the wake at stations 2 to 4; (f) profiles obtained across the whole cross-section at stations 2 to 5. For definition of symbols see Figure 6.18.

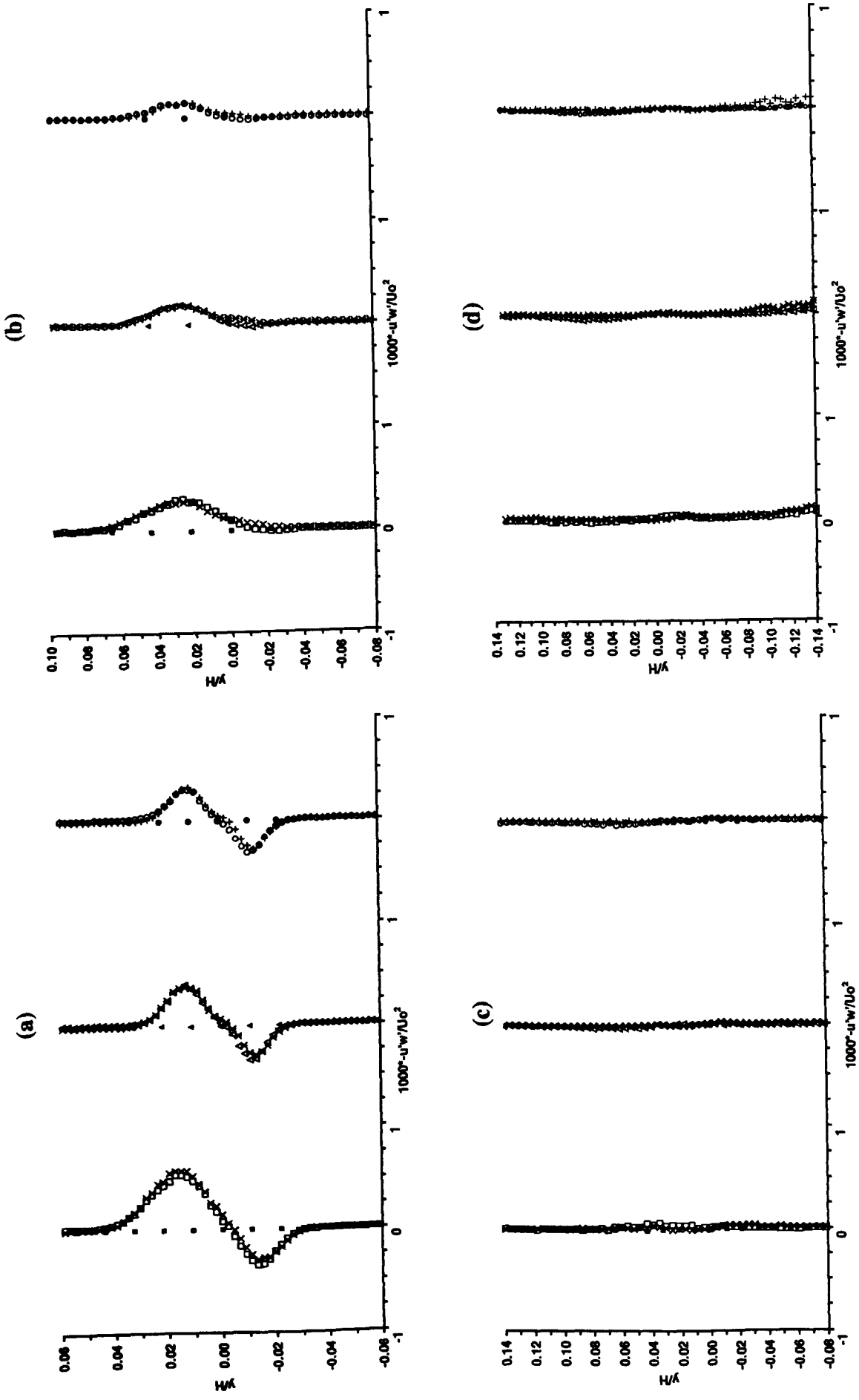
(a)
(b)
(c)
(d)
y/H
1000*-u'w'/Uo²

(e)

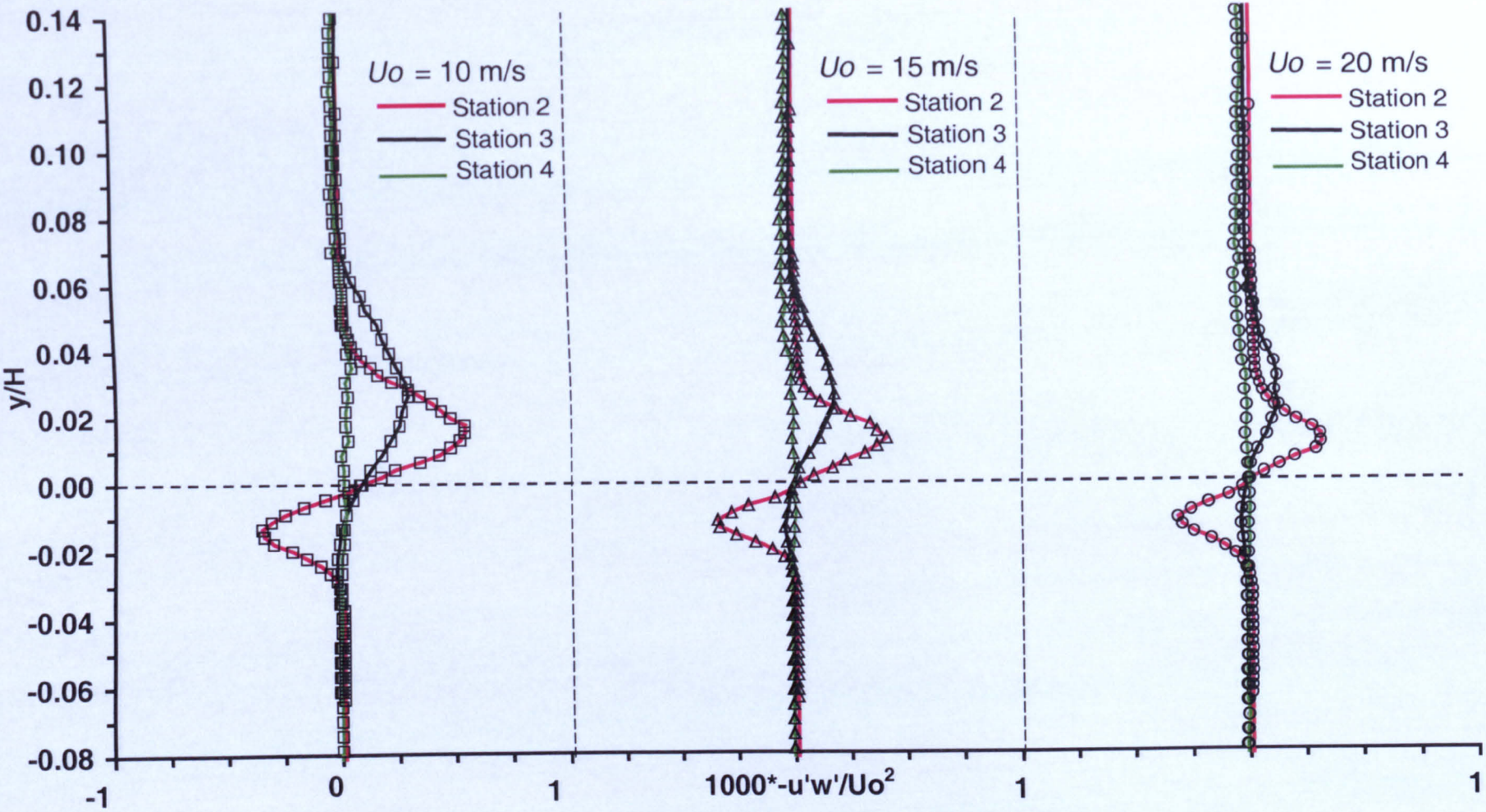

(Original in colour)

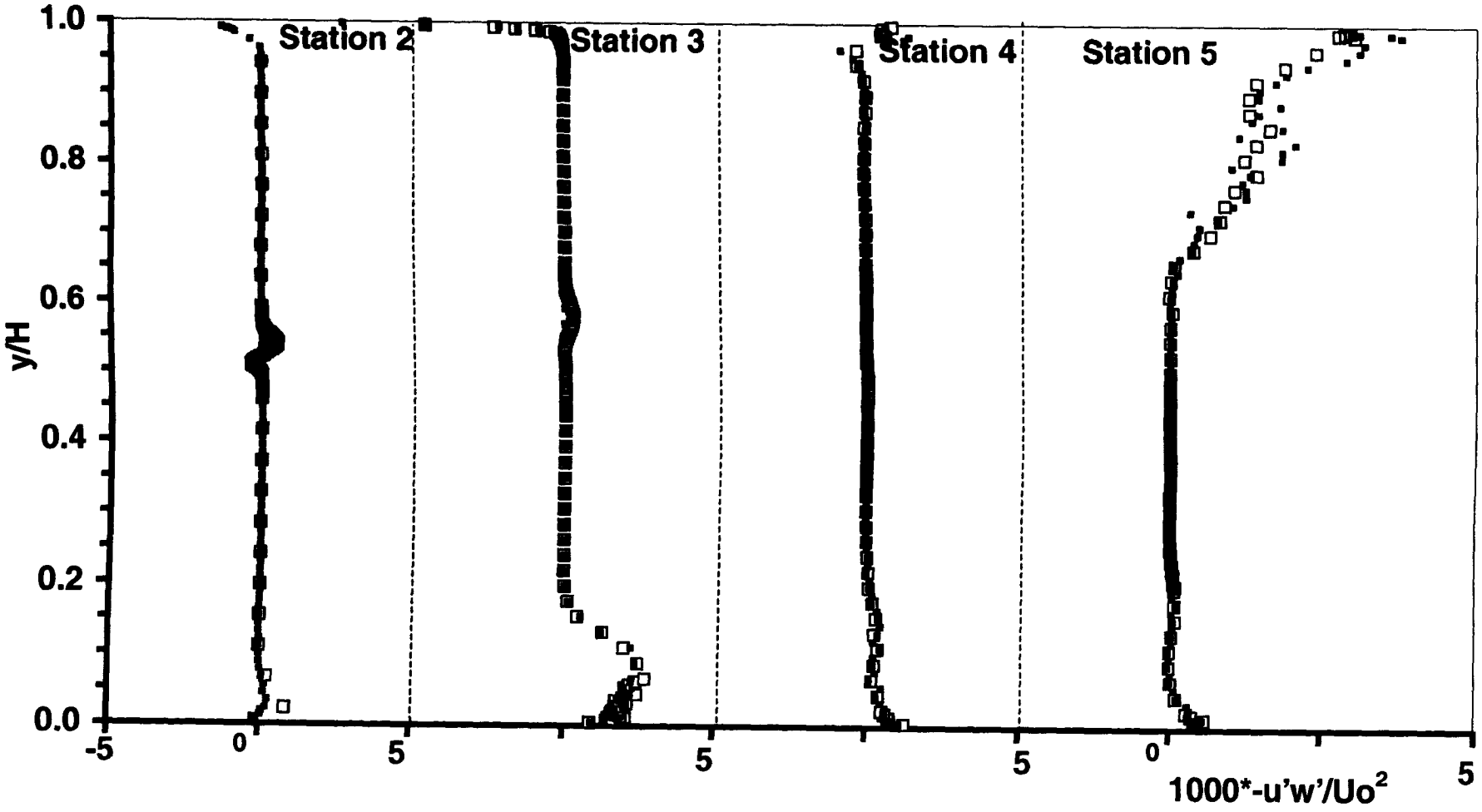

Figure 6.24: Profiles of turbulence shear stress $(-\overline{u'w'})$ in the normal direction: (a) wake at station 2; (b) wake at station 3; (c) wake at station 4; (d) wake at station 5; (e) comparison of profiles in the wake at stations 2 to 4; (f) profiles obtained across the whole cross-section at stations 2 to 5. For definition of symbols see Figure 6.18.

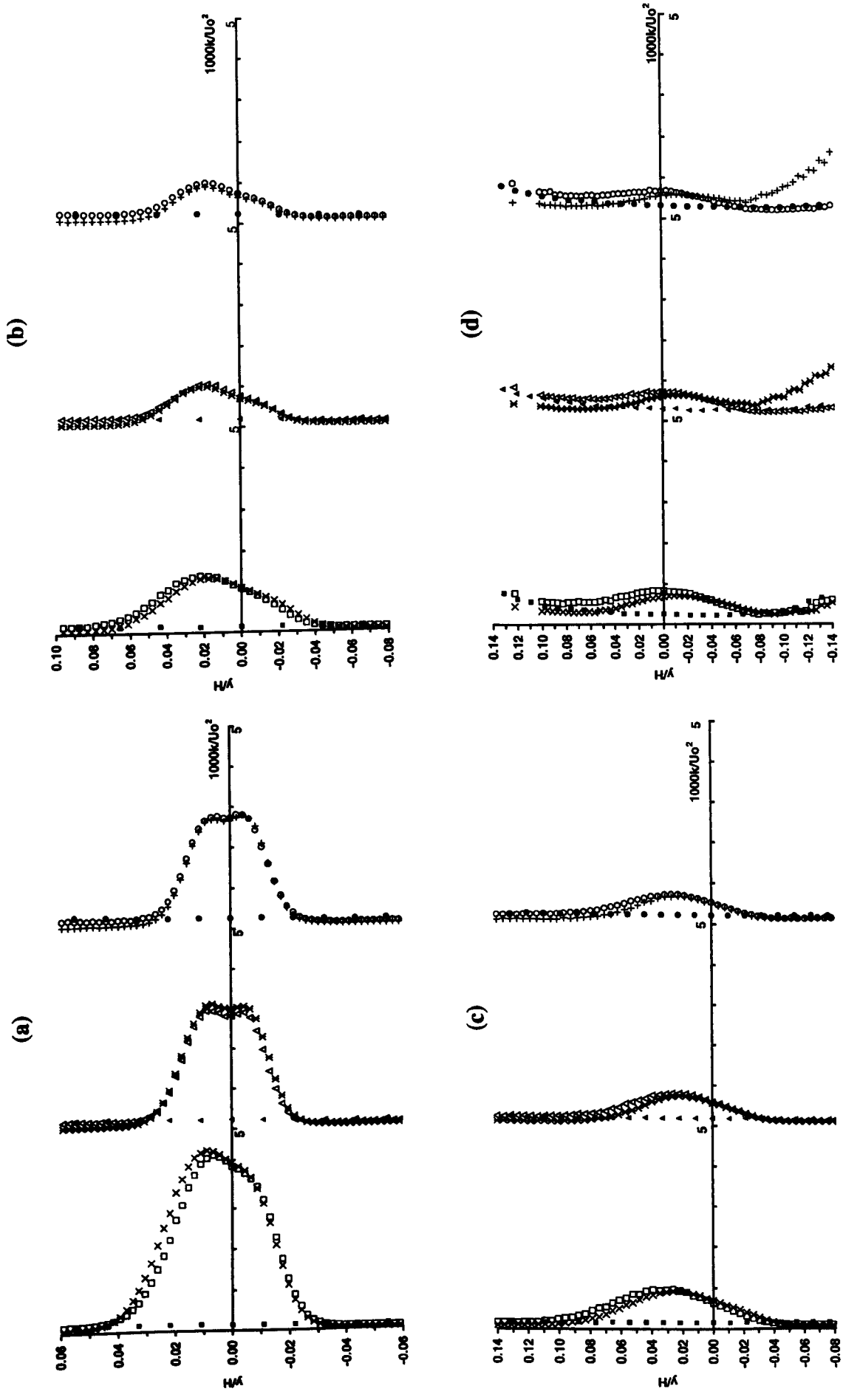
(a)
(b)
(c)
(d)
1000k/Uo²
y/H

(e)

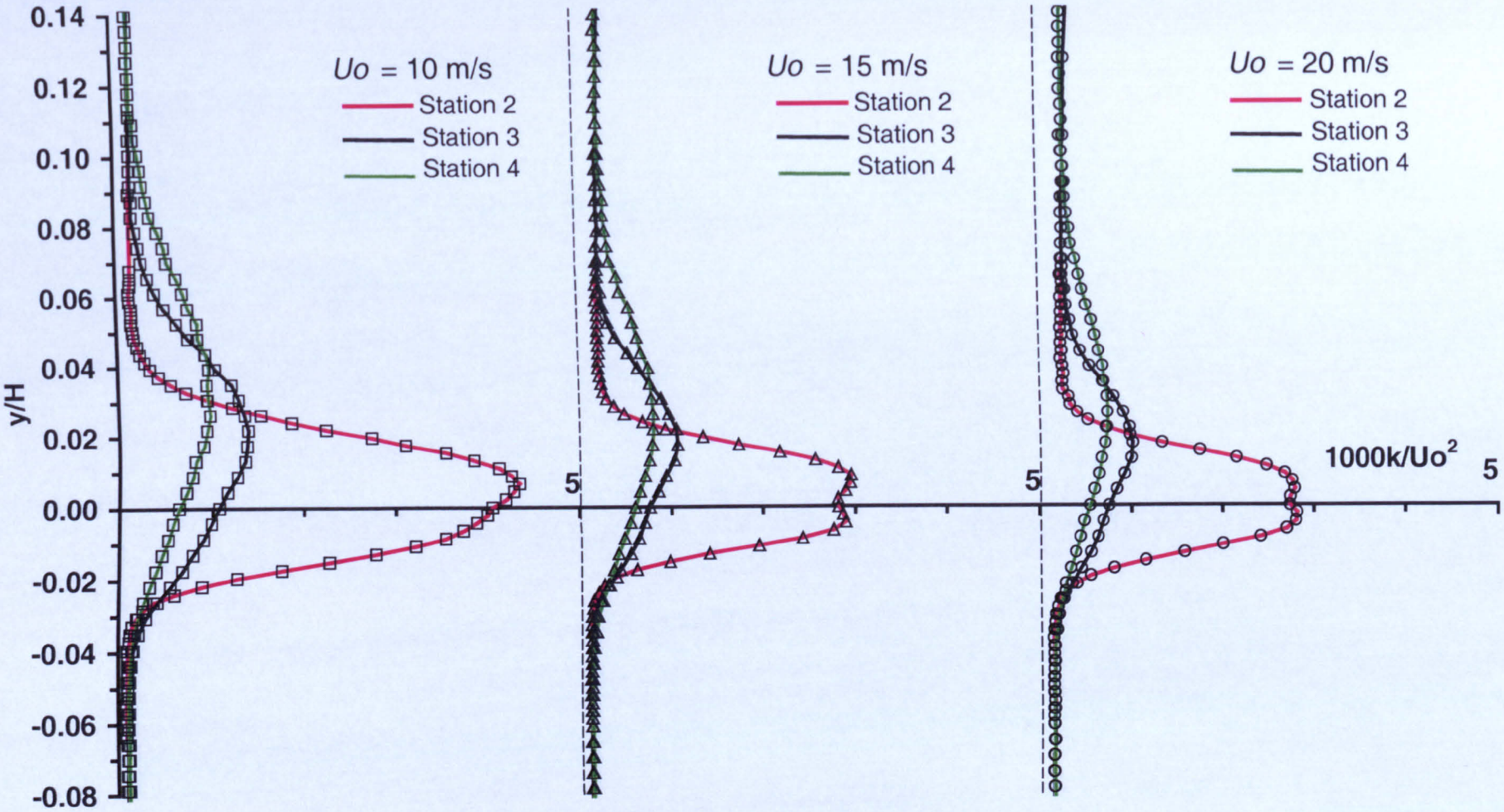

(Original in colour)

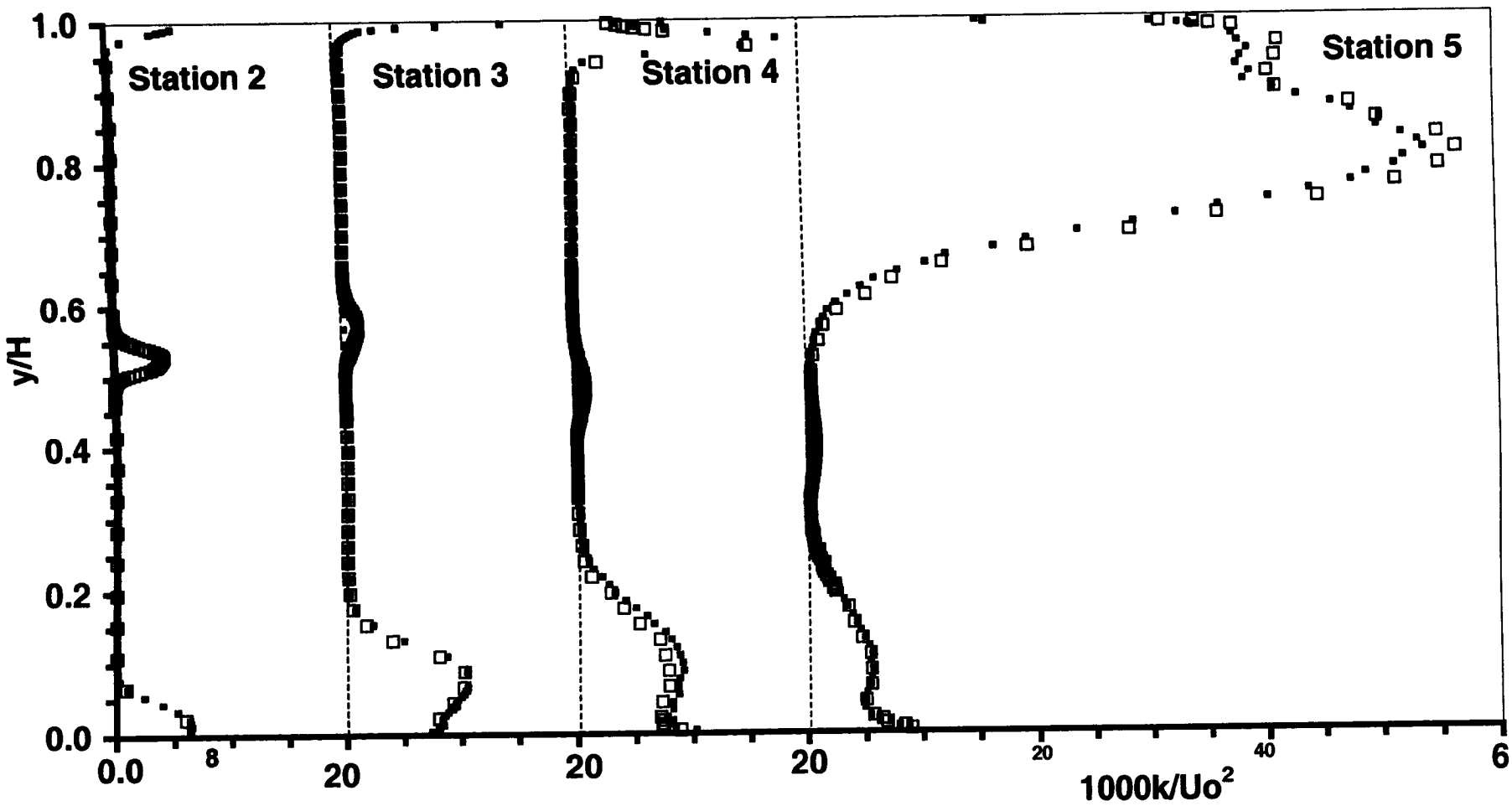

Figure 6.25: Profiles of turbulence kinetic energy in the normal direction: (a) wake at station 2; (b) wake at station 3; (c) wake at station 4; (d) wake at station 5; (e) comparison of profiles in the wake at stations 2 to 4; (f) profiles obtained across the whole cross-section at stations 2 to 5. For definition of symbols see Figure 6.18.

Chapter 7

7. NUMERICAL RESULTS AND COMPARISON WITH EXPERIMENT

7.1. Introduction

This Chapter describes the results of numerical investigation in the wake of an airfoil (NACA 0012). There are three main objectives in the analysis of this investigation. Firstly, to compare the computational predictions with the experimental results, which would indicate whether the mathematical models could accurately predict the experimental trends. Secondly, to obtain qualitative and quantitative information of the flow field within the flow domain, particularly in the curved wake region. Finally, to gain better understanding of the performances of discretisation schemes and near wall modelling. The simulations were performed using the CFD code FLUENT 5 and four turbulence models, namely, Reynolds Stress Model, standard k-ε model, Realizable k-ε model and RNG k-ε model. The code was executed on a Sun® UltraSparc® workstation running Solaris® 7 environment. In the following sections, the results of static pressure, mean and turbulence quantities obtained in the x-y and y-z planes of the flow domain are described in details.

7.2. Presentation of numerical results

The numerical results are presented in three forms, namely, distribution profiles, contour plots and vector plots. The distribution profiles (Figures 7.1 to 7.8) obtained at the symmetry plane (z/H = 0.5) are divided into the static pressure, mean velocity, wake parameters, turbulence intensities and the turbulence kinetic energy. The numerical results obtained in the present investigation could not be compared with other previous studies on curved wake of an airfoil due to the differences in geometrical dimensions and boundary conditions implemented. Therefore, the experimental results of the present investigation are extensively used to validate the numerical results. In order to compare directly with the experimental results, the numerical distribution profiles of mean

streamwise velocity component and turbulence intensities obtained at stations 2 to 5 are normalized with respect to the mainstream velocity U_0 at the inlet (station 1). Also, the turbulence shear stress $-\overline{u'v'}$ and the turbulence kinetic energy k are normalized using ${U_0}^2$. However, this comparison only revealed the overall differences, particularly the computed shift of the wake region. But, the computed shift was not consistent with the corresponding experimental shift at each station, which caused additional difficulties for direct comparison.

Hence, in order to compare the computed mean and turbulence quantities in the wake region with the experimental results, the method employed earlier in experimental investigation is chosen again, where the streamwise distance is defined as distance from the trailing edge of the airfoil along the line that connects the wake centre at each downstream station. The normal distance is measured perpendicular to this reference line (i.e. at the wake centre y = 0). The potential velocity U_p, which is the velocity value in the absence of the airfoil at the wake centreline, is used for normalization instead of the mainstream velocity U_0. The presented distribution profiles of this form at each station, particularly at stations 2 to 4, therefore, highlight the differing performances of turbulence models across the wake region in the x-y plane while contour plots reveal the overall flow phenomena within the flow domain.

For each measuring station, the profiles obtained from different turbulence models simulations are displayed together and compared with their corresponding experimental profiles. Also, the profiles in the wake region at each measuring station is enlarged and presented individually to distinguish their local variations. Both numerical and experimental profiles obtained across the whole cross-section at stations 2 to 5 are included in this investigation to show the flow characteristics and their general agreements with each other. The influence of the discretisation schemes on the mean and turbulence quantities are also presented in the form of distribution profiles, which can be found in Appendix VI.

The contour and vector plots presented here are obtained from simulations with the Reynolds Stress Model (RSM). Due to the fixed coordinate system used by the FLUENT

5 post-processor, the vector quantities, such as velocity components (except spanwise velocity component) and their fluctuations could not be plotted in the x-y plane of the bend section, where the flow direction changes from 0° to 90°. As an example, the streamwise velocity component at station 4 (exit of the bend) becomes the normal velocity component, and vice versa when using a fixed coordinate system throughout the flow domain. Therefore, the quantities which do not depend on the direction, such as velocity magnitude, static pressure and turbulence kinetic energy are the only quantities plotted as contour plots (z/H = 0.5) in the x-y plane. However, the problem associated with the fixed coordinate system in the y-z plane, particularly at station 3, was resolved by applying a so-called coordinate transformation technique (see Appendix IV), where the parameters are rotated in the anticlockwise direction (e.g. 45° at station 3) into the streamwise and normal directions.

The variations of velocity magnitude, static pressure and turbulence kinetic energy in the x-y plane and y-z plane (stations 2 to 5) are presented in Figures 7.9 to 7.14. Finally, the vector plots obtained in the y-z plane at stations 2 to 5 are presented in Figure 7.15, which would evaluate the effects of wake development on secondary motion in the bend.

7.2.1. Distribution profiles

The static pressure distribution on the concave and convex walls of the flow domain is presented Figure 7.1. The variations of streamwise velocity component is shown in Figure 7.2, while the variations of wake half-width and maximum velocity defect for the mainstream velocities of 10 and 20 m/s are shown in Figure 7.3. The turbulence intensities and the turbulence shear stress $-\overline{u'v'}$ are given in Figures 7.4 to 7.7. Finally, the distribution profiles of turbulence kinetic energy k are presented in Figure 7.8. The following sections describe each of these quantities in detail.

7.2.1.1. Static pressure

Two types of investigations were conducted on the concave and convex walls static pressure distribution to gain an understanding of the performance of both discretisation schemes and turbulence models. In the first analysis, the pressure coefficient profiles were obtained from simulations conducted in the absence of the airfoil using

Reynolds Stress Model and discretisation schemes QUICK and upwind. The second analysis was conducted in the presence of the airfoil using the discretisation scheme QUICK and all four turbulence models. Both results are compared with their corresponding experimental results in Figure 7.1 (a-b). There is a general agreement between predicted and experimental results, where the profiles show an adverse (positive) pressure gradient followed by a favourable (negative) pressure gradient on the concave wall of the bend and vice versa on the convex wall. The comparison of the static pressure distribution profiles obtained using different discretisation schemes (see also Appendix VI) with the experimental results in Figure 7.1 (a) shows good agreement, particularly on the concave wall. However, as expected on the convex wall, the higher order scheme QUICK shows some improvement within the bend (between stations 3 to 4) and beyond x/H = 3.5 in the downstream tangent.

Despite these improvements, large differences can be seen on the convex wall, particularly in the region between stations 4 and 5 (x/H = 2 to 3). Furthermore, in this region, particularly at station 4, the flow is close to separation but in the mean it remained attached as reported by previous flow visualisation studies by Ondore (1999). The frequent separation from the wall and subsequent reattachment before station 5 has also been reported, which is believed to be causing the abrupt change in the profile of the static pressure on the convex wall. The pressure distribution profiles obtained using different turbulence models in Figure 7.1 (b) collapse and agree closely with the experiment, particularly in the upstream tangent and the bend section. But, as seen in the first analysis, the larger discrepancies in the downstream tangent of the bend indicate that none on the turbulence models employed in the present investigation could predict the flow separation and reattachment feature. Also, the comparison (not presented here) between the predicted static pressure values in the presence and absence of the airfoil (Figure 7.1 (a) and (b)) indicates slightly larger values on the concave wall of the upstream tangent, when the airfoil is present. The increase in the reference static pressure value, which was also noted in the experimental results, led the concave and convex pressure coefficient profiles obtained in the presence of the airfoil to collapse at x/H = 4.2, whereas the profiles obtained in the absence of the airfoil did not. The presented pressure coefficient results of all four turbulence models indicate that the total static pressure drop (irrecoverable) along the concave and convex walls is smaller than their

corresponding experimental ones. Furthermore, the higher static pressure drop in the experimental results could be attributed to additional pressure losses due to wall friction and turbulence not presented adequately in the numerical model.

7.2.1.2. Mean velocity

The profiles of computed streamwise velocity component in the wake region at stations 2 to 5 are presented in Figure 7.2 (a-d), whereas their variations across the whole cross-section are shown on a separate graph in Figure 7.2 (e). In the wake region at station 2, the profiles of all four turbulence models agree closely with each other, however, at stations 3 to 5 significant differences can be seen, particularly between the k-ε based models and RSM, which indicate the different responses of the turbulence models due to the effects of curvature and pressure gradient. In this Figure, the comparison between experimental and computed profiles at each station indicates that the peak value and both sides of the wake region are over-predicted by all turbulence models. Furthermore, it is noted that the RSM over-predicts the peak of the wake region more at each station, particularly at stations 3 to 5 than the k-ε based models. Although the profiles of all turbulence models show greater peak values in the wake region, the general pattern of these profiles is similar to their corresponding experimental profiles at each station, particularly at stations 2 to 4, which also indicates asymmetric wake structure with respect to the wake centre. The computed shift of the wake region with respect to the concave wall of the duct is also over-predicted at each station by all turbulence models. Furthermore, at stations 2 and 3, the wake centre is shifted from the duct centreline towards the convex side by 16 mm and 35 mm, respectively, whereas it is reduced to 4 mm at station 4. Furthermore, at station 5, the wake centre is shifted towards the concave wall by 25 mm. Despite larger shift of the wake region at each station, the direction of the shift is consistent with their corresponding experimental ones.

The profiles obtained across the whole cross-section (Figure 7.2 e) at stations 2 to 4 show good agreement with the experimental results, where the flow accelerates on the convex side and decelerates on the concave side. However, as also reported by Ondore (1999), the experimental and computed profiles at station 5 show different flow patterns across the duct, where the flow is subjected to the recovery from the bend effects. Also, the

comparison between the experimental and computed profiles at this station indicates that the turbulence models employed in the present investigation could not predict the experimental trend correctly.

7.2.1.3. Wake parameters

The experimental and numerical values of the wake half-width and maximum velocity defect (W_0) for the mainstream velocities of 10 and 20 m/s are presented in Figure 7.3 (a-b). As calculated in the experimental work, the half-width of the wake was taken as the normal distance between the wake centreline and a point at which the wake defect equals half of its maximum value. But, in this Figure, the presented value of the half-width b'_{total} is the combined thickness of the inner side and outer side half-widths of the wake region. As seen earlier in the streamwise velocity profiles, the half-width values of all computed profiles show close agreement with each other at station 2, but differ significantly at stations 3 and 4. Also, as the streamwise distance from the airfoil increases the half-width increases due to wake spreading. A comparison (not presented here) between the half-widths of the inner side and outer side of the wake region indicated that the inner half-width is always larger than its corresponding outer side half-width at these stations. Despite showing features of the experimental results, the presented half-width values at stations 2 to 4 are over-predicted by all turbulence models. Furthermore, compared with the standard and Realizable k-ε models, the RSM and RNG k-ε model indicate some improvement at stations 3 and 4. The turbulence models also over-predict the maximum velocity defect value (Figure 7.3 b) at stations 2 to 4. But, the k-ε based models, particularly the Realizable and RNG k-ε models seem to be predicting the maximum velocity defect more closely than the RSM. However, the general patterns predicted by all turbulence models are similar to the corresponding experimental one.

7.2.1.4. Reynolds stresses

The numerical streamwise intensity profiles obtained at stations 2 to 5 are compared with their corresponding experimental profiles in Figure 7.4 (a-e). The predicted profile at station 2 (Figure 7.4 a) shows a large single peak value compared with double peaks seen in the experimental profile. However, the computed profile shows a tendency to predict

the double peak but just misses the smaller peak of the experimental profile, thus the peak is located on the same side (inner side) of the wake region as the dominant peak of the experimental profile. At this station, the predicted trend of the inner side wake region is in close agreement with the experimental profile, whereas larger discrepancies can be seen on the outer side of the wake region. At stations 3 and 4, the predicted peak is also located on the inner side of the wake region, but the comparison between predicted and experimental profiles show significant differences on both sides of the wake region. However, as seen earlier in the experimental results, the peak shifts further away from the wake centreline and flattens as the streamwise distance increases between stations 2 to 4, which makes the wake structure more and more asymmetric about the wake centreline. The predicted results at stations 2 to 4 indicate that the streamwise intensity value at the wake centreline at station 2 is reduced by 57% and 13% at stations 3 and 4, respectively. Compared with station 4, there is further reduction in the predicted streamwise intensity values in the wake region at station 5. At this station, the predicted and experimental profiles, particularly in the wake region show completely different patterns, where the computed values and the wake width are smaller compared with the corresponding experimental values and wake width.

The streamwise intensity profiles obtained across the whole cross-section in Figure 7.4 (e) show very good agreement with the experimental results, particularly in the central core region at stations 2 to 4. However, significantly larger discrepancies can be noticed in the near wall region due to the differences in the development of the boundary layers on the walls of the duct. Furthermore, it can be seen on the concave wall that the experimental boundary layer is significantly larger than the corresponding predicted boundary layer. Despite these variations in the near wall region, the computed profiles at these stations show the distinguishing feature of a wide bulge structure on the concave wall region. At station 5, the experimental and predicted profiles show a greater divergence between them, particularly on the convex wall and central core region, where the experimental values are well above the computed values.

The profiles of normal and spanwise intensities are presented in Figure 7.5 (a-e) and Figure 7.6 (a-e), respectively. At station 2, both computed intensities show similar magnitudes for the single peak located at the centre of the wake region. Furthermore, at

this station, the RSM over-predicts the spanwise intensity peak value while under-predicts the normal intensity peak value. At stations 3 and 4, the peaks of both intensities are shifted to the inner side of the wake region, where the values are generally lower than their respective experimental peak values. As seen earlier in the computed streamwise intensity profile at station 2, the predicted trends of both intensities on the inner side wake region correlate closely with the experimental profiles, whereas some discrepancies occurred on the outer side of the wake region. In contrast, at stations 3 and 4, larger discrepancies can be seen on the inner side of the wake region, whereas the outer side of the wake region agrees closely with the experimental results. However, the general pattern of both computed intensities at these stations is similar to their corresponding experimental profiles. As noted in the experimental profiles at stations 2 to 3, both computed intensity values at the wake centreline at station 2 are reduced by 50% at station 3 and further small reduction has occurred at stations 4 and 5. As seen earlier in the computed streamwise intensity profiles, both normal and spanwise intensity profiles obtained across the whole cross-section show very good agreement with the experimental results in the central core region at stations 2 to 4, whereas significant discrepancies can be noticed in the near wall region. Also, at station 5, both experimental intensity values on the convex wall are well above the computed values.

The computed profiles of turbulence shear stress $-\overline{u'v'}$ at stations 2 to 5 are presented in Figure 7.7 (a-e). The predicted profile at station 2 shows positive and negative peaks on the inner and outer sides of the wake region, respectively, as occurred in the experimental profile. Furthermore, the predicted peak value on the inner side is slightly greater than its corresponding peak value on the outer side of the wake region, which indicates an asymmetric structure about the wake centreline. Also, the comparison between experimental and predicted profiles in the wake region indicates that the RSM slightly under-predicts the inner side peak value, whereas predicted closely the outer side peak value. However, the predicted peak position on the outer wake side is shifted by 3.5 mm further towards the concave wall, while correctly predicted on the inner side of the wake region. Despite these small differences, the zero value of both computed and measured shear stresses occurs at the centre of the wake region, where the velocity gradient is zero. As was noted earlier in the intensity profiles at station 2, the predicted trend on the inner wake region correlates closely with the experimental profile, whereas some discrepancies

can be seen on the outer side of the wake region. At stations 3 and 4, larger discrepancies can be seen on both sides, particularly on the outer side of the wake region. At these stations, the predicted profiles show a single peak on the inner side of the wake region, whereas the experimental profiles indicate a double peak. However, it can be seen that the peak on the outer side of the wake region in the experimental profile is much smaller compared with its corresponding peak on the inner side of the wake region. The results, therefore, indicate greater effects of streamwise curvature and pressure gradient on the outer side of the wake region. The computed peak value and its position at station 3 agree closely with its corresponding experimental peak value and position, but the peak is slightly under-predicted at station 4. The predicted and experimental profiles show completely different patterns at station 5. But, at this station, the appearance of a small peak on the outer side of the predicted wake region could be due to the removal of the streamwise curvature and pressure gradient.

The profiles obtained across the whole cross-section (Figure 7.7 e) show that the computed values of the turbulence shear stress $-\overline{u'v'}$ at stations 2 to 4 are in good agreement with those obtained from measurements. At these stations, the computed and measured profiles in the central core region coincide over the major portion of the test section and show small values. However, the computed non-zero values in the near wall region, particularly on the concave wall show larger discrepancies with the experimental results. Due to the change of sign at the centre of the duct, both computed and measured turbulence shear stress values at stations 2 to 5 take positive and negative signs in the boundary layer regions of concave and convex walls, respectively. At station 5, although the general patterns of the predicted and experimental profiles are similar, large differences in magnitudes can be seen. The computed turbulence shear stress profile shows a small trough (negative peak) in the convex wall boundary layer region due to the boundary layer development on the downstream tangent following the exit from the bend. On the other hand, the large trough in the experimental profile may be attributed to the general nature of the flow in this region as was referred to above.

7.2.1.5. Turbulence kinetic energy (k)

The profiles of predicted turbulence kinetic energy (k) of all four turbulence models are

presented together with the experimental profiles in Figure 7.8 (a-e). The comparison between predicted and experimental results in the wake region at station 2 (Figure 7.8 a) indicates that the peaks are over-predicted by all turbulence models. Furthermore, the predicted peak by the Realizable k-ε model is the largest peak and located at the centre of the wake region, whereas, the RSM, standard and RNG k-ε models peaks are located on the inner side of the wake region as the experimental peak. However, compared with the standard k-ε model, the inner and outer sides of the wake region are predicted closely by the Realizable k-ε model. At this station the predicted profile by RSM coincides with the experimental profile over the major portion of the inner side wake region and also show some improvement on the outer side of the wake region, whereas large discrepancies can be observed in the k-ε based model profiles. At stations 3 and 4, all the predicted peaks are located on the inner side of the wake region, where the RSM under-predicts the peak value while k-ε based models over-predict it. At these stations, the RSM and RNG k-ε model correlate closely with the experimental results, particularly on the outer side of the wake region compared with the standard and Realizable k-ε models, which show larger discrepancies on both sides of the wake region.

The turbulence kinetic energy profiles obtained across the whole cross-section (Figure 7.8 e) show that the prediction of all four turbulence models agree closely with each other at station 2 and coincide in the central core region with those obtained from measurement. But, at stations 3 and 4, particularly in the region between the wake region and the convex wall, the standard k-ε model profiles show significant differences with measurements. Furthermore, these differences indicate that the standard k-ε model, which is based on the constant eddy-viscosity hypothesis, is incapable of predicting complex flows. However, the comparison between k-ε based models results indicate that the additional terms and functions in the transport equations of turbulence kinetic energy (k) and its dissipation rate (ε) of RNG k-ε models and Realizable k-ε models (see Chapter 4) are significantly improving the prediction of complex flows. At station 5, on the convex side, the large disparity between experimental and computed profiles indicates that the turbulence models employed in the present investigation are incapable of predicting separated flow in the present flow configuration.

7.2.2. Contour plots

The contour plots of static pressure, velocity magnitude and turbulence kinetic energy obtained in the x-y and y-z planes will be discussed in the following sections.

7.2.2.1. Static pressure

Figures 7.9 and 7.10 show the static pressure distribution in the x-y and y-z planes of the flow domain, respectively. As seen earlier in the experimental radial static pressure profiles at each station (Figure 6.6), the static pressure contour plot in the x-y plane indicates that the concave and convex sides of the bend are subjected to positive and negative pressure gradients, respectively. However, majority of the static pressure field in the upstream and downstream tangents are unaffected by the presence of the bend section. In Figure 7.9, the contour plot obtained in the absence of the airfoil shows similar pattern and magnitude as those obtained with the airfoil, therefore, the effects of the airfoil on the static pressure distribution in the duct can be considered to be small. On the other hand, the effect of bend on the static pressure distribution on the airfoil is apparent in this Figure. A comparison (not presented here) with similar static pressure contour plot obtained by omitting the small normal velocity component in the inlet boundary conditions indicated that the lift on the airfoil and the appearance of the stagnation point on the lower surface of the leading edge are due to the bend effects.

The presented static pressure contour plots in Figure 7.10 indicate insignificant variations in the spanwise direction at each station, thus demonstrating a high degree of two-dimensionality. Also, the static pressure distribution in the presence and absence of the airfoil shows very similar patterns at each station, hence the effects of the airfoil on the static pressure distribution in the spanwise direction can also be considered to be small. As noted in the experimental radial static pressure profiles, the contour plots show that the region subjected to positive static pressure (concave side) is significantly greater than the region affected by the negative static pressure (convex side). Also, the closely spaced constant static pressure lines (isobars) on the convex side of the bend section, particularly at stations 2 to 4 indicate sharp static pressure drop in the radial direction compared with the corresponding concave side.

7.2.2.2. Velocity magnitude

The distributions of velocity magnitude in the x-y and y-z planes of the flow domain are presented in Figure 7.11 and Figure 7.12, respectively. In Figure 7.11, despite fairly uniform inlet boundary conditions used, the velocity magnitude on the convex side of the upstream tangent is slightly higher than its corresponding concave side, which could be due to the effect of the bend. Also, in this region the boundary layer growth on the concave wall is greater than its corresponding one on the convex wall. As noted in the static pressure contour plots, the enlarged airfoil section in this Figure shows the stagnation point on the lower surface of the airfoil, but, the flow is fully attached and no separation at the trailing edge has occurred. In the bend section, on the convex side, the flow accelerates in the near wall region between stations 2 and 3 and decelerates between stations 3 and 4, which reflect the presence of favourable and adverse pressure gradients as noted in the static pressure contour plots. A distinguishing feature on the concave wall of this region is the development of a thicker boundary layer compared with its corresponding one on the convex wall. In the downstream tangent, where the flow undergoes recovery from the bend effects, the boundary layer on convex wall grows more rapidly than its corresponding one develops on the concave wall. However, majority of the flow region in the downstream tangent is unaffected by these developing boundary layers. The comparison between the velocity magnitude contour plots obtained in the presence and absence of the airfoil indicates insignificant variations in both upstream tangent and the bend section. But, in the downstream tangent, the presence of the airfoil has suppressed the boundary layer growth on the convex surface.

In Figure 7.12, the spanwise variations of velocity magnitude in the presence and absence of the airfoil show similar uniform patterns at stations 2 and 3, but, at stations 4 and 5, significant variations, particularly on the convex side occurred due to the recovery from the bend effects. It is noted that the boundary layers developing on the sidewalls at each station are suppressed by the presence of the airfoil. Despite these variations, the contour plots obtained in the y-z plane at each station indicate symmetrical pattern about the central plane ($z/H = 0.5$) of the flow domain.

7.2.2.3. Turbulence kinetic energy (k)

The variations of the turbulence kinetic energy k in the x-y and y-z planes are presented in Figure 7.13 and Figure 7.14, respectively. In Figure 7.13, the turbulence kinetic energy values in the upstream tangent, particularly in the inviscid core region remain small and constant. The enlarged airfoil section in this Figure shows the boundary layer development on the surfaces of the airfoil, where the boundary layer on the upper surface is initially thinner than the corresponding one on the lower surface. However, at the trailing edge of the airfoil, the thickness of the upper surface boundary layer is slightly greater than the corresponding boundary layer on the lower surface, which could be due to the bend effects. The differing effects of the concave wall compared with the convex wall on the turbulence field near the wall can also be seen in Figure 7.13. The turbulence is enhanced on the concave wall compared with the convex wall, where the high turbulence level is confined to a region very close to the wall. The comparison of the turbulence kinetic energy plots obtained in the presence and absence of the airfoil in this Figure indicates insignificant differences outside the wall region of the duct in the upstream tangent and in the bend section. However, in the wall region on the convex side in the downstream tangent, the presence of the airfoil has reduced the turbulence kinetic energy in the boundary layer region. Within the bend, however, the presence of the airfoil has the effect of increasing the turbulence energy on the convex wall, but these changes are confined to a very thin region near the wall.

The spanwise variations in Figure 7.14 show significant variations in the near wall region at each station. At station 2, the comparison reveals that the boundary layers on the sidewalls are compressed when the airfoil is present, while they are unaltered on the concave and convex walls. Also, the absence of the wavy pattern on the graph in the near sidewall region indicates that the secondary flow motion has not been established in the flow at the station. Compared with station 2, the near wall variations (wavy pattern) increase significantly at stations 3 to 5. These are mainly attributed to the formation of small vortices near the wall when the airfoil is present. The turbulence kinetic energy is also enhanced by these vortices. These flow features will be referred to below when the vector plots of the velocity field are presented.

7.2.3. Vector plots

The velocity vector plots in the y-z plane at stations 2 to 5 are presented in Figure 7.15. At station 2, the fluid motion is relatively simple compared with that in stations 3 to 5, where cross-flow secondary motions as a result of an imbalance between radial pressure gradient force and centrifugal force, are present. At station 3, part of the fluid migrating from the concave side to the convex side along the sidewalls is interrupted by the wake and boundary layer interaction, which takes place on the sidewalls and lead to the formation of smaller vortices near the wall region. At this station, two pairs of such vortices can be seen, one at a distance of y/H = 0.15 on the concave side, and the other at y/H = 0.67 on the convex side, measured from the concave wall. The vortex on the concave side is significantly larger than the corresponding one on the convex side. As the fluid flows from station 3 towards station 5, the lower vortex moves upwards, whereas the upper vortex remains relatively unchanged. As the wake of the airfoil is shifted downwards between these stations, suggests that there is a strong interaction between the wake and the vortices in the near sidewall region. At station 5, the wake is significantly weakened and the flow is redeveloping in the downstream tangent, following the exit from the bend with, and displaying two counter-rotating vortices, typical of flows in curved ducts.

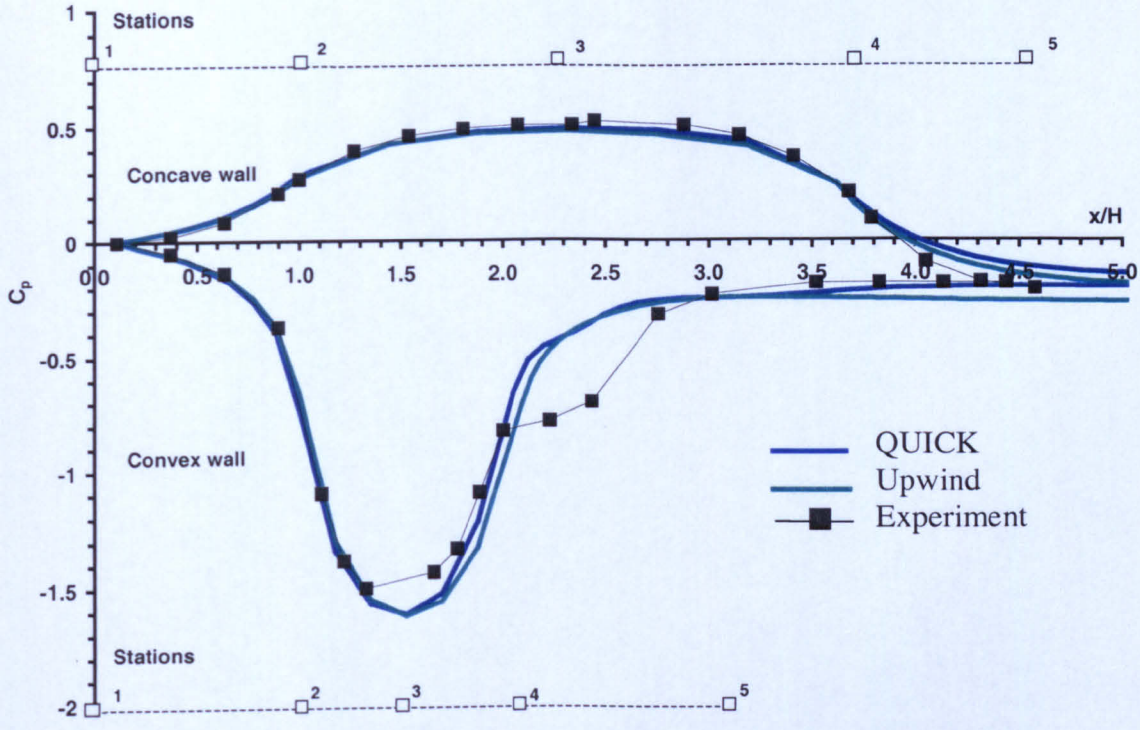

(a)

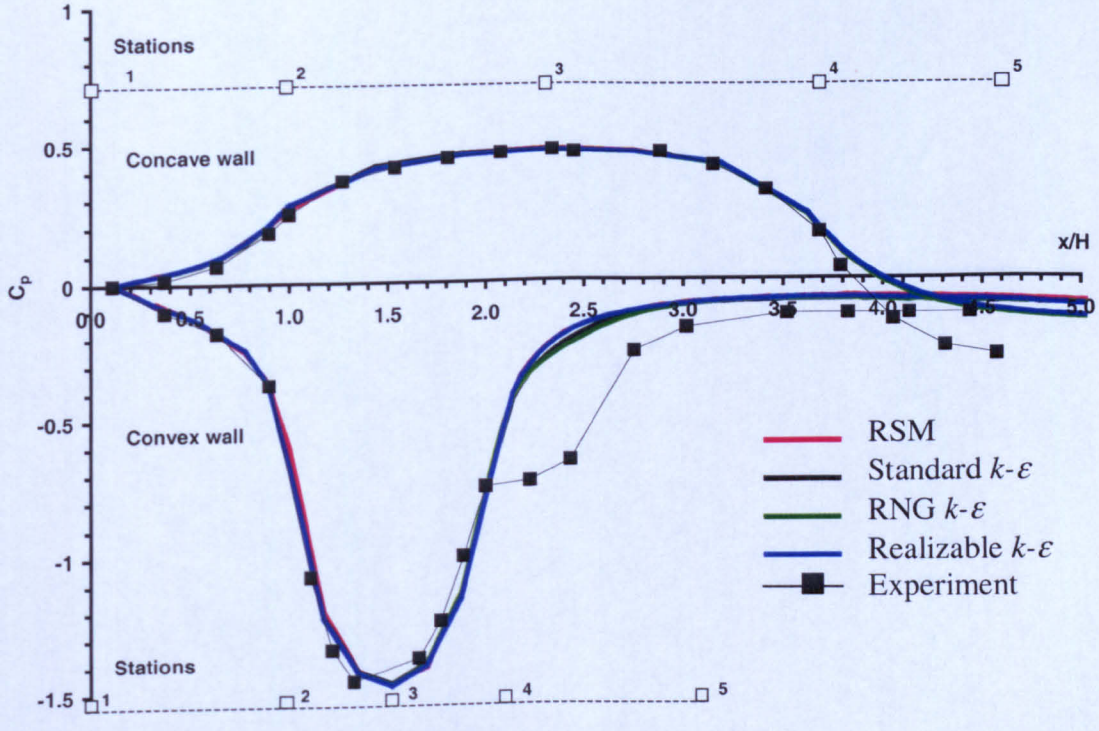

(b)

Figure 7.1: Comparison of numerical pressure coefficient along the concave and convex walls of the duct with experimental pressure coefficient: (a) no airfoil, different discretisation schemes, RSM (b) with airfoil, different turbulence models, QUICK scheme. (Original in colour).

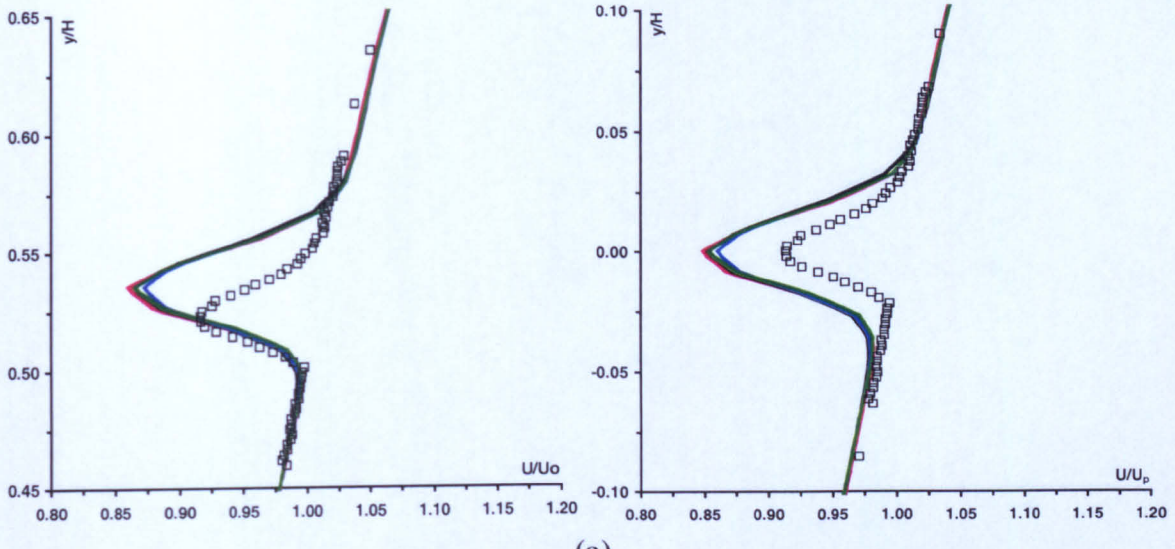

(a)

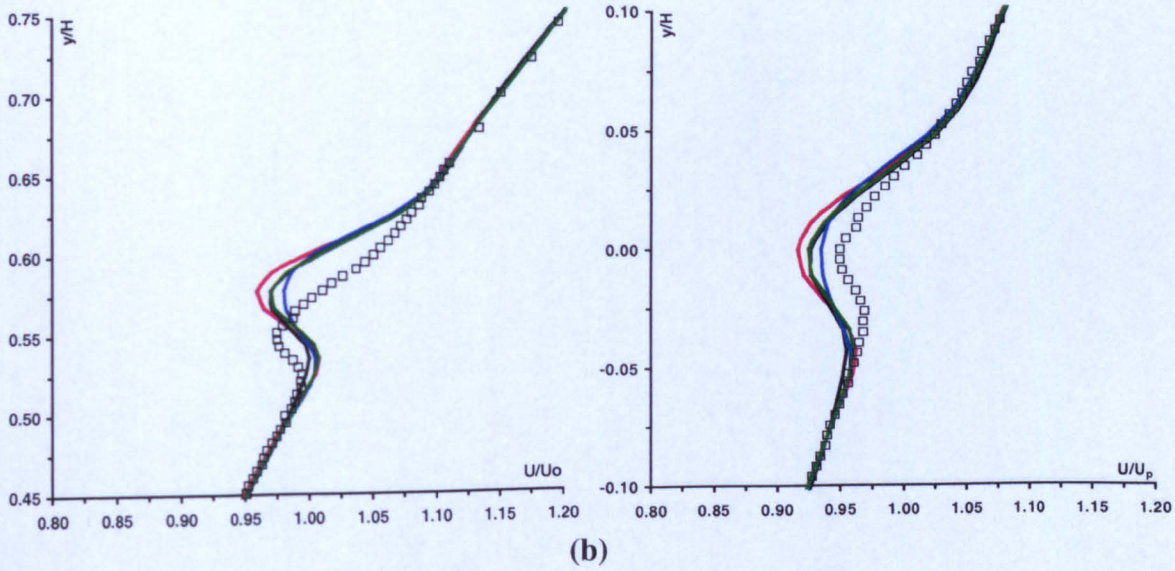

(b)

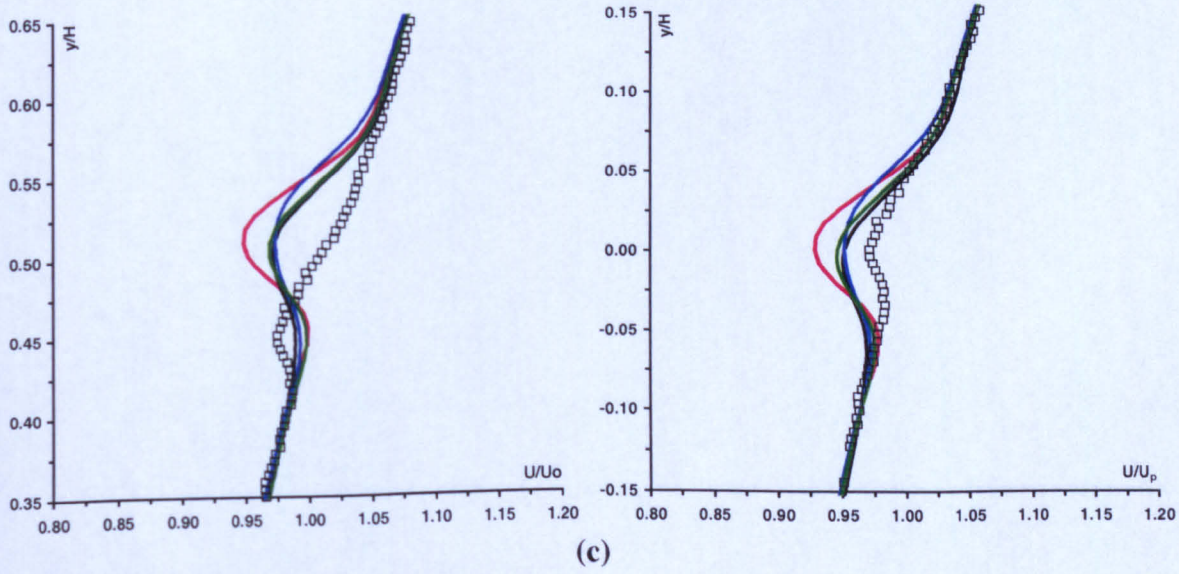

(c)

(Original in colour)

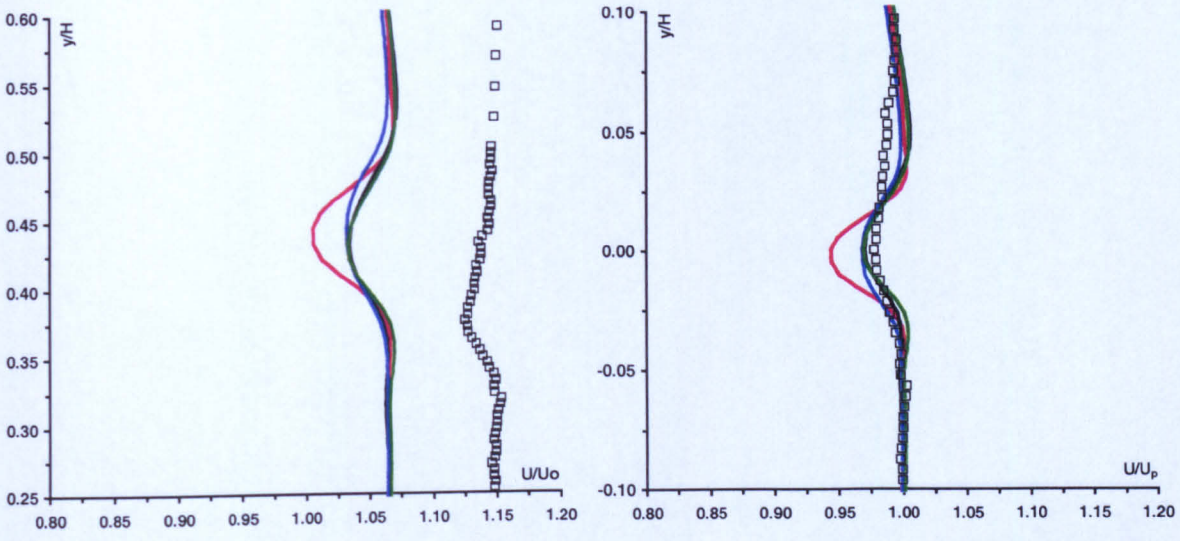

(d)

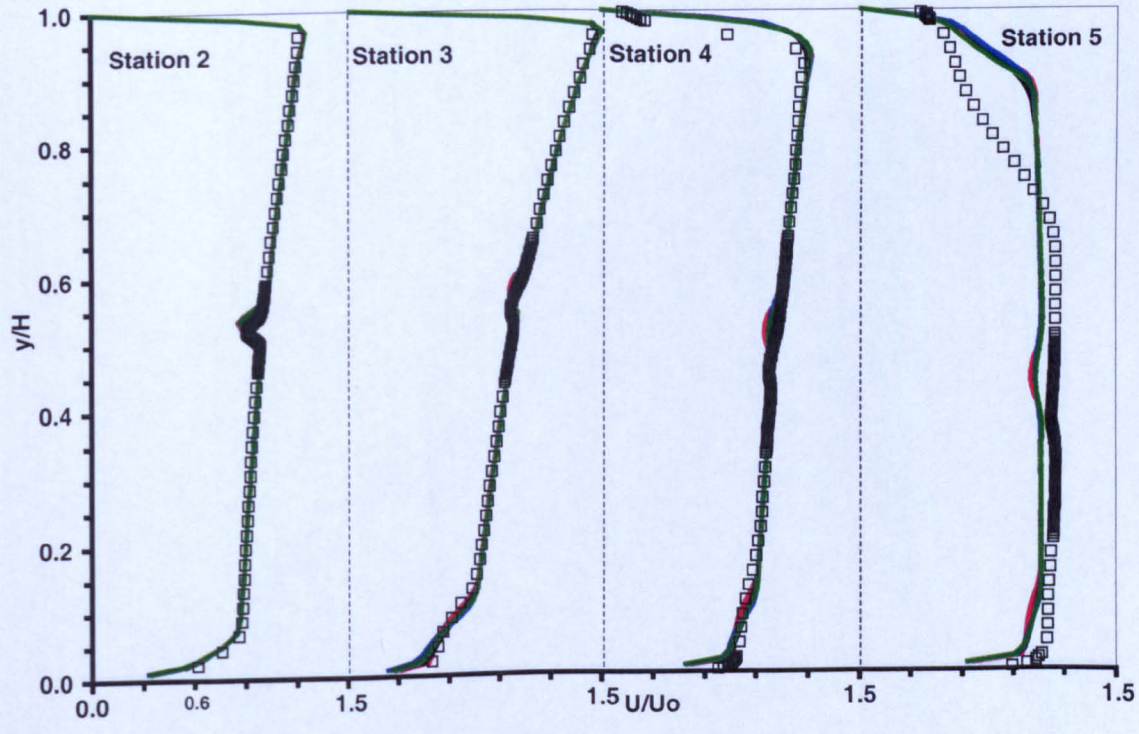

(e)

Figure 7.2: Comparison of numerical streamwise velocity component (obtained using QUICK scheme) with experiment: (a) station 2; (b) station 3; (c) station 4; (d) station 5; (e) stations 2 to 5 (across the whole cross-section).

———, RSM; ———, Standard k-ε; ———, RNG k-ε; ———, Realizable k-ε; □, Experiment.

(Original in colour)

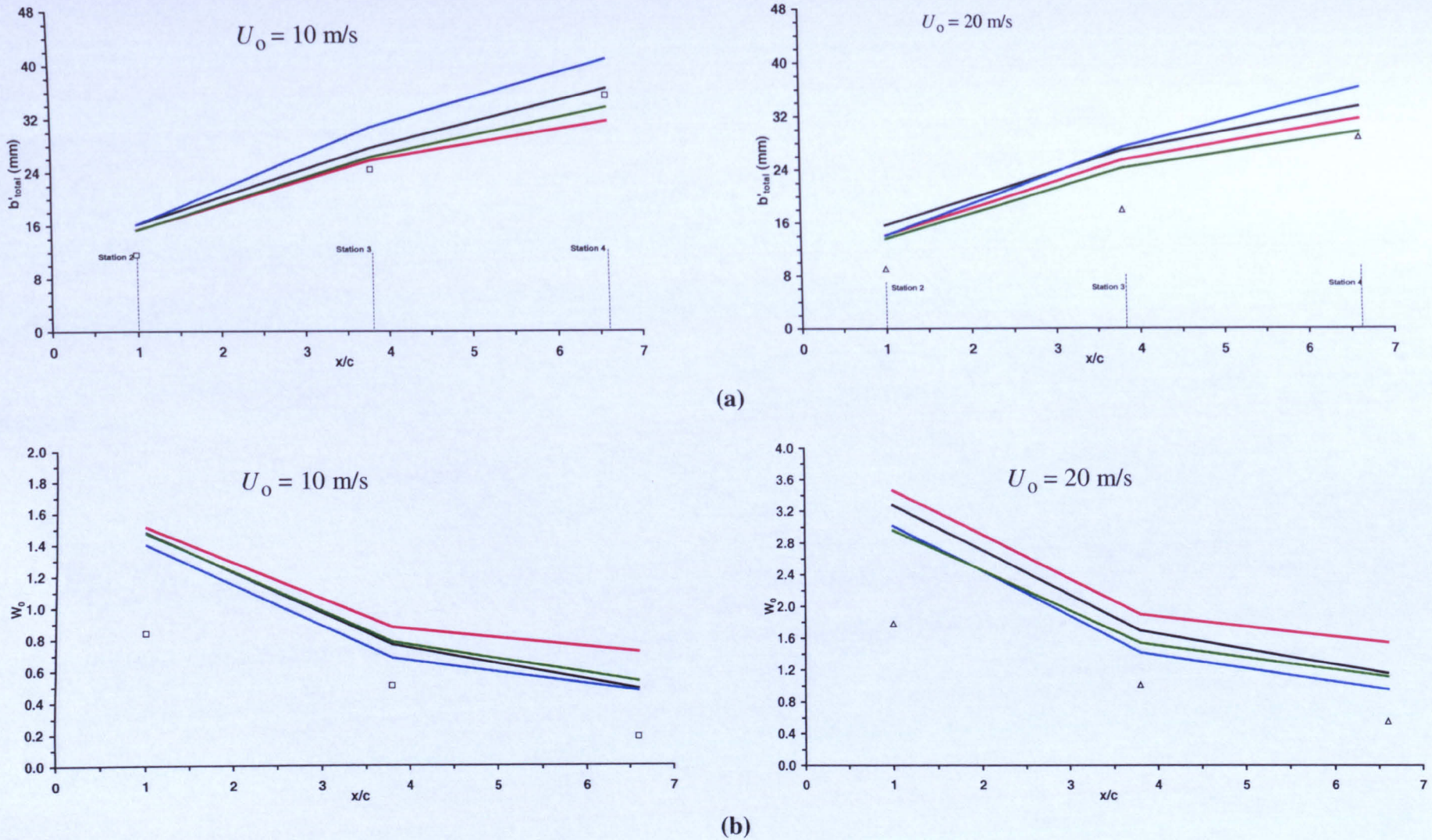

Figure 7.3: Comparison of wake parameters component (obtained using QUICK scheme) at stations 2 to 4: (a) total wake half-width (inner side + outer side); (b) maximum velocity defect. (Original in colour).

———, RSM; ———, Standard k-ε; ———, RNG k-ε; ———, Realizable k-ε; □, Experiment U_o = 10 m/s; Δ, Experiment U_o = 20 m/s.

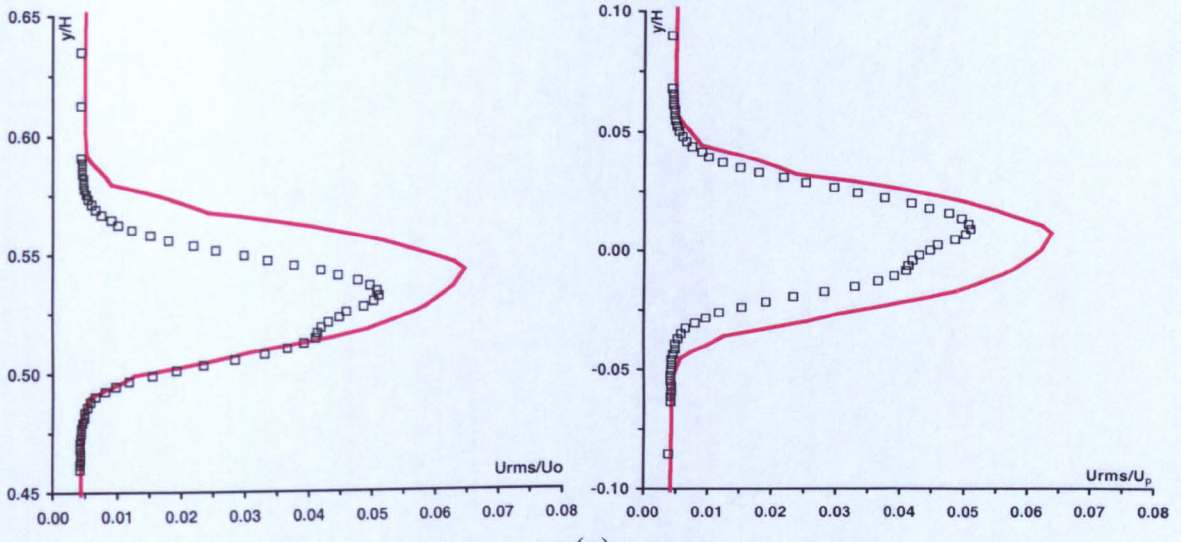

(a)

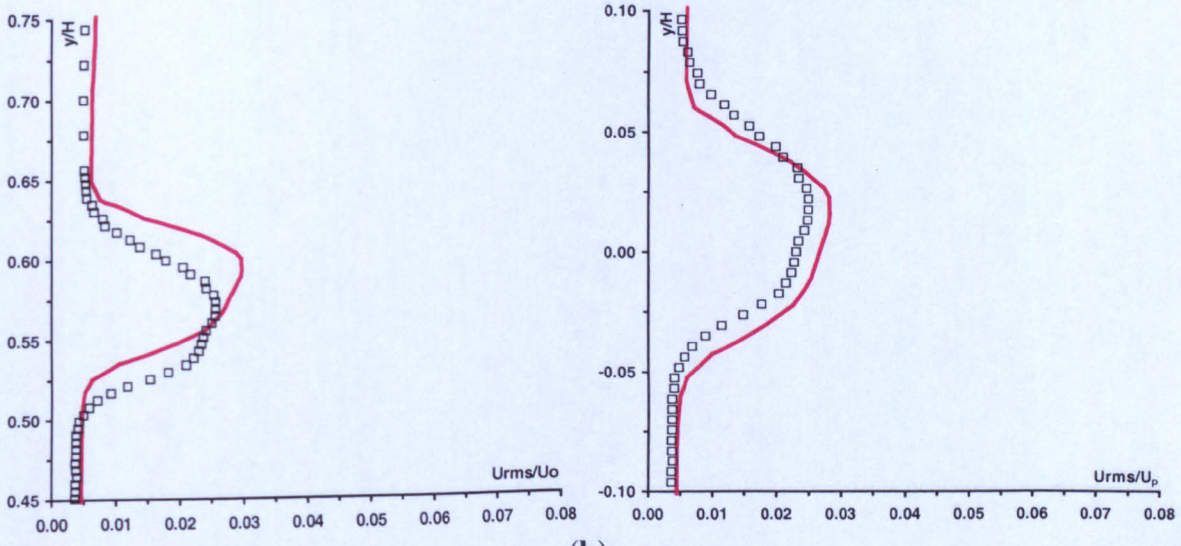

(b)

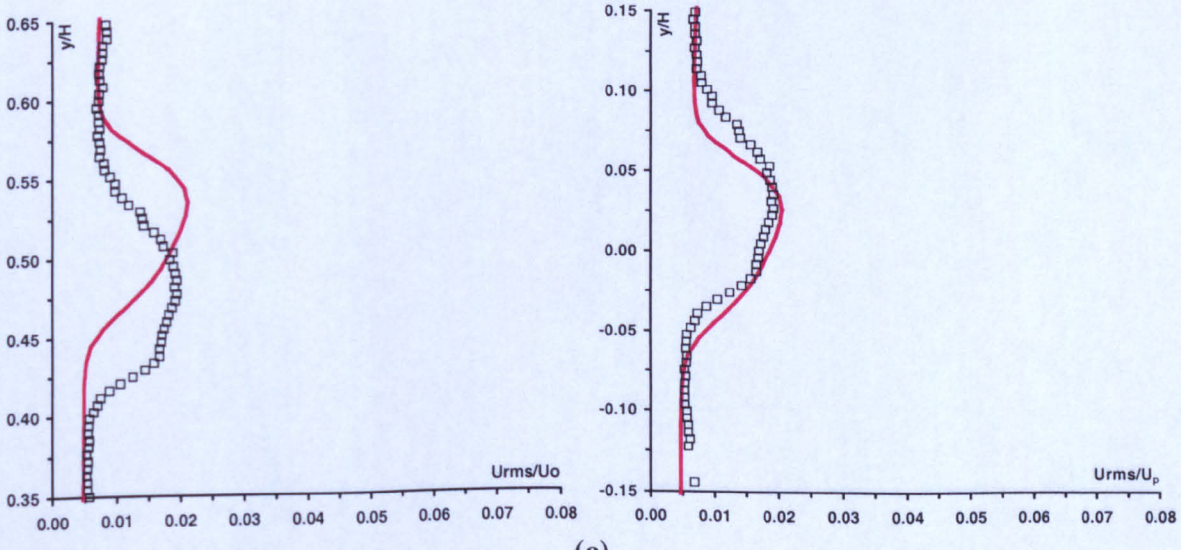

(c)

(Original in colour)

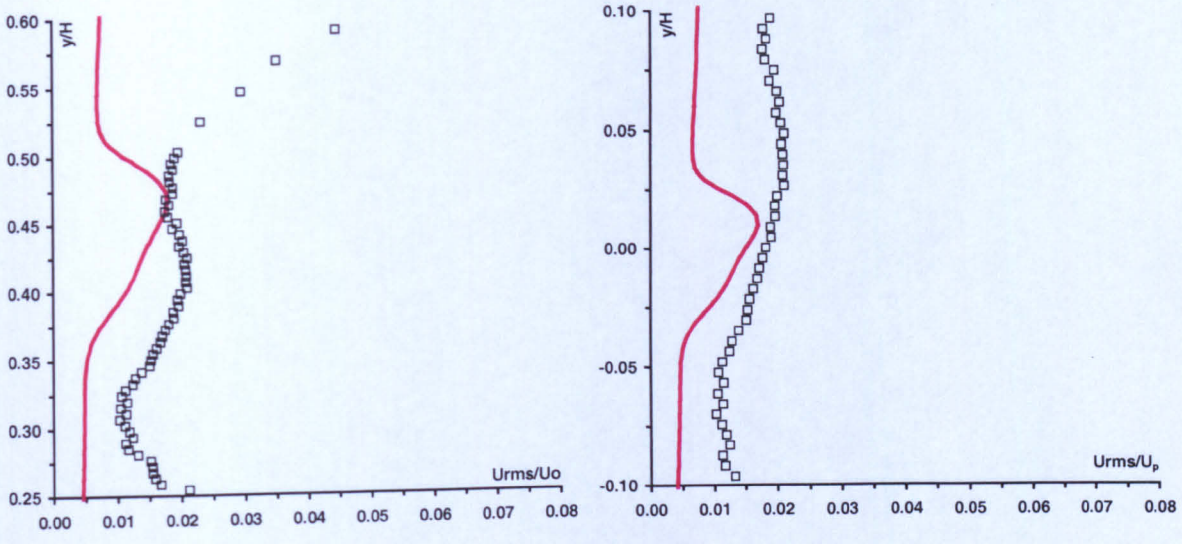

(d)

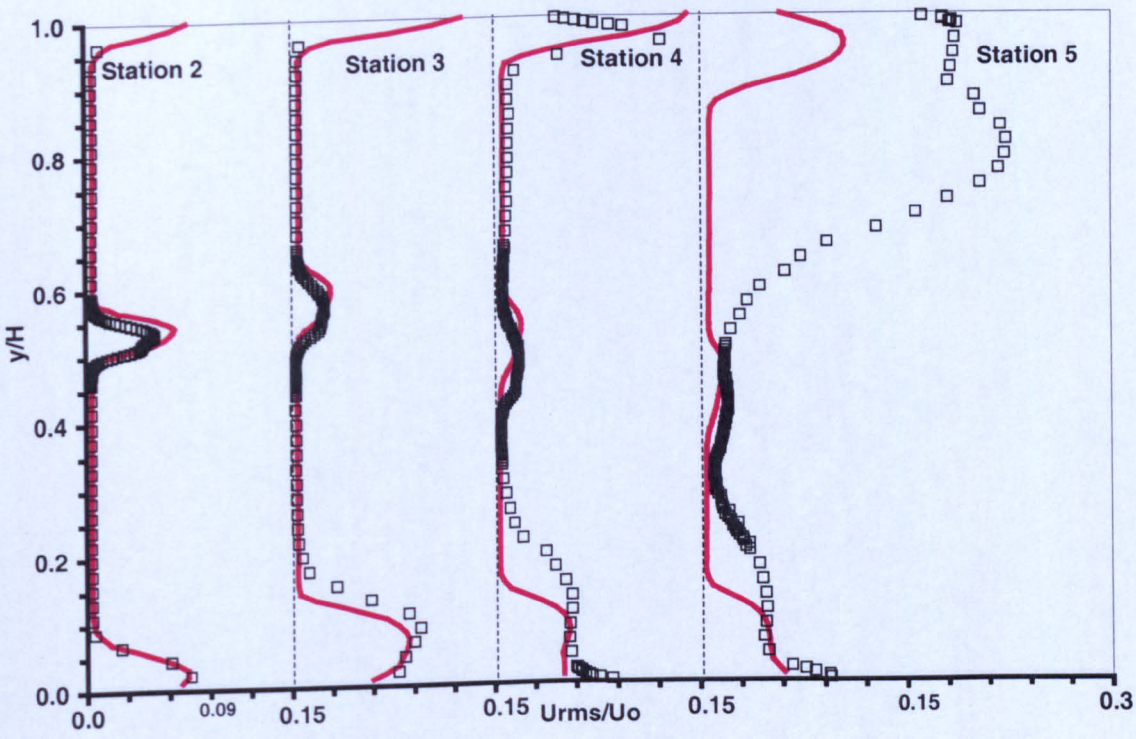

(e)

Figure 7.4: Comparison of numerical streamwise intensity (obtained using QUICK scheme) with experiment: (a) station 2; (b) station 3; (c) station 4; (d) station 5; (e) stations 2 to 5 (across the whole cross-section).

———, RSM; □, Experiment.

(Original in colour)

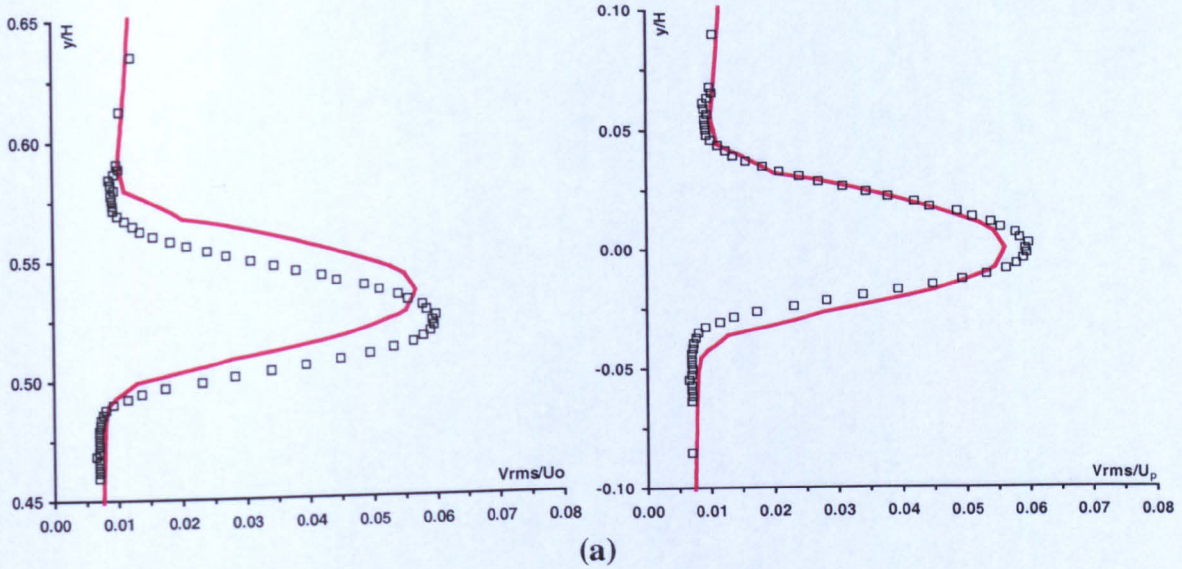

(a)

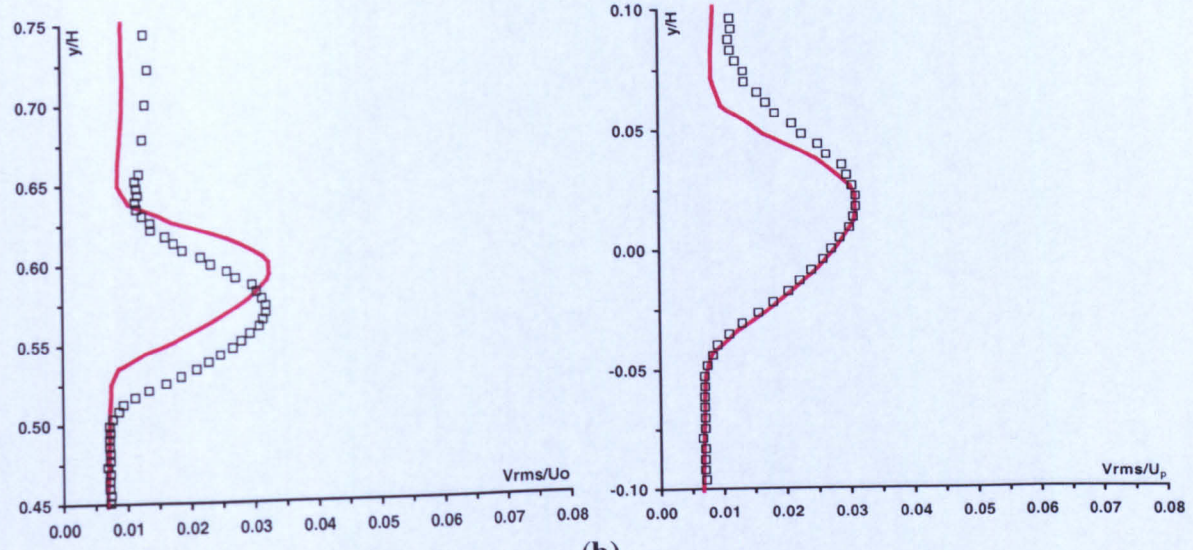

(b)

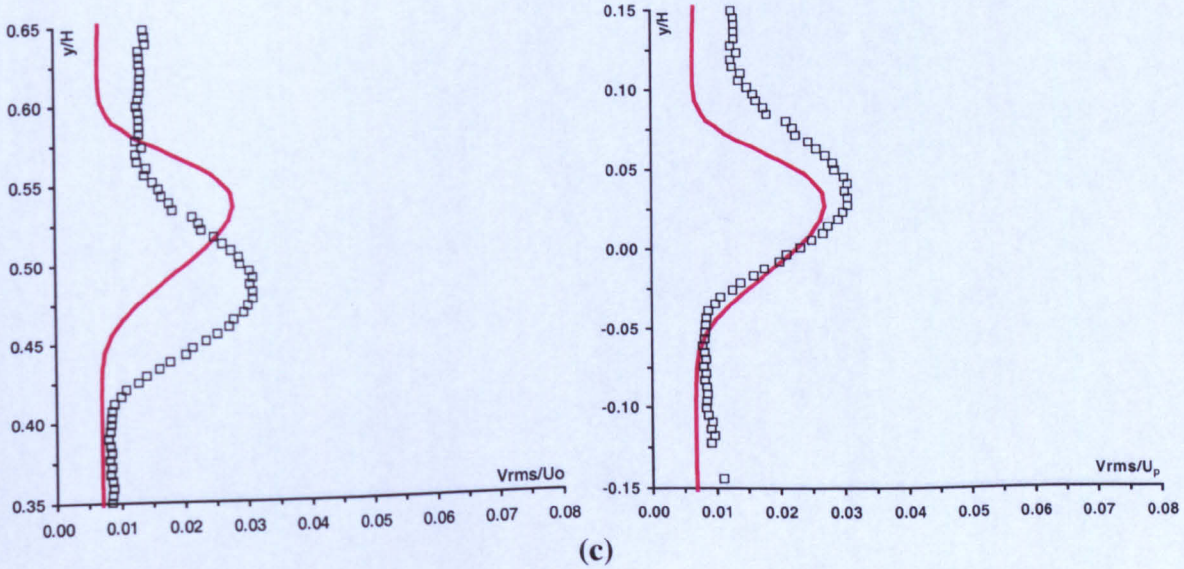

(c)

(Original in colour)

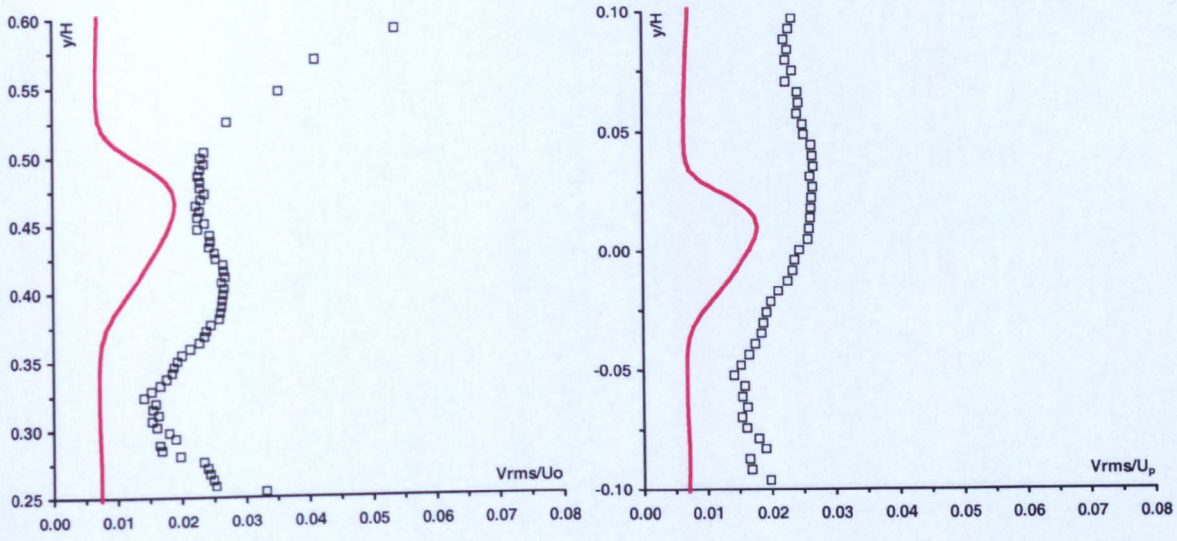

(d)

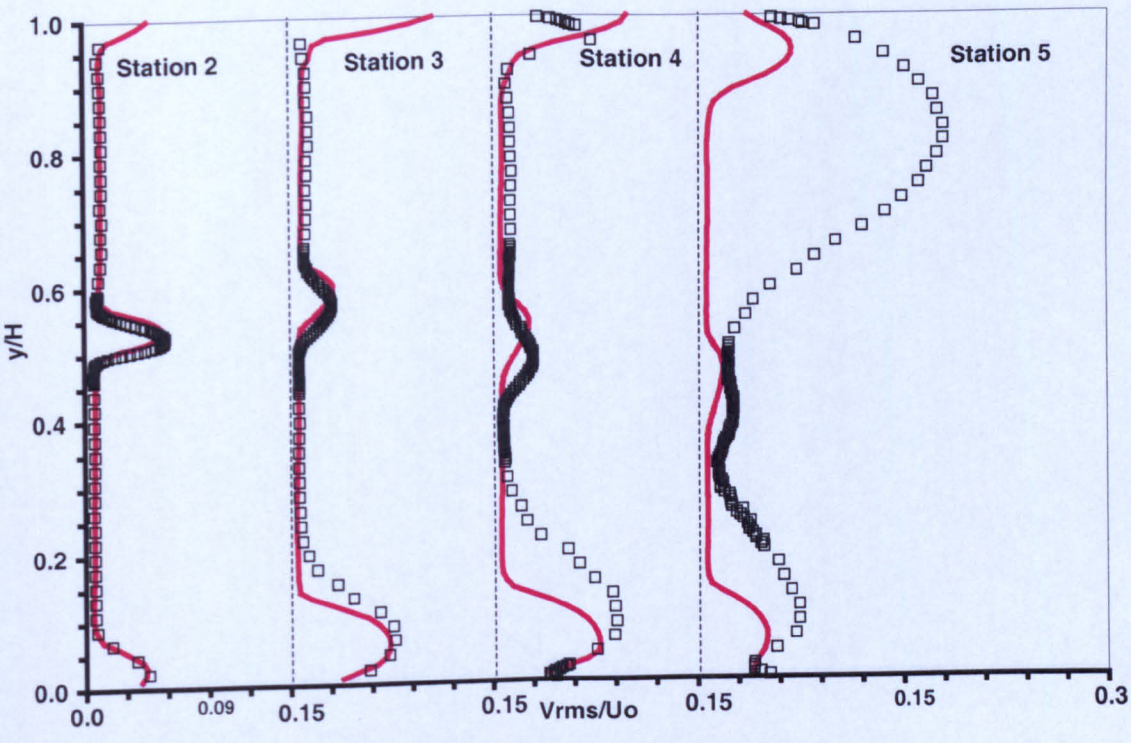

(e)

Figure 7.5: Comparison of numerical normal intensity (obtained using QUICK scheme) with experiment: (a) station 2; (b) station 3; (c) station 4; (d) station 5; (e) stations 2 to 5 (across the whole cross-section).

——, RSM; □, Experiment.

(Original in colour)

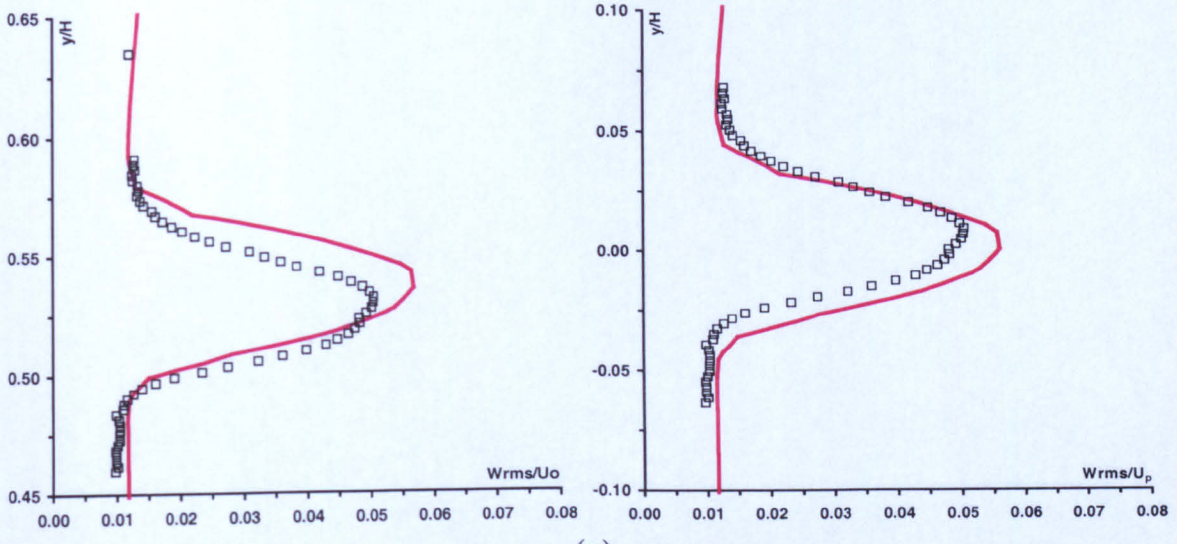

(a)

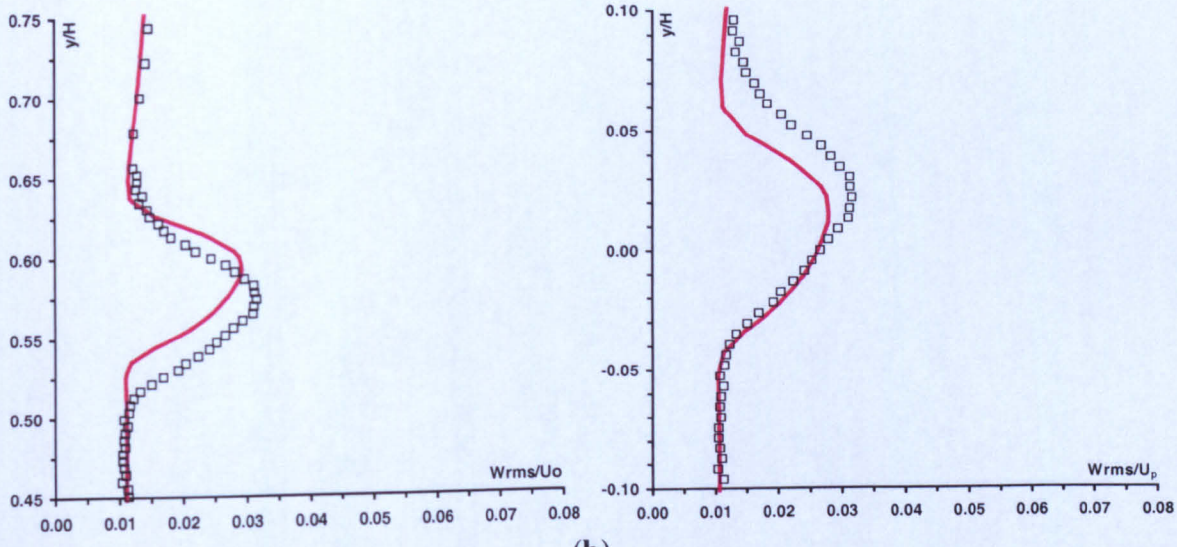

(b)

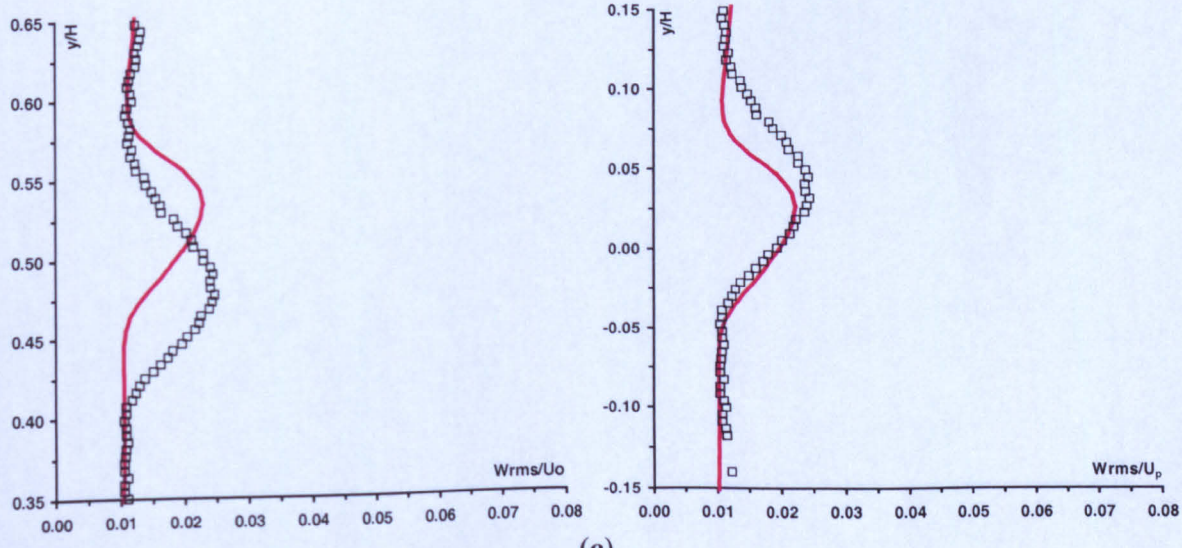

(c)

(Original in colour)

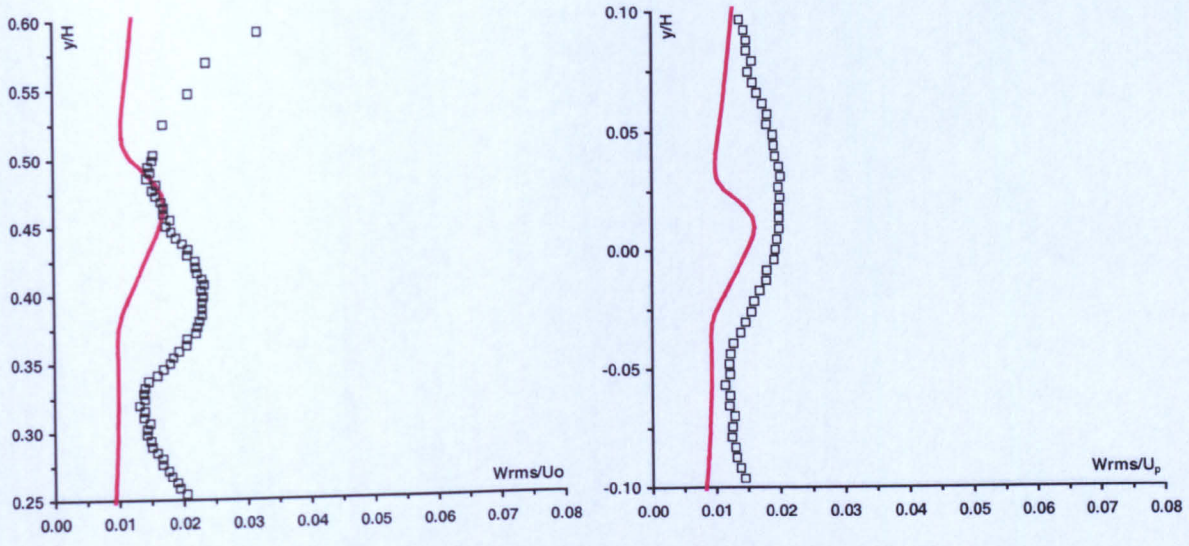

(d)

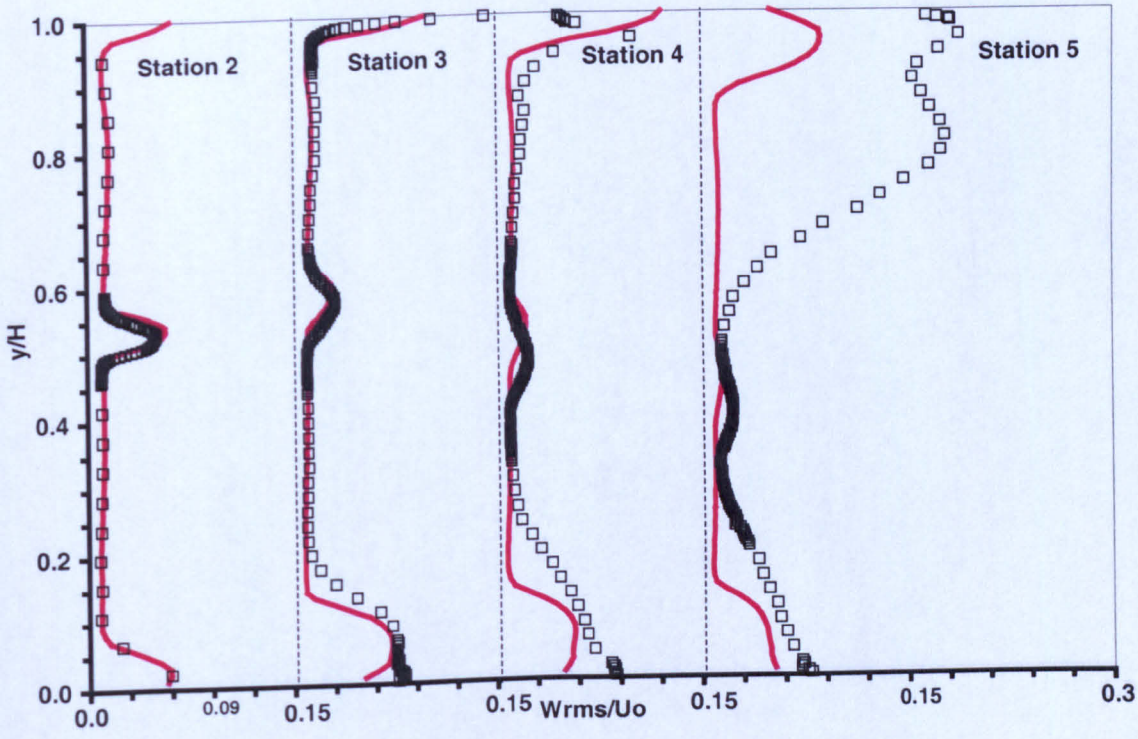

(e)

Figure 7.6: Comparison of numerical spanwise intensity (obtained using QUICK scheme) with experiment: (a) station 2; (b) station 3; (c) station 4; (d) station 5; (e) stations 2 to 5 (across the whole cross-section).

———, RSM; □, Experiment.

(Original in colour)

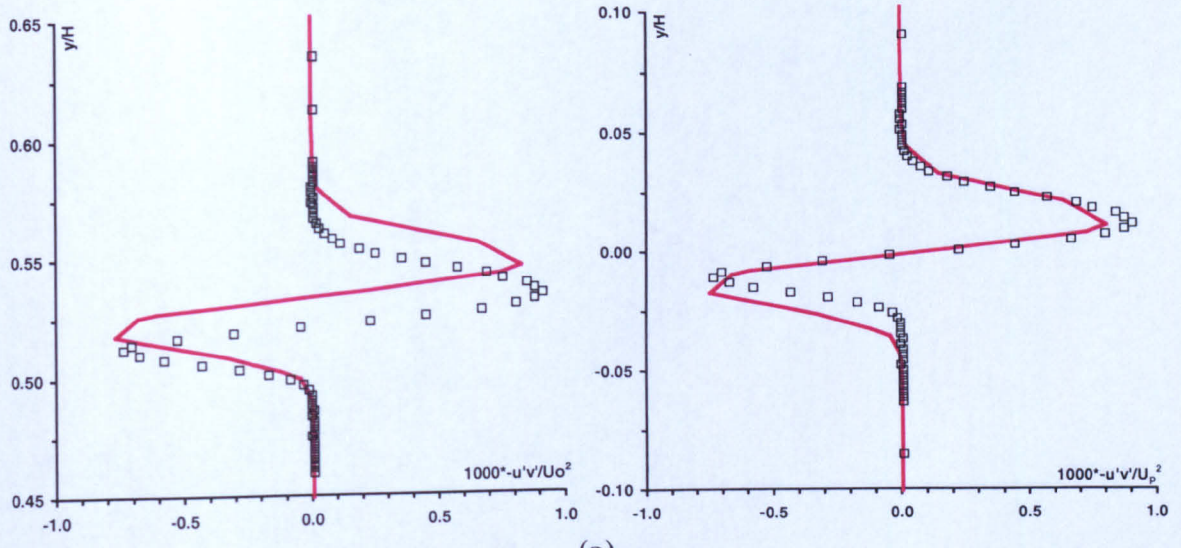

(a)

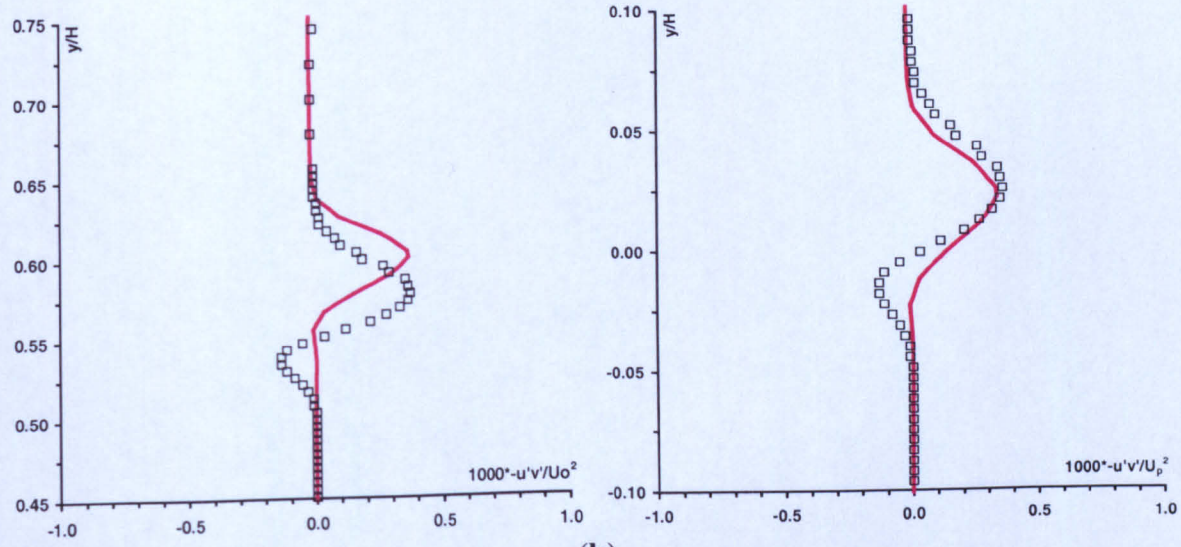

(b)

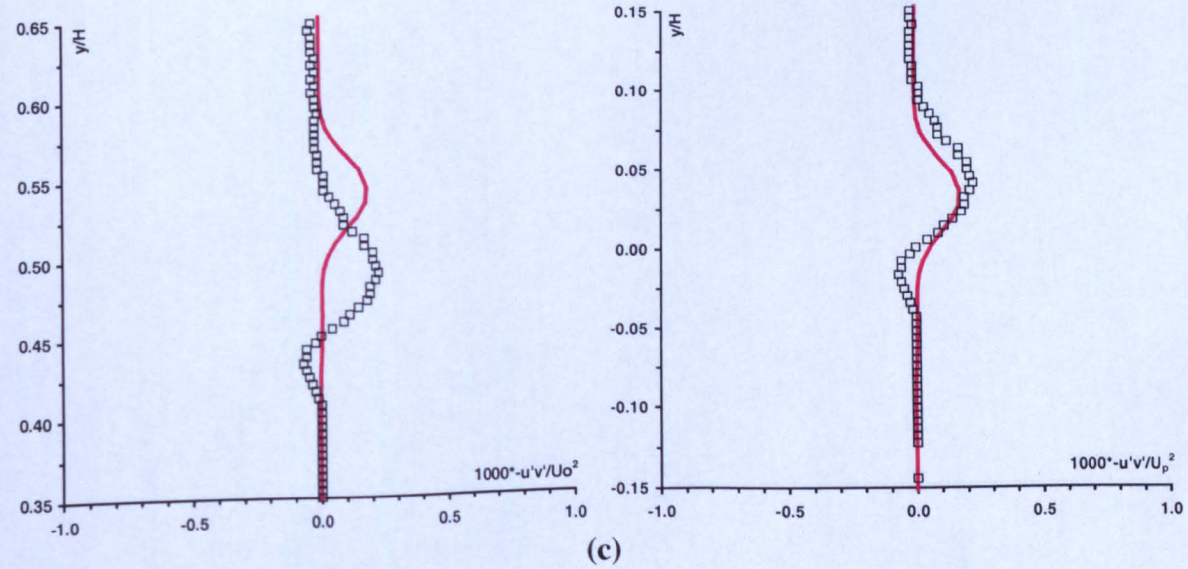

(c)

(Original in colour)

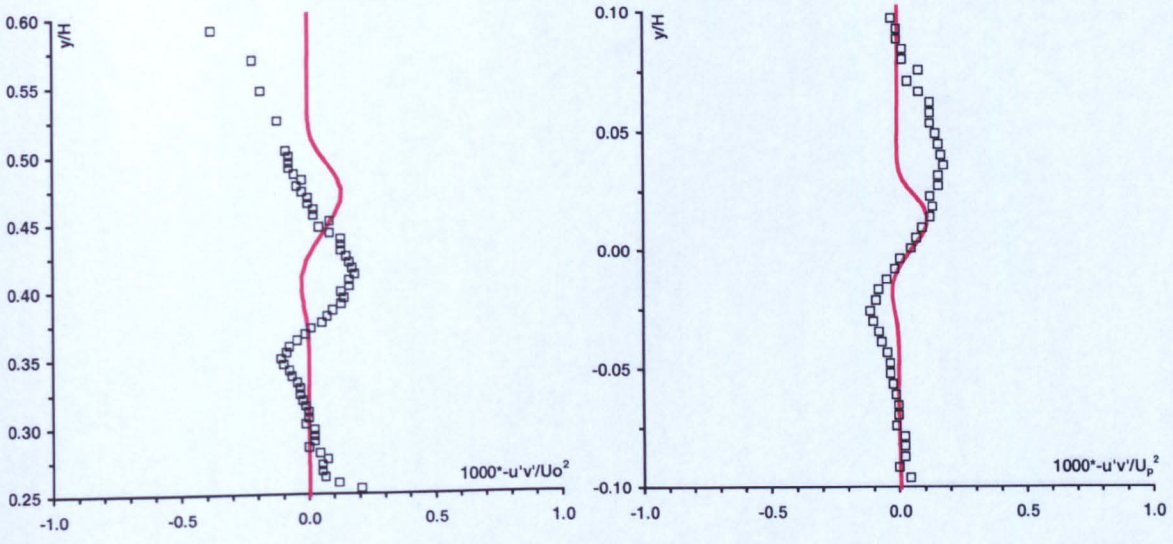

(d)

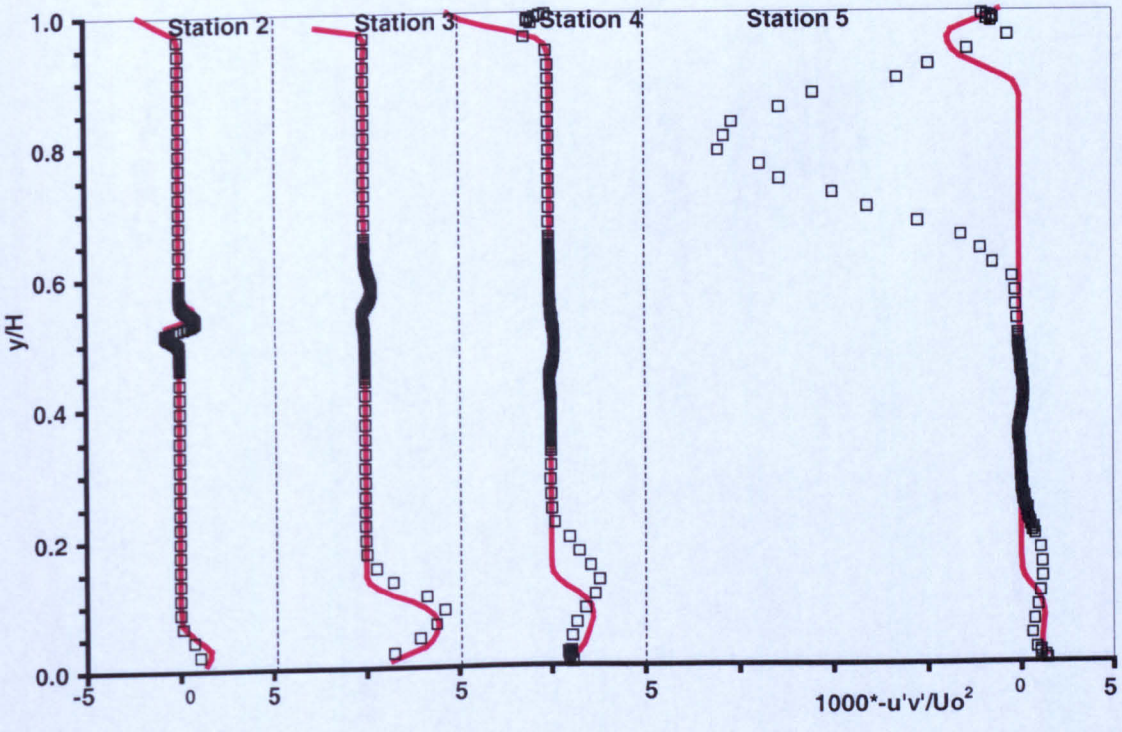

(e)

Figure 7.7: Comparison of numerical turbulence shear stress $-\overline{u'v'}$ (obtained using QUICK scheme) with experiment: (a) station 2; (b) station 3; (c) station 4; (d) station 5; (e) stations 2 to 5 (across the whole cross-section).

——, RSM; □, Experiment.

(Original in colour)

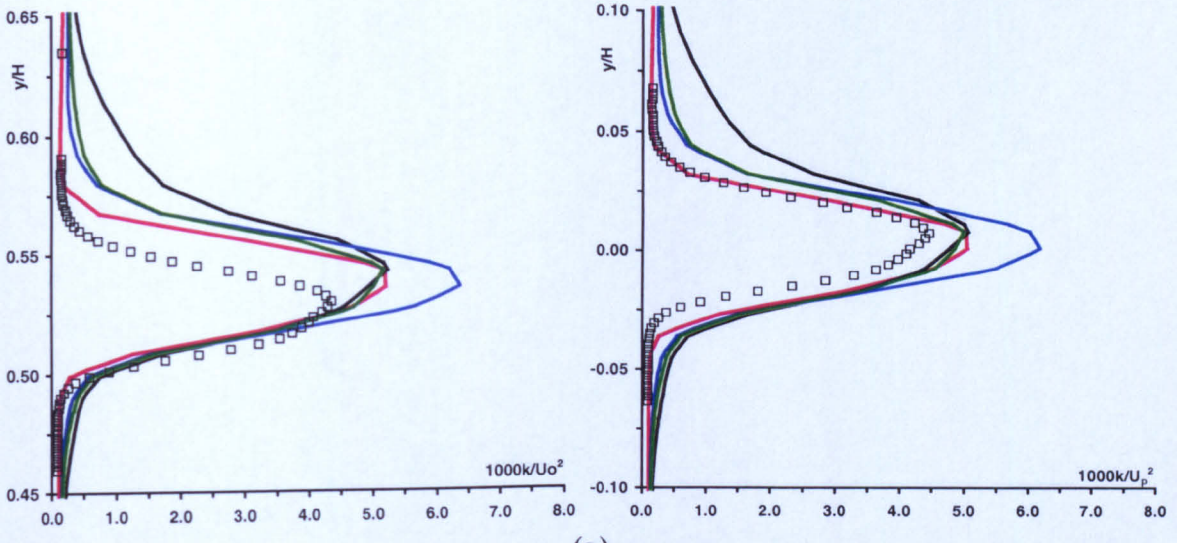

(a)

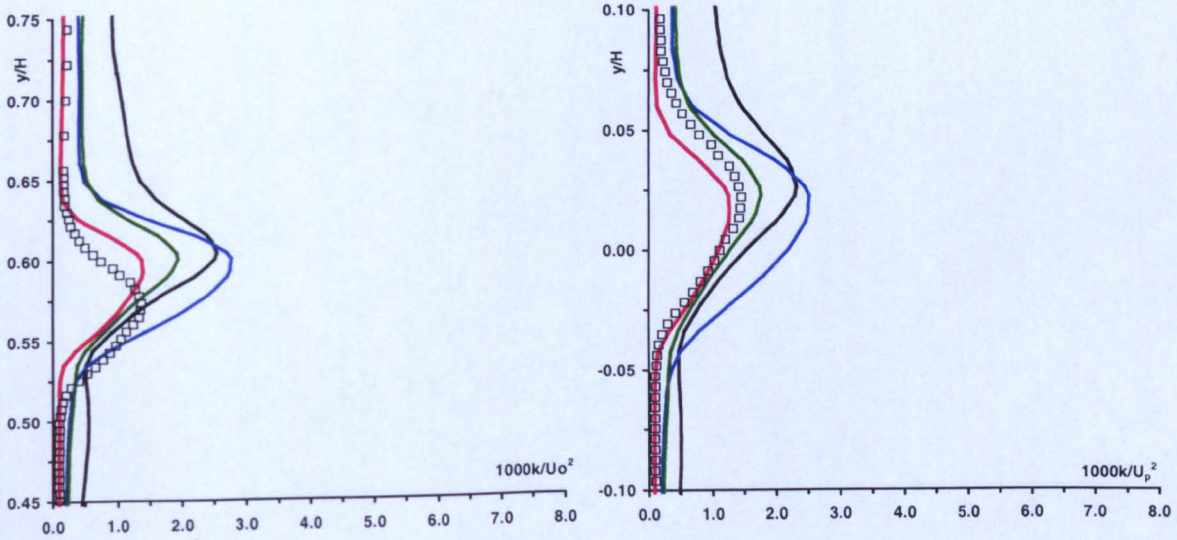

(b)

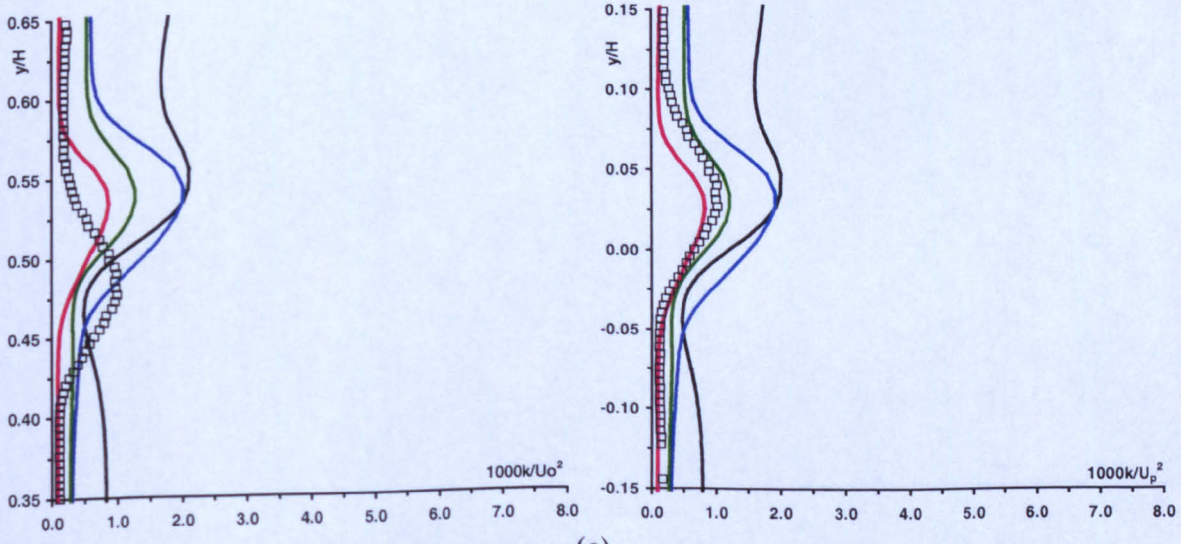

(c)

(Original in colour)

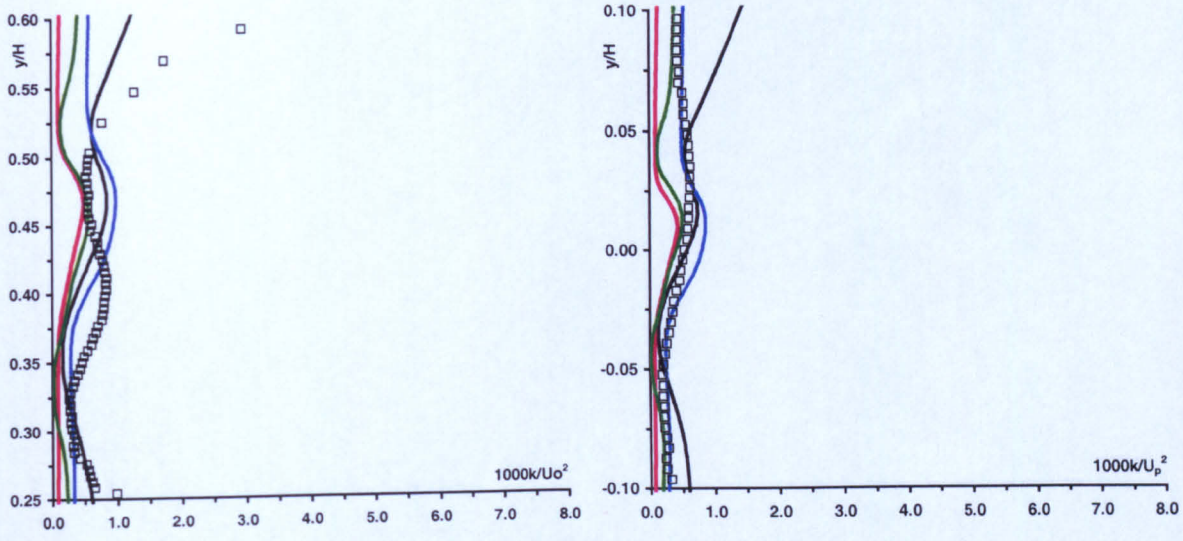

(d)

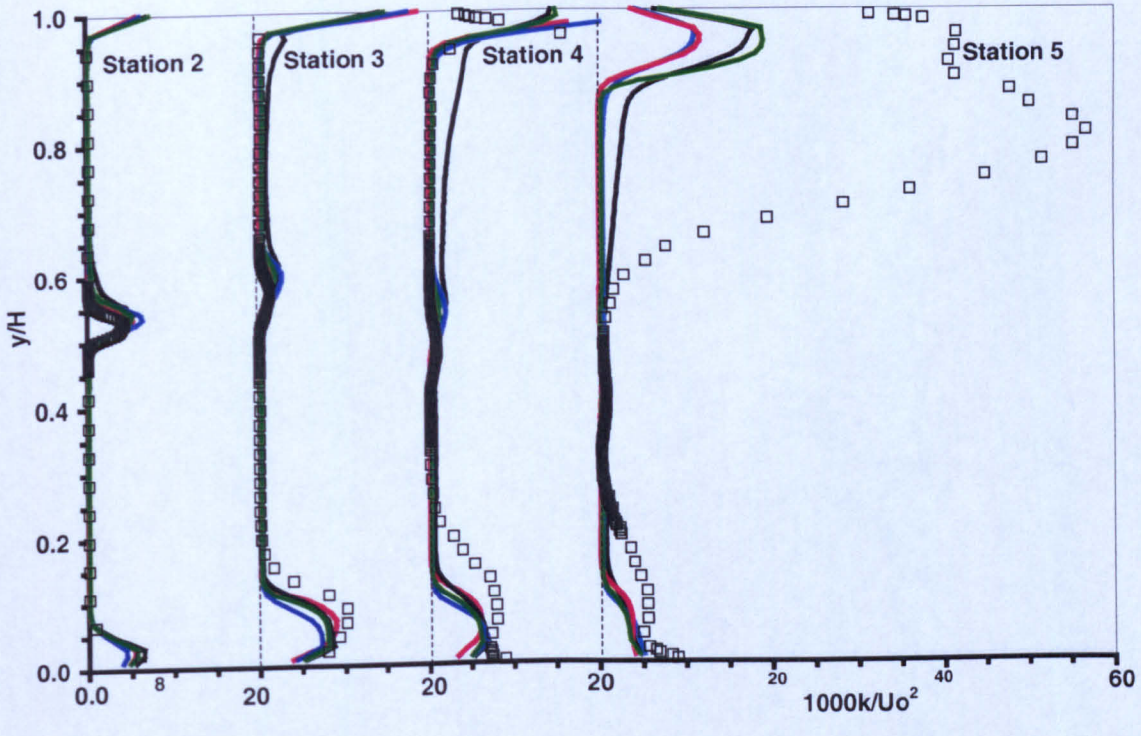

(e)

Figure 7.8: Comparison of numerical turbulence kinetic energy (obtained using QUICK scheme) at z/H = 0.5 with experiment: (a) station 2; (b) station 3; (c) station 4; (d) station 5; (e) stations 2 to 5 (across the whole cross-section).

———, RSM; ———, Standard k-ε; ———, RNG k-ε; ———, Realizable k-ε; □, Experiment.

(Original in colour)

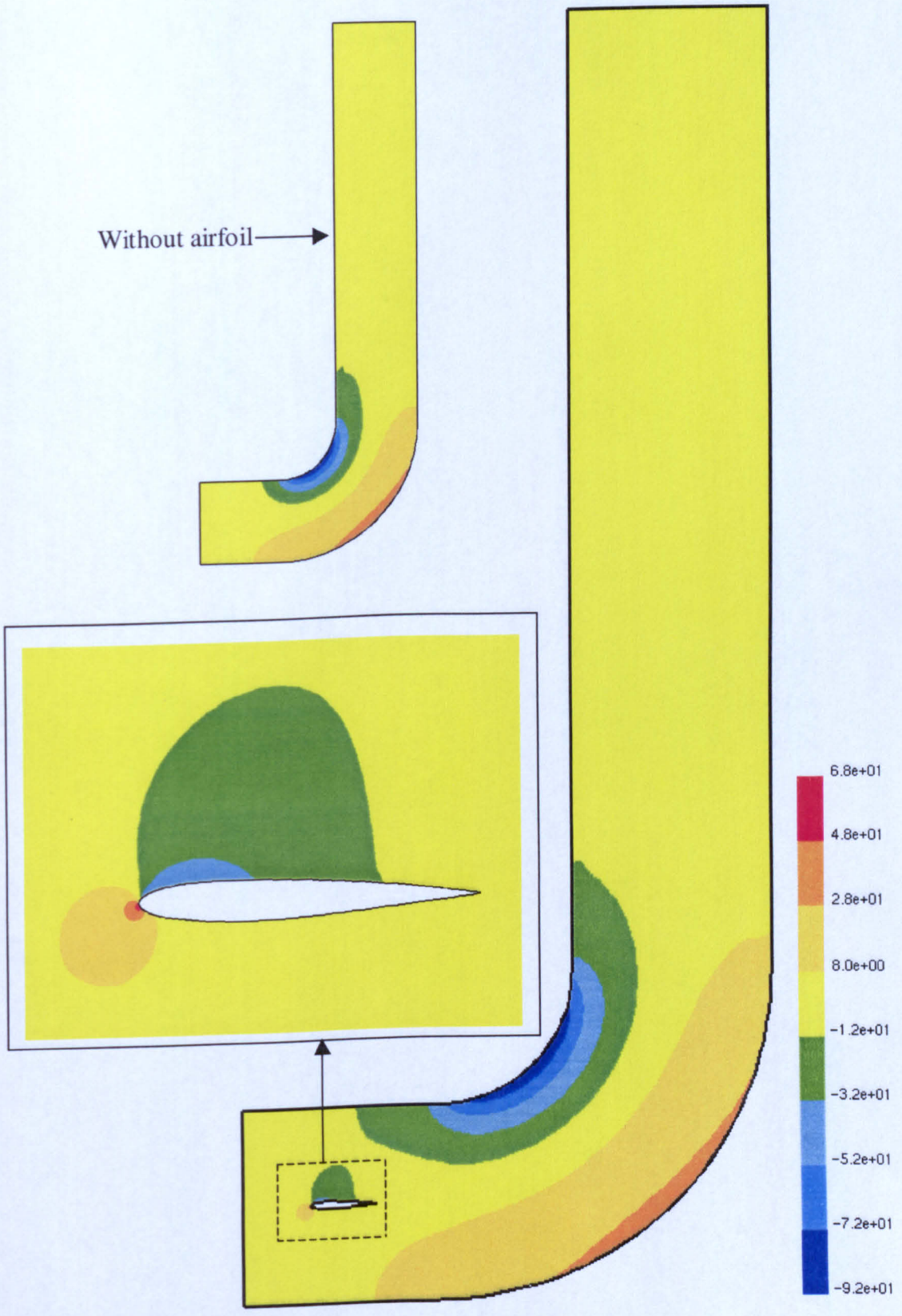

Figure 7.9: Static pressure (N/m^2) distribution (obtained using RSM and QUICK scheme) of the flow domain at z/H = 0.5 on the x-y plane. The pressure reference point is set at the inlet. (Original in colour).

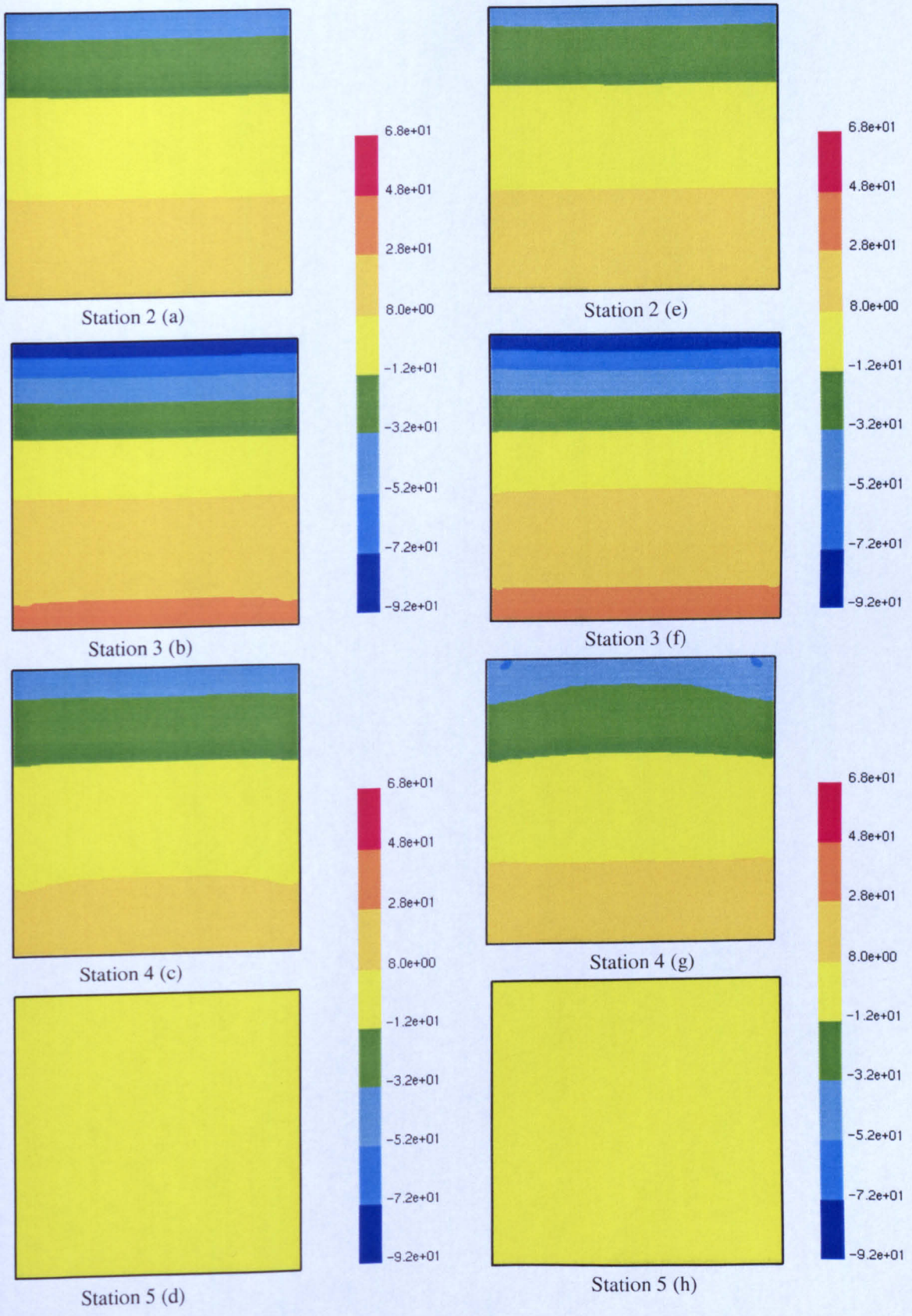

Figure 7.10: Static pressure (N/m^2) distribution (obtained using RSM and QUICK scheme) on the y-z plane at stations 2 to 5: (a-d) with airfoil, (e-h) without airfoil. The pressure reference point is set at the inlet (Original in colour).

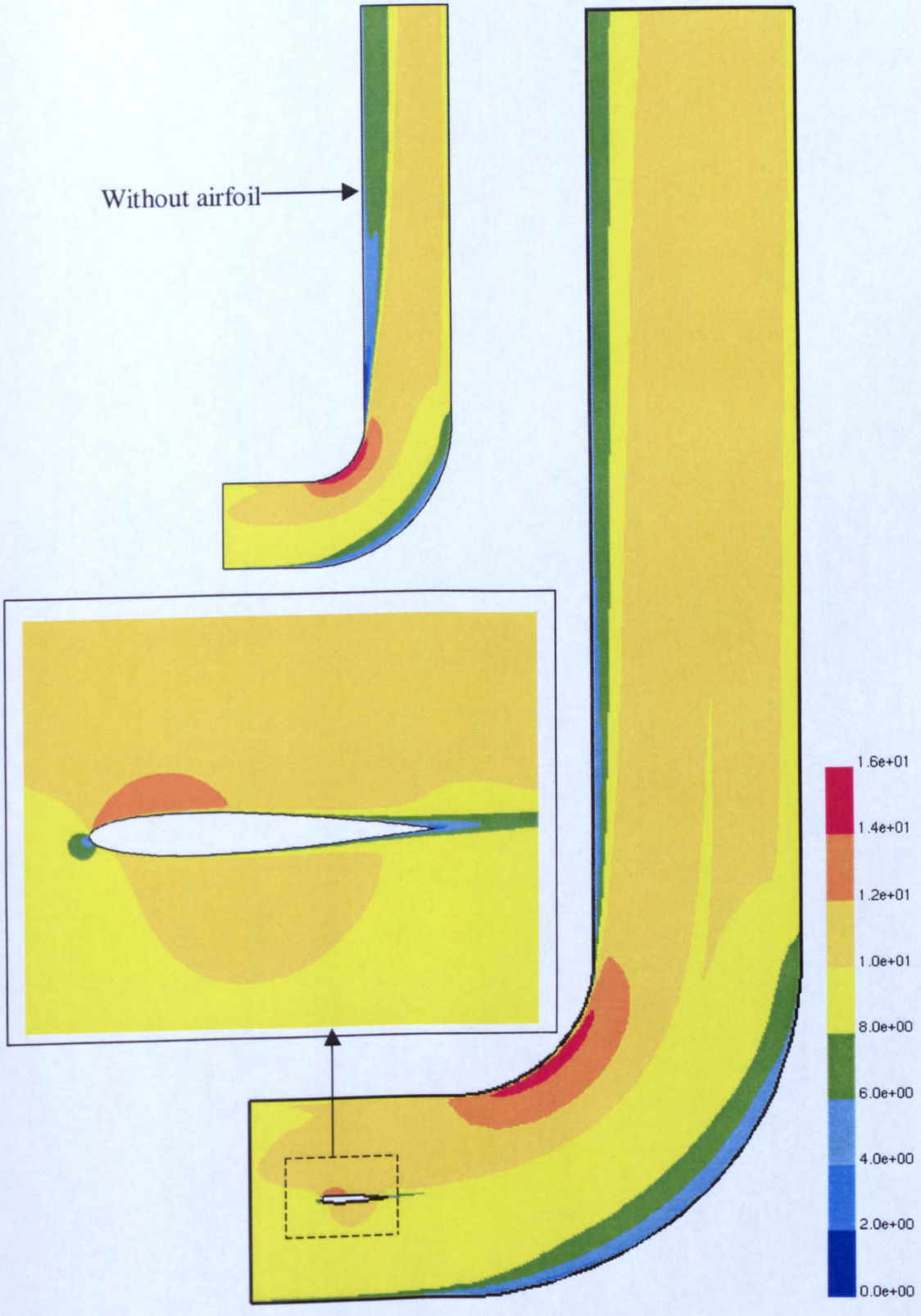

Figure 7.11: Velocity magnitude (m/s) distribution (obtained using RSM and QUICK scheme) of the flow domain at z/H = 0.5 on the x-y plane. (Original in colour).

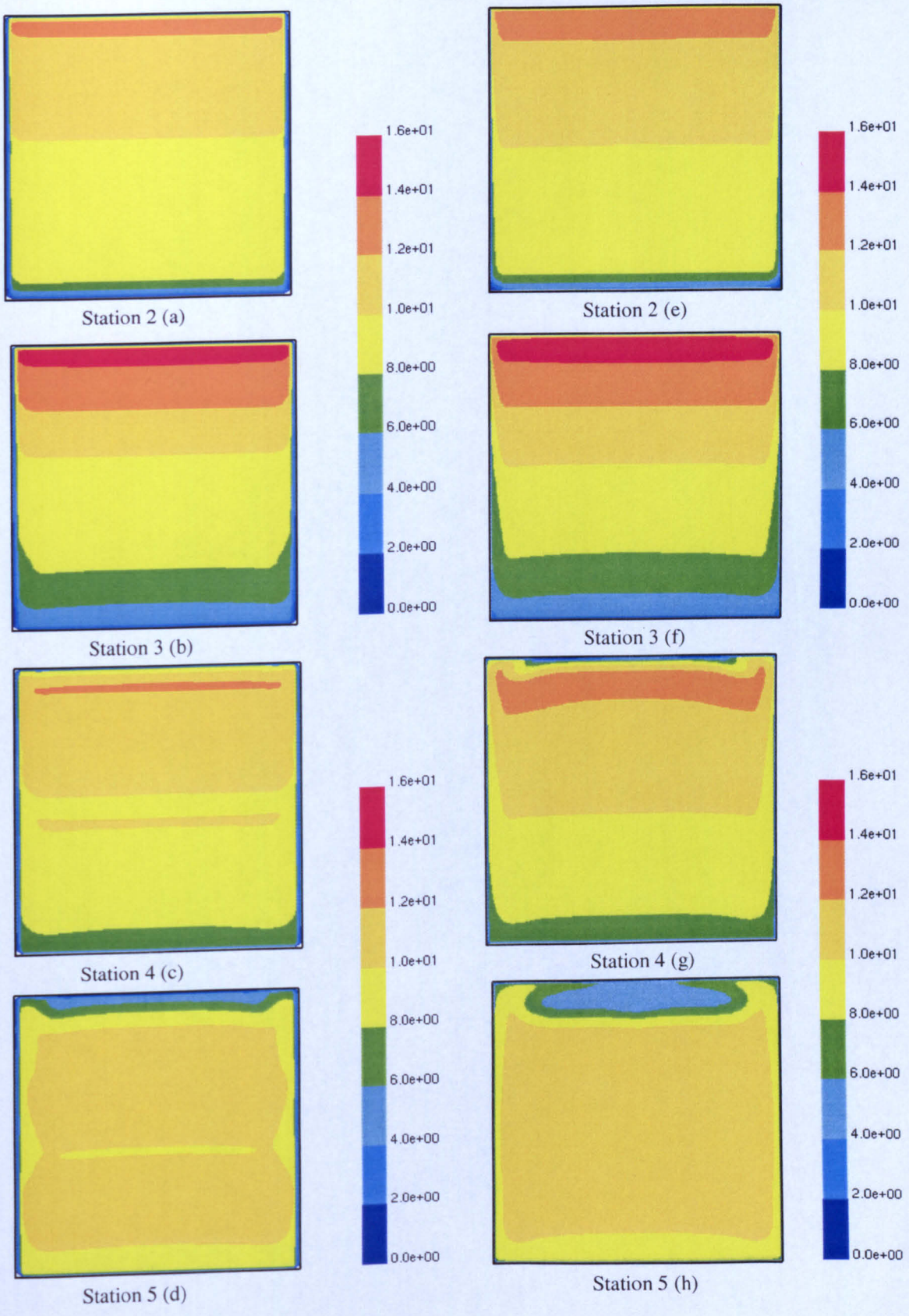

Figure 7.12: Velocity magnitude (m/s) distribution (obtained using RSM and QUICK scheme) on the y-z plane at stations 2 to 5: (a-d) with airfoil, (e-h) without airfoil (Original in colour).

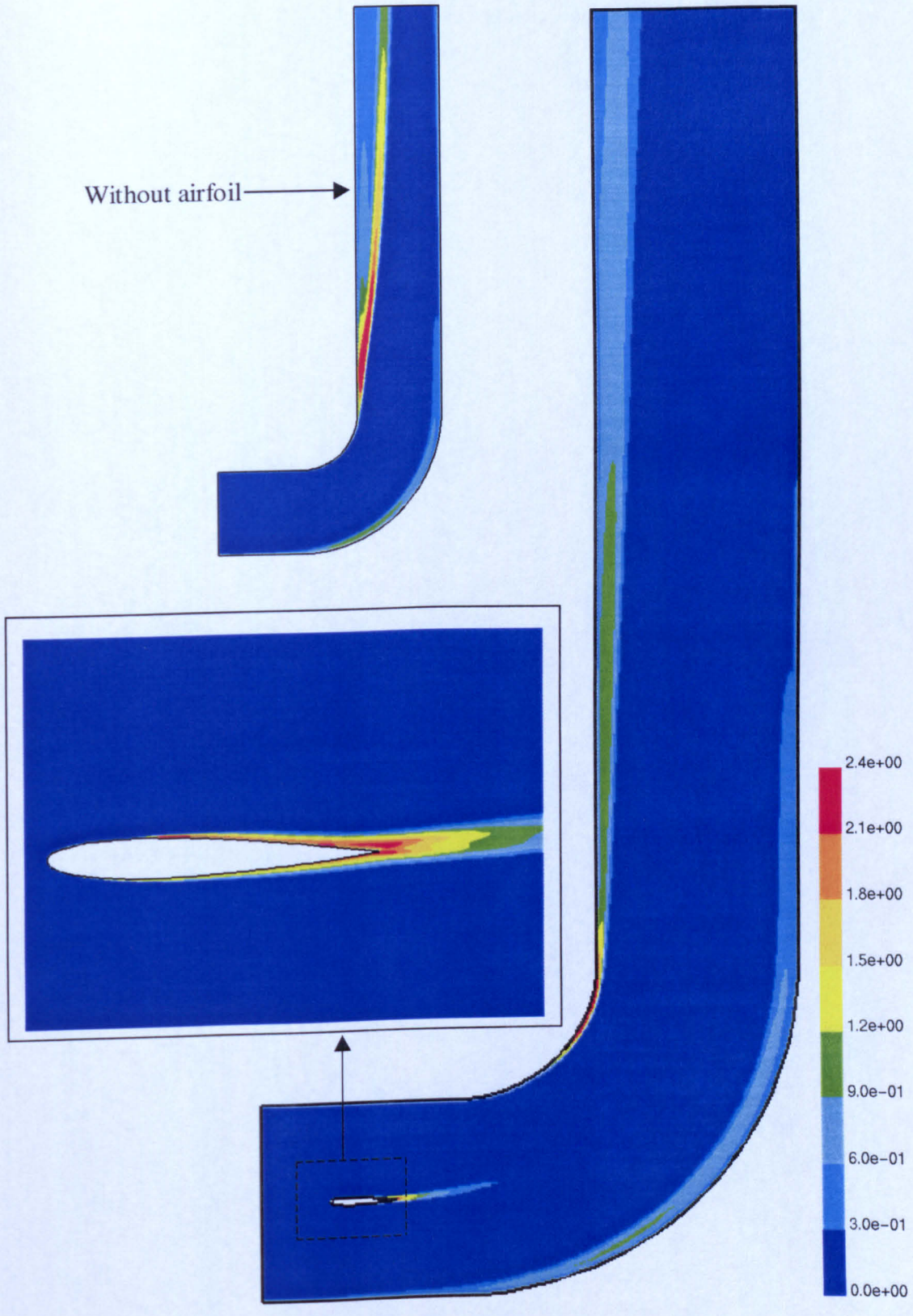

Figure 7.13: Turbulence kinetic energy (m^2/s^2) distribution (obtained using RSM and QUICK scheme) of the flow domain at z/H = 0.5 on the x-y plane. (Original in colour).

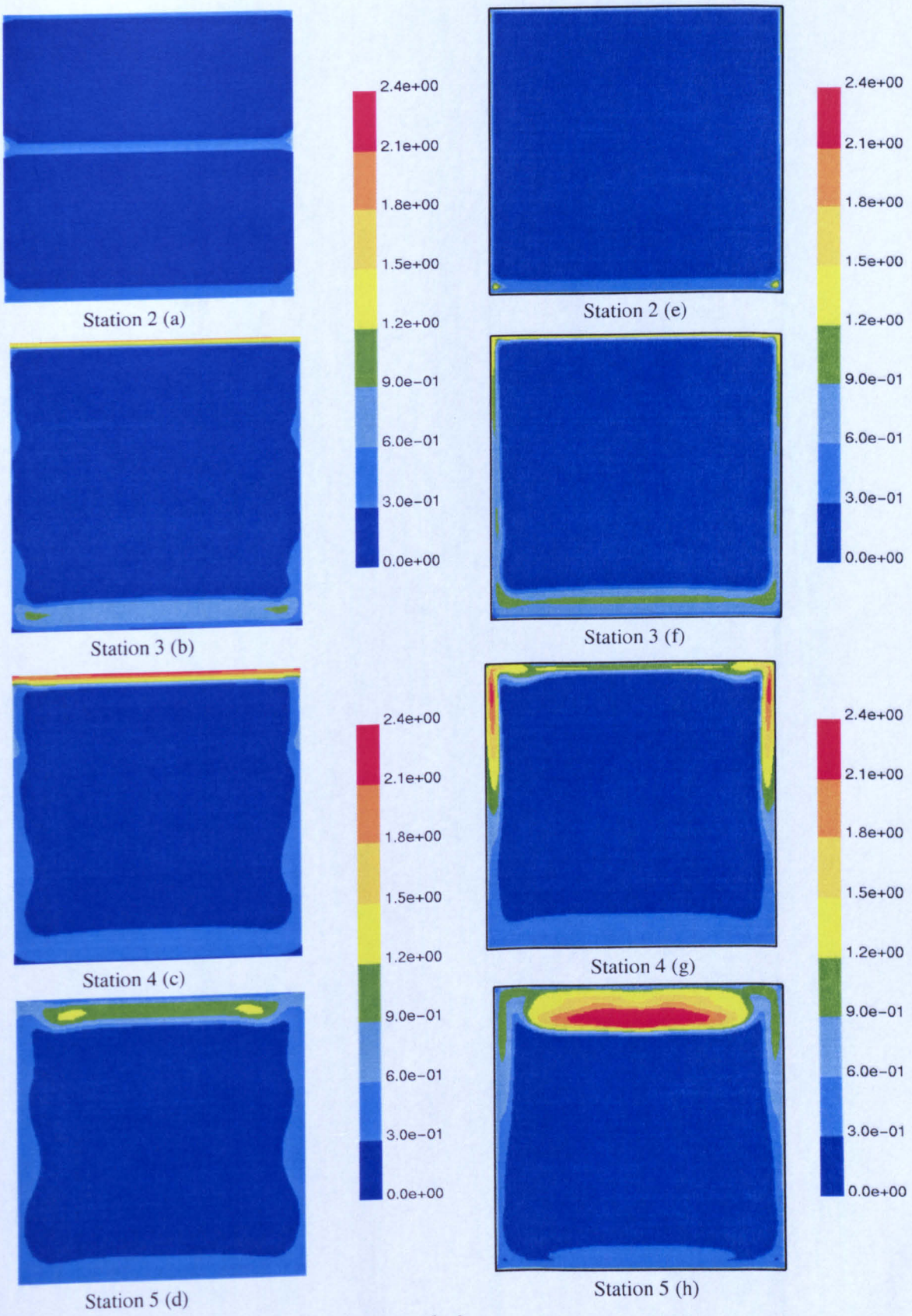

Figure 7.14: Turbulence kinetic energy (m^2/s^2) distribution (obtained using RSM and QUICK scheme) on the y-z plane at stations 2 to 5: (a-d) with airfoil, (e-h) without airfoil. (Original in colour).

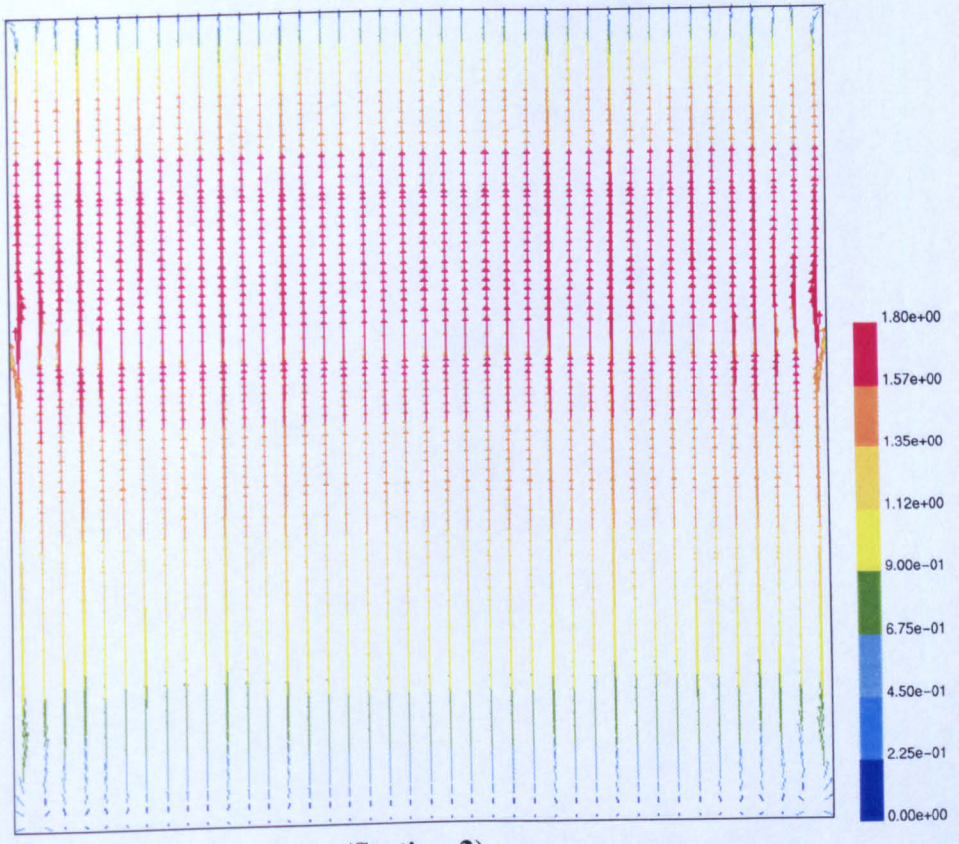

(Station 2)

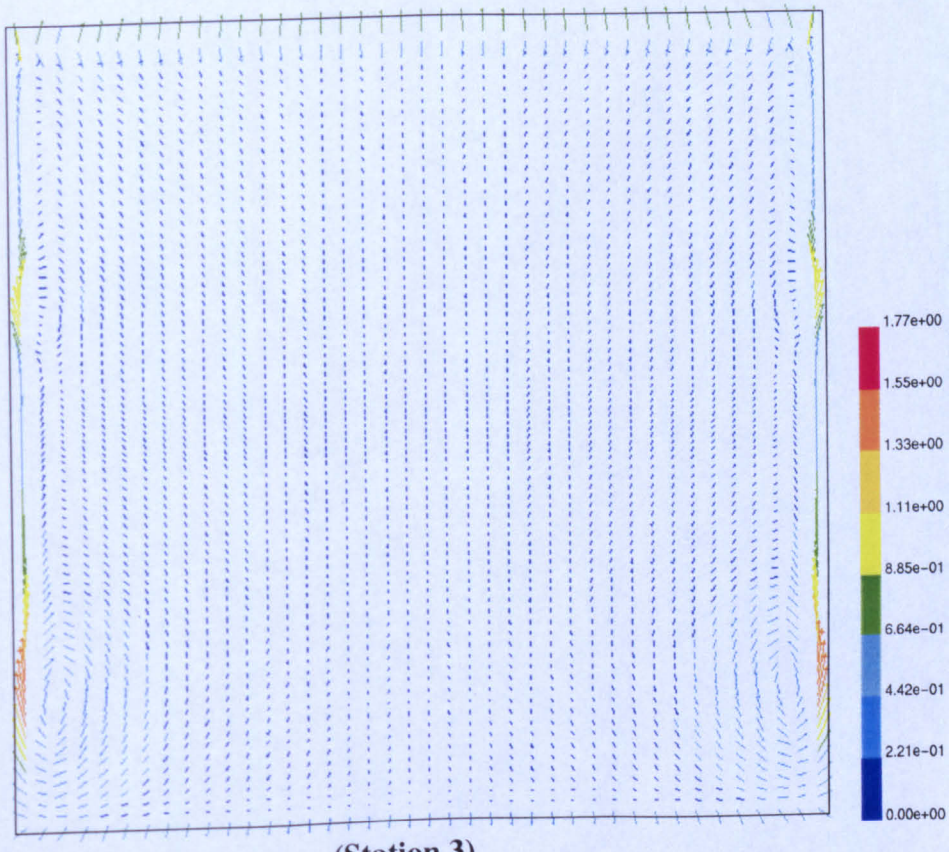

(Station 3)

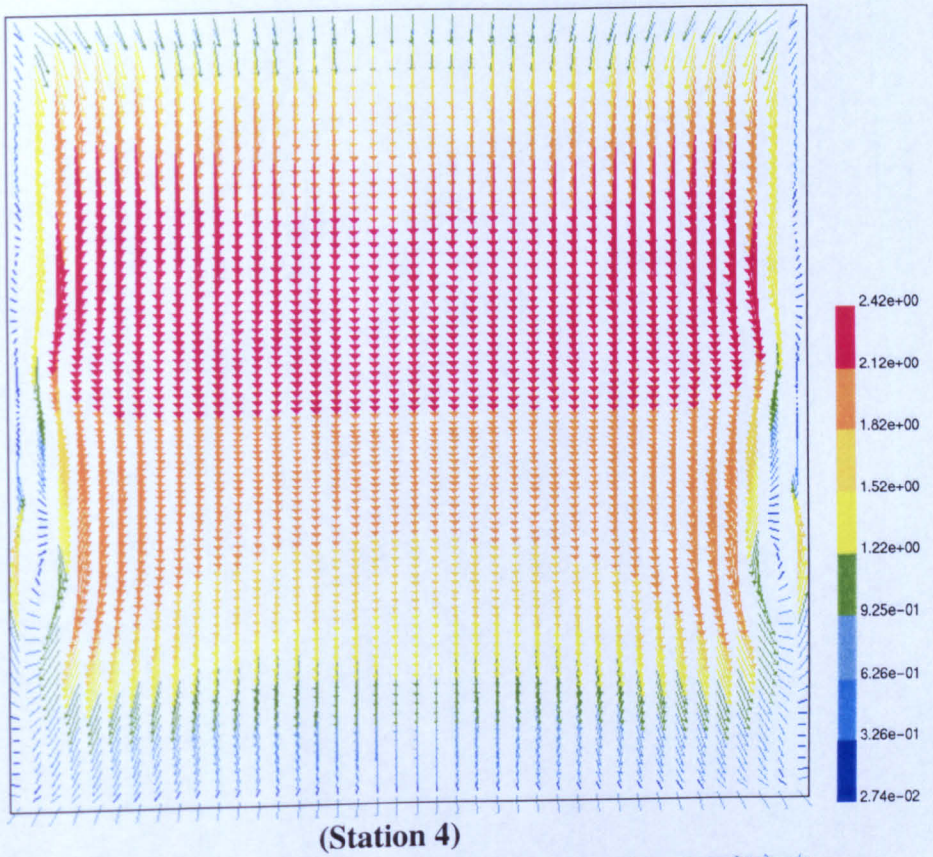

(Station 4)

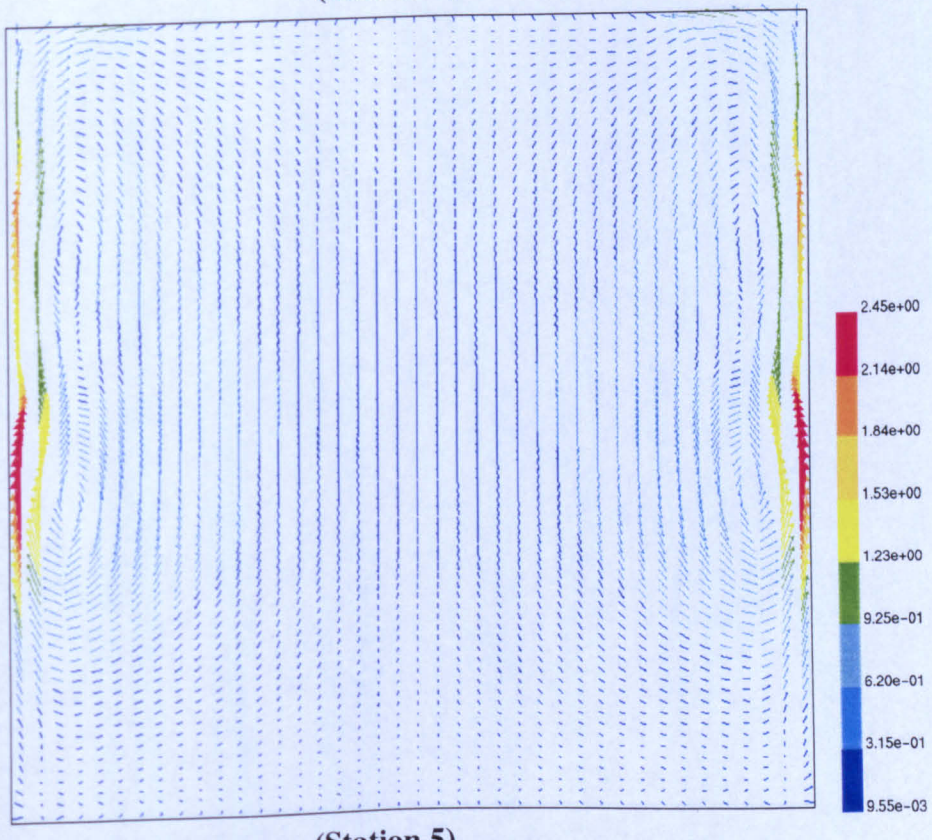

(Station 5)

Figure 7.15: The velocity magnitude (m/s) distribution (obtained using RSM and QUICK scheme) on the y-z plane at stations 2 to 5.
(Original in colour).

Chapter 8

8. CONCLUSIONS AND RECOMMENDATIONS

8.1. Conclusions

In this Chapter, the main conclusions emerging from the detailed experimental and numerical investigations conducted on a turbulent airfoil (NACA 0012) wake subjected to the combined effects of streamwise curvature and pressure gradient are summarized. The conclusions of experimental and numerical works are detailed separately followed by recommendations for further research on curved wakes.

8.1.1. Experimental investigation

The experimental static pressure distribution on the concave and convex walls of the flow domain indicated an adverse (positive) pressure gradient on the concave surface and favourable (negative) pressure gradient on the convex surface between stations 1 and 2. But, in between stations 3 and 4, the pressure gradients on the concave and convex walls became favourable and adverse, respectively. Also, on the convex wall, the flattening of the static pressure profile in the close proximity of station 4 (bend exit) indicated that the flow was close to separation. Therefore, within the flow domain, particularly in the bend section, the curvature and the changes in the pressure gradient contributed to the existence of a complex flow phenomenon.

Despite variations in the boundary layer region, the mean and turbulence quantities at station 1 were approximately symmetrical with respect to the central plane ($z/H = 0.5$) of the flow domain. Also, the measurements in the normal and spanwise directions at the centre of this station showed a large inviscid region with streamwise turbulence intensity of 0.3% of the mainstream velocity. Therefore, the airfoil is located in a uniform flow with low turbulence level which provides a suitable upstream flow conditions to study the wake of an airfoil, both experimentally and theoretically.

Both probe calibration error and misalignment error investigations showed that they can affect significantly the measured values of the normal and spanwise velocity components, but the effects on the turbulence quantities are small. Also, changes in the sampling frequency within a range of 8 kHz to 12 kHz did not affect the mean and turbulence quantities significantly. Thus, considering that careful attention was paid to the alignment of the probe and calibration, the experimental data has been obtained with a good degree of accuracy.

The spanwise measurements at the wake centre at stations 2 to 5 showed symmetrical profiles about the central plane (z/H = 0.5) as also occurred at station 1. Hence, the measurements were limited to two planes only, namely, at z/H = 0.5 and 0.6 in the wake region.

The following conclusions were made:

1) Due to the effects of streamwise curvature and pressure gradient, the mean velocity profiles at each measuring station of the bend showed an asymmetric wake structure about the wake centreline. Also, in the absence of the airfoil, the mean velocity distribution in the curved section approximately followed a linear profile across the wake region. The results showed that the development of the wake region was not affected by the boundary layers on the concave and convex walls of the duct within which the airfoil was placed, particularly in the upstream tangent and in the bend section.

2) The derived half-widths at stations 2 to 4 indicated larger magnitude on the inner side of the wake region than their corresponding ones on the outer side. Also, the half-width of both sides increased as the streamwise distance from the airfoil trailing edge increased. But, increases in the mainstream velocity reduced the half-width of both sides of the wake region.

3) The derived maximum velocity defect increased as the mainstream velocity increased. But, unlike the half-width of the wake region, the results showed a reduction in their magnitudes as the streamwise distance from the airfoil trailing

edge increased.

4) The magnitude of all measured Reynolds stresses in the wake region increased with increasing mainstream velocity. But, the peaks and bulge structure in the intensity profiles, particularly in the streamwise and spanwise intensities in the wake region were more pronounced at higher mainstream velocities.

5) The curvature and pressure gradient enhanced the Reynolds stresses on the inner side of the wake region and suppressed it on the outer side of the wake region. Furthermore, the turbulence shear stresses were influenced more strongly by the combined curvature and pressure gradient than the normal stresses.

8.1.2. Numerical investigation

The three-dimensional computations predicted the overall features of the flow satisfactorily. Based on the comparison with the experimental results, the following conclusions were made:

1) The trends exhibited in the experimental static pressure distribution on the concave and convex walls were predicted closely by all turbulence models. Using higher order scheme of QUICK indicated some improvement in the bend section and in the downstream tangent of the flow domain. However, the experimental trend at the exit of the bend, particularly on the convex wall was not predicted correctly by any of the turbulence models employed, which could be due to the flow being close to separation at this location.

2) At station 2, the mean streamwise velocity profiles predicted by all turbulence models agreed closely with each other. But, as the streamwise distance increased, the differences between the k-ε based models and the RSM increased, which indicated different responses of turbulence models to the effects of curvature and pressure gradient. At each measuring station, the peak value and the shift of the wake region were over-predicted by all turbulence models.

3) All the numerical results indicated asymmetric wake structure with respect to the

wake centreline as occurred in the experimental results. The profiles obtained across the whole cross-section of the bend section (stations 2 to 4) showed good agreement with the experimental results, but the experimental flow pattern at station 5, particularly on the convex side was not correctly predicted by any of the turbulence models. Furthermore, using the higher order scheme of QUICK indicated some improvement at this station.

4) The wake half-width of all turbulence models showed close agreement with each other at station 2 but varied significantly at stations 3 and 4. The comparison with the experimental results indicated that the turbulence models over-predict the wake half-width and the maximum velocity defect at each station.

5) The Reynolds stresses $\overline{u'^2}$, $\overline{v'^2}$, $\overline{w'^2}$ and $-\overline{u'v'}$ obtained from the RSM simulation showed fairly good agreement with the experimental profiles at stations 2 to 4. Despite small differences in their peak values and the shift of the wake region, the model not only satisfactorily captured the asymmetry in the profiles at each station but also indicated strong influence of the curvature and pressure gradient on the turbulence shear stress $-\overline{u'v'}$ compared with normal stresses. Using the higher order scheme of QUICK indicated significant improvements in the boundary layer region of concave and convex walls at each measuring station.

6) At stations 2 to 4, the predicted turbulence kinetic energy (k) of RSM and RNG k-ε model showed good agreement with the experimental results compared with the results of the standard and Realizable k-ε models. This comparison, therefore, indicated that the additional terms and functions in the transport equations of k and its dissipation rate (ε) of the RNG and Realizable k-ε models can significantly improve the prediction of complex flows.

7) The use of the two-layer zonal model for the near-wall region of the airfoil was essential in obtaining the degree of agreement between predictions and experiments.

8) The velocity field in the y-z plane at stations 3 to 5 indicated the formation of the secondary motion in the bend section due to the imbalance between radial pressure

gradient force and centrifugal force. But, part of fluid migrating from the concave side to the convex side along the sidewalls was interrupted by the wake and boundary layer interaction process, which led to the formation of two pairs of small vortices.

9) The results as shown in the contour plots in the x-y and y-z planes showed that the boundary layers on the convex wall of the downstream tangent and on the sidewalls of the flow domain were compressed by the presence of the airfoil. The turbulence quantities in the sidewalls boundary layer region were also affected by smaller vortices generated from the secondary motion. However, the plots obtained in the y-z plane showed a symmetry condition with respect to the central plane of the duct (z/H = 0.5), thus a high degree of two-dimensionality.

8.2. Recommendations for future work

The present study could be extended experimentally as well as numerically. The recommendations for further research on turbulent airfoil wake in a curved duct are as follows:

1) It is well known that the wake behind a solid body is mainly influenced by the boundary layers developing on the surfaces of the body. Therefore, the present investigation may be extended experimentally as well as numerically to analyse the wake structure of asymmetrical bodies, such as curved plate or airfoil, where the boundary layers on upper and lower surfaces are significantly different due to the profile of the body and local curvature. This type of investigation has not been considered at all in the previous studies on curved wakes.

2) The present study may be extended experimentally to include non-isothermal situations, where a heated body, such as an airfoil could be used. Such studies could provide different set of experimental data for validation of numerical models involving heat transfer.

3) Further work could include a study of mean and turbulence quantities in the curved wake region of an airfoil at various angles of attack, which has been kept zero in the previous studies and also in the present investigation.

4) Although the experimental part of the study was concentrated on obtaining mean and turbulence quantities, the flow field was not examined visually, which can be done using smoke visualisation technique. This will provide more detailed information about the wake structure, particularly the growth of the wake region in the bend.

5) Although the use of the two-layer zonal model on the airfoil was found to be superior to the standard wall functions method, the discrepancies between the experimental and numerical results could still be partially due to the near wall modelling. Therefore, future work is recommended on improvement of the near

wall modelling.

6) Because of the use of the two-layer zonal model, a substantial number of cells were required close to the walls of the flow domain. Once the two-layer model is invoked within the FLUENT code (version 5), it is applied to all the walls of the flow domain. Future work, therefore, should be directed towards implementing different near wall treatments at different walls. This approach would reduce the computational requirements, such as computer time and memory substantially.

Appendix I- Geometry of the wind tunnel

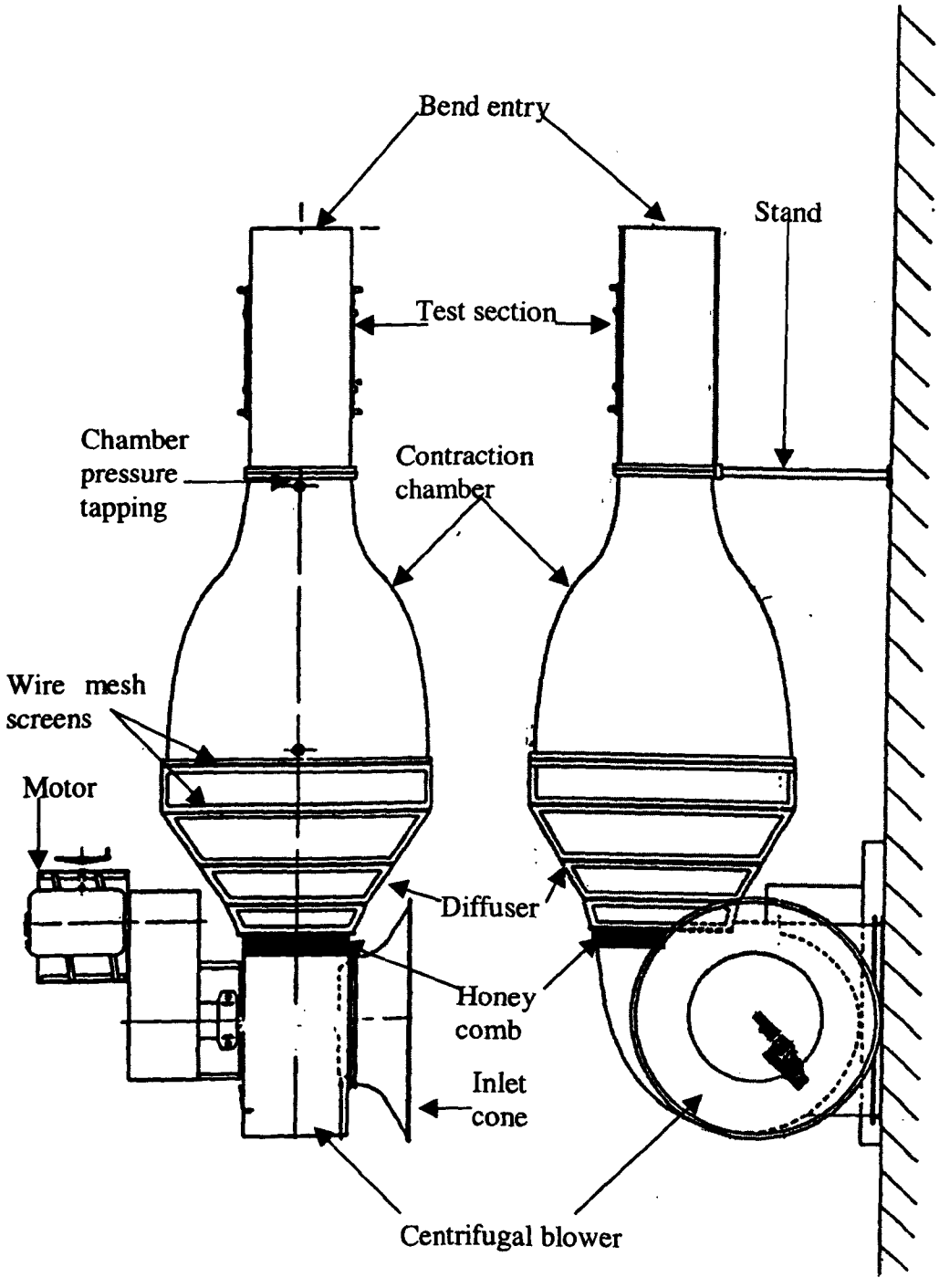

Figure A1.1: A schematic diagram of the wind tunnel.

Appendix II - Geometry of the airfoil

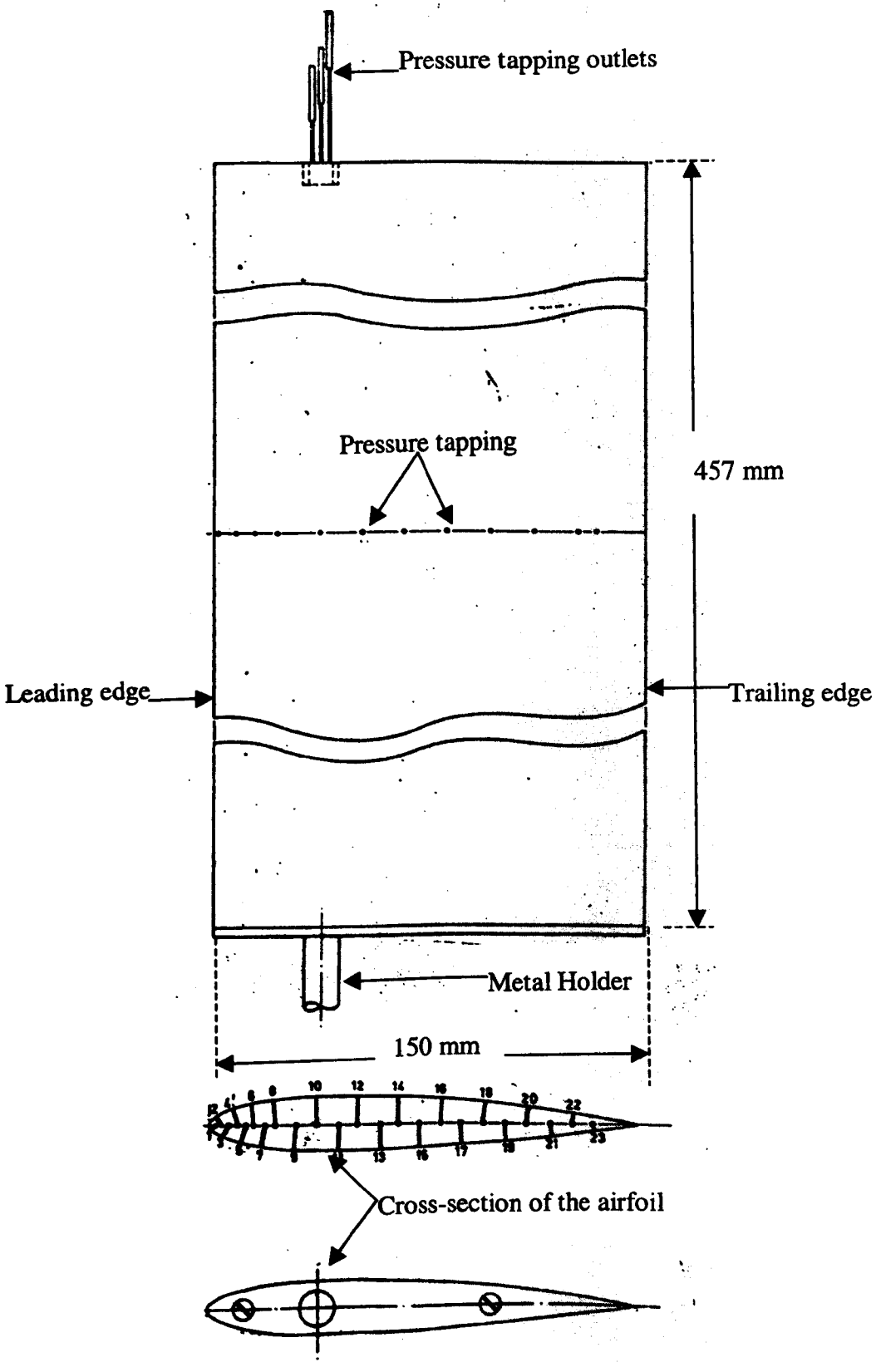

Figure A2.1: A schematic diagram of the airfoil.

Appendix III - Experimental results

T_a = 296 K, P_a = 766 mm Hg	
Contraction-section static pressure difference ($mm\ H_2O$)	**Pitot –static tube Pressure difference** ($mm\ H_2O$)
0.00	0.00
1.00	0.63
2.00	1.43
2.90	2.17
3.75	2.87
5.00	3.89
5.75	4.50
6.65	5.21
7.55	5.96
8.55	6.75
9.55	7.60
10.35	8.25
11.05	8.84
12.35	9.96
12.85	10.33
13.80	11.10
14.85	12.01
15.75	12.74
16.25	13.12
17.25	13.92
17.95	14.55
19.25	15.58
19.95	16.17
20.65	16.71
22.25	18.07
23.25	18.87
23.85	19.45
25.55	20.80
26.35	21.47
27.15	22.06
30.45	24.86
31.50	25.72
33.95	27.70
35.50	28.98
37.20	30.38

(a)

T_a = 294 K, P_a = 101.4 (kPa)				
Jet velocity (m/s)	**Wire 1 voltage** (volts)	**Wire 2 voltage** (volts)	**Wire 1 velocity** (m/s)	**Wire 2 velocity** (m/s)
0.00	1.41	1.35	0.00	0.00
1.01	1.59	1.52	1.00	1.00
2.04	1.68	1.61	2.04	2.05
3.02	1.75	1.68	3.05	3.05
4.05	1.80	1.73	4.11	4.10
5.06	1.84	1.77	5.01	5.01
6.06	1.88	1.80	6.03	6.03
6.97	1.91	1.83	6.96	6.95
7.91	1.94	1.86	7.89	7.89
9.06	1.97	1.89	9.04	9.03
10.05	1.99	1.92	10.04	10.03
11.20	2.02	1.94	11.20	11.21
12.19	2.04	1.96	12.19	12.20
13.08	2.06	1.98	13.09	13.09
14.06	2.08	2.00	14.08	14.08
14.70	2.10	2.01	14.74	14.73
16.00	2.12	2.04	16.02	16.03
17.02	2.14	2.06	17.04	17.04
18.02	2.16	2.07	18.03	18.03
18.95	2.17	2.09	18.95	18.96
19.88	2.19	2.10	19.89	19.89
20.81	2.20	2.12	20.81	20.81
21.66	2.21	2.13	21.65	21.64
22.77	2.23	2.14	22.76	22.77
23.68	2.24	2.16	23.66	23.66
24.81	2.26	2.17	24.78	24.79

(b)

Table A3.1: Calibrations results; (a) Tunnel calibration, (b) Cross-wire probe calibration.

Distance (mm)	Angle of attack = +5° P_a = 767 (mm Hg) T_a = 300 (K) U_o = 14.9 (m/s) P_o = 4.43 (mm H_2O)			Angle of attack = 0° P_a = 767 (mm Hg) T_a = 300 (K) U_o = 14.9 (m/s) P_o = 4.47 (mm H_2O)			Angle of attack = -5° P_a = 767 (mm Hg) T_a = 301 (K) U_o = 14.6 (m/s) P_o = 4.25 (mm H_2O)		
	Pressure* (mm H_2O)	Pressure* (Pa)	C_p	Pressure* (mm H_2O)	Pressure* (Pa)	C_p	Pressure* (mm H_2O)	Pressure* (Pa)	C_p
1.5	13.60	133.42	0.68	-13.30	-130.47	-1.31	-34.65	-339.92	-3.02
7.6	5.35	52.48	0.07	-10.45	-102.51	-1.10	-29.05	-284.98	-2.59
15.2	2.85	27.96	-0.12	-8.85	-86.82	-0.98	-15.60	-153.04	-1.54
22.9	1.65	16.19	-0.21	-7.95	-77.99	-0.91	-13.25	-129.98	-1.36
38.1	0.65	6.38	-0.28	-6.35	-62.29	-0.80	-10.15	-99.57	-1.12
53.3	0.70	6.87	-0.28	-4.65	-45.62	-0.67	-7.25	-71.12	-0.89
68.6	1.15	11.28	-0.24	-3.35	-32.86	-0.58	-4.65	-45.62	-0.69
83.8	1.85	18.15	-0.19	-2.35	-23.05	-0.50	-2.55	-25.02	-0.53
99.1	2.45	24.03	-0.15	-1.15	-11.28	-0.41	-0.65	-6.38	-0.38
114.3	3.15	30.90	-0.10	1.25	12.26	-0.24	0.85	8.34	-0.26
129.5	3.65	35.81	-0.06	2.75	26.98	-0.13	2.75	26.98	-0.12

(a)

Distance (mm)	Angle of attack = +5° P_a = 767 (mm Hg) T_a = 300 (K) U_o = 14.9 (m/s) P_o = 4.43 (mm H_2O)			Angle of attack = 0° P_a = 767 (mm Hg) T_a = 300 (K) U_o = 14.9 (m/s) P_o = 4.47 (mm H_2O)			Angle of attack = -5° P_a = 767 (mm Hg) T_a = 301 (K) U_o = 14.6 (m/s) P_o = 4.25 (mm H_2O)		
	Pressure* (mm H_2O)	Pressure* (Pa)	C_p	Pressure* (mm H_2O)	Pressure* (Pa)	C_p	Pressure* (mm H_2O)	Pressure* (Pa)	C_p
0.8	-9.60	-94.18	-1.04	16.65	163.34	0.90	18.35	180.01	1.09
3.8	-10.15	-99.57	-1.09	10.65	104.48	0.45	17.35	170.20	1.02
11.4	-7.95	-77.99	-0.92	5.55	54.45	0.08	12.10	118.70	0.61
19.1	-6.65	-65.24	-0.83	3.45	33.84	-0.08	9.05	88.78	0.37
30.5	-5.25	-51.50	-0.72	2.45	24.03	-0.15	6.85	67.20	0.20
45.7	-3.25	-31.88	-0.57	2.55	25.02	-0.14	5.75	56.41	0.12
61.0	-1.85	-18.15	-0.47	2.85	27.96	-0.12	5.25	51.50	0.08
76.2	-0.85	-8.34	-0.39	3.25	31.88	-0.09	5.05	49.54	0.06
91.4	0.10	0.98	-0.32	3.80	37.28	-0.05	4.95	48.56	0.05
106.7	1.95	19.13	-0.18	4.35	42.67	-0.01	5.05	49.54	0.06
121.9	3.00	29.43	-0.11	4.95	48.56	0.04	5.05	49.54	0.06
137.2	3.80	37.28	-0.05	5.35	52.48	0.06	4.95	48.56	0.05

(b)

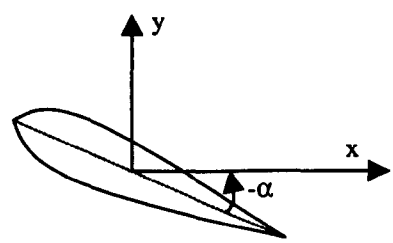

* Static pressure relative to atmospheric pressure.

Table A3.2: Airfoil pressure coefficient: (a) upper surface, (b) lower surface.
(Distance measured along chord length)

x/H	Concave static pressure with airfoil P_a = 748 (mm Hg) T_a = 290 (K), U_o = 9.95 (m/s)			Concave static pressure without airfoil P_a = 748 (mm Hg) T_a = 289 (K), U_o = 10.2 (m/s)		
	Pressure* (mm H_2O)	Pressure* (Pa)	C_p	Pressure* (mm H_2O)	Pressure* (Pa)	C_p
0.109	2.15	21.092	0.000	1.9	18.639	0.000
0.372	2.25	22.073	0.017	2.05	20.111	0.023
0.635	2.55	25.016	0.066	2.45	24.035	0.086
0.897	3.25	31.883	0.182	3.25	31.883	0.210
1.000	3.65	35.807	0.248	3.65	35.807	0.272
1.269	4.35	42.674	0.363	4.45	43.655	0.397
1.538	4.65	45.617	0.413	4.85	47.579	0.459
1.807	4.85	47.579	0.446	5.05	49.541	0.490
2.077	4.95	48.560	0.462	5.15	50.522	0.506
2.341	5	49.050	0.471	5.15	50.522	0.506
2.449	4.95	48.560	0.462	5.25	51.503	0.521
2.879	4.95	48.560	0.462	5.15	50.522	0.506
3.148	4.65	45.617	0.413	4.85	47.579	0.459
3.414	4.1	40.221	0.322	4.25	41.693	0.366
3.681	3.15	30.902	0.165	3.25	31.883	0.210
3.790	2.4	23.544	0.041	2.5	24.525	0.093
4.053	1.25	12.263	-0.149	1.3	12.753	-0.093
4.315	0.65	6.377	-0.248	0.75	7.358	-0.179
4.578	0.45	4.415	-0.281	0.55	5.396	-0.210

x/H	Convex static pressure with airfoil P_a = 754 (mm Hg) T_a = 290 (K), U_o = 9.81 (m/s)			Convex static pressure without airfoil P_a = 754 (mm Hg) T_a = 292 (K), U_o = 9.84 (m/s)		
	Pressure* (mm H_2O)	Pressure* (Pa)	C_p	Pressure* (mm H_2O)	Pressure* (Pa)	C_p
0.11	1.2	11.772	0.000	1.55	15.206	0.000
0.37	0.6	5.886	-0.101	1.25	12.263	-0.051
0.63	0.15	1.472	-0.177	0.75	7.358	-0.135
0.90	-1	-9.810	-0.371	-0.65	-6.377	-0.371
1.11	-5.15	-50.522	-1.071	-4.95	-48.560	-1.096
1.22	-6.75	-66.218	-1.341	-6.65	-65.237	-1.383
1.33	-7.45	-73.085	-1.459	-7.35	-72.104	-1.501
1.66	-6.95	-68.180	-1.375	-6.95	-68.180	-1.433
1.77	-6.15	-60.332	-1.240	-6.35	-62.294	-1.332
1.89	-4.75	-46.598	-1.004	-4.95	-48.560	-1.096
2.00	-3.25	-31.883	-0.751	-3.35	-32.864	-0.826
2.23	-3.15	-30.902	-0.734	-3.1	-30.411	-0.784
2.44	-2.7	-26.487	-0.658	-2.6	-25.506	-0.700
2.75	-0.35	-3.434	-0.261	-0.35	-3.434	-0.320
3.02	0.15	1.472	-0.177	0.15	1.472	-0.236
3.52	0.45	4.415	-0.126	0.45	4.415	-0.185
3.83	0.45	4.415	-0.126	0.45	4.415	-0.185
4.13	0.45	4.415	-0.126	0.45	4.415	-0.185
4.44	0.45	4.415	-0.126	0.45	4.415	-0.185

* Static pressure relative to atmospheric pressure.

Table A3.3: Pressure coefficient measurements on the concave and convex walls of the Bend. (Distance x is measured from station 1)

y (mm)	Station 1 P_a = 772 (mm Hg) T_a = 295 (K) U_o = 9.2 (m/s) P_o = 1.9 (mmH_2O)		Station 2 P_a = 753 (mm Hg) T_a = 287 (K) U_o = 9.6 (m/s) P_o = 2.0 (mmH_2O)		Station 3 P_a = 760 (mm Hg) T_a = 286 (K) U_o = 9.5 (m/s) P_o = 2.0 (mmH_2O)		Station 4 P_a = 746 (mm Hg) T_a = 295 (K) U_o = 9.5 (m/s) P_o = 1.9 (mmH_2O)		Station 5 P_a = 747 (mm Hg) T_a = 296 (K) U_o = 9.3 (m/s) P_o = 1.9 (mmH_2O)	
	Pressure* (mm- H_2O)	C_p	Pressure* (mm- H_2O)	C_p	Pressure* (mm- H_2O)	C_p	Pressure* (mm- H_2O)	C_p	Pressure* (mm- H_2O)	C_p
3	1.95	0.01	3.50	0.25	4.85	0.50	3.25	0.24	0.55	-0.26
13	---	---	3.50	0.25	4.75	0.48	3.15	0.22	0.55	-0.26
23	2.05	0.03	3.50	0.25	4.75	0.48	3.05	0.20	0.55	-0.26
33	---	---	3.45	0.25	4.65	0.47	2.95	0.19	0.55	-0.26
43	2.05	0.03	3.40	0.24	4.65	0.47	2.85	0.17	0.55	-0.26
53	---	---	3.35	0.23	4.55	0.45	2.75	0.15	0.55	-0.26
63	2.05	0.03	3.30	0.22	4.50	0.44	2.65	0.13	0.55	-0.26
73	---	---	3.25	0.21	4.40	0.42	2.65	0.13	0.55	-0.26
83	2.05	0.03	3.15	0.19	4.30	0.40	2.55	0.11	0.55	-0.26
103	2.05	0.03	3.05	0.18	4.05	0.36	2.35	0.07	0.55	-0.26
113	---	---	3.00	0.17	3.95	0.34	2.25	0.06	0.55	-0.26
123	2.05	0.03	2.90	0.15	3.75	0.31	2.15	0.04	0.55	-0.26
133	---	---	2.85	0.14	3.65	0.29	1.95	0.00	0.55	-0.26
143	2.05	0.03	2.75	0.12	3.50	0.26	1.85	-0.02	0.55	-0.26
153	---	---	2.65	0.11	3.35	0.24	1.75	-0.04	0.55	-0.26
163	2.05	0.03	2.55	0.09	3.25	0.22	1.55	-0.07	0.55	-0.26
173	---	---	2.45	0.07	3.05	0.18	1.45	-0.09	0.55	-0.26
183	1.95	0.01	2.35	0.05	2.90	0.16	1.35	-0.11	0.55	-0.26
203	1.95	0.01	2.20	0.03	2.55	0.09	1.05	-0.17	0.45	-0.28
213	---	---	2.10	0.01	2.35	0.06	0.85	-0.20	0.45	-0.28
223	1.95	0.01	1.95	-0.02	2.20	0.03	0.75	-0.22	0.45	-0.28
233	---	---	1.85	-0.03	2.00	0.00	0.65	-0.24	0.45	-0.28
243	1.85	-0.01	1.75	-0.05	1.80	-0.04	0.45	-0.28	0.45	-0.28
253	---	---	1.65	-0.07	1.55	-0.08	0.25	-0.31	0.45	-0.28
263	1.80	-0.02	1.55	-0.09	1.35	-0.12	0.15	-0.33	0.45	-0.28
273	---	---	1.35	-0.12	1.15	-0.15	0.00	-0.36	0.35	-0.29
283	1.75	-0.03	1.20	-0.15	0.90	-0.20	-0.15	-0.39	0.35	-0.29
303	1.70	-0.04	0.95	-0.19	0.40	-0.29	-0.55	-0.46	0.25	-0.31
313	---	---	0.75	-0.23	0.05	-0.35	-0.75	-0.50	0.15	-0.33
323	1.70	-0.04	0.60	-0.25	-0.15	-0.38	-0.85	-0.52	0.05	-0.35
333	---	---	0.45	-0.28	-0.50	-0.45	-1.05	-0.56	0.00	-0.36
343	1.65	-0.05	0.25	-0.31	-0.85	-0.51	-1.35	-0.61	-0.05	-0.37
353	---	---	0.15	-0.33	-1.25	-0.58	-1.55	-0.65	-0.05	-0.37
363	1.65	-0.05	0.00	-0.36	-1.65	-0.65	-1.65	-0.67	-0.15	-0.39
373	---	---	-0.15	-0.38	-2.05	-0.72	-1.85	-0.70	-0.15	-0.39
383	1.60	-0.06	-0.35	-0.42	-2.50	-0.80	-2.05	-0.74	-0.15	-0.39
403	1.60	-0.06	-0.65	-0.47	-3.55	-0.99	-2.30	-0.79	-0.15	-0.39
413	---	---	-0.75	-0.49	-4.15	-1.09	-2.45	-0.82	-0.05	-0.37
423	1.60	-0.06	-0.95	-0.52	-4.75	-1.20	-2.55	-0.83	-0.05	-0.37
433	---	---	-1.05	-0.54	-5.35	-1.31	-2.60	-0.84	0.05	-0.35
443	1.60	-0.06	-1.05	-0.54	-5.95	-1.41	-2.60	-0.84	0.15	-0.33
453	---	---	-1.05	-0.54	-6.65	-1.54	---	---	---	---

* Static pressure relative to atmospheric pressure.

Table A3.4: Pressure coefficient measurements in the normal direction at each station. Normal distance y is measured from the lower (concave) wall.

Station 1 – mean velocities and turbulence quantities

U_o = 9.9 (m/s), P_a = 759 (mm Hg), T_a = 293 (K), z/H = 0.5

y (mm)	Umean (m/s)	Urms (m/s)	Vmean (m/s)	Vrms (m/s)	Wmean (m/s)	Wrms (m/s)	$\overline{u'v'}$ (m^2/s^2)	$\overline{u'w'}$ (m^2/s^2)
1.4	6.31	0.84	0.19	0.58	0.48	0.74	-0.120	-0.198
1.6	6.45	0.82	0.20	0.56	0.30	0.72	-0.136	-0.180
1.8	6.65	0.80	0.18	0.55	0.19	0.70	-0.132	-0.161
2	6.78	0.79	0.17	0.53	0.10	0.68	-0.137	-0.143
2.2	6.86	0.78	0.17	0.52	0.07	0.67	-0.140	-0.126
2.4	7.02	0.77	0.16	0.51	0.03	0.66	-0.136	-0.125
2.6	7.11	0.76	0.16	0.50	0.02	0.66	-0.135	-0.120
2.8	7.19	0.75	0.15	0.50	-0.02	0.65	-0.137	-0.115
3	7.21	0.74	0.14	0.50	-0.04	0.65	-0.136	-0.104
3.2	7.31	0.74	0.14	0.50	-0.05	0.64	-0.136	-0.110
3.4	7.42	0.73	0.13	0.50	-0.06	0.64	-0.138	-0.102
3.6	7.45	0.73	0.13	0.49	-0.08	0.63	-0.133	-0.106
3.8	7.52	0.73	0.12	0.49	-0.09	0.64	-0.139	-0.099
4	7.61	0.72	0.11	0.48	-0.09	0.63	-0.133	-0.103
4.2	7.64	0.71	0.12	0.48	-0.10	0.62	-0.128	-0.101
4.4	7.71	0.71	0.11	0.48	-0.11	0.62	-0.132	-0.101
4.6	7.77	0.71	0.12	0.48	-0.11	0.62	-0.132	-0.102
4.8	7.82	0.70	0.11	0.48	-0.12	0.61	-0.131	-0.107
5	7.86	0.68	0.11	0.47	-0.13	0.61	-0.126	-0.100
5.5	8.00	0.68	0.10	0.46	-0.15	0.60	-0.123	-0.099
6	8.10	0.68	0.11	0.46	-0.15	0.60	-0.124	-0.100
6.5	8.29	0.66	0.09	0.45	-0.17	0.58	-0.120	-0.098
7	8.42	0.65	0.09	0.44	-0.17	0.56	-0.112	-0.090
7.5	8.52	0.64	0.09	0.44	-0.18	0.56	-0.111	-0.091
8	8.62	0.63	0.10	0.42	-0.19	0.54	-0.103	-0.085
8.5	8.74	0.62	0.09	0.42	-0.19	0.53	-0.103	-0.086
9	8.79	0.60	0.10	0.41	-0.20	0.52	-0.097	-0.082
9.5	8.93	0.58	0.10	0.39	-0.21	0.50	-0.090	-0.079
10	9.02	0.57	0.10	0.39	-0.21	0.48	-0.088	-0.071
10.5	9.13	0.55	0.10	0.37	-0.21	0.47	-0.078	-0.072
11	9.18	0.54	0.10	0.36	-0.22	0.45	-0.074	-0.069
11.5	9.30	0.51	0.10	0.34	-0.22	0.43	-0.065	-0.066
12	9.36	0.49	0.10	0.33	-0.22	0.42	-0.060	-0.063
13	9.52	0.43	0.11	0.30	-0.24	0.37	-0.047	-0.050
14	9.65	0.39	0.11	0.27	-0.25	0.32	-0.037	-0.044
15	9.76	0.33	0.11	0.24	-0.26	0.29	-0.027	-0.037
16	9.84	0.28	0.12	0.21	-0.27	0.23	-0.019	-0.024
17	9.92	0.20	0.12	0.18	-0.28	0.20	-0.010	-0.019
18	9.94	0.16	0.12	0.15	-0.29	0.17	-0.006	-0.011
19	9.99	0.12	0.12	0.13	-0.28	0.14	-0.003	-0.008
20	10.00	0.10	0.12	0.25	-0.29	0.12	-0.002	-0.005
30	10.01	0.04	0.11	0.24	-0.28	0.07	0.001	0.000
40	9.98	0.04	0.10	0.25	-0.29	0.09	0.000	0.000
50	9.98	0.04	0.10	0.24	-0.30	0.10	0.001	0.000
60	9.97	0.04	0.09	0.24	-0.30	0.10	0.001	0.000
70	9.98	0.04	0.09	0.25	-0.29	0.09	0.001	-0.001

Contd...

80	9.96	0.04	0.11	0.27	-0.27	0.09	0.001	-0.001
90	9.94	0.04	0.11	0.29	-0.27	0.10	0.001	-0.001
100	9.95	0.04	0.13	0.31	-0.24	0.11	0.001	-0.001
110	9.93	0.04	0.14	0.33	-0.23	0.11	0.001	-0.001
120	9.91	0.03	0.15	0.36	-0.23	0.12	0.000	-0.001
130	9.93	0.04	0.16	0.38	-0.24	0.12	0.000	-0.001
140	9.92	0.04	0.17	0.40	-0.26	0.12	0.000	0.000
150	9.91	0.04	0.18	0.42	-0.27	0.13	0.000	0.000
160	9.90	0.04	0.19	0.44	-0.27	0.12	0.000	0.000
170	9.91	0.04	0.20	0.47	-0.25	0.12	0.000	0.000
180	9.90	0.04	0.22	0.50	-0.25	0.13	0.000	0.000
190	9.91	0.04	0.22	0.51	-0.25	0.12	0.000	0.000
200	9.92	0.04	0.22	0.52	-0.26	0.13	0.000	0.000
210	9.90	0.04	0.21	0.53	-0.23	0.12	0.000	0.000
220	9.91	0.04	0.22	0.53	-0.23	0.13	0.000	0.000
230	9.91	0.04	0.22	0.55	-0.21	0.12	0.000	0.000
240	9.92	0.04	0.20	0.55	-0.19	0.12	0.000	0.000
250	9.93	0.04	0.20	0.54	-0.17	0.12	0.000	0.000
260	9.92	0.04	0.17	0.53	-0.16	0.14	0.001	-0.001
270	9.93	0.04	0.16	0.51	-0.16	0.15	0.001	-0.001
280	9.94	0.04	0.13	0.48	-0.15	0.15	0.001	-0.002
290	9.96	0.04	0.11	0.46	-0.16	0.15	0.001	-0.001
300	9.97	0.04	0.08	0.43	-0.18	0.16	0.001	-0.002
310	9.96	0.04	0.07	0.40	-0.21	0.16	0.000	-0.001
320	9.95	0.04	0.07	0.39	-0.26	0.17	0.001	0.000
330	9.95	0.04	0.04	0.35	-0.31	0.17	0.000	0.000
340	9.94	0.05	0.03	0.32	-0.37	0.18	0.000	0.000
350	9.95	0.05	0.02	0.30	-0.42	0.17	0.000	0.000
360	9.92	0.05	0.02	0.28	-0.51	0.18	0.000	0.001
370	9.93	0.05	0.04	0.27	-0.55	0.16	0.000	0.001
380	9.90	0.05	0.03	0.25	-0.56	0.16	0.000	0.001
390	9.79	0.05	-0.01	0.22	-0.58	0.14	0.000	0.001
400	9.76	0.04	0.01	0.22	-0.56	0.12	0.000	0.000
410	9.73	0.05	0.04	0.24	-0.50	0.12	0.000	0.000
420	9.70	0.04	0.07	0.28	-0.44	0.13	0.000	-0.001
430	9.73	0.04	0.18	0.38	-0.35	0.13	0.000	-0.001
440	9.74	0.06	0.30	0.52	-0.27	0.12	0.001	0.000
441	9.74	0.07	0.32	0.54	-0.25	0.12	0.001	0.001
442	9.73	0.08	0.35	0.56	-0.25	0.13	0.002	0.002
443	9.73	0.11	0.38	0.59	-0.22	0.15	0.004	0.003
444	9.72	0.14	0.40	0.62	-0.21	0.17	0.006	0.006
445	9.72	0.20	0.44	0.65	-0.24	0.21	0.011	0.013
445.5	9.71	0.22	0.45	0.20	-0.23	0.23	0.014	0.017
446	9.67	0.24	0.42	0.21	-0.21	0.26	0.016	0.023
446.5	9.67	0.28	0.43	0.24	-0.21	0.28	0.023	0.027
447	9.62	0.35	0.44	0.27	-0.21	0.30	0.033	0.032
447.5	9.59	0.37	0.46	0.28	-0.21	0.34	0.037	0.041
448	9.50	0.44	0.47	0.31	-0.22	0.36	0.049	0.044
448.5	9.46	0.47	0.49	0.33	-0.22	0.39	0.055	0.052
449	9.38	0.52	0.51	0.35	-0.23	0.41	0.068	0.056
449.5	9.34	0.55	0.52	0.36	-0.22	0.45	0.078	0.061
450	9.19	0.61	0.53	0.39	-0.22	0.47	0.097	0.067

Contd...

450.2	9.14	0.62	0.53	0.40	-0.23	0.48	0.105	0.067
450.2	9.14	0.62	0.55	0.41	-0.23	0.50	0.103	0.073
450.6	9.09	0.64	0.55	0.41	-0.22	0.51	0.108	0.077
450.8	9.06	0.66	0.55	0.42	-0.24	0.53	0.116	0.076
451	9.02	0.67	0.56	0.43	-0.24	0.53	0.122	0.078
451.2	8.95	0.69	0.56	0.45	-0.23	0.54	0.128	0.077
451.4	8.90	0.70	0.56	0.45	-0.24	0.55	0.138	0.079
451.6	8.85	0.70	0.57	0.46	-0.23	0.56	0.140	0.076
451.8	8.79	0.72	0.58	0.47	-0.23	0.57	0.150	0.078
452	8.72	0.73	0.58	0.47	-0.24	0.58	0.149	0.079
452.2	8.67	0.74	0.58	0.48	-0.24	0.59	0.158	0.085
452.4	8.59	0.76	0.59	0.49	-0.26	0.60	0.170	0.079
452.6	8.53	0.76	0.59	0.50	-0.24	0.61	0.168	0.081
452.8	8.46	0.78	0.59	0.50	-0.24	0.62	0.176	0.079
453	8.41	0.78	0.60	0.51	-0.26	0.63	0.180	0.076
453.2	8.38	0.78	0.61	0.52	-0.24	0.64	0.185	0.075
453.4	8.25	0.79	0.60	0.53	-0.25	0.64	0.194	0.080
453.6	8.17	0.80	0.61	0.53	-0.26	0.65	0.196	0.077
453.8	8.10	0.82	0.61	0.54	-0.26	0.67	0.201	0.086
454	7.98	0.80	0.61	0.55	-0.26	0.67	0.206	0.083
454.2	7.89	0.81	0.61	0.55	-0.26	0.67	0.210	0.086
454.4	7.81	0.82	0.61	0.56	-0.28	0.68	0.220	0.080
454.6	7.70	0.81	0.61	0.56	-0.29	0.69	0.216	0.091
454.8	7.57	0.82	0.61	0.57	-0.30	0.70	0.222	0.096
455	7.49	0.82	0.60	0.59	-0.33	0.71	0.228	0.096
455.2	7.38	0.84	0.61	0.60	-0.36	0.72	0.231	0.115
455.4	7.26	0.85	0.59	0.61	-0.41	0.74	0.239	0.135

Table A3.5: Measurements of mean and turbulence quantities in the normal direction (y) at station1.

Station 2 – mean velocities and turbulence quantities

U_o = 9.84 (m/s), P_a = 769 (mm Hg), T_a = 295 (K), z/H = 0.5

y (mm)	Umean (m/s)	Urms (m/s)	Vmean (m/s)	Vrms (m/s)	Wmean (m/s)	Wrms (m/s)	$\overline{u'v'}$ (m^2/s^2)	$\overline{u'w'}$ (m^2/s^2)
10	6.09	0.75	0.42	0.45	0.24	0.63	-0.102	-0.085
20	7.49	0.60	0.65	0.37	0.31	0.44	-0.070	-0.055
30	8.47	0.25	0.82	0.19	0.37	0.25	-0.013	-0.025
40	8.63	0.06	0.92	0.08	0.40	0.17	0.000	-0.013
50	8.69	0.04	0.98	0.07	0.42	0.09	0.000	0.000
60	8.72	0.04	1.03	0.07	0.44	0.09	0.000	0.000
70	8.78	0.04	1.09	0.07	0.46	0.10	0.000	0.000
80	8.82	0.03	1.14	0.07	0.49	0.09	0.000	0.000
90	8.86	0.03	1.20	0.07	0.52	0.09	0.000	0.000
100	8.93	0.03	1.26	0.07	0.55	0.09	0.000	-0.001
110	8.98	0.03	1.32	0.07	0.58	0.10	0.000	-0.001
120	9.02	0.03	1.37	0.07	0.62	0.10	0.000	-0.001
130	9.09	0.03	1.43	0.07	0.65	0.10	0.000	-0.001
140	9.14	0.03	1.48	0.07	0.66	0.10	0.000	-0.001
150	9.17	0.03	1.52	0.07	0.67	0.11	0.000	-0.001
160	9.21	0.04	1.56	0.07	0.68	0.11	0.000	-0.001
170	9.29	0.04	1.61	0.07	0.69	0.11	-0.001	-0.001
180	9.34	0.04	1.65	0.07	0.71	0.11	-0.001	-0.001
190	9.43	0.04	1.69	0.07	0.73	0.11	-0.001	-0.001
200	9.49	0.04	1.72	0.07	0.73	0.11	-0.001	-0.001
210	9.59	0.04	1.76	0.07	0.74	0.10	-0.001	-0.001
211	9.56	0.04	1.74	0.07	0.73	0.11	-0.001	-0.001
212	9.57	0.04	1.75	0.07	0.73	0.11	-0.001	-0.001
213	9.60	0.04	1.75	0.07	0.74	0.11	-0.001	-0.001
214	9.60	0.04	1.76	0.06	0.73	0.10	-0.001	-0.001
215	9.62	0.04	1.76	0.07	0.73	0.11	-0.001	-0.001
217	9.62	0.04	1.76	0.07	0.73	0.11	0.000	-0.001
218	9.63	0.04	1.76	0.07	0.74	0.11	-0.001	-0.001
219	9.63	0.05	1.76	0.07	0.73	0.11	-0.001	-0.001
220	9.65	0.05	1.77	0.07	0.74	0.11	-0.001	-0.001
221	9.67	0.05	1.77	0.07	0.74	0.11	0.000	-0.001
222	9.66	0.05	1.77	0.08	0.74	0.12	-0.001	-0.001
223	9.68	0.06	1.77	0.08	0.74	0.12	0.000	0.000
224	9.68	0.06	1.78	0.09	0.74	0.12	0.000	0.000
225	9.69	0.08	1.77	0.11	0.74	0.13	0.000	0.001
226	9.69	0.10	1.77	0.13	0.74	0.15	0.001	0.002
227	9.70	0.12	1.78	0.17	0.74	0.17	0.003	0.005
228	9.71	0.15	1.77	0.23	0.74	0.20	0.008	0.009
229	9.73	0.19	1.78	0.28	0.73	0.25	0.016	0.015
230	9.64	0.23	1.77	0.33	0.71	0.29	0.027	0.021
231	9.58	0.28	1.76	0.38	0.69	0.34	0.041	0.029
232	9.49	0.32	1.74	0.44	0.67	0.38	0.055	0.033
233	9.39	0.36	1.72	0.48	0.66	0.42	0.064	0.034
234	9.30	0.38	1.70	0.52	0.64	0.46	0.070	0.030
235	9.18	0.40	1.68	0.55	0.63	0.47	0.067	0.024
237	8.97	0.41	1.62	0.58	0.63	0.50	0.029	0.007

Contd...

238	8.94	0.42	1.61	0.58	0.63	0.51	0.004	-0.003
239	8.93	0.44	1.60	0.58	0.65	0.51	-0.022	-0.008
240	8.94	0.45	1.59	0.58	0.65	0.52	-0.043	-0.017
241	9.02	0.47	1.60	0.57	0.68	0.53	-0.064	-0.023
242	9.05	0.49	1.60	0.56	0.71	0.53	-0.077	-0.034
243	9.17	0.50	1.62	0.54	0.72	0.54	-0.084	-0.042
244	9.27	0.50	1.63	0.53	0.73	0.53	-0.087	-0.047
245	9.35	0.48	1.64	0.50	0.74	0.52	-0.084	-0.051
246	9.46	0.47	1.67	0.47	0.75	0.50	-0.081	-0.053
247	9.55	0.44	1.67	0.43	0.74	0.48	-0.072	-0.053
248	9.60	0.41	1.70	0.41	0.76	0.44	-0.066	-0.047
249	9.67	0.37	1.71	0.37	0.78	0.41	-0.055	-0.043
250	9.70	0.33	1.72	0.34	0.78	0.38	-0.043	-0.039
251	9.73	0.29	1.73	0.30	0.78	0.35	-0.034	-0.034
252	9.79	0.25	1.75	0.26	0.80	0.33	-0.024	-0.029
253	9.80	0.21	1.76	0.23	0.79	0.29	-0.018	-0.022
254	9.82	0.18	1.76	0.20	0.80	0.26	-0.011	-0.016
255	9.87	0.15	1.78	0.18	0.81	0.24	-0.008	-0.013
256	9.89	0.12	1.78	0.15	0.80	0.22	-0.005	-0.009
257	9.87	0.10	1.78	0.13	0.80	0.20	-0.003	-0.007
258	9.90	0.09	1.79	0.12	0.81	0.18	-0.002	-0.005
259	9.89	0.07	1.79	0.11	0.80	0.17	-0.001	-0.004
260	9.91	0.06	1.80	0.10	0.81	0.17	-0.001	-0.003
261	9.92	0.06	1.80	0.09	0.81	0.15	-0.001	-0.002
262	9.95	0.05	1.81	0.09	0.82	0.15	0.000	-0.002
263	9.95	0.05	1.80	0.09	0.82	0.14	-0.001	-0.002
264	9.96	0.05	1.81	0.09	0.82	0.14	0.000	-0.002
265	9.98	0.05	1.81	0.09	0.83	0.14	0.000	-0.002
266	9.98	0.05	1.82	0.09	0.83	0.13	-0.001	-0.002
267	9.98	0.04	1.82	0.09	0.84	0.13	-0.001	-0.001
268	9.99	0.04	1.82	0.09	0.84	0.14	-0.001	-0.001
269	10.01	0.04	1.82	0.10	0.84	0.13	-0.001	-0.001
270	10.03	0.04	1.83	0.10	0.84	0.14	-0.001	-0.001
280	10.11	0.04	1.84	0.10	0.87	0.13	-0.001	-0.001
290	10.24	0.04	1.85	0.12	0.89	0.13	-0.001	-0.001
300	10.33	0.04	1.84	0.13	0.90	0.13	-0.001	-0.001
310	10.48	0.04	1.85	0.12	0.90	0.13	-0.001	-0.001
320	10.59	0.04	1.85	0.13	0.89	0.14	-0.002	-0.002
330	10.71	0.04	1.83	0.12	0.87	0.15	-0.002	-0.002
340	10.84	0.05	1.82	0.13	0.81	0.16	-0.002	-0.002
350	10.97	0.05	1.80	0.13	0.75	0.17	-0.002	-0.002
360	11.07	0.05	1.79	0.12	0.66	0.17	-0.002	-0.002
370	11.20	0.05	1.76	0.13	0.57	0.18	-0.002	-0.002
380	11.36	0.05	1.72	0.13	0.49	0.18	-0.003	-0.002
390	11.43	0.05	1.63	0.12	0.40	0.18	-0.002	-0.001
400	11.60	0.05	1.51	0.12	0.35	0.17	-0.002	-0.001
410	11.71	0.04	1.41	0.12	0.29	0.15	-0.001	-0.001
420	11.79	0.05	1.25	0.11	0.28	0.14	0.000	-0.001
430	11.90	0.05	1.13	0.10	0.27	0.14	0.000	-0.001

Table A3.6: Measurements of mean and turbulence quantities in the normal direction (y) at station 2.

Station 3 – mean velocities and turbulence quantities

U_o = 9.85 (m/s), P_a = 765 (mm Hg), T_a = 293 (K), **z/H** = 0.5

y (mm)	Umean (m/s)	Urms (m/s)	Vmean (m/s)	Vrms (m/s)	Wmean (m/s)	Wrms (m/s)	$\overline{u'v'}$ (m^2/s^2)	$\overline{u'w'}$ (m^2/s^2)
10	4.90	0.77	0.19	0.57	-0.31	0.79	-0.145	0.193
20	5.25	0.82	0.21	0.72	-0.16	0.78	-0.276	0.249
30	5.56	0.89	0.24	0.76	-0.10	0.78	-0.363	0.275
40	6.04	0.93	0.19	0.74	-0.07	0.74	-0.410	0.251
50	6.60	0.84	0.12	0.65	-0.13	0.65	-0.314	0.204
60	7.23	0.57	0.00	0.46	-0.17	0.47	-0.141	0.134
70	7.51	0.33	-0.04	0.34	-0.24	0.31	-0.054	0.047
80	7.69	0.13	-0.10	0.20	-0.27	0.20	-0.005	0.014
90	7.79	0.08	-0.14	0.14	-0.30	0.13	-0.001	0.003
100	7.92	0.05	-0.19	0.09	-0.33	0.11	0.001	-0.001
110	8.04	0.04	-0.21	0.08	-0.32	0.10	0.001	-0.001
120	8.14	0.04	-0.23	0.07	-0.32	0.10	0.001	-0.001
130	8.26	0.04	-0.26	0.07	-0.33	0.11	0.000	-0.001
140	8.38	0.04	-0.27	0.07	-0.33	0.11	0.001	-0.001
150	8.52	0.03	-0.29	0.07	-0.36	0.12	0.000	0.000
160	8.63	0.04	-0.31	0.07	-0.38	0.12	0.000	0.000
170	8.77	0.04	-0.32	0.07	-0.40	0.12	0.000	0.000
180	8.86	0.04	-0.33	0.07	-0.41	0.12	0.000	0.000
190	9.01	0.03	-0.35	0.07	-0.46	0.12	0.000	0.000
200	9.13	0.04	-0.35	0.07	-0.45	0.11	0.000	0.000
202	9.16	0.04	-0.36	0.07	-0.45	0.11	0.000	0.000
204	9.19	0.04	-0.36	0.07	-0.45	0.11	0.000	0.000
206	9.22	0.04	-0.37	0.07	-0.46	0.12	0.000	0.000
208	9.24	0.04	-0.37	0.07	-0.46	0.12	0.000	0.000
210	9.27	0.04	-0.37	0.07	-0.46	0.11	0.000	0.000
212	9.30	0.04	-0.37	0.07	-0.46	0.11	0.000	0.000
214	9.34	0.04	-0.38	0.07	-0.47	0.11	0.000	0.000
216	9.36	0.04	-0.37	0.07	-0.48	0.11	0.000	0.000
218	9.38	0.04	-0.38	0.07	-0.47	0.11	0.000	0.000
220	9.42	0.04	-0.38	0.07	-0.48	0.11	0.000	0.000
222	9.45	0.04	-0.38	0.07	-0.50	0.11	0.000	0.000
224	9.48	0.04	-0.39	0.07	-0.48	0.11	0.000	0.000
226	9.52	0.04	-0.40	0.07	-0.49	0.12	0.000	0.000
228	9.52	0.04	-0.41	0.07	-0.50	0.11	0.000	0.000
230	9.57	0.05	-0.41	0.08	-0.49	0.12	0.000	0.000
232	9.59	0.06	-0.41	0.08	-0.52	0.12	0.001	0.000
234	9.61	0.07	-0.42	0.09	-0.51	0.13	0.001	0.000
236	9.64	0.09	-0.42	0.11	-0.51	0.14	0.003	0.001
238	9.64	0.11	-0.42	0.13	-0.51	0.16	0.005	0.001
240	9.65	0.15	-0.43	0.16	-0.53	0.17	0.008	0.002
242	9.62	0.18	-0.43	0.18	-0.51	0.20	0.011	0.002
244	9.58	0.20	-0.43	0.20	-0.50	0.21	0.013	0.001
246	9.52	0.21	-0.43	0.22	-0.52	0.23	0.013	0.000
248	9.47	0.22	-0.43	0.24	-0.51	0.25	0.011	-0.002
250	9.46	0.23	-0.44	0.26	-0.49	0.26	0.005	-0.005
252	9.45	0.23	-0.45	0.27	-0.47	0.27	-0.003	-0.009

Contd...

254	9.50	0.23	-0.46	0.28	-0.48	0.29	-0.011	-0.013
256	9.58	0.24	-0.47	0.30	-0.48	0.30	-0.020	-0.018
258	9.60	0.25	-0.48	0.31	-0.47	0.32	-0.026	-0.022
260	9.66	0.25	-0.49	0.31	-0.47	0.32	-0.031	-0.026
262	9.72	0.25	-0.49	0.31	-0.48	0.33	-0.034	-0.027
264	9.81	0.25	-0.50	0.30	-0.48	0.32	-0.035	-0.030
266	9.87	0.23	-0.51	0.30	-0.47	0.32	-0.034	-0.029
268	9.96	0.23	-0.50	0.29	-0.47	0.31	-0.033	-0.025
270	10.06	0.21	-0.52	0.26	-0.47	0.29	-0.027	-0.022
272	10.13	0.20	-0.51	0.25	-0.48	0.28	-0.025	-0.019
274	10.19	0.17	-0.52	0.23	-0.49	0.25	-0.017	-0.017
276	10.24	0.16	-0.52	0.21	-0.46	0.23	-0.015	-0.012
278	10.31	0.13	-0.52	0.18	-0.47	0.21	-0.009	-0.010
280	10.36	0.12	-0.52	0.17	-0.46	0.19	-0.007	-0.006
282	10.40	0.10	-0.51	0.16	-0.46	0.18	-0.004	-0.004
284	10.44	0.08	-0.52	0.14	-0.50	0.17	-0.001	-0.002
286	10.48	0.08	-0.51	0.13	-0.47	0.15	-0.001	-0.002
288	10.54	0.06	-0.52	0.12	-0.48	0.15	0.000	-0.001
290	10.56	0.06	-0.51	0.11	-0.45	0.14	0.000	-0.001
292	10.62	0.05	-0.52	0.11	-0.47	0.14	0.001	0.000
294	10.66	0.05	-0.52	0.12	-0.47	0.13	0.001	-0.001
296	10.70	0.05	-0.53	0.11	-0.46	0.13	0.001	0.000
298	10.73	0.05	-0.52	0.11	-0.47	0.13	0.001	0.000
300	10.77	0.05	-0.53	0.12	-0.46	0.13	0.001	-0.001
310	11.00	0.05	-0.56	0.12	-0.45	0.13	0.002	-0.001
320	11.17	0.05	-0.58	0.13	-0.47	0.14	0.002	-0.002
330	11.40	0.05	-0.60	0.13	-0.49	0.15	0.002	-0.001
340	11.60	0.05	-0.60	0.13	-0.52	0.15	0.001	-0.001
350	11.85	0.05	-0.63	0.13	-0.56	0.16	0.001	0.000
360	12.09	0.05	-0.64	0.13	-0.62	0.19	0.001	0.000
370	12.31	0.05	-0.64	0.15	-0.71	0.19	0.001	0.001
380	12.58	0.05	-0.64	0.14	-0.82	0.18	0.001	0.001
390	12.86	0.05	-0.66	0.14	-0.91	0.20	0.001	0.001
400	13.15	0.05	-0.75	0.13	-1.00	0.19	0.001	0.001
410	13.48	0.05	-0.81	0.13	-1.07	0.17	0.002	0.001
420	13.67	0.05	-0.87	0.13	-1.06	0.17	0.001	0.001
430	14.04	0.05	-0.89	0.11	-1.02	0.16	0.001	0.000
440	14.21	0.08	-1.11	0.10	-1.01	0.18	0.001	0.002

Table A3.7: Measurements of mean and turbulence quantities in the normal direction (y) at station 3.

Station 4 – mean velocities and turbulence quantities

U_o = 9.80 (m/s), P_a = 755 (mm Hg), T_a = 288 (K), **z/H** = 0.5

y (mm)	Umean (m/s)	Urms (m/s)	Vmean (m/s)	Vrms (m/s)	Wmean (m/s)	Wrms (m/s)	$\overline{u'v'}$ (m^2/s^2)	$\overline{u'w'}$ (m^2/s^2)
10	7.40	0.57	0.08	0.52	-0.40	0.82	-0.094	-0.055
20	7.55	0.53	0.13	0.72	-0.39	0.70	-0.098	-0.044
30	7.64	0.52	0.11	0.84	-0.26	0.66	-0.121	-0.022
40	7.75	0.52	-0.02	0.85	-0.17	0.63	-0.160	-0.030
50	7.89	0.54	-0.16	0.84	-0.13	0.58	-0.207	-0.042
60	8.05	0.54	-0.30	0.83	-0.11	0.54	-0.228	-0.030
70	8.27	0.49	-0.49	0.70	-0.08	0.46	-0.187	-0.035
80	8.47	0.42	-0.64	0.60	-0.13	0.40	-0.132	-0.022
90	8.59	0.36	-0.74	0.52	-0.15	0.32	-0.088	-0.010
100	8.73	0.20	-0.93	0.33	-0.13	0.26	-0.018	-0.008
110	8.78	0.14	-1.03	0.24	-0.15	0.18	-0.004	-0.004
120	8.82	0.11	-1.12	0.20	-0.16	0.16	0.000	-0.001
130	8.91	0.09	-1.22	0.13	-0.19	0.13	0.002	-0.001
140	8.96	0.07	-1.32	0.10	-0.20	0.12	0.000	0.000
150	9.00	0.06	-1.40	0.09	-0.20	0.11	0.000	0.000
152	9.01	0.06	-1.42	0.09	-0.21	0.11	0.000	0.000
154	9.03	0.06	-1.44	0.09	-0.22	0.11	0.000	0.000
156	9.06	0.06	-1.45	0.09	-0.21	0.11	0.000	0.000
158	9.06	0.05	-1.47	0.08	-0.21	0.11	0.000	0.000
160	9.08	0.05	-1.49	0.08	-0.21	0.11	0.000	0.001
162	9.07	0.05	-1.50	0.08	-0.22	0.10	0.000	0.001
164	9.07	0.05	-1.51	0.08	-0.22	0.10	0.000	0.001
166	9.10	0.05	-1.53	0.08	-0.23	0.11	0.000	0.001
168	9.11	0.05	-1.56	0.08	-0.22	0.10	0.000	0.000
170	9.14	0.05	-1.57	0.08	-0.22	0.10	0.000	0.000
172	9.14	0.05	-1.59	0.08	-0.22	0.11	0.000	0.000
174	9.18	0.05	-1.60	0.08	-0.23	0.11	0.000	0.000
176	9.18	0.05	-1.62	0.08	-0.23	0.11	0.000	0.001
178	9.19	0.05	-1.64	0.08	-0.24	0.11	0.000	0.001
180	9.21	0.05	-1.66	0.08	-0.23	0.11	0.000	0.001
182	9.22	0.05	-1.67	0.08	-0.24	0.10	0.000	0.001
184	9.23	0.06	-1.69	0.08	-0.23	0.11	0.000	0.000
186	9.26	0.07	-1.71	0.08	-0.24	0.11	0.000	0.000
188	9.27	0.07	-1.73	0.08	-0.24	0.12	0.001	0.000
190	9.27	0.08	-1.74	0.09	-0.24	0.12	0.002	0.000
192	9.25	0.10	-1.75	0.10	-0.25	0.13	0.003	0.000
194	9.27	0.12	-1.76	0.12	-0.23	0.14	0.004	0.000
196	9.25	0.14	-1.78	0.13	-0.25	0.15	0.005	-0.001
198	9.23	0.15	-1.79	0.15	-0.23	0.16	0.006	-0.001
200	9.20	0.16	-1.80	0.17	-0.22	0.17	0.005	-0.002
202	9.18	0.16	-1.82	0.19	-0.21	0.18	0.005	-0.001
204	9.16	0.16	-1.81	0.20	-0.20	0.19	0.002	-0.001
206	9.16	0.16	-1.83	0.22	-0.20	0.20	0.000	-0.001
208	9.18	0.16	-1.85	0.24	-0.18	0.21	-0.004	0.000
210	9.20	0.17	-1.87	0.25	-0.18	0.22	-0.008	-0.003
212	9.23	0.17	-1.89	0.26	-0.18	0.22	-0.010	-0.002

Contd...

214	9.21	0.18	-1.90	0.28	-0.17	0.24	-0.013	-0.002
216	9.29	0.18	-1.94	0.28	-0.18	0.24	-0.016	-0.003
218	9.31	0.18	-1.96	0.29	-0.17	0.24	-0.017	-0.002
220	9.32	0.18	-1.97	0.29	-0.17	0.24	-0.017	-0.005
222	9.38	0.18	-2.01	0.29	-0.17	0.24	-0.019	-0.003
224	9.37	0.18	-2.01	0.29	-0.17	0.24	-0.020	-0.004
226	9.42	0.18	-2.03	0.29	-0.18	0.24	-0.019	-0.001
228	9.46	0.17	-2.06	0.27	-0.17	0.23	-0.018	-0.001
230	9.49	0.18	-2.06	0.27	-0.19	0.23	-0.018	-0.002
232	9.53	0.16	-2.09	0.26	-0.17	0.21	-0.015	-0.001
234	9.58	0.16	-2.10	0.25	-0.17	0.21	-0.015	-0.001
236	9.59	0.15	-2.13	0.23	-0.18	0.20	-0.011	0.002
238	9.63	0.13	-2.16	0.21	-0.17	0.19	-0.008	0.000
240	9.65	0.13	-2.16	0.21	-0.17	0.18	-0.008	0.001
242	9.67	0.13	-2.16	0.20	-0.16	0.16	-0.007	0.001
244	9.71	0.11	-2.20	0.17	-0.17	0.16	-0.005	0.002
246	9.73	0.10	-2.21	0.17	-0.17	0.15	-0.003	0.001
248	9.74	0.09	-2.24	0.16	-0.17	0.15	-0.001	0.001
250	9.76	0.09	-2.24	0.15	-0.17	0.14	-0.001	0.001
252	9.76	0.08	-2.25	0.14	-0.17	0.14	-0.001	0.001
254	9.80	0.08	-2.28	0.13	-0.16	0.12	0.001	0.001
256	9.80	0.08	-2.27	0.13	-0.16	0.12	0.001	0.001
258	9.84	0.07	-2.29	0.12	-0.15	0.11	0.001	0.002
260	9.85	0.07	-2.32	0.12	-0.15	0.12	0.002	0.001
262	9.87	0.07	-2.33	0.13	-0.15	0.11	0.002	0.001
264	9.89	0.07	-2.34	0.12	-0.15	0.11	0.002	0.001
266	9.92	0.07	-2.36	0.12	-0.15	0.11	0.002	0.001
268	9.94	0.07	-2.38	0.12	-0.14	0.11	0.002	0.000
270	9.92	0.07	-2.39	0.12	-0.15	0.11	0.001	0.001
272	9.96	0.06	-2.42	0.12	-0.14	0.11	0.002	0.001
274	9.99	0.07	-2.42	0.12	-0.15	0.12	0.002	0.001
276	10.01	0.07	-2.45	0.12	-0.14	0.11	0.003	0.001
278	10.02	0.07	-2.47	0.13	-0.14	0.11	0.002	0.001
280	10.02	0.07	-2.48	0.13	-0.14	0.11	0.003	0.001
282	10.04	0.07	-2.49	0.13	-0.14	0.12	0.002	0.000
284	10.07	0.07	-2.53	0.13	-0.16	0.12	0.003	0.001
286	10.08	0.07	-2.54	0.13	-0.14	0.12	0.002	0.001
288	10.11	0.07	-2.57	0.13	-0.16	0.12	0.003	0.002
290	10.12	0.07	-2.57	0.12	-0.15	0.13	0.003	0.002
292	10.10	0.08	-2.58	0.13	-0.16	0.13	0.003	0.000
294	10.13	0.08	-2.61	0.13	-0.16	0.13	0.004	0.001
296	10.15	0.08	-2.63	0.13	-0.15	0.12	0.003	0.001
298	10.17	0.08	-2.64	0.14	-0.15	0.13	0.004	0.002
300	10.19	0.08	-2.67	0.13	-0.17	0.12	0.003	0.002
310	10.26	0.09	-2.76	0.14	-0.18	0.13	0.005	0.002
320	10.34	0.09	-2.85	0.14	-0.21	0.14	0.004	0.003
330	10.41	0.10	-2.94	0.14	-0.27	0.16	0.004	0.003
340	10.49	0.09	-3.02	0.14	-0.32	0.16	0.004	0.005
350	10.58	0.10	-3.09	0.15	-0.37	0.17	0.005	0.006
360	10.59	0.11	-3.13	0.14	-0.43	0.20	0.004	0.008
370	10.66	0.11	-3.19	0.13	-0.49	0.20	0.004	0.007
380	10.69	0.11	-3.23	0.13	-0.51	0.22	0.006	0.005

Contd...

390	10.76	0.12	-3.24	0.13	-0.47	0.23	0.006	0.006
400	10.83	0.11	-3.16	0.12	-0.54	0.19	0.005	0.001
410	10.90	0.11	-3.08	0.11	-0.49	0.24	0.005	0.001
420	11.04	0.16	-2.97	0.12	-0.44	0.31	0.006	0.006
430	10.57	0.46	-2.61	0.28	-0.57	0.45	0.014	0.031
440	6.84	1.16	-1.32	0.69	-0.63	0.99	0.116	0.032
450	2.34	0.90	0.36	0.59	0.01	0.60	0.081	-0.046
451	2.10	0.81	0.39	0.55	-0.03	0.54	0.101	-0.049
452	1.90	0.70	0.42	0.53	-0.03	0.53	0.099	-0.054
453	1.72	0.64	0.40	0.50	-0.12	0.50	0.096	-0.052
454	1.59	0.58	0.34	0.46	-0.17	0.50	0.066	-0.053
455	1.37	0.51	0.27	0.41	-0.29	0.48	0.041	-0.081

Table A3.8: Measurements of mean and turbulence quantities in the normal direction (y) at station 4.

Station 5 – mean velocities and turbulence quantities

U_o = 9.85 (m/s), P_a = 750 (mm Hg), T_a = 287 (K), **z/H** = 0.5

y (mm)	Umean (m/s)	Urms (m/s)	Vmean (m/s)	Vrms (m/s)	Wmean (m/s)	Wrms (m/s)	$\overline{u'v'}$ (m^2/s^2)	$\overline{u'w'}$ (m^2/s^2)
2	8.04	0.91	0.29	0.51	-0.16	0.76	-0.133	-0.091
4	8.79	0.90	0.27	0.45	-0.28	0.74	-0.125	-0.083
6	9.39	0.80	0.27	0.40	-0.47	0.69	-0.100	-0.117
8	9.48	0.73	0.32	0.40	-0.42	0.70	-0.100	-0.073
10	9.69	0.64	0.33	0.40	-0.43	0.69	-0.080	-0.057
20	9.83	0.48	0.46	0.55	-0.45	0.63	-0.057	-0.022
30	9.93	0.45	0.44	0.69	-0.35	0.59	-0.067	-0.006
40	9.91	0.46	0.44	0.72	-0.28	0.54	-0.085	-0.002
50	9.94	0.47	0.45	0.72	-0.21	0.52	-0.097	-0.002
60	10.00	0.46	0.39	0.66	-0.16	0.47	-0.109	-0.008
70	10.07	0.44	0.35	0.61	-0.13	0.42	-0.107	-0.020
80	10.13	0.42	0.33	0.57	-0.11	0.40	-0.100	-0.017
90	10.21	0.35	0.24	0.47	-0.12	0.33	-0.072	-0.015
92	10.22	0.32	0.23	0.45	-0.13	0.32	-0.058	-0.018
94	10.23	0.35	0.24	0.47	-0.12	0.30	-0.066	-0.012
96	10.29	0.30	0.21	0.41	-0.14	0.30	-0.049	-0.012
98	10.27	0.30	0.22	0.41	-0.13	0.29	-0.049	-0.013
100	10.29	0.27	0.21	0.39	-0.14	0.28	-0.040	-0.011
102	10.31	0.26	0.19	0.36	-0.14	0.26	-0.034	-0.009
104	10.28	0.25	0.18	0.36	-0.15	0.23	-0.034	-0.007
106	10.34	0.23	0.18	0.35	-0.15	0.24	-0.029	-0.007
108	10.31	0.27	0.20	0.38	-0.16	0.23	-0.035	-0.005
110	10.36	0.22	0.18	0.32	-0.15	0.23	-0.022	-0.006
112	10.35	0.20	0.17	0.30	-0.16	0.22	-0.019	-0.005
114	10.33	0.18	0.15	0.28	-0.16	0.21	-0.012	-0.005
116	10.33	0.20	0.17	0.32	-0.17	0.20	-0.019	-0.002
118	10.36	0.16	0.13	0.24	-0.18	0.19	-0.011	-0.003
120	10.35	0.15	0.13	0.24	-0.19	0.18	-0.006	-0.002
122	10.36	0.15	0.15	0.23	-0.18	0.17	-0.005	-0.001
124	10.39	0.15	0.13	0.23	-0.19	0.17	-0.005	-0.001
126	10.34	0.15	0.13	0.23	-0.19	0.16	-0.007	0.000
128	10.37	0.13	0.11	0.19	-0.19	0.16	-0.004	-0.001
130	10.35	0.11	0.10	0.16	-0.19	0.15	0.000	-0.001
132	10.37	0.11	0.10	0.16	-0.19	0.15	-0.002	0.000
134	10.39	0.12	0.10	0.18	-0.18	0.14	-0.002	-0.001
136	10.37	0.11	0.09	0.17	-0.21	0.14	-0.002	0.000
138	10.36	0.11	0.10	0.16	-0.21	0.14	0.001	0.000
140	10.37	0.10	0.09	0.15	-0.19	0.14	0.000	0.000
142	10.35	0.11	0.08	0.16	-0.20	0.13	0.000	0.000
144	10.35	0.10	0.07	0.15	-0.21	0.13	0.001	0.000
146	10.33	0.11	0.06	0.15	-0.21	0.13	0.002	0.000
148	10.33	0.10	0.05	0.14	-0.21	0.13	0.003	0.000
150	10.32	0.11	0.04	0.15	-0.21	0.13	0.003	0.001
152	10.32	0.12	0.04	0.16	-0.20	0.14	0.004	0.000
154	10.33	0.12	0.04	0.17	-0.20	0.14	0.006	0.000
156	10.26	0.13	0.03	0.18	-0.21	0.15	0.007	0.000

Contd...

158	10.27	0.15	0.02	0.18	-0.20	0.16	0.009	-0.001
160	10.23	0.15	0.02	0.19	-0.19	0.17	0.010	-0.002
162	10.20	0.15	0.01	0.19	-0.18	0.18	0.008	-0.001
164	10.19	0.16	0.01	0.21	-0.17	0.19	0.007	-0.002
166	10.18	0.16	0.00	0.22	-0.17	0.20	0.004	-0.002
168	10.18	0.16	-0.01	0.23	-0.15	0.20	0.001	-0.002
170	10.16	0.17	-0.01	0.23	-0.15	0.21	-0.001	-0.001
172	10.17	0.17	-0.02	0.24	-0.14	0.21	-0.005	0.000
174	10.14	0.18	-0.03	0.25	-0.13	0.22	-0.007	0.000
176	10.13	0.18	-0.03	0.25	-0.13	0.22	-0.009	0.001
178	10.15	0.19	-0.05	0.25	-0.12	0.22	-0.012	0.001
180	10.13	0.19	-0.06	0.25	-0.13	0.22	-0.013	0.001
182	10.13	0.19	-0.05	0.26	-0.11	0.22	-0.012	0.002
184	10.11	0.20	-0.08	0.26	-0.11	0.22	-0.015	0.001
186	10.16	0.20	-0.07	0.25	-0.12	0.22	-0.015	0.001
188	10.17	0.20	-0.07	0.26	-0.11	0.22	-0.017	0.003
190	10.15	0.20	-0.08	0.26	-0.11	0.21	-0.016	0.002
192	10.18	0.20	-0.09	0.26	-0.11	0.21	-0.015	0.003
194	10.19	0.20	-0.08	0.24	-0.11	0.21	-0.014	0.003
196	10.20	0.20	-0.09	0.24	-0.10	0.20	-0.012	0.003
198	10.21	0.19	-0.10	0.23	-0.11	0.20	-0.012	0.004
200	10.24	0.20	-0.10	0.24	-0.10	0.19	-0.012	0.003
202	10.23	0.19	-0.12	0.24	-0.09	0.18	-0.008	0.002
204	10.27	0.18	-0.12	0.22	-0.09	0.18	-0.004	0.003
206	10.25	0.19	-0.13	0.23	-0.09	0.17	-0.008	0.002
208	10.30	0.17	-0.13	0.22	-0.09	0.17	-0.002	0.003
210	10.28	0.17	-0.12	0.22	-0.10	0.16	-0.002	0.001
212	10.29	0.18	-0.14	0.22	-0.10	0.16	0.000	0.003
214	10.29	0.17	-0.14	0.22	-0.09	0.16	0.000	0.003
216	10.29	0.18	-0.13	0.23	-0.10	0.15	0.002	0.002
218	10.27	0.18	-0.15	0.22	-0.09	0.15	0.004	0.001
220	10.29	0.18	-0.13	0.22	-0.10	0.15	0.002	0.002
222	10.27	0.18	-0.15	0.22	-0.09	0.14	0.005	0.001
224	10.31	0.18	-0.16	0.22	-0.09	0.14	0.007	0.001
226	10.26	0.18	-0.18	0.23	-0.09	0.14	0.007	0.001
228	10.25	0.18	-0.18	0.22	-0.09	0.15	0.007	0.001
230	10.27	0.19	-0.16	0.23	-0.10	0.15	0.008	0.001
240	10.27	0.22	-0.18	0.26	-0.10	0.16	0.011	0.000
250	10.27	0.28	-0.22	0.34	-0.12	0.20	0.017	0.001
260	10.20	0.34	-0.27	0.40	-0.13	0.23	0.020	0.000
270	10.21	0.43	-0.29	0.52	-0.20	0.31	0.035	-0.007
280	10.15	0.60	-0.33	0.71	-0.25	0.40	0.132	0.004
290	10.09	0.71	-0.33	0.83	-0.27	0.50	0.195	-0.001
300	10.00	0.90	-0.34	0.98	-0.28	0.71	0.290	-0.013
310	9.68	1.24	-0.32	1.16	-0.28	0.86	0.503	-0.074
320	9.33	1.52	-0.29	1.33	-0.26	1.10	0.752	-0.128
330	8.94	1.74	-0.20	1.44	-0.31	1.26	0.922	-0.160
340	8.35	1.96	-0.16	1.56	-0.33	1.42	1.183	-0.173
350	7.78	2.10	-0.07	1.62	-0.31	1.59	1.279	-0.206
360	7.17	2.14	0.00	1.69	-0.33	1.68	1.486	-0.279
370	6.65	2.15	-0.01	1.73	-0.35	1.70	1.457	-0.238
380	6.04	2.11	0.08	1.73	-0.34	1.67	1.417	-0.277

Contd...

390	5.54	1.97	0.00	1.69	-0.31	1.60	1.185	-0.321
400	5.14	1.93	-0.07	1.66	-0.26	1.54	1.017	-0.255
410	4.80	1.74	-0.12	1.56	-0.27	1.48	0.603	-0.254
420	4.76	1.76	-0.09	1.46	-0.31	1.52	0.448	-0.278
430	4.68	1.78	-0.07	1.31	-0.45	1.66	0.258	-0.370
440	4.59	1.79	0.04	1.11	-0.54	1.80	0.056	-0.473
450	4.05	1.81	0.31	0.83	-0.48	1.74	0.139	-0.596
451	3.95	1.75	0.32	0.75	-0.47	1.73	0.162	-0.543
452	3.94	1.77	0.36	0.72	-0.50	1.65	0.129	-0.564
453	3.71	1.71	0.39	0.65	-0.44	1.58	0.140	-0.582

Table A3.9: Measurements of mean and turbulence quantities in the normal direction (y) at station 5.

Appendix IV - Coodinate transformation in the bend

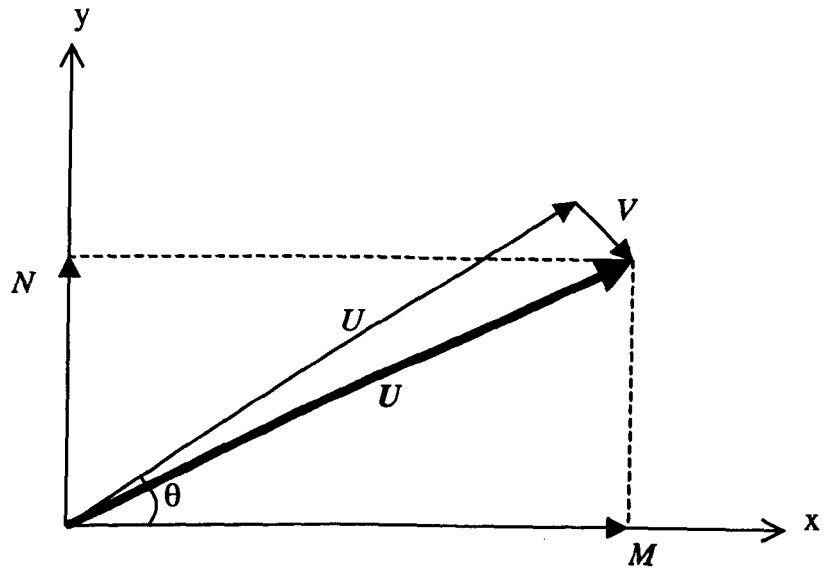

M and N are horizontal and vertical velocity components, respectively.

U and V are streamwise and radial velocity components, respectively.

$\theta = 45^0$ at station 3.

$$M = U\cos\theta + V\sin\theta \tag{A4.1}$$

$$N = U\sin\theta - V\cos\theta \tag{A4.2}$$

Similarly:

$$U = M\cos\theta + N\sin\theta = aM + bN \tag{A4.3}$$

$$V = M\sin\theta - N\cos\theta = cM - dN \tag{A4.4}$$

Where $a = d = \cos\theta$ and $b = c = \sin\theta$.

$$M = \overline{M} + m' \;,\; N = \overline{N} + n' \;,\; U = \overline{U} + u' \;,\; V = \overline{V} + v' \tag{A4.5}$$

The time-averaged of Equations (A4.3) and (A4.4) can be written as:

$$\overline{U^2} = \overline{a^2M^2} + \overline{b^2N^2} + \overline{2abMN} \tag{A4.6}$$

$$\overline{V^2} = \overline{c^2M^2} + \overline{d^2N^2} - \overline{2cdMN} \tag{A4.7}$$

Substituting Equation (A4.5) into Equations (A4.6) and (A4.7), yields:

$$\overline{u'^2} = a^2\overline{m'^2} + b^2\overline{n'^2} + 2ab\overline{m'n'} \tag{A4.8}$$

$$\overline{v'^2} = c^2\overline{m'^2} + d^2\overline{n'^2} - 2cd\overline{m'n'} \tag{A4.9}$$

$$\overline{u'v'} = ac\overline{m'^2} + (bc - ad)\overline{m'n'} - bd\overline{n'^2} \tag{A4.10}$$

where

$$\overline{UV} = \overline{U}\,\overline{V} + \overline{u'v'} \tag{A4.11}$$

Appendix V- Computational domain grid distribution

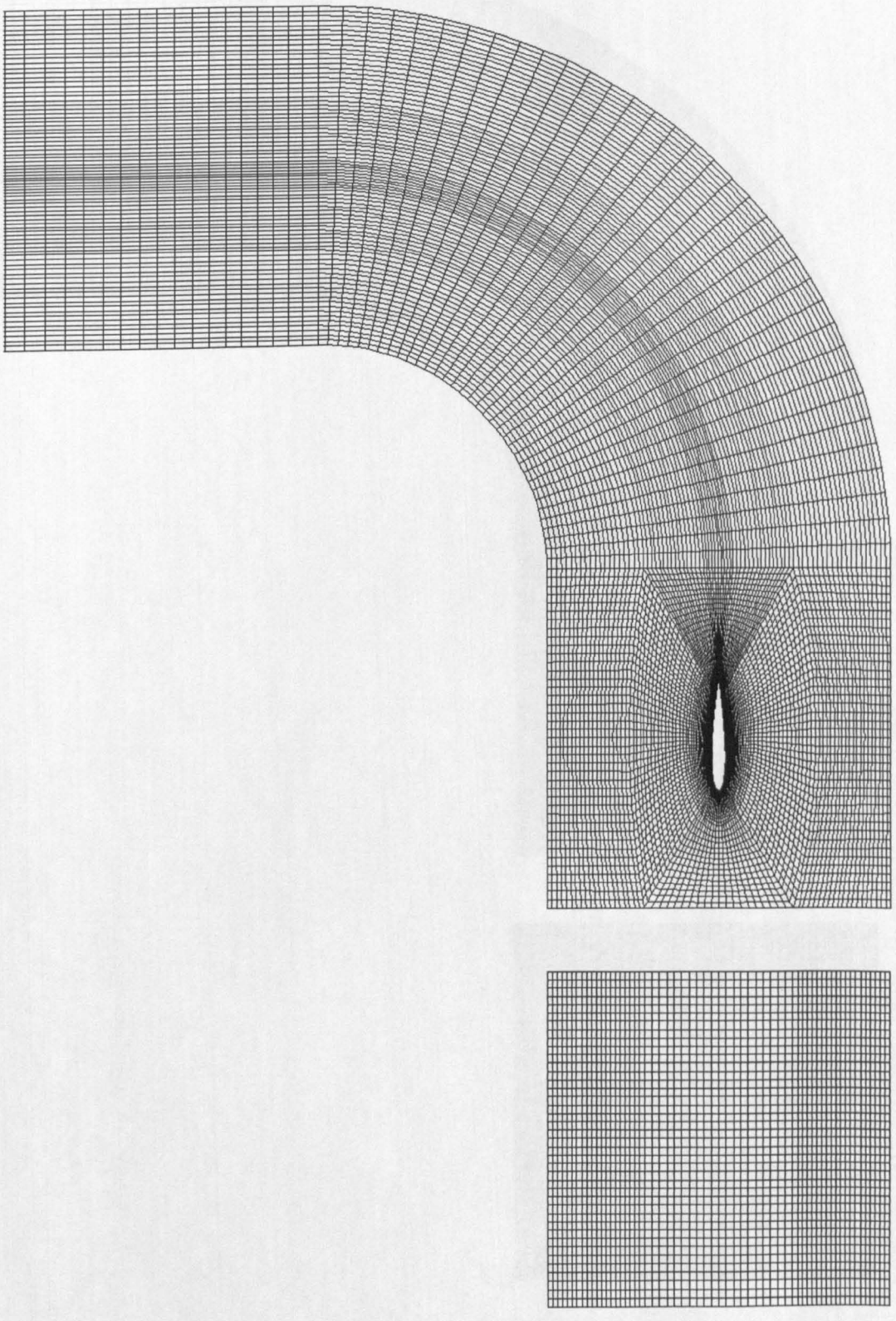

Figure A5.1: Grid distribution of the computational flow domain with airfoil; (a) y-z plane, (b) x-y plane.

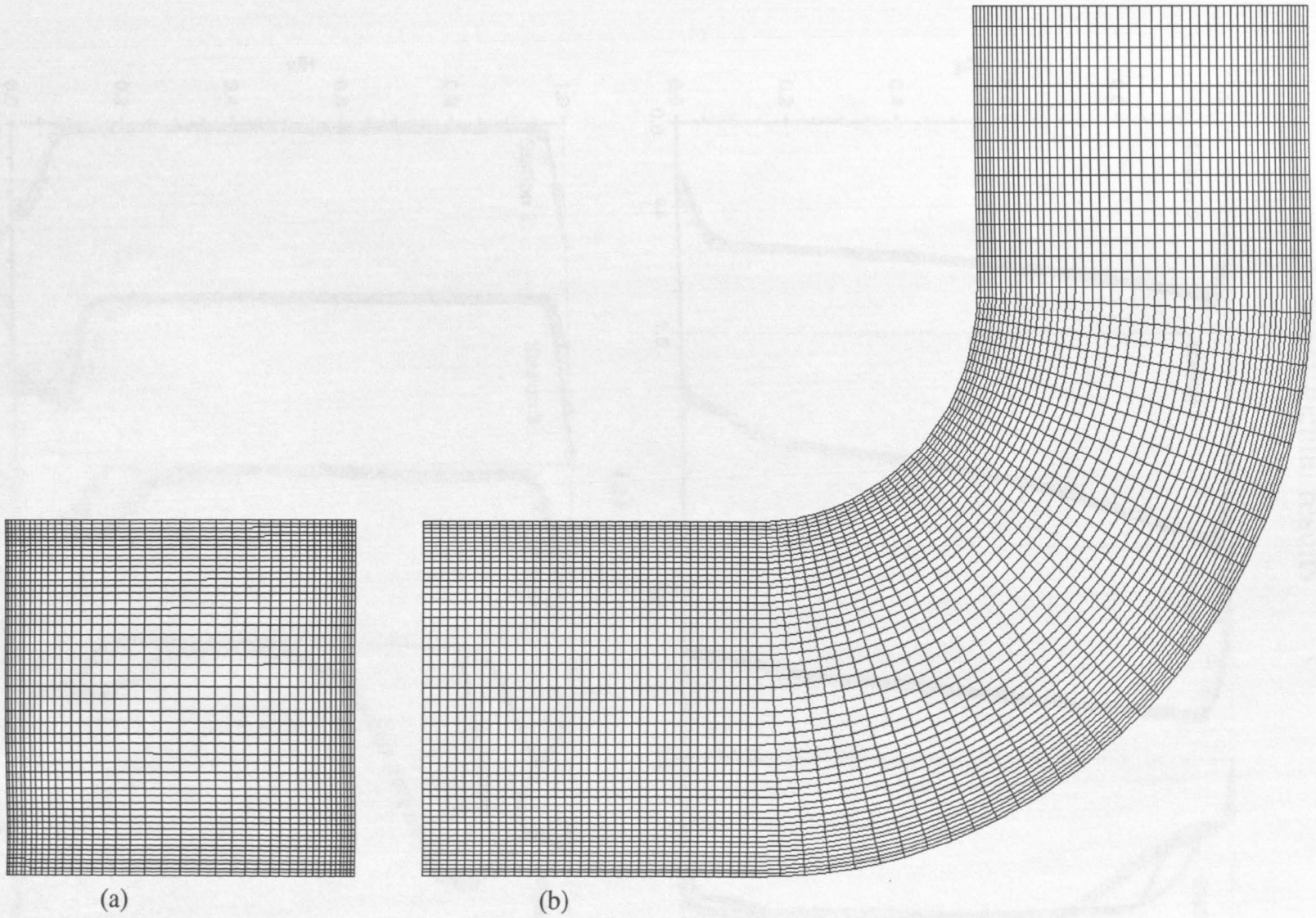

Figure A5.2: Grid distribution of the computational flow domain without airfoil; (a) y-z plane, (b) x-y plane.

Appendix VI - Comparison of different discretisation schemes with experimental results

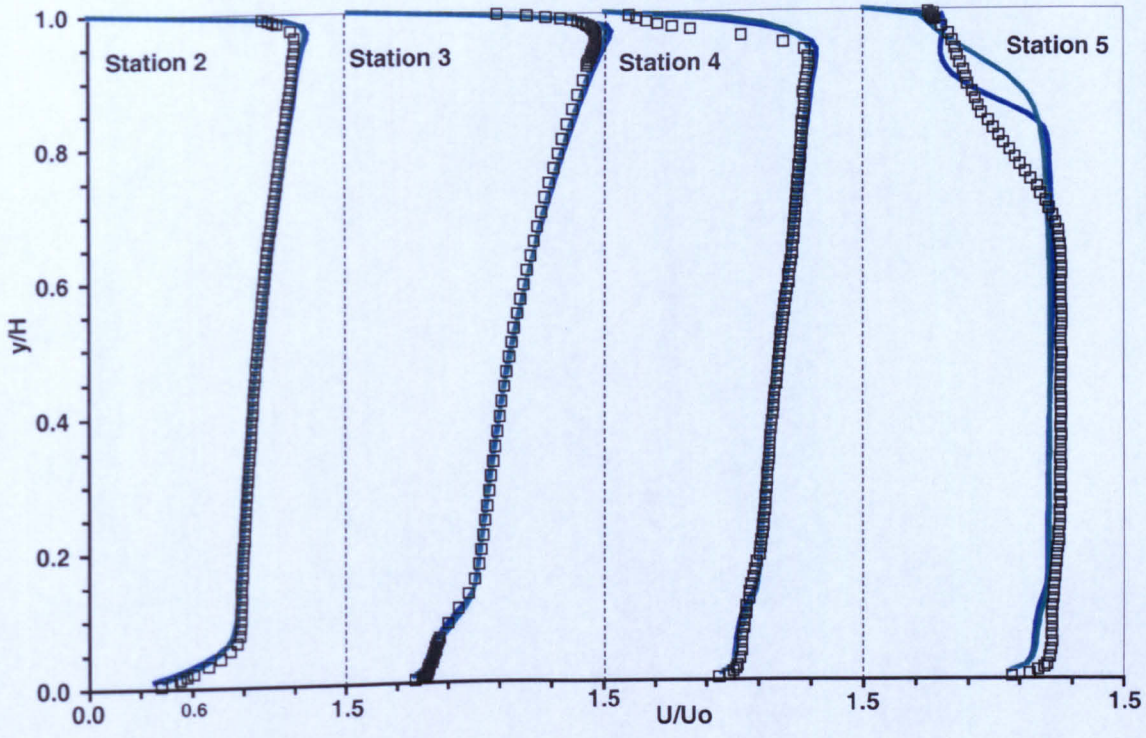

(a)

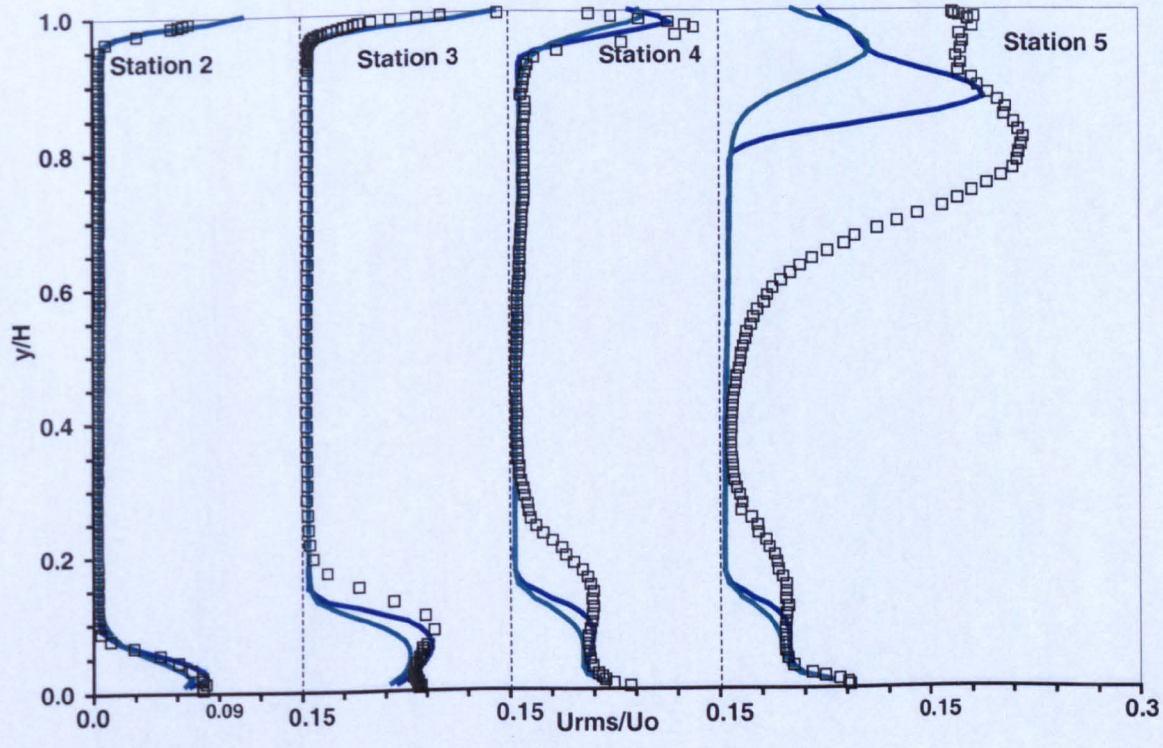

(b)

(Original in colour)

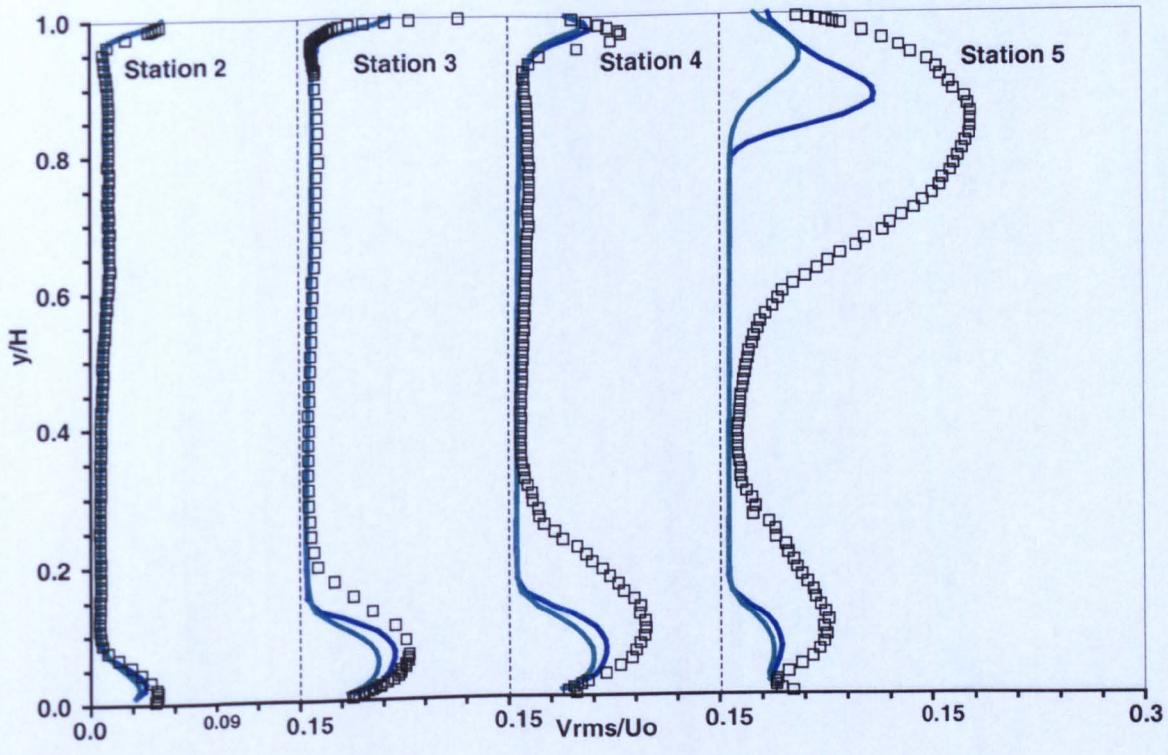

(c)

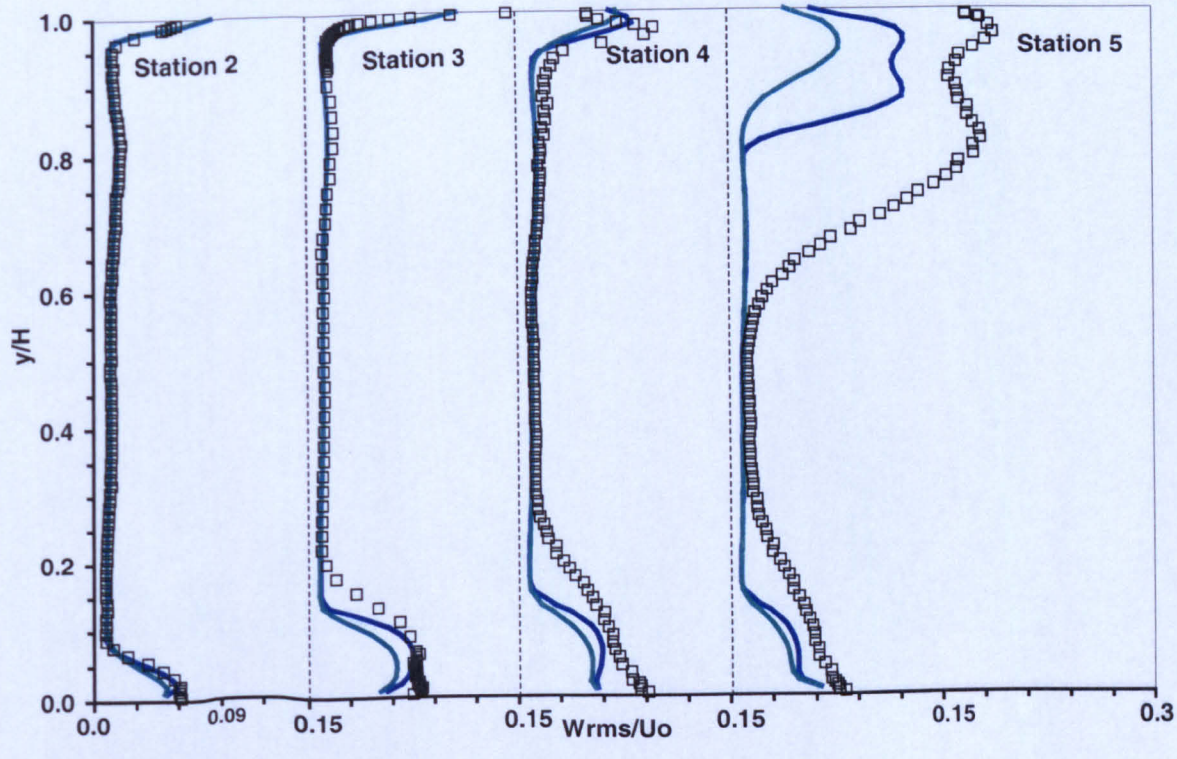

(d)

(Original in colour)

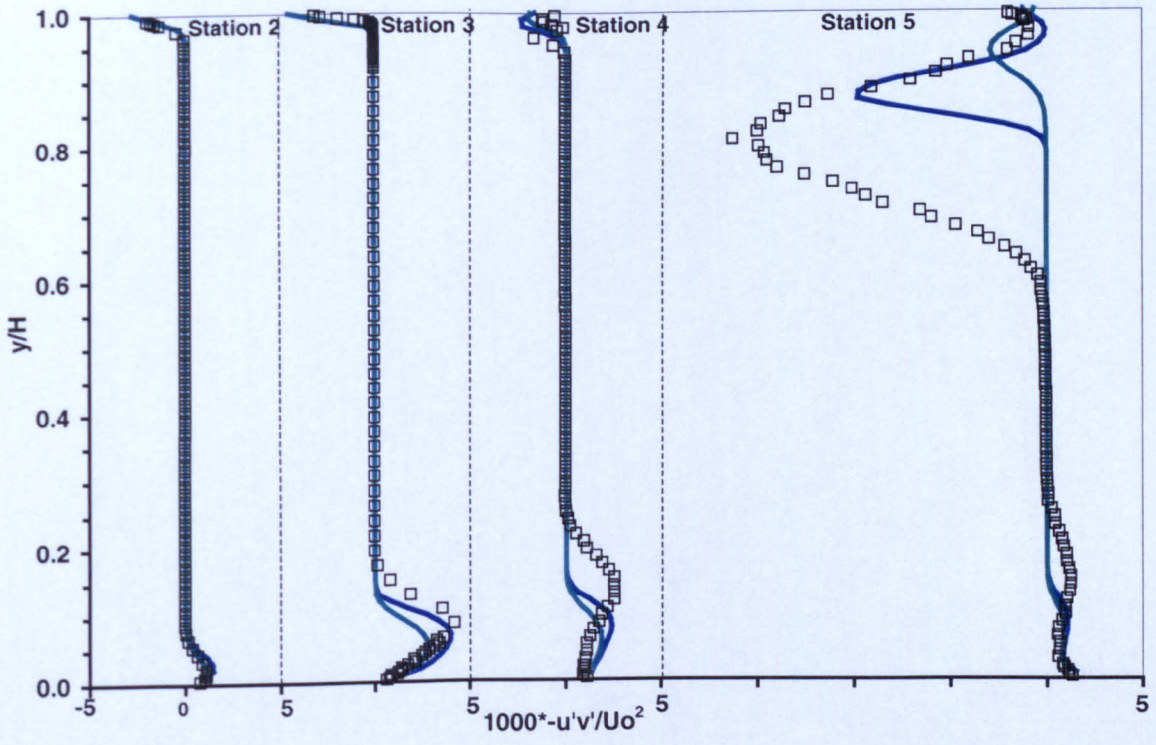

(e)

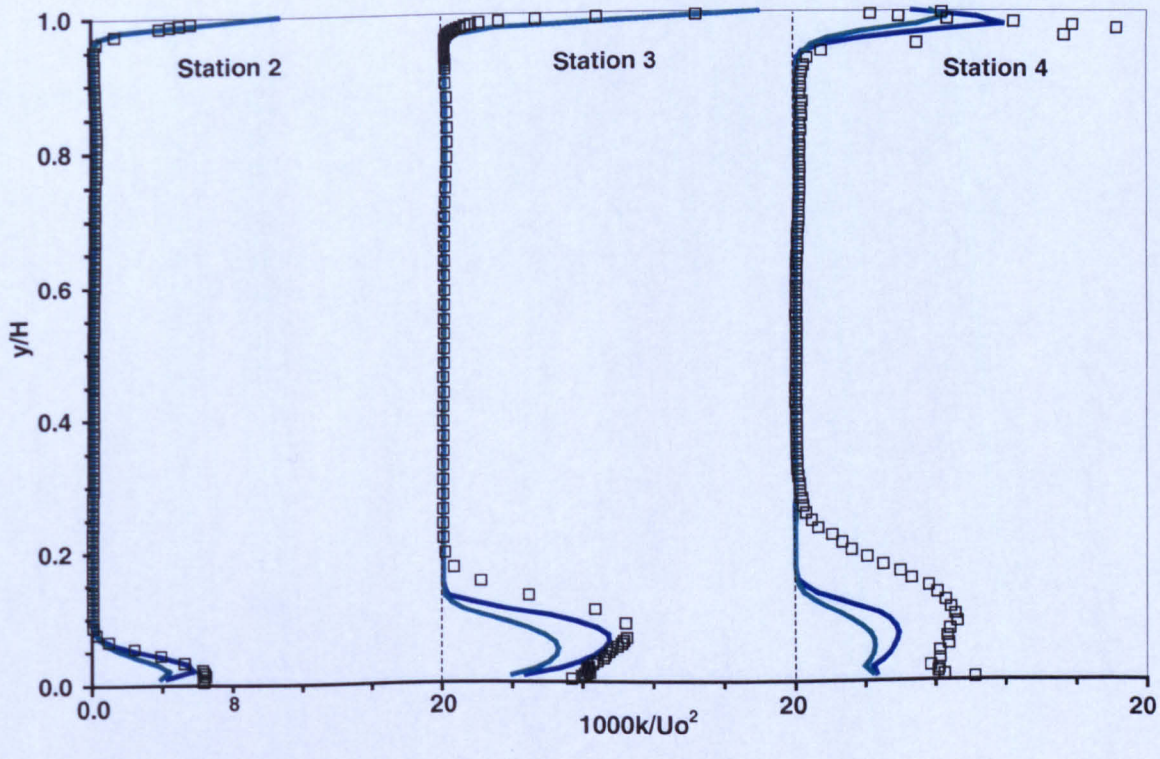

(f)

(Original in colour)

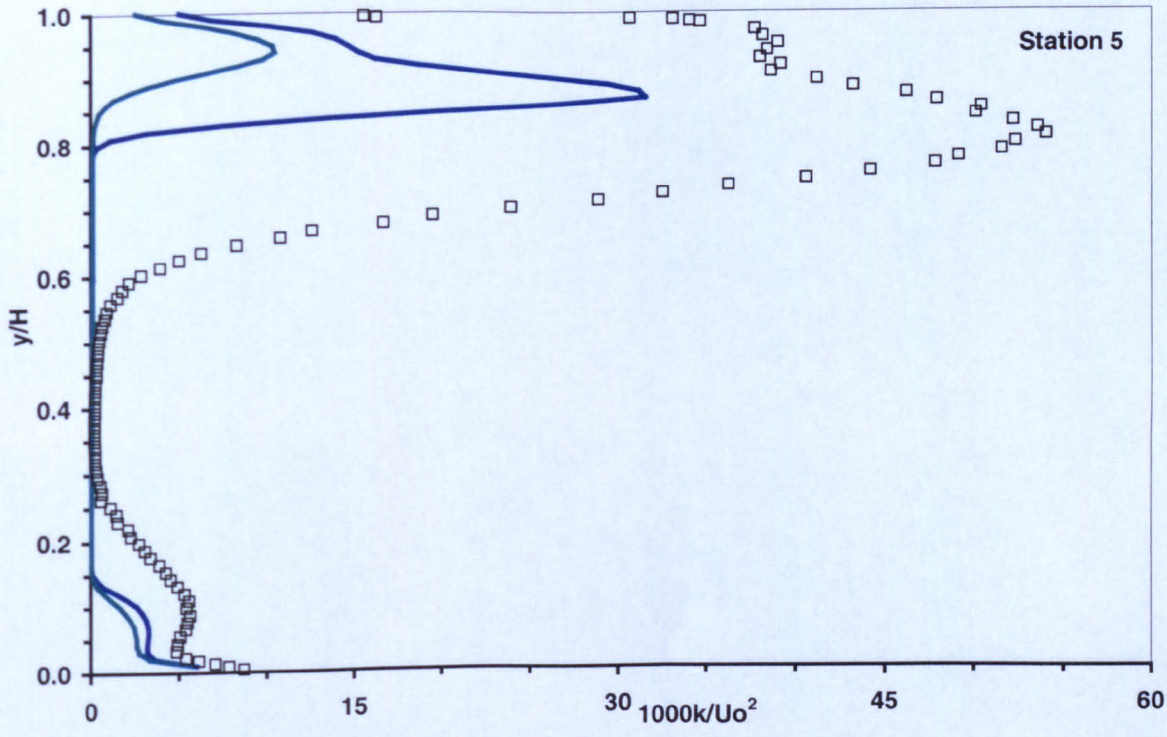

(g)

Figure A6.1: Comparison of different discretisation schemes (obtained using RSM) with experimental results at stations 2 to 5. (a) mean streamwise velocity component, (b) streamwise intensity, (c) normal intensity, (d) spanwise intensity, (e) turbulence shear stress $(-\overline{u'v'})$, (f) turbulence kinetic energy (k) at stations 2 to 4, (g) turbulence kinetic energy (k) at station 5. (Original in colour)

———, QUICK; ———, First order upwind; □, Experiment.

Appendix VII – Contour plots of Reynolds stresses in the wake

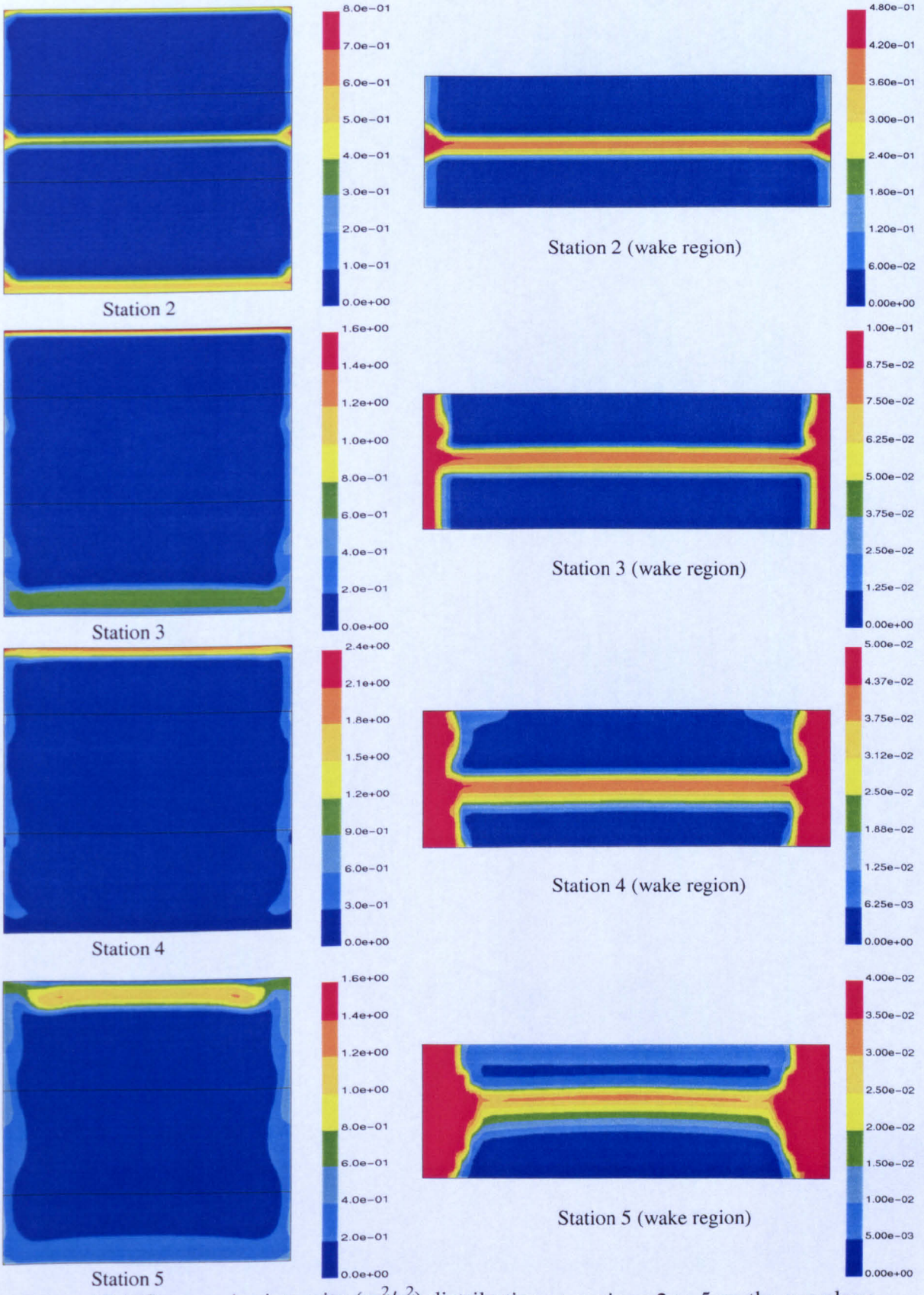

Figure A7.1: Streamwise intensity (m^2/s^2) distribution at stations 2 to 5 on the y-z plane. (Original in colour).

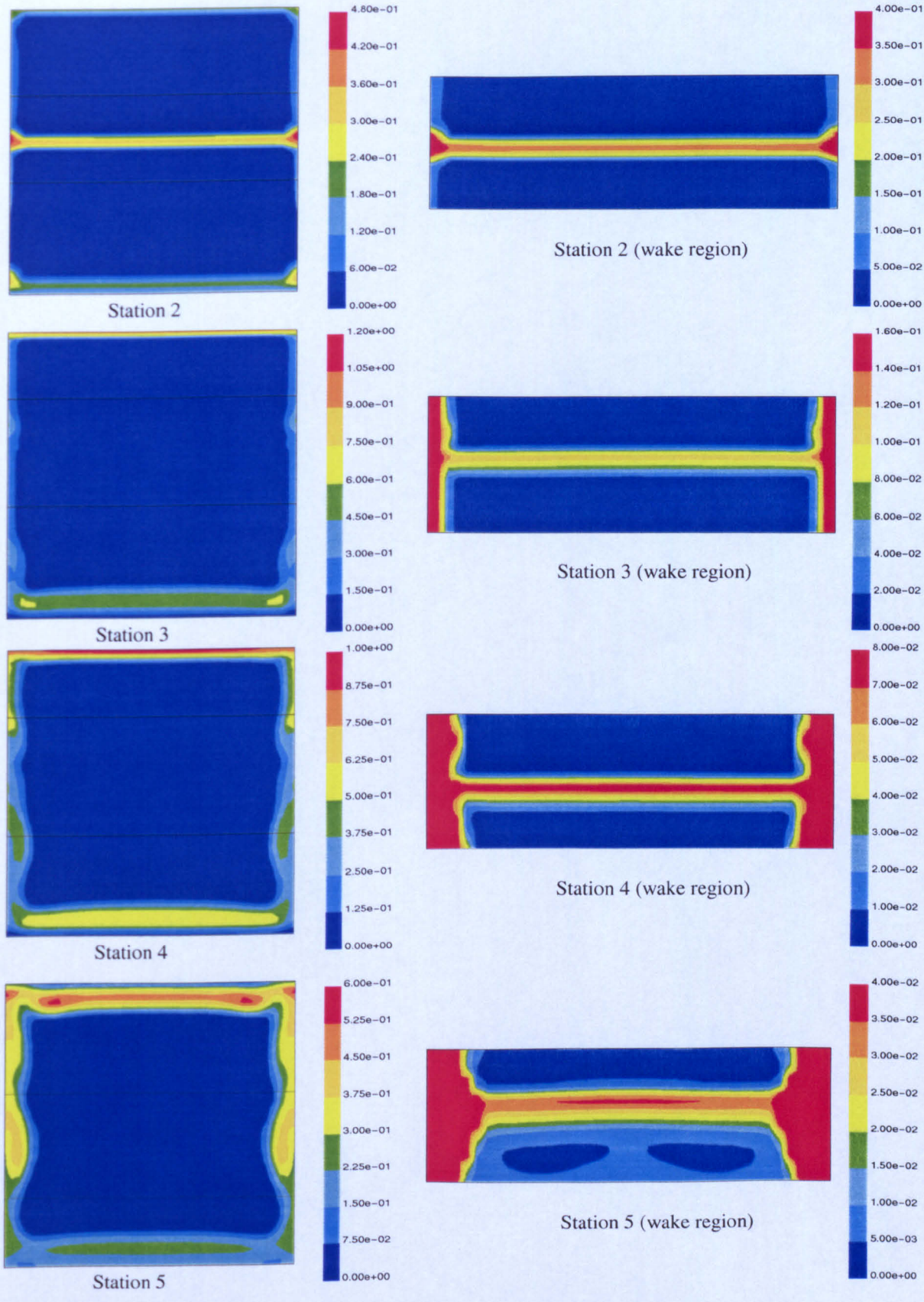

Figure A7.2: Normal intensity (m^2/s^2) distribution at stations 2 to 5 on the y-z plane. (Original in colour).

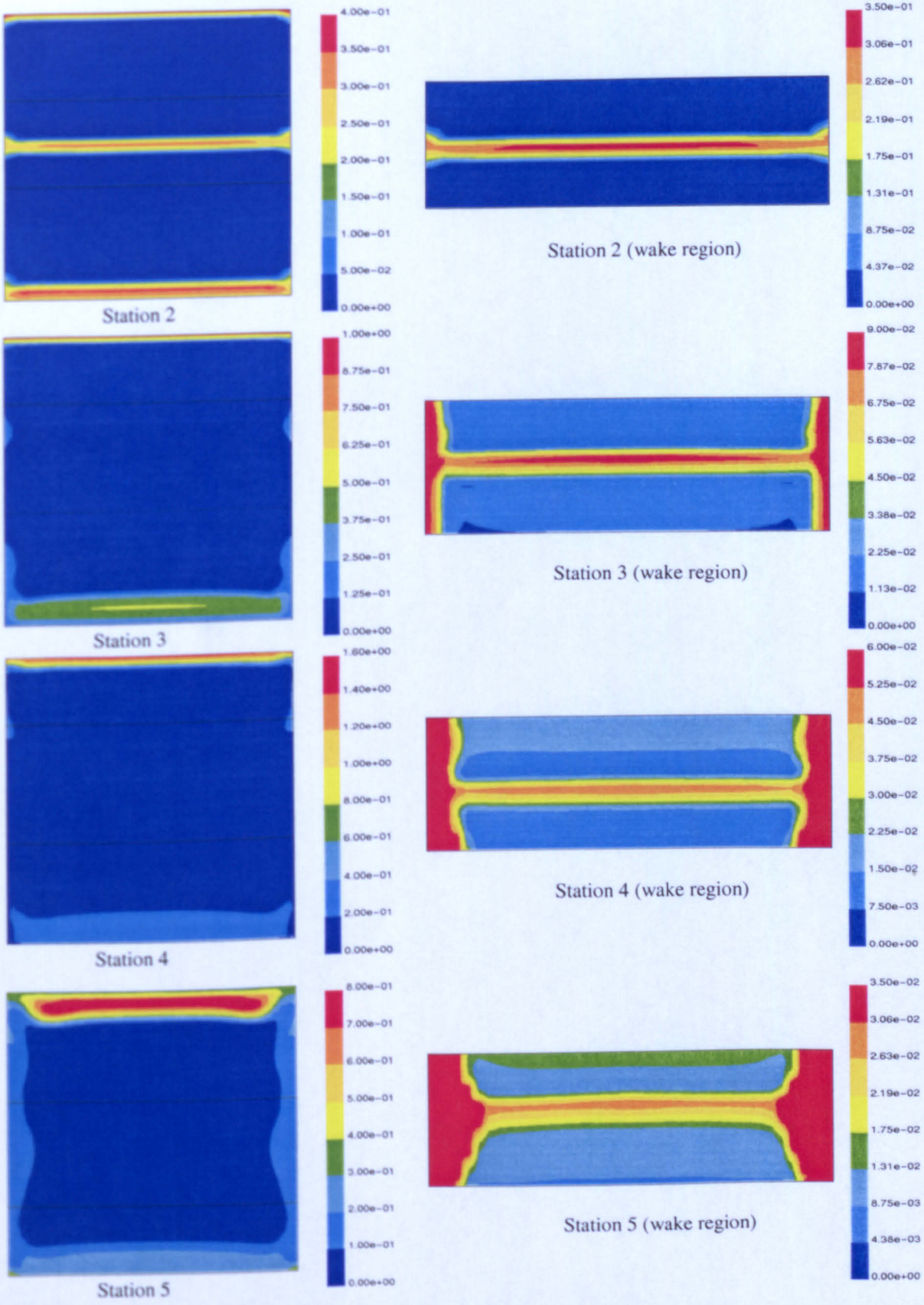

Figure A7.3: Spanwise intensity (m^2/s^2) distribution at stations 2 to 5 on the y-z plane. (Original in colour).

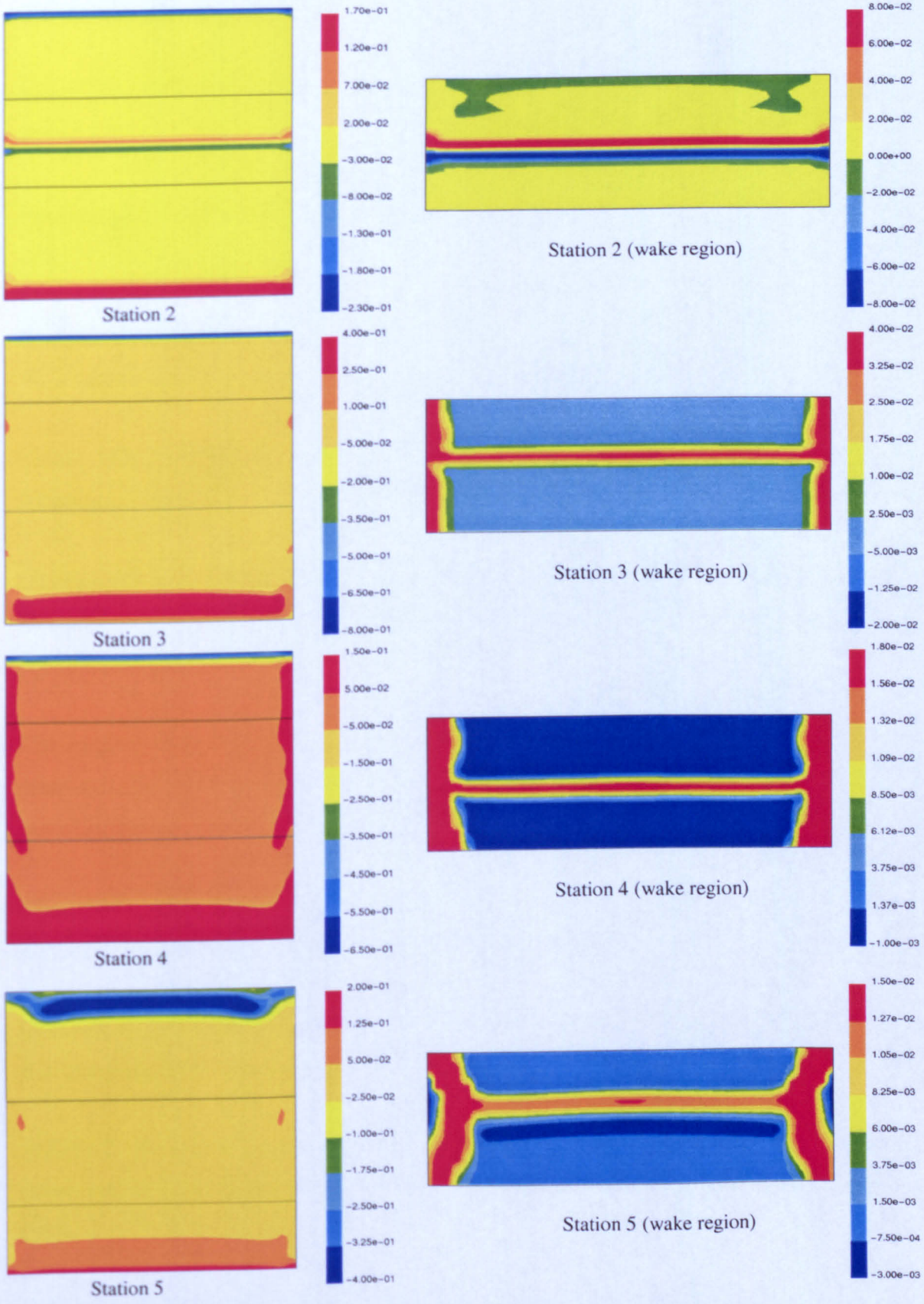

Figure A7.4: Turbulence shear stress $-\overline{u'v'}$ (m^2/s^2) distribution at stations 2 to 5 on the y-z plane. (Original in colour).

REFERENCES

Alber, I.E., (1980), Turbulent wake of a thin flat plate, *AIAA Journal*, Vol. 18, 1044-1051.

Bradshaw, P., (1973), Effects of streamline curvature on turbulent flow, *AGARDograph* 169.

Bradshaw, P., (1976), Complex turbulent flows, Theoratical and Applied Mechanics, W.T. Koiter, ed. North-Holland Publishing Company, (1976).

Bruun, H.H., (1995), Hot-wire Anemometry: Principles and signal analysis, *Oxford University Press.*

Champagne, F.H and Sleicher, C.A., (1967b), Turbulence measurements with inclined Hot-wires, part II, Hot-wire response equations, *Journal of Fluid Mechanics*, Vol. 28, pp. 177-182.

Champagne, F.H, Sleicher, C.A. and Wehrmann, O.H., (1967a), Turbulence measurements with inclined Hot-wires, part I, Heat transfer experiments with inclined hot wire, *Journal of Fluid Mechanics*, Vol. 28, pp. 153-175.

Chen, H.C., and Patel, V.C, (1988), Near wall turbulence models for complex flows including seperation, *AIAA Journal*, Vol. 26(6), pp. 641-648.

Chevray, R. and Kovasznay, L.S.G., (1969), Turbulence measurements in the wake of a thin flat plate, *AIAA Journal*, Vol. 7, pp. 1641-1643.

FLUENT 5 User's guide, (1998), Fluent Incorporated, Worldwide Corporate Headquaters, Centerra Resource Park, 10 Cavendish Court, Lebanon, NH 03766-1442, USA.

Goldstein, R.J., (1983), Fluid Mechanics measurements, Hemisphere Publication

Corporation.

Hinze, J.O., (1975), Turbulence, 2nd Edition, McGraw-Hill, New York.

John, J., Schobeiri, M.T., (1996), Development of a two-dimensional turbulent wake in a curved channel with a positive streamwise pressure gradient, Transactions of the ASME, *Journal of Fluids Engineering*, Vol. 118, pp. 292-298.

Kim, S.E., Choudhury, D. and Patel, B., (1997), Computations of complex turbulent flows using the commercial code FLUENT, In *proceedings of the ICASE / LaRC / AFOSR Symposium on modeling complex turbulent flows*, Hampton, Virginia.

Kotb, N.A.E., (1988), Flow in sharp bends with or without a guide vane; an experimental and numerical study, Ph.D. Thesis, Department of Mechanical Engineering, Brunel University.

Koyama, H.S., (1983), Effects of streamline curvature on laminar and turbulent wakes, *Proc. of Forth Symp. On Turbulent Shear Flows*, University of Karlsruhe, Karlsruhe, Germany, pp. 141-155.

Launder, B.E., Spalding, D.B., (1972b), Mathematical models of turbulence, Academic press, New York.

Launder, B.E., Spalding, D.B., (1974), The numerical computation of turbulent flows, *Computer Methods in Applied Mechanics and Engineering* 3, pp. 269-289.

Launder, B.E., Spalding, D.B., (1972a), Turbulence models and their application to the prediction of internal flows, *Heat and Fluid Flow*, Vol. 2, No. 1, pp. 43-55.

Leonard, B.P., (1979), A stable and accurate convective modelling procedure based on Quadratic upstream interpolation, *Computer Methods in Applied Mechanics and Engineering*, Vol. 19, pp. 59-98.

Lomas, C.G., (1986), Hot-wire Anemometer, Cambridge University Press.

Mokhtarzadeh-Dehghan, M.R. and Yuan, Y.M., (2002), Measurement of turbulence quantities and bursting period in developing turbulent boundary layers on the concave and convex walls of a 90° square bend, *Journal of experimental Thermal and Fluid Science*, under review.

Nakayama, A., (1987), Curvature and pressure-gradient effects on a small-defect wake, *Journal of Fluid Mechanics*, Vol. 175, pp. 215-246.

Narasimhan, J.L, Ramjee, V., Diwakar, Philip. M. and Tulapurkara. E.G., (1991), Prediction of wake in a curved duct, *International Journal for Numerical Methods in Fluids*, Vol.13, pp. 907-916.

Ondore, F.A., (1999), An experimental and numerical investigation of turbulent flows in a square duct with 90° bend, Ph.D. Thesis, Department of Mechanical Engineering, Brunel University.

Patankar, S.V. and Spalding, D.B., (1972), A calculation procedure for heat, mass and momentum transfer in three-dimensional parabolic flows, *Journal of Heat and Mass Transfer*, Vol. 15, p. 1787.

Patankar, S.V., (1988), Recent developments in computational heat transfer, *Journal of Heat Transfer*, Vol. 110, pp. 1037-1045.

Patel, V.C., Rodi, W., Scheuerer, G., (1985), Turbulence models for near-wall and low Reynolds number flows: A review, *AIAA Journal*, Vol. 23, no. 9, pp. 1308-1319.

Perry, A.E., (1982), Hot-wire Anemometry, Oxford, Clarendon.

Ramaprian, B.R., Patel, V.C. and Sastry, M.S., (1981), Turbulent wake development behind streamlined bodies, Institute of Hydraulic Research, University of Iowa city, IIHR Rept 231.

Ramaprian, B.R., Patel, V.C. and Sastry, M.S., (1982), The symmetric turbulent wake of a flat plate, *AIAA Journal*, Vol. 20, pp. 1228-1235.

Ramjee .V and Neelakandan, D., (1990), Curvature effects on the wake of an airfoil and other bodies, *Fluid Dynamics Research* 6, pp. 1-13.

Ramjee, V. and Neelakandan, D., (1989), Development of wake of a rectangular cylinder in a curved stream, *Experiments in Fluids* 7, pp. 395-399.

Ramjee, V., Tulapurkara, E.G. and Rajasekar, R., (1988), Development of airfoil wake in a longitudinally curved stream, *AIAA Journal*, Vol. 26, No 8, pp. 948-953.

Reynolds, A.J., (1974), Turbulent flows in Engineering, John Wiley & Sons Ltd, London.

Rodi, W., (1980), Turbulence models and their applications in hydraulics- A state of the art review, *International association for hydraulic research, Delft.*

Savil, A.M., (1983), The turbulence structure of a highly curved two-dimensional wake, *Proceeding of the IUTAM symposium on complex turbulent flows*, edited by R. Dumas, and F. Fulachier, Springer-Verlag, Berlin, pp.185-197.

Schlichting. H., (1979), Boundary layer theory, Translated by J. Kestin. Forth Edittion.

Schobeiri, M.T., John, J., Pappu, K., (1996), Development of two-dimensional wakes within curved channels: Theoretical framework and experimental investigation, Transactions of the ASME, *Journal of Turbomachinery*, Vol. 118, pp. 506-518.

Schobeiri, M.T., Pappu, K. and John, J., (1995), Theoretical and Experimental study of development of two-dimensional steady and unsteady wakes within curved channels, *Journal of Fluids Engineering*, Vol. 117, pp. 593-598.

Shih, T.H., Liou, W.W., Shabbir, A. and Zhu, J., (1995), A new k-ε Eddy-viscosity

model for high Reynolds number turbulent flows- Model development and validation. *Computers Fluids*, 24(3), pp. 227-238.

Starke, A.R., Henkes, R.A.W.M., Tummers, M.J., (1999), Effects of curvature and pressure gradient on a turbulent near wake, *Journal of Experimental Thermal and Fluid Science*, 19, pp. 49-56.

Streamline / StreamWare Installation & user's guide, Vol. 1-3, Dantec Measurement Technology A/S, Denmark., (2000).

Tulapurkara, E.G., Ramjee, V. and Jacob, G., (1994), Development of wake in presence of both curvature and pressure gradient, FED-Vol.184, *Boundary layer and free Shear flows*, ASME 1994, pp. 195-202.

Tulapurkara, E.G., Ramjee, V. and Jacob, G., (1995), Development of a bluff body wake under the combined influence of curvature and pressure gradient, *Experiments in Fluids* 18, pp. 311-318.

Tulapurkara, E.G., Ramjee. V. and Jacob, G., (1996), Prediction of aerfoil wake subjected to the effects of curvature and pressure gradient, *International Journal for Numerical Methods in Fluids*, Vol. 22, pp. 29-41.

Tulapurkara, E.G., Vengadesan, S. and Lakshminarasimhan, J., (1993), Computation of turbulent asymmetric wake, *International Journal for Numerical Methods in Fluids*, Vol. 16, pp. 239-248.

Versteeg, H.K. and Malalasekera, W., (1995), An introduction to Computational fluid dynamics, The finite volume method, Longmans Scientific and Technical books.

Ward-Smith, A.J., (1971), Pressure losses in ducted flows. Butterworth, London.

Weygandt, J.H and Rabindra, D.M., (1995), Three-dimensional structure of straight and curved plane wakes, *Journal of Fluid Mechanics*, Vol. 282, pp. 279-311.

Wolfstein, M., (1969), The velocity and temperature distribution of one dimensional flow with turbulence augmentation and pressure gradient, *International Journal of Heat and Mass Transfer*, Vol.12, pp. 301-318.

Yakhot, V., Orszag, S.A., Thangam, S., Gatski, T.B. and Speziale, C.G., (1992), Development of turbulence models for shear flows by a double expansion technique, *Phys. Fluids A*, Vol. 4, No. 7, pp. 1510-1520.

Yuan, Y.M., (1991), An experimental study of coherent structures in turbulent boundary layers, Ph.D. Thesis, Department of Mechanical Engineering, Brunel University.

BIBLIOGRAPHY

Bradshaw, P., (1970), Prediction of the turbulent near wake of a symmetrical airfoil, *AIAA Journal*, Vol. 8, pp. 1507-1508.

Carlson, J.R., Duquesne, N., Rumsey, C.L., Gatski, T.B., (2001), Computation of turbulent wake flows in variable pressure gradient, Computers & Fluids, no. 30, pp. 161-187.

CFX-4 User Manual, (1997), UK Atomic Energy Agency Technology.

Gartshore, I.S., (1967), Two-dimensional turbulent wakes, *Journal of Fluid Mechanics*, Vol. 30, part 3, pp. 547-560.

Hah, C. and Lakshminarayana, B., (1982), Measurements and prediction of mean velocity and turbulence structure in the near wake of an airfoil, *Journal of Fluids Mechanics*, Vol. 111, pp. 251-282.

Haji - Haidari, H. and Smith, C.R., (1988), Development of the turbulent near wake of a tapered thick flat plate, *Journal of Fluid Mechanics*, Vol. 189, pp. 135-163.

Huffman, G.D. and Ng, B.S.H., (1978), Modeling of an asymmetric turbulent near wake using the interaction hypothesis, *AIAA Journal*, Vol. 16, pp. 193-194.

John, J., Schobeiri, M.T., (1996), Development of a two-dimensional turbulent wake in a curved channel with a positive streamwise pressure gradient, Transactions of the ASME, *Journal of Fluids Engineering*, Vol.118, pp. 292-299.

Kotb, N.A.E., Mokhtarzadeh-Dehghan, M.R., Ward-Smith, A.J., (1998), A numerical study of laminar and turbulent flows in a two-dimensional bend with or without a guide vane, *International Journal for Numerical Methods in Engineering*, Vol. 26, pp. 245-262.

Patel, V.C., Chen, H.C., (1987), Turbulent wake of a flat plate, *AIAA Journal*, Vol. 25, no. 8, pp. 1078-1085.

Patel, V.C., Scheuerer, G., (1982), Calculation of two-dimensional near and far wakes, *AIAA Journal*, Vol. 20, no. 7, pp. 900-907.

Rodi, W., (1980), Examples of turbulence models for incompressible flows, *AIAA Journal*, Vol. 20, No. 7, pp. 872-879.

Tulapurkara, E.G., Ramjee, V. and Rajasekar, R., (1990), Interaction between boundary layer and wakes of different bodies, *AIAA Journal*, Vol. 28, No. 6, pp. 1032-1037.

Tummers, M.J., Passchier, D.M., Henkes, R.A.W.M., (1997), Experimental investigation of an adverse pressure gradient wake and comparison with calculations, *Experimental Thermal and Fluid Science*, Vol. 14, pp. 17-24.